The University Of Sheffield.

Access to Electronic Thesis

Author:	Alistair Brown
Thesis title:	Patient-Specific Local and Systemic Haemodynamics in the Presence of a Left Ventricular Assist Device
Qualification:	PhD

This thesis was embargoed until 1st June 2015.

If this electronic thesis has been edited by the author it will be indicated as such on the title page and in the text.

The University Of Sheffield.

PATIENT-SPECIFIC LOCAL AND SYSTEMIC HAEMODYNAMICS IN THE PRESENCE OF A LEFT VENTRICULAR ASSIST DEVICE

ALISTAIR GRAHAM BROWN

School of Medicine and Biomedical Sciences

Department of Cardiovascular Science

Medical Physics Group

Submitted for the degree of PhD

Submission Date

February 2012

ABSTRACT

The ability to accurately and efficiently simulate cardiovascular dynamics has the opportunity to improve the diagnosis and intervention of vascular disease. Due to a reducing number of donor hearts, left ventricular assist devices (LVAD - mechanical blood pumps) are gaining prevalence in the treatment of severe left ventricular dysfunction. The interaction of the LVAD and native cardiovascular system is the main focus of this thesis. Computational fluid dynamic (CFD) models, of varying complexity and structure, are applied to a patient-specific aorta in the presence of a left ventricular assist device. The downstream boundary conditions of the CFD model are described initially as a simple Windkessel model before embedding the 3D domain in a closed loop 0D description of the entire cardiovascular system, incorporating models of the heart valves, chambers and the blood pump. It is shown that a turbulence model is required to simulate the haemodynamics of the assisted aorta and a compressible fluid, tuned to produce a desired wave speed, gives an accurate and efficient approximation of the wave propagation effects induced by the interaction between the blood and the elastic vessel wall. A series of CFD simulations, employing the complex 0D description of the assisted cardiovascular system, investigated the conditions under which the aortic valve opens during left ventricular support. It is found that, for a patient with moderate heart failure, the aortic valve will open when the Berlin Heart INCOR LVAD is operating at speeds of less than or equal to 5000 rpm.

ACKNOWLEDGEMENTS

Three and half years in the making and here it is...but it would not have been possible without help from some friends.

I owe a huge debt of gratitude to my supervisors Rod Hose, Pat Lawford and Yubing Shi who have put up with much and taught me even more, and to the EU project ‘euHeart’ for its financial support.

To all the occupants of I108 through the years, THANK YOU. A better bunch of misfits I could not have asked for...from Martins cheesy dad jokes to in depth DIY discussions with Ben, there has always been someone to make me smile when things were not going so well and to ask thought provoking question when things were going well.

A huge thank you goes to all my family; Mum for your unconditional optimism and belief. Dad *(my MS Word guru)* for all your vastly overpriced consultations. Stew for taking me out and getting me drunk when needed. Louise, my beautiful soon to be wife, for the seemingly never ending words of encouragement and of course not forgetting our two lovely (most of the time) dogs for helping me to forget about it all while running like a mad man through the fields surrounding Sheffield.

CONTENTS

LIST OF FIGURES

LIST OF TABLES

NOMENCLATURE

Symbol	Description	Units
$(\boldsymbol{\nabla} \times \boldsymbol{U})$	Vorticity vector	s^{-1}
$\bar{e}_i$	Activation function for the i^{th} heart chamber	Dimensionless
$\sim$	Fluctuation of a variable	Unit as variable
$\breve{}$	Resolved portion of variable	Unit as variable
$\bar{}$	Time averaged variable	Unit as variable
Γ_{stiff}	Local mesh stiffness	m^{-1}
C'	Capacitance per unit length	$m^3\ s^2\ kg^{-1}$
CV_j	Flow coefficient of the j^{th} heart valve	$m^3\ Pa^{-0.5}\ s^{-1}$
$E_{i,}$	Characteristic elastance of the i^{th} heart chamber	$kg\ s^{-2}\ m^{-4}$ ($Pa\ m^{-3}$)
L'	Inertance per unit length	$kg\ m^{-5}$
L_{Ref}	Reference length	m
L_{vk}	von Karman length scale	m
N_c	Number of cells	Dimensionless
N_s	Number of species	Dimensionless
R_c	Universal gas constant (8.3144621...)	$J\ mol^{-1}\ K^{-1}$
$S_{\emptyset}$	Additional species volumetric source term	s^{-1}
T_{pwb}	Time period used to define $\bar{e}_i$ for the atria	s
T_{pww}	Time period used to define $\bar{e}_i$ for the atria	s

T_s	Time period used to define $\bar{e}_i$ for the ventricle	s
e_i	Time varying heart chamber elastance	kg s^{-2} m^{-4} (Pa m^{-3})
$n_{i,k}$	Particle number fraction of the k^{th} species in the i^{th} cell	Dimensionless
p_{sol}	Order of the numerical solution	Dimensionless
r_0	Initial vessel radius	m
r_{max}	Radius	m
r_{mesh}	Refinement ratio of computational meshes	Dimensionless
w_i	Weighting factor of the i^{th} cell	Dimensionless
μ_{sgs}	Sub-grid scale eddy viscosity	kg m^{-1} s^{-1} (Pa s)
μ_t	Turbulent eddy viscosity	kg m^{-1} s^{-1} (Pa s)
ρ_s	Solid density	kg m^{-3}
σ_θ	Left ventricular meridional wall stress	mmHg
ϕ_{QP}	Relative phase of the pressure and flow waves	Dimensionless
$'$	Unresolved portion of variable	Unit as variable
$\emptyset$	Additional species	Units as species
C	Compliance	m^4 s^2 kg^{-1}
c	Wave speed in a fluid (Moens-Kortweg equation)	m s^{-1}
D	Diameter	m
dt	Time step	s
E	Youngs Modulus	kg m^{-1} s^{-2} (Pa)
f_{ex}	Estimate of the solution variable based on extrapolation	Unit as variable

f_i	Solution of variable on the i^{th} computational mesh	Unit as variable
g	gravity	$m^2 s^{-1}$
h	Vessel wall thickness	m
h_i	Reference length of the i^{th} computational mesh	m
k	Turbulent kinetic energy	$m^2 s^{-2}$
k	Wave number	m^{-1}
L	Inertance	kg m^{-4}
L	Length	m
M	Molar mass	kg mol^{-1}
n	Number of points used in relative error calculation	Dimensionless
P (also p)	Pressure	kg $m^{-1} s^{-2}$ (Pa)
Q	Volume flow rate	$m^3 s^{-1}$
r	Radial distance from the centreline	m
R	Resistance	kg $m^{-4} s^{-1}$
Re	Reynolds number	Dimensionless
S	Information entropy	Dimensionless
T	Period of a heart cycle	s
T	Temperature	K
t	Time	s
t_η	Kolmogorov time scale	s
u	Fluid velocity in x-direction	m s^{-1}

U	Fluid velocity vector	m s^{-1}
u_*	Frictional velocity at nearest wall	m s^{-1}
v	Fluid velocity in y-direction	m s^{-1}
w	Fluid velocity in w-direction	m s^{-1}
w_{max}	Maximum fluid velocity at the inlet	m s^{-1}
x	Position in first of three orthogonal spatial dimensions	m
y	Position in second of three orthogonal spatial dimensions	m
y^+	Non-dimensional measure of wall distance	Dimensionless
y_n	Distance from wall to first grid point	m
y_w	Distance to nearest wall	m
z	Position in third of three orthogonal spatial dimensions	m
η	Kolmogorov length scale	m
μ	Fluid viscosity	kg m^{-1} s^{-1} (Pa s)
υ	Kinematic viscosity (μ/ρ)	m^2 s^{-1}
V	Volume	m^3
δ	Displacement	m
ε	Turbulent eddy dissipation	m^2 s^{-3}
κ	Relative/Normalised entropy	Dimensionless
ν	Poisson's ratio	Dimensionless
π	Pi	Dimensionless
ρ	Fluid density	kg m^{-3}

τ	Shear Stress	Pa
τ	Diastolic Pressure Decay Time Constant	s
ω	Frequency/Turbulent frequency	s^{-1}
ω	Relaxation factor	Dimensionless
ω	Rotation rate of left ventricular assist device	rpm
ϵ	Average energy dissipation per unit mass	$m^2 s^{-3}$

CHAPTER 1

INTRODUCTION & LITERATURE REVIEW

MOTIVATION 1.1

The ability to accurately simulate cardiovascular dynamics has already improved the efficiency of design and development strategies, used within the medical device industry. The next milestone in this exciting field is to identify whether these technologies are robust and efficient enough to be translated to the clinic, where their impact could improve both diagnostic and interventional medicine.

HEART FAILURE 1.1.1

Cardiovascular disease (CVD) is responsible for 1 in 3 of all deaths in the UK, corresponding to approximately 191,000 deaths in 2008 [1]. Cardiomyopathy is a form of CVD which causes detrimental changes, *remodelling*, to the structure and contractility of the heart muscle (the myocardium). These changes result in a reduced cardiac output and often leave the native heart unable to generate sufficient output to adequately perfuse the peripheral organs and extremities. At the present time the

principal long-term treatment for cardiomyopathy is heart transplantation but with numbers of donor hearts decreasing every year (18% less heart donors in 2008 than 2007 in the UK [2]) there is a need for an alternative treatment option.

VENTRICULAR ASSIST DEVICES 1.2

A ventricular assist device (VAD) is a mechanical blood pump that supports a diseased ventricle, maintaining an adequate supply of blood to the patient's body and organs. VADs are principally used to support the left ventricle and as such this will be the configuration considered in this thesis. VADs are also used to support the right side of the heart in cases of right ventricular dysfunction although this is far rarer. However, in left ventricular cardiomyopathy there is a backup of fluid in the pulmonary system, which causes an increase in pulmonary pressure that can often be the cause of the right ventricular dysfunction. Implantation of a left ventricular assist device (LVAD) reduces the pulmonary pressure and in turn the load on the right ventricle, which may reverse the dysfunction and negate the need for a right ventricular assist device (RVAD).

Early designs of VADs involved relatively large and hence extracorporeal displacement pumps, such as the Berlin Heart EXCOR (Figure 1-1), aimed to mimic the contractility of the native heart. In order to achieve this the device required mechanical valves and other moving parts [3], which have the potential to fail. However, since these are extracorporeal devices, they can be replaced with relative ease should failure or dysfunction occur.

The second generation of VADs were simpler rotary pumps, here the only moving part is the impellor itself [4]. Rotary pumps have seen a steady increase in popularity over the last 10 years. The primary advantages are their small size (they are completely contained within the chest cavity, reducing the risk of infection), the minimal number of moving parts and their low power consumption [5]. Although it is possible to produce pulsatile flow from a rotary pump the current clinical protocol is to run the device at a constant rate of rotation (continuous mode) to prevent regurgitant flow through the VAD. Experience has shown that a layer of cells form

on the impeller and in some patients localised thrombi are also found on the impeller blades but cause no adverse effect. In the event of regurgitant flow (this is where blood moves backwards through the pump towards the heart) these thrombi can be dislodged, due to the change in the fluid forces, producing emboli which may block a downstream vessel leading, in the worst case scenario, to a stroke and even death.

The design of the third and current generation of VADs, such as the Berlin Heart INCOR (Figure 1-2), was motivated in part by a clinical demand for long term use. These have a magnetically levitated impeller. The magnetic bearing maximises pump efficiency and removes any mechanical wear associated with the mechanical bearing employed by second generation VADs, thereby improving the life-expectancy of the pump [4] [6].

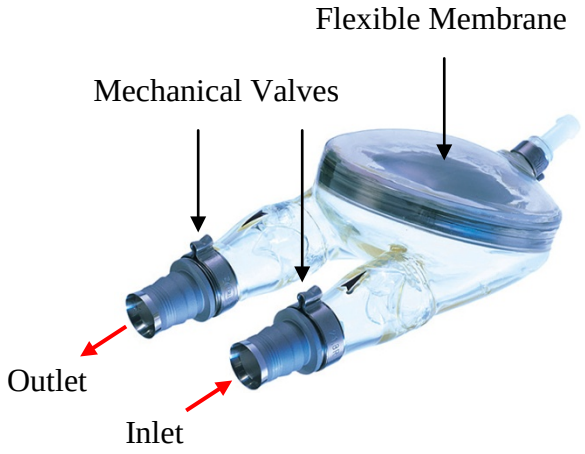

FIGURE 1-1 – ILLUSTRATION OF BERLIN HEART EXCOR DISPLACEMENT VAD

The Berlin Heart INCOR VAD (Figure 1-2) is the particular focus of this thesis. It measures just 120mm in length and has a diameter of 30mm. There are two fixed vanes located at the inlet and outlet of the pump, either side of the magnetically suspended impeller (Figure 1-1), which reduce the degree of damage to the blood as it moves through the device. To reduce further the effects of blood damage and thrombus formation all blood contacting surfaces of the pump are coated with the heparin-based Carmeda BioActive Surface. The INCOR is controlled to operate within the range of 3000 to 10,000 rpm and is able to produce a flow rate of between 4-5 litres per minute when operating at 7,500 rpm against a pressure of 100mmHg.

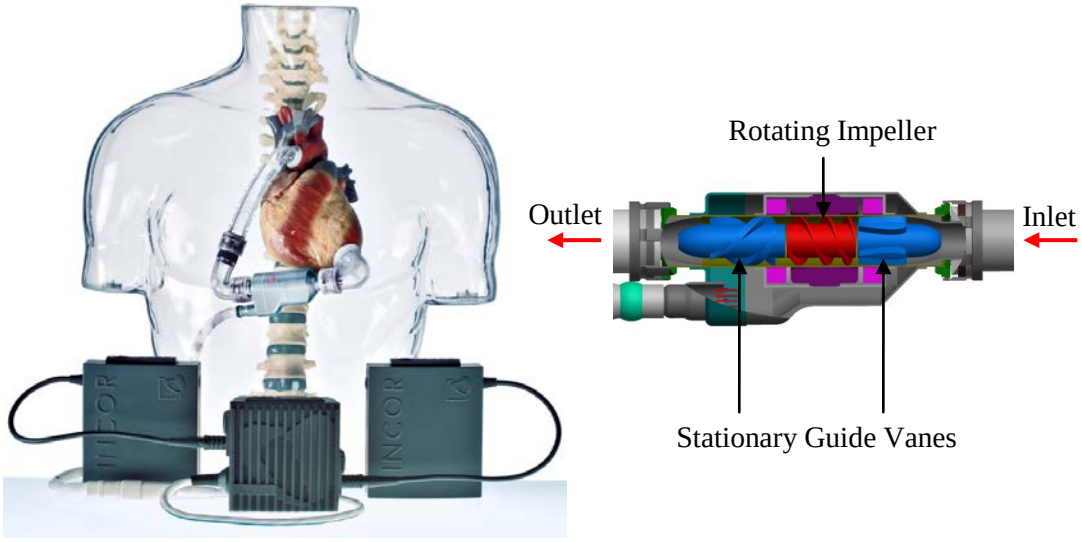

FIGURE 1-2 - ILLUSTRATION OF BERLIN HEART INCOR ROTARY VAD

VADs are an excellent example of where computational techniques are already being used in the medical device industry to improve current designs [7]. The spacing between the impeller and the pump housing as well as the impeller design is known to influence the magnitude of the shear stresses experienced by the blood cells as they move through the pump. Computational studies allow engineers to evaluate different gap distances, under a wide range of flow rates, to identify the optimal design.

INTERACTION OF LVAD AND CARDIOVASCULAR SYSTEM 1.2.1

Both displacement and rotary LVADs are connected to the ventricle in a parallel arrangement via inflow and outflow cannulas [4, 5]. The inflow cannula is attached to either the apex of the left ventricle or to the left atrium, while the outflow cannula is connected to the ascending or descending aorta. Numerical and experimental studies have investigated the merits of alternative locations for both inflow and outflow anastomoses.

Vandenberghe *et al.* and Koakianitis *et al.* demonstrated, using a lumped parameter model, that locating the inflow cannula of a rotary pump at the ventricular apex resulted in a reduction of the ventricular wall tension and the ventricular volume when compared to cannulating the atrium [8, 9]. While an *in vivo* study in calves concluded that, for displacement type VADs, under severe heart failure conditions,

the atrial configuration produced a greater stroke volume and required a less invasive procedure. However, in less severe heart failure conditions the ventricular configuration produced the largest stroke volume. An important factor to be considered is the clinical aim. In order to promote myocardial recovery it is important for the myocardium to receive a good supply of blood. Good myocardial perfusion is achieved with ventricular cannulation but not with atrial cannulation. These factors have led to the ventricular apex being the favoured site for the inflow cannula. Recent 3D numerical studies have concentrated on the influence of cannula design on the ventricular flow field [10].

The location of the outflow anastomosis has also been investigated in both numerical and experimental studies. DiGiorgi *et al.* and Litwak *et al* employed a mock circulation loop to investigate aortic haemodynamics with the outflow cannula located in the ascending aorta (AA) and the descending aorta (DA), under both displacement or rotary pump support [11, 12]. Both studies reported regions of stagnant fluid in the ascending aorta and the aortic arch when the cannula was connected to the DA, which were not apparent in the AA configuration. Dye washout periods were found to be at least 5 times greater in the DA configuration, under VAD support of 4 litres per minute [12]. These findings have been confirmed in a number of computational studies [13]. Kar *et al.* employed a 2D steady state model of the aorta to compare the AA and DA anastomotic sites, reporting turbulent structures in both models with stagnant fluid apparent in the ascending aorta of the DA configuration [13]. May-Newman *et al.* demonstrated that it is not only the location of the anastomosis but also the angle of insertion that significantly influences the structures within the flow field, concluding that a smaller angle between the cannula and aorta produces fewer secondary flow structures [14]. Laumen *et al.* conducted an experimental study of a steady state, patient-specific assisted aorta to validate a numerical model which was then used to simulate numerous cannula locations [15]. The group reported an error in the computed flow field of less than 10%, which is within the accuracy of the experimental technique used (particle image velocimetry). The location of the outflow cannula was seen to influence the distribution of flow within the aorta [15]. However, the use of constant pressure boundary conditions suggests these differences may be due to the dynamic

pressures in the system and in the physiological condition one would expect the natural homeostatic mechanisms to preserve the required flow distributions. In work conducted as part of this PhD Brown *et al.* performed a transient analysis of a 3D patient-specific assisted aorta with the outflow cannula located in the AA, the DA and the aortic arch [16]. The authors concluded that the AA configuration not only prevented fluid stagnation in the aorta but also reduced the magnitude of wall shear stress resulting from the jet of blood impacting on the aortic wall adjacent to the anastomosis.

Another area that has the potential to improve the prognosis of LVAD implantation is the design of the outflow cannula itself. For cardiopulmonary bypass (CPB) Minakawa *et al.* investigated, *in vitro*, the effects of cannula end design, on the turbulence and flow patterns in the aorta, concluding that patient specific cannula choice was as important as the cannulation site in terms of preserving physiological flow patterns [17]. Stühle *et al.* compared three commercially available cardiopulmonary bypass cannulae end designs in a numerical study, reporting that the outlet design has a high influence on flow distribution and wall shear stress magnitudes [18]. However, as in [15], the use of a constant pressure boundary condition means the influence on flow distributions may be somewhat exaggerated. To the best of the author's knowledge there have been no publications relating to this in the context of VADs which is certainly surprising.

CLINICAL COMPLICATIONS 1.2.1

The most desirable use for an LVAD is as a bridge to recovery, negating the need for a donor heart. However, a major complication/limitation in the successful explantation of an LVAD in this scenario, is aortic valve fusion [19, 20]. There is an extremely high incidence of aortic valve fusion in continuous flow LVAD's. This is a direct consequence of reduced transvalular flow. In a recent study, Mudd *et al.* found that 8 out of 9 patients under continuous ventricular support showed signs of aortic valve fusion, even after a relatively short period (one patient showing mild valve fusion after just 33 days) [21]. At LVAD explantation, if the aortic valve commissures are found to be fused, there are two courses of action; an artificial valve may be implanted, resulting in increased levels of patient trauma, or

alternatively the explantation procedure is abandoned [22]. An intuitive method for reducing the occurrence of valve fusion is to ensure the aortic valve opens and closes periodically. The Berlin Heart INCOR VAD has a mechanism to promote just this [23]. The rotational speed of the impeller is slowed periodically to help the weakened ventricle overcome the aortic pressure and open the valve.

Flow related thrombus formation within the aorta is an uncommon complication of ventricular support [24]. However, the consequences of such a thrombus are potentially serious, including occlusion of downstream vessels and possible myocardial infarction. The primary cause of aortic thrombosis is stagnant blood which remains undisturbed for long periods, allowing platelet aggregation. This is clearly to be avoided and CFD simulations can help to identify configurations of the VAD and vasculature which may avoid the development of such regions.

Nishimura *et al.* investigated morphological changes in the aortic wall induced by long term VAD support [25]. Healthy goats were divided into three groups; the first had their left ventricle supported by a rotary blood pump, the second with a pulsatile blood pump and the third were employed as a control group. After approximately 100 days of support the three groups were sacrificed and the descending aortas removed. The aortic wall thickness was found to have reduced by approximately 30% in the rotary pump group, when compared to the pulsatile pump and control group. The morphology of the aortic wall was also altered in the rotary pump group, with the amount of smooth muscle cells (SMC) seen to reduce. It was suggested that this decrease in SMCs would lead to reduced contractility which could impair the vessel's ability to respond to changes in the local environment (i.e. the range of vasodilation and constriction may be reduced). No investigation of the material properties was conducted, although clearly they are likely to have changed.

MODELLING THE CARDIOVASCULAR SYSTEM 1.3

The study of haemodynamics has been a subject of interest and investigation dating back as far as the ancient Greeks and Aristotle [26]. In more recent times researchers have produced both analytical descriptions [27, 28] and numerical models [29, 30] to approximate the behaviour of blood flow in the cardiovascular system. Due to the complex nature of the governing fluid equations, analytical solutions have only been derived for relatively simple systems. The most well-known analytical solutions are probably those derived by Womersley. In 1955 Womersley published a general solution to describe the velocity profile in a rigid tube under pulsatile conditions [31, 32], he went on to extend this solution to consider a longitudinally tethered elastic tube [27]. These and other analytical solutions have aided researchers in their understanding of cardiovascular flows but are limited to descriptions of the local flow field characteristics in simple geometries. In order to explore more global effects or the flow field characteristics in more realistic geometries one must employ some form of numerical model. Numerical models vary widely in complexity from relatively simple lumped-parameter models or one dimensional analyses to complex three dimensional analyses which may include both the fluid dynamics and the motion of the vessel wall. One dimensional models are not reviewed in this thesis but an interested reader is referred to van de Vosse and Stergiopulos [33] for a comprehensive review.

LUMPED PARAMETER MODELS 1.3.1

Lumped parameter models enable a simplified description of the global behaviour of the cardiovascular system (see Shi *et al.* for a comprehensive review [34]). The vasculature can be divided into any number of compartments depending on the level of detail required. A limitation of this approach is the assumption that the distribution of the variable of interest (generally pressure and flow) is uniform within a single compartment. That is to say, if you represent the entire cardiovascular system with a single compartment then you are making the assumption that the pressure and flow is the same at all points within the vasculature. Clearly this is not true, as it is well known that pressure, flow and displacement waves propagate

through the circulatory system with a finite wave speed [35]. However, it may be an acceptable assumption for a specific research question.

The behaviour of an individual compartment is often described using an electrical circuit analogy. In electrical circuits it is the voltage difference that drives the current around an electric circuit, while in fluid mechanics the pressure difference drives the flow. Electrical components, namely capacitors, resistors and inductances, produce an electrical impedance which in fluid mechanics is comparable to the effects of vessel wall compliance, frictional losses (viscous dissipation) and fluid inertia, respectively. The most commonly applied compartment model is the Windkessel. This representation has been modified over the years from a simple two-element model, first proposed by Stephen Hales in 1733 [36] and later represented mathematically by Otto Frank in 1899 [36, 37]. The original two-element Windkessel model (Figure 1-3) consists of a capacitor in parallel with a resistor. The capacitor characterises the compliance of the vessel walls and hence the ability of the vessel to store blood, while the resistor represents the pressure drop across the system due primarily to the arterioles and capillaries resistance to flow [38, 39]. The two element Windkessel is able to accurately predict the behaviour of the arterial system at low frequencies but becomes erroneous at higher frequencies [40-42].

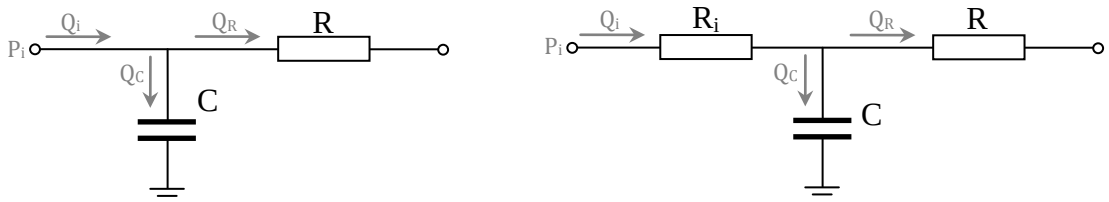

FIGURE 1-3 – TWO ELEMENT (LEFT) AND THREE ELEMENT (RIGHT) WINDKESSEL ELEMENTS

Landes added a third element (Figure 1-3) to the basic model in 1943 to improve the response at higher frequencies [34, 43]. This addition is often attributed to Westerhoff who did a considerable amount of work characterising the response of the three element Windekessel [44]. As such the three element Windkessel (Figure 1-3) is also known as the Westkessel [45, 46]. It becomes important to remember that in the three element model it is the total resistance, i.e. the sum of the two resistors, which represents the vascular resistance.

A further development to the Windkessel model came in 1982 when Burattini *et al.* proposed the incorporation of a fourth element, inductance, into the compartment model [47]. The inductance relates directly to the inertial properties of the blood and has since been incorporated into the three element Windkessel in both series and parallel arrangements (Figure 1-4) [47, 48]. Deswysen *et al.* compared the relative performance of the two, three and the four element Windkessel models and found the four element, with inductance connected in series (the parallel configuration was not considered), to produce the most physiologically accurate response [49]. Sharp *et al.* arrived at the same conclusion, finding that the four element Windkessel, with an in-series inductance (the parallel configuration was also considered in this study), produced the closest approximation to the aortic input impedance in children [50].

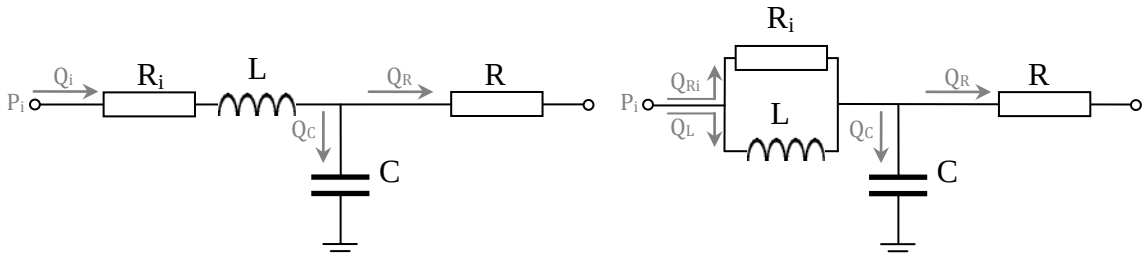

FIGURE 1-4 – TWO CONFIGURATIONS OF THE FOUR ELEMENT WINDKESSEL MODEL, SERIES CONNECTION (LEFT) AND PARALLEL CONNECTION (RIGHT)

At this point it is worth noting that, as the number of elements in the Windkessel model increases, so in turn do the number of possible element combinations. Perhaps even more importantly, as the complexity of the compartment model increases so does the resource needed to tune each component, as they no longer directly represent anatomical parameters and have to be computed via iterative or optimisation schemes.

Single compartment models make up one subgroup of lumped parameter models used in the field of cardiovascular mechanics. As mentioned previously, the major limitation of such models is the assumption that the pressure and flow waveforms are the same at all points throughout the vasculature. It is possible to improve the accuracy of the single compartment models by linking a number of these compartments, each representing a specific region of the cardiovascular system.

Many researchers have used this approach and the number of individual compartments used is purely dependent on the requirements of the research question [8, 9, 29, 51-55]. Tsuruta *et al.* employed a four compartment system to evaluate the use of drug treatments in heart failure [54]. The lumped model comprised a compartment describing each side of the heart and the pulmonary and systemic loops were also described by separate compartment models. The group employed a three element Windkessel model, for both the pulmonary and systemic compartments. Shi *et al.* employed a more complex multi compartment model to investigate the cardiovascular response to pulsatile and continuous flow LVADs [53]. The group divided the systemic circulation into 5 compartments (aortic root, arteries, arterioles, capillaries and veins) and chose a different combination of electrical components to describe the different properties of the 5 systems. For example, as the capillaries are responsible for a large proportion of the vascular resistance and have a relatively steady blood supply (i.e. minimal inductance or compliance effects), they can be modelled as a purely resistive compartment, whilst other regions, such as the arteries, require a resistor, inductor and capacitor to accurately represent their behaviour [53].

THREE DIMENSIONAL COMPUTATIONAL FLUID DYNAMICS 1.3.2

Lumped parameter models characterise the gross behaviour of the cardiovascular system but are unable to describe the local haemodynamics in a region of interest. In order to predict these detailed flow structures one must employ a technique known as computational fluid dynamics (CFD). CFD allows the prediction of two or three dimensional flow fields by solving the governing equations of fluid motion, namely the Navier-Stokes and Continuity equations (which for an incompressible fluid are shown in Equations 1-1 and Equation 1-2) [56].

$$\rho\frac{\partial u}{\partial t}+\nabla\cdot(\rho u\boldsymbol{U})=-\frac{\partial p}{\partial x}+\frac{\partial \tau_{xx}}{\partial x}+\frac{\partial \tau_{yx}}{\partial y}+\frac{\partial \tau_{zx}}{\partial z}$$

$$\rho\frac{\partial v}{\partial t}+\nabla\cdot(\rho v\boldsymbol{U})=-\frac{\partial p}{\partial y}+\frac{\partial \tau_{xy}}{\partial x}+\frac{\partial \tau_{yy}}{\partial y}+\frac{\partial \tau_{zy}}{\partial z}$$

$$\rho\frac{\partial w}{\partial t}+\nabla\cdot(\rho w\boldsymbol{U})=-\frac{\partial p}{\partial z}+\frac{\partial \tau_{xz}}{\partial x}+\frac{\partial \tau_{yz}}{\partial y}+\frac{\partial \tau_{zz}}{\partial z}$$

EQUATIONS 1-1

$$\nabla\cdot\boldsymbol{U}=0$$

EQUATION 1-2

Where ρ is the fluid density, u, v and w are the components of velocity in the x, y and z directions. p is the pressure, t is time, $\boldsymbol{U}$ is the velocity vector and τ is the shear stress.

The Navier-Stokes equations are partial differential equations (PDEs) which must be transformed into a system of non-linear algebraic equations that can then be solved iteratively. To construct the system of equations the region of interest must be spatially and temporally discretised and a set of boundary conditions assigned, to identify any walls and describe the upstream and downstream environment. Spatial discretisation is achieved by dividing the region of interest into a number of finite areas/volumes, known as the computational mesh, over which the equations are solved. Temporal discretisation is achieved by selecting a time-marching scheme, which is used to incrementally progress towards the end of the solution time. The degree of spatial and temporal discretisation can have a significant impact on the accuracy of the numerical results, thus it is good practise to conduct both mesh and time-step convergence studies to ensure the solution is not influenced by either of these factors.

Researchers have employed CFD models to predict the flow field in numerous geometries from curved tubes [57] to models that consider the interaction of the blood and the vessel wall (termed fluid structure interaction models or simply FSI) in such intricate structures as the aortic valve [58]. As the complexity of cardiovascular simulation improves, due in part to the advances in modern day computing, research

has moved to characterising patient-specific flow fields with the ultimate objective of improving diagnostic and interventional medicine. An important factor in successfully achieving this aim is the application of appropriate boundary conditions. It is of no use to conduct comprehensive studies that employ complex modelling strategies with highly refined spatial and temporal discretisation but have poorly defined boundary conditions. In this case, one is ultimately left with a very numerically accurate solution for the wrong problem. Multi-scale models, when used appropriately, can ensure that boundary conditions are physiologically realistic. This is especially important in FSI simulations, where the speed of the propagating wave will influence the correct relative alignment of the boundary conditions. If the alignment is poorly represented spurious reflections occur in the system, which are not representative of the *in-vivo* condition.

MULTI-SCALE MODELLING 1.3.3

The term 'multi-scale modelling' has become somewhat of a buzz word in the cardiovascular CFD community.

Multi-scale modelling is the coupling of different order numerical models at a common interface across which they can communicate. This is important in cardiovascular mechanics because the response of the circulatory system occurs over a range of time and length scales. An example of this is a stenosis, i.e. the narrowing of a vessel lumen. A stenosis produces local changes in the flow field, increasing the fluid velocities and wall shear stresses. Although these effects are localised they also result in global changes to the pressure and flow waveforms which propagate through the entire system. In order to capture these multi-scale changes one must explicitly model the local and global scales. This can be achieved by coupling zero dimensional lumped parameter compartment models, representing the global response of the vasculature, to two or three dimensional models of the region of interest.

Vignon-Clementel *et al.* demonstrated the importance of using coupled boundary conditions in an idealised iliac bifurcation with a stenosis in one branch [59]. The group compared the predicted distributions of flow and pressure in the model under three outlet boundary conditions; a constant pressure, a resistance and an impedance.

The alternative conditions resulted in significantly different flow distributions, with the impedance boundary producing physiologically reasonable predictions.

The use of coupled multi-scale models to describe the interaction of a region of interest and the downstream impedance of the cardiovascular system is clearly the most appropriate method for simulating vascular flow fields. In the specific application of aortic haemodynamics the use of lumped parameter compartment models is gaining prevalence to achieve this (and is discussed further in Section 1.4.2) [60-63] . Yet there are still authors work being published which draws conclusions based on the results of simulations with constant pressure boundary conditions [15, 18]. These, in truth, bear little semblance to reality.

AORTIC HAEMODYNAMICS 1.4

The main focus of this thesis is to characterise the changes in aortic haemodynamics induced by the presence of an LVAD. To do this one must first understand the characteristics of the native flow field.

IN VIVO CHARACTERISATION 1.4.1

Flow in the healthy human aorta (Figure 1-5) is pulsatile, due to the periodic contraction of the heart. The compliance of the vessel wall results in pressure, flow and displacement waves propagating out from the heart with a finite speed, determined by the wall dimensions, the fluid and structural material properties and the external tissue support. Blood ejected from the heart is rotated through at least 180 degrees over a distance of approximately 10cm, moving through a non-planar (right handed twist) and tapering curvature [64]. This motion produces complex structures in the flow field and occurs at Reynolds numbers that can be described as transitional, further complicating the haemodynamics [65].

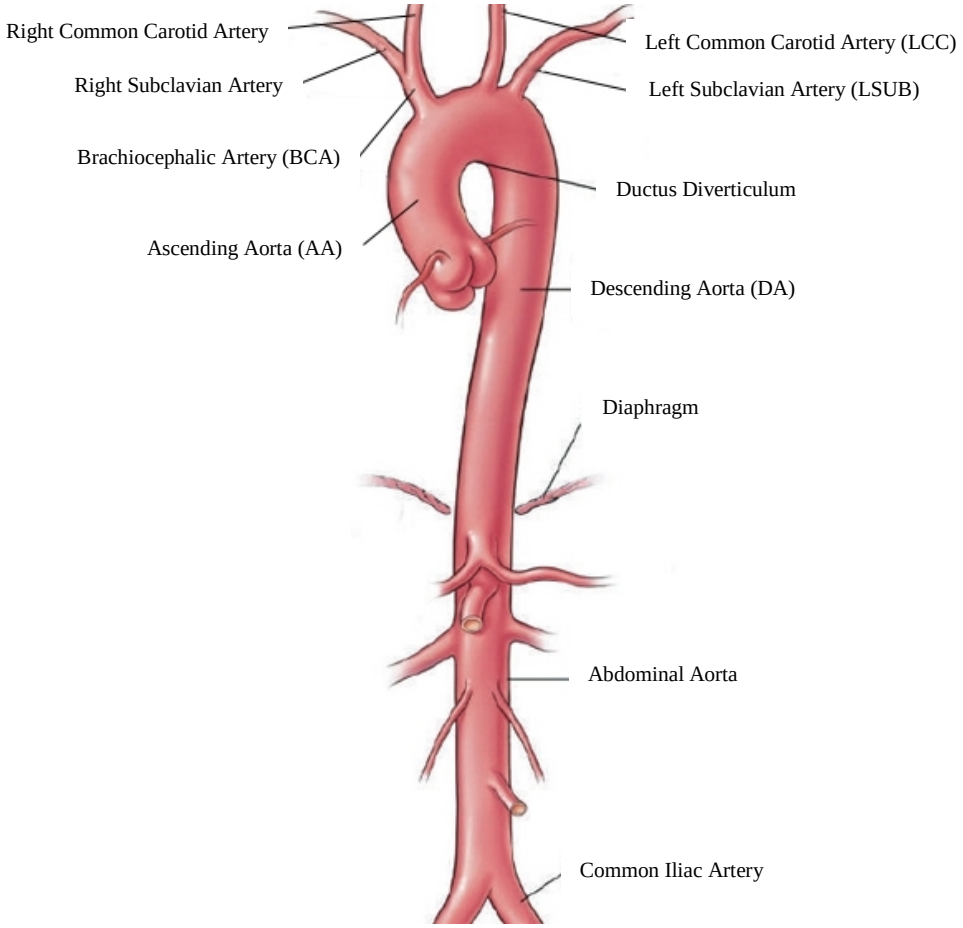

FIGURE 1-5 – HUMAN AORTIC ANATOMY

Phase contrast Magnetic Resonance Imaging (MRI) angiography has enabled researchers to non-invasively capture the 4D flow field of the human aorta, shedding light on the detailed haemodynamics of both diseased and healthy individuals [64-67]. Flow in the aorta is dominated by helical structures which become most prominent during the deceleration phase of systole and can remain throughout diastole [64]. Depending on the anatomy of the individual there is either; a single right handed helical structure within the ascending aorta and the arch or two counter rotating helical structures, often referred to as Dean vortices, after the mathematician who first described the general phenomenon [55-58]. The central core of these structures was reported by Kilner *et al.* to be mobile through the cardiac cycle, observing a general movement from the inner wall of the ascending aorta to the subjects right side [64]. The high velocity jet of blood is seen to detach from the wall as it moves through the aortic arch somewhere around the ductus diverticulum (Figure 1-5), where a recirculating vortex is formed. In the descending aorta there is

significantly more variation between subjects, with some preserving the right handed helical structures observed in the ascending aorta, whilst in others the structures reverse forming left handed helical structures.

It is proposed that the creation of such swirling flows is in fact an evolutionary trait, since helical structures minimise the chance of flow separation, reduce the rate of energy decay and hence improve the efficiency of the system [68].

NUMERICAL CHARACTERISATION 1.4.2

The understanding that pressure, flow and displacement waves propagate through the cardiovascular system with a finite wave speed drives us to employ complex modelling strategies, such as FSI, to simulate aortic haemodynamics; arguably the most sophisticated simulations of the aorta are those published by the research groups at Stanford University (USA) and INRIA (France) [60-62].

Kim *et al.* from the Stanford group used 0D compartment models to describe the inlet and outlet boundary conditions in both a healthy and diseased patient-specific aorta [61]. While Feinstein *et al.* used the same configuration of boundary conditions to investigate alternative intervention options in a patient with an aortic coarctation [62]. The inlet boundary condition employed a representation of the left side of the heart, with the ventricle based on the variable elastance model initially proposed by Suga *et al.* [69]. In this model the pressure is assumed to have a linear relationship to the ventricular volume and the ventricular elastance. The volume is computed from the difference in the flow into and out of the ventricle and the elastance is given as a function of time. The compartment models coupled to the outlet boundaries contained a three element Windkessel, with the parameters of all components tuned to approximate the measured response in the patient. The interaction of the fluid and structural mechanics of the aorta were considered using the coupled momentum method described by Figueroa *et al.* [70]. In both cases the vessel wall properties were chosen to lie within the physiological range and the aortic structures were constrained with fixed supports at the inlet and at all the outlets. The use of fixed mechanical constraints is not physiologically accurate and illustrates one of the major limitations of FSI models. In an attempt to improve the representation of the *in-vivo* structural support Moireau *et al.* proposed the use of dashpot and spring

constraints across the entire aortic wall, to represent the external tissue support. Data assimilation methods were used to compute the characteristics of the dashpots and springs, such that the computed displacements better approximated the clinically acquired 4D image data. The validity of the approach was demonstrated in an Arbitrary Lagrangian–Eulerian (ALE) implementation as well as in a coupled momentum method approach.

The most comprehensive simulation of an aorta under left ventricular support was described by Bazilevs *et al.* who employed an FSI model to evaluate the flow field changes brought about by the inclusion of an LVAD [63]. Three configurations were considered, no support (all flow through the aortic valve), partial LVAD support (flow through both the aortic valve and the LVAD cannula) and full support (all flow through the LVAD cannula). The inlet flow rates were prescribed and the outlet pressures are described by resistance boundary conditions. The LVAD cannula was attached to the descending aorta and was defined as having a rigid wall. The vessel wall was further supported by fixed constraints enforced at the inlet and outlet boundaries. The results demonstrated that during complete ventricular support regions of stagnant fluid were apparent in the ascending aorta, which could predispose to thrombus formation and valve fusion, as well as regions of excessively high wall shear stress around the anastomosis.

THESIS OUTLINE 1.5

The following Chapters describe the undulating scenery that has comprised my work over the last three years. Each Chapter begins with a ‘Motivation’ section which clarifies why the subject matter is of consequence and its place within the bigger picture already outlined in Section 1.1.

Chapter 2 describes the validation of the CFD code used throughout this thesis. The work was conducted as part of an initiative led by the Food and Drug Administration (FDA) who seek to develop a gold standard protocol for CFD simulations of cardiovascular devices, which may then be accepted as part of the substantial dossier required for FDA certification. The following Chapter (3) describes an analytical

solution for a 1D tube coupled to the 0D representation of a 2 or 3 element Windkessel model. A technique is developed to optimise the Windkessel parameters to produce a desired pressure response for a known flow waveform. The approach is validated in an analytical system, where the desired parameters are known, before being applied to patient-specific data. Chapter 4 aims to identify the importance of the interaction of the vessel wall and the fluid and presents a compressible fluid model, which can capture the gross dynamics of the propagating waves, as a possible alternative to full FSI simulations. These analysis strategies are considered in three geometries; a uniform cylinder, a patient-specific aorta and the same aorta with the inclusion of a left ventricular assist device. In Chapter 5 the long standing debate, whether a turbulence model is required to accurately capture aortic haemodynamics, is explored in both the native and assisted case.

Results and findings from the first four analysis Chapters are brought together in Chapter 6 to investigate the influence of the LVAD outflow cannula position on the aortic flow field. Chapter 7 presents the most comprehensive multi-scale model of the assisted vasculature to date. The model is used to investigate under what conditions the aortic valve may open during LVAD support, which, as discussed previously, is important to prevent aortic valve fusion. Finally Chapter 8 summarises the findings documented within this thesis.

An Appendix has also been included that contains copies of all first author publications associated with this PhD thesis.

CHAPTER 2

FOOD & DRUG ASSOCIATION CFD BENCHMARK

MOTIVATION 2.1

Any form of numerical simulation requires careful and comprehensive validation to give confidence in the accuracy of the computed results. Validation is especially important in computational fluid dynamics (CFD), where there are a large number of operator dependent decisions that must be made. The user must choose the density of the computational mesh, the size of the time-step, the criteria of convergence as well as many other variables.

There are two general forms of validation; comparison with an analytical solution and comparison with, *in vitro* or *in vivo,* measured data. In the case of fluid mechanics only the most simple, idealised, systems have mathematically derived analytical solutions and so the use of experimentally measured data is important.

THE BENCHMARK 2.2

The Food and Drug Administration (FDA) have identified the need for well validated CFD simulations to support applications for medical device approval. A clear concern is the distinct lack of what might be termed a '*Gold Standard'* protocol for the computation of CFD flow field predictions. In an attempt to remedy this, the FDA have begun a "*Critical Path Initiative"* to construct such a methodology [71].

To do this the FDA designed a fluid flow benchmark with features relevant to many complex cardiovascular devices. A challenge was put to the CFD community, in the world of both academia and industry, to employ their skills to predict the flow field within the benchmark for a number of given flow rates. Whilst the computational community were conducting simulations, the FDA commissioned three independent laboratories to perform *in vitro* studies of the benchmark, using particle image velocimetry (PIV) and pressure sensors to characterise the flow field. Comparisons were then made between the computational predictions and the experimental data, with the view of identifying a *Gold Standard* CFD methodology.

The benchmark has an idealised, three dimensional geometry, constructed from three cylinders (Figure 2-1) and is designed so that it can be implemented with the fluid moving in either direction. In the case where the flow moves from left to right, in regard to Figure 2-1, the fluid will encounter a conical concentrator, a constricted region and a sudden expansion. From here on, this case is referred to as the 'Sudden Expansion model/geometry'. In the alternative case, where the flow moves from right to left, the fluid encounters a sudden constriction, followed by a conical diffuser. Only the results for the Sudden Expansion geometry are reported here allowing a more in-depth analysis of the experimental and computational results.

Conical diffusers/concentrators and sudden expansions/contractions are characteristic features found in a wide range of medical equipment, from complex haemodialysis machines to simple IV fluid delivery systems, and importantly in the context of this thesis, LVAD cannulas. The ability to predict accurately the flow structures within these types of geometries provides an exciting, cost effective, possibility for improving their design through simulation based development.

FIGURE 2-1 – THE FDA FLUID FLOW BENCHMARK

MODEL CONSTRUCTION 2.2.1

The FDA specified the precise geometry (Figure 2-2) of the constriction, the diffuser and the expansion, but chose not to define an inlet or an outlet length or what boundary conditions to impose. It is believed this was done to assess how the CFD community constructed a problem of this type and whether any conclusions could be drawn as to the necessary domain length or application of the boundary conditions.

Steady, laminar flow in a cylindrical domain will reach an equilibrium state, at a distance (known as *the entrance* or *development length*) along the cylinder, where the force due to the pressure difference across the domain, equals the flow retarding, viscous force [72]. At this point the flow is said to be fully developed and the velocity profile takes the form of a parabola. It was deemed appropriate that the inlet velocity profile of the FDA benchmark took a fully developed, parabolic form.

An advantage of CFD simulations is the ability to enforce specific constraints on the fluid at the boundaries, so, a developed velocity profile was enforced at the inlet, negating the requirement of an entrance length that is necessary for *in vitro* studies. An inlet length of 5 diameters ($5D_i$ –Figure 2-2) was used in the construction of the CFD model.

The mathematical representation of a fully developed laminar flow profile in a rigid cylindrical domain of uniform cross-section can be shown to be:

$$w(r) = w_{max}\left\{1 - \left(\frac{r}{r_{max}}\right)^2\right\}$$

EQUATION 2-1

Where r is the radial distance from the centreline, r_{max} is the radius of the cylinder and w_{max} is the maximum fluid velocity at the inlet:

$$w_{max} = \frac{2Q}{\pi {r_{max}}^2}$$

EQUATION 2-2

Where Q is the volume flow rate.

It is important that the outlet boundary condition has no influence on the flow field in the region of interest. In an effort to find the appropriate outlet length for a problem of this kind the current literature, on simulating flows over a backward facing step and in conical diffusers, was inspected. A *Gold Standard* outlet length of approximately 20 diameters ($20D_o$ Figure 2-2) was identified [73, 74]. In accordance with this finding an outlet length of 20 diameters was employed in the CFD model. A constant relative pressure of 0Pa was applied at the outlet boundary. Since the system has rigid walls the chosen value of pressure is purely a reference value and it is the change in pressure along the benchmark which is of interest.

The flow rates of interest (Table 2.1) and the fluid properties were also specified by the FDA. The fluid was classified as incompressible and Newtonian, with a density and viscosity of 1056 kgm^{-3} and 0.0035 Pas respectively, to represent human blood flowing in large vessels (large relative to the size of a red blood cell, > 1 mm diameter, so negating the Fahraeus-Lindquist effect [75]). From the prescribed flow rates, the equivalent maximum inlet velocities were computed (Table 2.1), using Equation 2-2.

These values were subsequently used to describe the parabolic form of the inlet velocity profile (Equation 2-1).

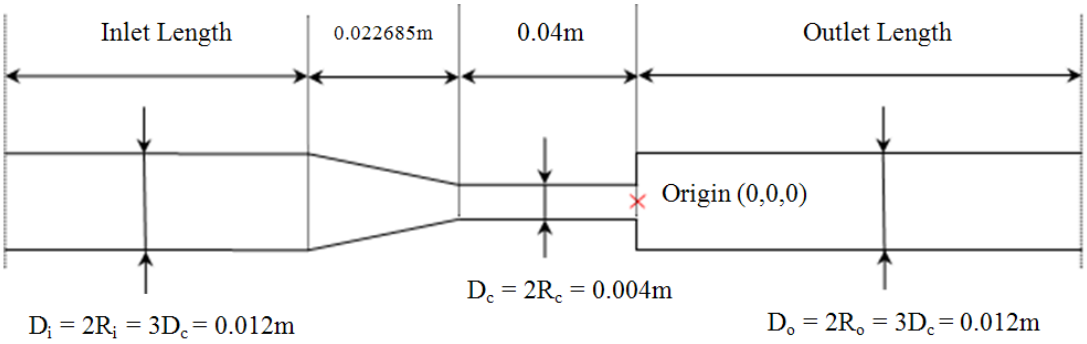

FIGURE 2-2 - GEOMETRY OF THE BENCHMARK, AS SPECIFIED BY THE FDA

Flow rate (m^3s^{-1})	**Reynolds Number (= $\rho w D_c/\mu$)**	**w_{max} (ms^{-1})**
$5.20624x10^{-6}$	500	0.0921
$2.08250x10^{-5}$	2000	0.368
$3.64437x10^{-5}$	3500	0.644
$5.20624x10^{-5}$	5000	0.921
$6.76811x10^{-5}$	6500	1.20

TABLE 2.1 - FLOW RATES OF INTEREST, AS DEFINED BY THE FDA AND THE CORRESPONDING MAXIMUM VELOCITIES

MESH CONSTRUCTION 2.2.2

A hexahedral mesh was constructed in ANSYS classic (ANSYS, Canonsburg, PA, USA) by means of a parameterised script file. The density of the mesh was non-uniform, with increased element density in areas of interest and regions of high gradients such as the near wall region.

The benchmark flow rates span the laminar, transitional and turbulent regions and as such a turbulence model (the theory of which is described in Section 2.3) may be required at the higher flow rates. Turbulence models often employ wall functions to predict accurately the flow field near the wall and require certain conditions to be met in terms of the mesh size. Large Eddy Simulations (LES) and Shear Stress Transport (SST) turbulence models require that the first grid point be located at a

distance from the wall such that the y^+ value is no greater than 2. The y^+ value is a non dimensional measure of wall distance which depends on the fluid properties, the frictional velocity at the nearest wall and the distance to this wall (Equation 2-3).

$$y^+ = \frac{u_* y_w \rho}{\mu}$$

EQUATION 2-3

Where u_* is the fictional velocity and y_w is the distance to local wall.

One can approximate the required distance to the first grid point to obtain a desired value of y^+ using the following relation:

$$y_n = D y^+ \sqrt{80} Re^{(-13/14)}$$

EQUATION 2-4

Since the y^+ value depends on the Reynolds number all meshes had a y_n value such that the y^+ of the highest Reynolds number simulation was approximately 2.

LES models are known to be strongly sensitive to variations in mesh density and elemental aspect ratios. As such, care was taken to minimise sudden changes in these parameters. Four meshes were constructed for the sudden expansion benchmark geometry. Table 2.2 contains information on the parameters of each mesh and Figure 2-3 illustrates the variation of the mesh density in Mesh SE-2.

Mesh Name	Number of Elements	Max Element Volume (m^3)
SE-1	437,424	6.33×10^{-10}
SE-2	1,629,072	1.49×10^{-10}
SE-3	3,021,392	8.18×10^{-11}
SE-4	6,992,700	4.09×10^{-11}

TABLE 2.2 - MESH INFORMATION FOR THE FDA BENCHMARK

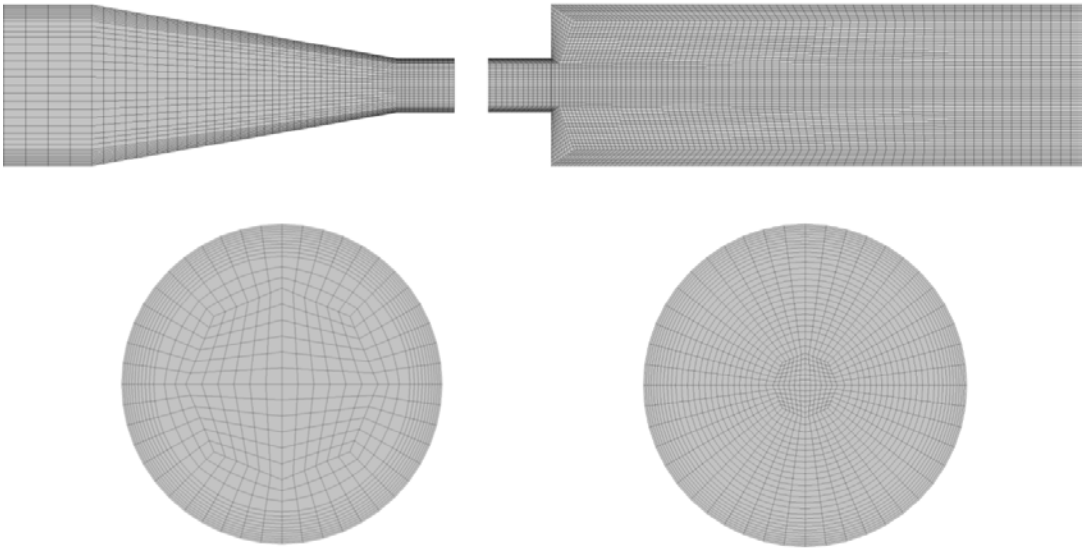

FIGURE 2-3 - ILLUSTRATION OF MESH DENSITY (SE-2): MESH PROFILES AT INLET AND OUTLET

THEORETICAL DESCRIPTION OF THE NUMERICAL MODELS 2.3

The flow rates of interest, for the described benchmark, encompass laminar, transitional and turbulent regimes. In principal the Navier-Stokes and Continuity equations fully describe the flow features in all of these cases. However, transitional and turbulent flow fields contain varying length and time scales [76], all of which must be resolved by the appropriate mesh and time-step size in order to accurately capture the dynamics of these regimes. A numerical simulation that can achieve this is termed a Direct Numerical Simulation (DNS). Kolmogorov derived a number of formulae [76, 77] that identify the spatial (Equation 2-5) and temporal (Equation 2-6) resolution required to perform a DNS.

$$\eta = \left(\frac{\nu^3}{\epsilon}\right)^{1/4}$$

EQUATION 2-5

$$t_\eta = \left(\frac{\upsilon}{\epsilon}\right)^{1/2}$$

EQUATION 2-6

Where υ is the kinematic viscosity (μ/ρ) and ϵ is the average energy dissipation per unit mass, which can be approximated by:

$$\epsilon = \left(\frac{\bar{u}^3}{L_{Ref}}\right)$$

EQUATION 2-7

Where $\bar{u}$ is the average velocity in the domain and L_{Ref} is the reference length, in this case the diameter.

Applying these relations to the second case of interest (Reynolds number 3500), one would require approximately 740 million elements in the constriction alone and a time-step size of 0.023 ms to achieve DNS. These requirements far outweigh the computing resources that are currently available locally and so an alternative approach is needed.

Fortunately, turbulence is a stochastic process and as such, statistical models have been developed to compute the averaged quantities of velocity and pressure. However, these statistical models suffer from what is known as the *closure problem*, that is, there are more unknowns than there are equations and so further assumptions are needed to facilitate the solution of the problem [76].

The following sections describe the theory of the different numerical models, be it a laminar or statistical turbulence model, which have been employed to predict the flow field of the FDA benchmark in this thesis.

LAMINAR THEORY 2.3.1

Implementation of a laminar model requires the standard transient incompressible Navier-Stokes (Equations 1-1) and Continuity (Equation 1-2) equations to be solved for the described system. This form of the equations consider the temporal changes

in the flow field and can be further simplified, for the benchmark problem, to the steady form of the equations (Equations 2-10).

$$\rho\frac{\partial u}{\partial t}+\nabla\cdot(\rho u\boldsymbol{U})=-\frac{\partial p}{\partial x}+\frac{\partial \tau_{xx}}{\partial x}+\frac{\partial \tau_{yx}}{\partial y}+\frac{\partial \tau_{zx}}{\partial z}$$

$$\rho\frac{\partial v}{\partial t}+\nabla\cdot(\rho v\boldsymbol{U})=-\frac{\partial p}{\partial y}+\frac{\partial \tau_{xy}}{\partial x}+\frac{\partial \tau_{yy}}{\partial y}+\frac{\partial \tau_{zy}}{\partial z}$$

$$\rho\frac{\partial w}{\partial t}+\nabla\cdot(\rho w\boldsymbol{U})=-\frac{\partial p}{\partial z}+\frac{\partial \tau_{xz}}{\partial x}+\frac{\partial \tau_{yz}}{\partial y}+\frac{\partial \tau_{zz}}{\partial z}$$

EQUATIONS 2-8

$$\nabla\cdot\boldsymbol{U}=0$$

EQUATION 2-9

$$\nabla\cdot(\rho u\boldsymbol{U})=-\frac{\partial p}{\partial x}+\frac{\partial \tau_{xx}}{\partial x}+\frac{\partial \tau_{yx}}{\partial y}+\frac{\partial \tau_{zx}}{\partial z}$$

$$\nabla\cdot(\rho v\boldsymbol{U})=-\frac{\partial p}{\partial y}+\frac{\partial \tau_{xy}}{\partial x}+\frac{\partial \tau_{yy}}{\partial y}+\frac{\partial \tau_{zy}}{\partial z}$$

$$\nabla\cdot(\rho w\boldsymbol{U})=-\frac{\partial p}{\partial z}+\frac{\partial \tau_{xz}}{\partial x}+\frac{\partial \tau_{yz}}{\partial y}+\frac{\partial \tau_{zz}}{\partial z}$$

EQUATIONS 2-10

These equations have been employed to investigate whether the different flow fields have any significant temporal fluctuations.

SHEAR STRESS TRANSPORT THEORY 2.3.2

As mentioned above, statistical turbulence models solve the problem in terms of averaged flow quantities. To do this the equations of motion are modified to give the Reynolds Averaged Navier-Stokes (RANS) equations. The velocity can be decomposed into a time averaged velocity, $\overline{\boldsymbol{U}}$, and a velocity fluctuation, $\widetilde{\boldsymbol{u}}$, such that:

$$\boldsymbol{U} = \bar{\boldsymbol{U}} + \tilde{\boldsymbol{u}}$$

EQUATION 2-11

By decomposing each variable as described (this is known as Reynolds decomposition), substituting them into the transient incompressible Navier-Stokes and Continuity equations and averaging we find the RANS equations (Equation 2-12 and Equation 2-13). Note for convenience they have been written in Cartesian form.

$$\rho\left(\frac{\partial \bar{\boldsymbol{U}}_i}{\partial t} + \bar{\boldsymbol{U}}_j \frac{\partial \bar{\boldsymbol{U}}_i}{\partial x_j}\right) = -\frac{\partial \bar{P}}{\partial x_i} + \frac{\partial}{\partial x_j}\left(\mu \frac{\partial \bar{\boldsymbol{U}}_i}{\partial x_j} - \rho\overline{\tilde{\boldsymbol{u}}_i \tilde{\boldsymbol{u}}_j}\right)$$

EQUATION 2-12

$$\frac{\partial \bar{\boldsymbol{U}}_i}{\partial x_j} = 0$$

EQUATION 2-13

The RANS equations include a term, $\rho\overline{\tilde{\boldsymbol{u}}_i \tilde{\boldsymbol{u}}_j}$, which is a pseudo stress known as the Reynolds Stress. It is this Reynolds Stress term that causes the closure problem, since the $\rho\overline{\tilde{\boldsymbol{u}}_i \tilde{\boldsymbol{u}}_j}$ term is an unknown. In laminar flow, of a Newtonian fluid, the shear stress is a product of the velocity gradient, $\frac{\partial \boldsymbol{U}_i}{\partial x_j}$, and the fluid viscosity (Equation 2-14).

$$\tau_{laminar} = \mu \frac{\partial \boldsymbol{U}_i}{\partial x_j}$$

EQUATION 2-14

Boussinesq's hypothesis, which he proposed in 1877, describes the Reynolds Stresses in a similar form to the laminar relation, as a product of the turbulent eddy viscosity, μ_t, and the averaged velocity gradient, $\frac{\partial \bar{\boldsymbol{U}}_i}{\partial x_j}$:

$$\rho\overline{\tilde{\boldsymbol{u}}_i \tilde{\boldsymbol{u}}_j} = \mu_t \frac{\partial \bar{\boldsymbol{U}}_i}{\partial x_j}$$

EQUATION 2-15

The turbulent eddy viscosity is an unknown quantity and so this hypothesis still suffers from a closure problem. Modern day turbulence models employ different formulations to describe the turbulent eddy viscosity, thereby closing the equations and allowing flow field predictions to be computed.

The Shear Stress Transport (SST) turbulence model solves a combination of the $k-\omega$ and $k-\varepsilon$ two equation turbulence models, depending on the local position with relation to a wall and the flow parameters [78]. Two equation turbulence models solve an additional two partial differential equations that describe the transport of the turbulent velocity scale and the turbulent length scale. k describes the turbulent kinetic energy, while ω and ε represent the turbulent frequency and the turbulent eddy dissipation respectively. In the $k-\omega$ turbulence model the turbulent eddy viscosity is characterised as a function of the turbulent kinetic energy and the turbulent frequency (Equation 2-16), hence the name $k-\omega$. In a similar manner the turbulent eddy viscosity is described by Equation 2-17 in the $k-\varepsilon$ model.

$$\mu_t = \rho \frac{k}{\omega}$$

EQUATION 2-16

$$\mu_t = 0.09\rho \frac{k^2}{\varepsilon}$$

EQUATION 2-17

Both the $k-\omega$ and $k-\varepsilon$ models have well documented short comings. The $k-\omega$ implementation is sensitive to the prescribed levels of turbulence in the free stream (i.e. what is defined at the inlet) but is advantageous in the near wall region where the equations better represent the near wall effects [79, 80]. While the $k-\varepsilon$ model performs poorly in complex flow systems where adverse pressure gradients should result in flow separation but can in the worst case be completely missed but outperforms the $k-\omega$ model in the free stream regions [80].

The SST model of Menter [79] employs a blending function which results in the $k-\omega$ model dominating in the near wall region and the $k-\varepsilon$ model dominating in the free stream region. There is also the inclusion of an additional limiter on the

turbulent eddy viscosity, which considers the transport of the turbulent shear stresses, producing even more accurate predictions of the separation and reattachment locations.

A further variant of this standard SST model is the consideration of transitional effects [80]. A correlation based model, which depends on the local flow variables, is available in ANSYS-CFX [78]. The model solves an additional two transport equations (in addition to the turbulent length and velocity scale equations), one for intermittency and another for the onset criteria of the transition. In the event that the transitional model is activated the result is to limit the turbulent viscosity to some degree, based on the experimental correlations. It is important to note that the transitional model does not try to capture the true physics of the flow.

The transitional variant of the SST turbulence model was selected for use in the investigation of the FDA benchmark because of its ability to accurately compute the location and degree of flow separation within transitional flow regimes. In the benchmark problem there are regions, such as the conical diffuser and sudden expansion, within which the accurate prediction of flow separation is vital to the accurate computation of the flow structures.

LARGE EDDY SIMULATION THEORY 2.3.3

As discussed previously, transitional and turbulent flow fields contain a wide range of both length- and time-scales. Eddies with the largest length- and time-scales are the most energetic and have the greatest influence on the global flow structures. Large Eddy Simulations (LES) solve a set of filtered Navier-Stokes equations to spatially and temporally resolve the largest, most energetic, eddies and employ a statistical model to predict what are termed the *sub-grid scale* (SGS) eddies. LES models require a far higher spatial resolution than the RANS turbulence models and of course, resolves temporal fluctuations. Therefore, LES models require a large number of time-steps to achieve a time averaged solution.

The Navier-Stokes equations are spatially filtered based on the size of the computational mesh used to discretise the fluid domain. A variable, $\boldsymbol{U}$, is decomposed into a resolved portion, $\breve{\boldsymbol{U}}$, and an unresolved portion, $\boldsymbol{U}'$, where:

$$\boldsymbol{U} = \breve{\boldsymbol{U}} + \mathbf{U}'$$

EQUATION 2-18

The spatially filtered Navier-Stokes equations, for an incompressible fluid, take the form:

$$\frac{\partial \breve{\boldsymbol{U}}_i}{\partial t} + \frac{\partial}{\partial x_j}\left(\breve{\boldsymbol{U}}_i \breve{\boldsymbol{U}}_j\right) = -\frac{1}{\rho}\frac{\partial \breve{p}}{\partial x_i} + \frac{\partial}{\partial x_j}\left\{\mu\left(\frac{\partial \breve{\boldsymbol{U}}_i}{\partial x_j} + \frac{\partial \breve{\boldsymbol{U}}_j}{\partial x_i}\right)\right\} - \frac{\partial \tau_{ij}}{\partial x_j}$$

EQUATION 2-19

Where τ_{ij} are the SGS stresses, described by:

$$\tau_{ij} = \widetilde{\boldsymbol{U}_i \boldsymbol{U}_j} - \breve{\boldsymbol{U}}_i \breve{\boldsymbol{U}}_j$$

EQUATION 2-20

Spatial filtering of the Navier-Stokes equations again results in a turbulent closure problem. As in the RANS situation, Boussinesq's hypothesis is employed to close the equations. Unlike the RANS case, the statistical model need only calculate the SGS eddy viscosity. This quantity is related to the SGS stresses and the fully resolved strain rate tensor as shown:

$$\left(\tau_{ij} - \frac{\delta_{ij}}{3}\tau_{kk}\right) = 2\mu_{sgs}\left(\frac{\partial \breve{U}_i}{\partial x_j} + \frac{\partial \breve{U}_j}{\partial x_i}\right)$$

EQUATION 2-21

Where μ_{sgs} is the SGS eddy viscosity.

Within the CFD package, ANSYS-CFX (ANSYS, Canonsburg, USA), there are three different SGS models that can be employed to describe the SGS eddy viscosity [78]. The Wall Adapted Local Eddy viscosity (WALE) model is recommended in the user documentation, as it has improved eddy viscosity predictions in wall bounded laminar flows (i.e. the turbulent viscosity reduces to zero whereas this is not the case in the alternative Smagorinsky model). This suggests that it is the best model to accurately resolve the transition from laminar to turbulent flow, which is likely to

occur in the FDA benchmark. For full details of the mathematical description of the WALE model see Nicoud and Durcros [81].

SCALE ADAPTIVE SIMULATION THEORY 2.3.4

The Scale Adaptive Simulation – Shear Stress Transport (SAS-SST) turbulence model is a class of Unsteady Reynolds Averaged Navier Stokes (URANS) models. The SAS-SST model solves the RANS equations for stationary flow fields (in the case of interest this is the transitional variant of the SST model described in section 2.3.2). However, in regions where the flow exhibits temporal fluctuations the model reduces μ_t based on the length scale of the resolved eddies. Assessment of the resolved eddy size is based on the von Kármán length scale (κ):

$$L_{vk} = \kappa \left(\frac{\partial \boldsymbol{U}_i}{\partial x_j} \Big/ \frac{\partial^2 \boldsymbol{U}}{\partial x_j \partial x_j} \right)$$

EQUATION 2-22

The von Kármán length scale is incorporated into the transport equation of the turbulent eddy frequency as shown:

$$\frac{\partial \rho\omega}{\partial t} + \frac{\partial}{\partial x_j}(\rho U_j \omega) = \alpha \frac{\omega}{k} P_k - \rho\beta\omega^2 + Q_{SAS} + \frac{\partial}{\partial x_j}\left[\left(\mu + \frac{\mu_t}{\sigma_\omega}\right)\frac{\partial}{\partial x_j}\right] + (1 - F_1)\frac{2\rho}{{\sigma_\omega}^2}\frac{1}{\omega}\frac{\partial k}{\partial x_j}\frac{\partial \omega}{\partial x_j}$$

EQUATION 2-23

Where σ_ω and ${\sigma_\omega}^2$ are the values for the $k - \varepsilon$ regime of the SST model and:

$$Q_{SAS} = max\left[\rho\zeta_2\kappa S^2 \left(\frac{L}{L_{vk}}\right)^2 - C \cdot \frac{2\rho k}{\sigma_\Phi} max\left(\frac{1}{\omega^2}\frac{\partial \omega}{\partial x_j}\frac{\partial \omega}{\partial x_j}, \frac{1}{k^2}\frac{\partial k}{\partial x_j}\frac{\partial k}{\partial x_j}\right), 0\right]$$

EQUATION 2-24

For full details of the mathematical representation and the model parameters chosen for the SAS-SST model see Egorov and Menter [82].

SUDDEN EXPANSION RE 500: RESULTS AND DISCUSSION 2.4

The following sections describe and compare the flow field predictions computed by each of the numerical models discussed. Although for the FDA initiative all flow rates, have been simulated in both the Sudden Expansion and Conical Diffuser geometry, only two flow rates within the Sudden Expansion geometry are analysed in detail here, due to size restrictions placed on this thesis. The flow rates that will be analysed in detail correspond to a Reynolds Number, in the constriction, of 500 and 3500. These were chosen because they correspond to flow regimes which are laminar (Reynolds number 500) and transitional (Reynolds number 3500).

The focus of the latter part of this thesis is on computing flow fields within patient-specific aortas, both with and without the inclusion of the Berlin Heart (Berlin, Germany) INCOR, left ventricular assist device. The INCOR is attached to the native aorta via an outflow cannula with a constant diameter of 12mm and is commonly set to supply a flow rate of around 4-5 litres per minute, depending on the condition of the patient. Under these conditions the Reynolds number within the cannula is around 3200. This is very close to the FDA benchmark at a Reynolds number of 3500 and hence it is likely to be the most valuable study for this thesis.

ANALYTICAL SOLUTION 2.4.1

Although there is no derived analytical solution for this system, it is possible to gauge a gross first approximation of the total pressure drop across the benchmark using a combination of Bernoulli's equation (Equation 2-25) and Poiseuille’s law (Equation 2-26). Poiseuille’s law allows the calculation of the pressure drop across a uniform cylinder with a fully developed laminar flow field, such as within the inlet region of the benchmark. One can also make the assumption that this is true for the outlet and constriction of the benchmark, although admittedly this is likely to be a source of error. Bernoulli’s equation is based on the conservation of energy momentum, but it can be interpreted as stating that the sum of the kinetic and potential energy remains constant along a fluid streamline. This equation is valid for steady flow of an inviscid fluid. Whilst the fluid within the benchmark is not itself

inviscid, the viscous effects are likely to be small and so it is deemed appropriate for use as a first order prediction. Bernoulli's equation is used to compute the pressure drop through the conical constrictor and to give a range of pressure recovery through the expansion.

$$^1/_2\, v^2 + gz + \frac{P}{\rho} = constant$$

EQUATION 2-25

Where v is the velocity of the fluid, g is gravitational acceleration, z is the elevation, P is the pressure and ρ is the fluid density.

$$\Delta P = \frac{8Q\mu L}{\pi {r_{max}}^4}$$

EQUATION 2-26

Where Q is the volume flow rate, μ is the fluid viscosity, L is the length and r_{max} is the radius of the cylinder.

Applying these rules to the benchmark, at a Reynolds number of 500, results in a calculated pressure drop of 2.15 Pa along the inlet cylinder, 89.5 Pa through the constrictor, 116 Pa across the constriction, and 8.6 Pa along the outlet cylinder. At the sudden expansion one can apply Bernoulli's equation to approximate the upper bound of the pressure recovery. However, it is known that under adverse pressure gradients and in regions of flow recirculation Bernoulli's principal is unable to capture the associated energy losses. As such an upper and lower bound of the pressure recovery, through the sudden expansion, has been computed. Based on the described principals the range of the total pressure drop across the benchmark is 126-216 Pa (Figure 2-4).

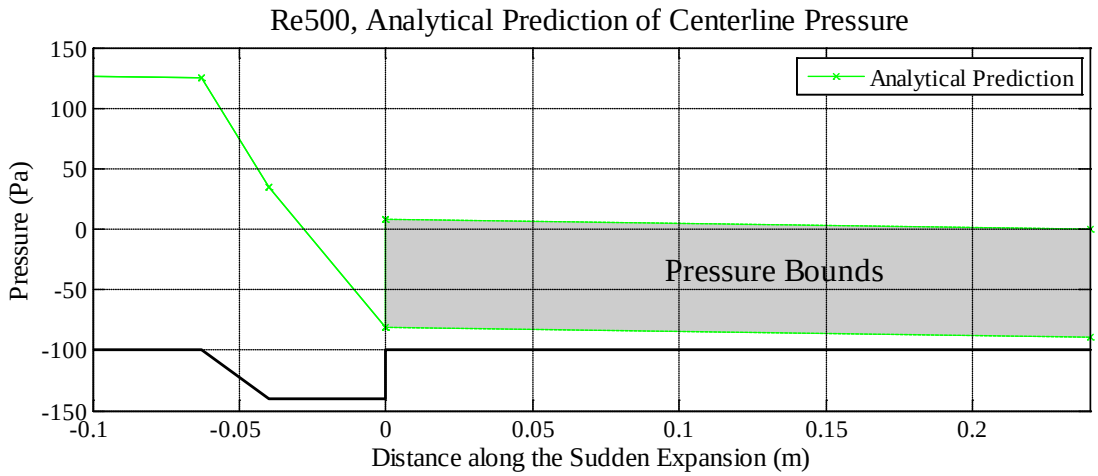

FIGURE 2-4 - ANALYTICAL PREDICTION OF PRESSURE AT RE500

ASSESSMENT OF NUMERICAL CONVERGENCE 2.4.2

Convergence of the CFD simulations was assessed by monitoring the root mean squared (RMS) residuals of pressure and momentum, in all three dimensions. In the documentation for ANSYS-CFX (ANSYS, Canonsburg, USA) the default convergence criteria, of $1x10^{-4}$, is described as offering *"relatively loose convergence, but may be sufficient for many engineering applications"* [78].

To ensure that the choice of convergence criteria had no effect on the predicted flow field a simple study was conducted in the Sudden Expansion geometry, employing the coarse mesh at the lowest flow rate. Five, steady laminar simulations were conducted with convergence criteria for the RMS residuals of $1x10^{-3}$, $1x10^{-4}$, $1x10^{-5}$, $1x10^{-6}$ and $1x10^{-7}$. The distribution of the predicted axial velocity and pressure along the centreline and the variation of the wall shear stress (WSS) along the length of the domain are shown in Figure 2-5 and Figure 2-6.

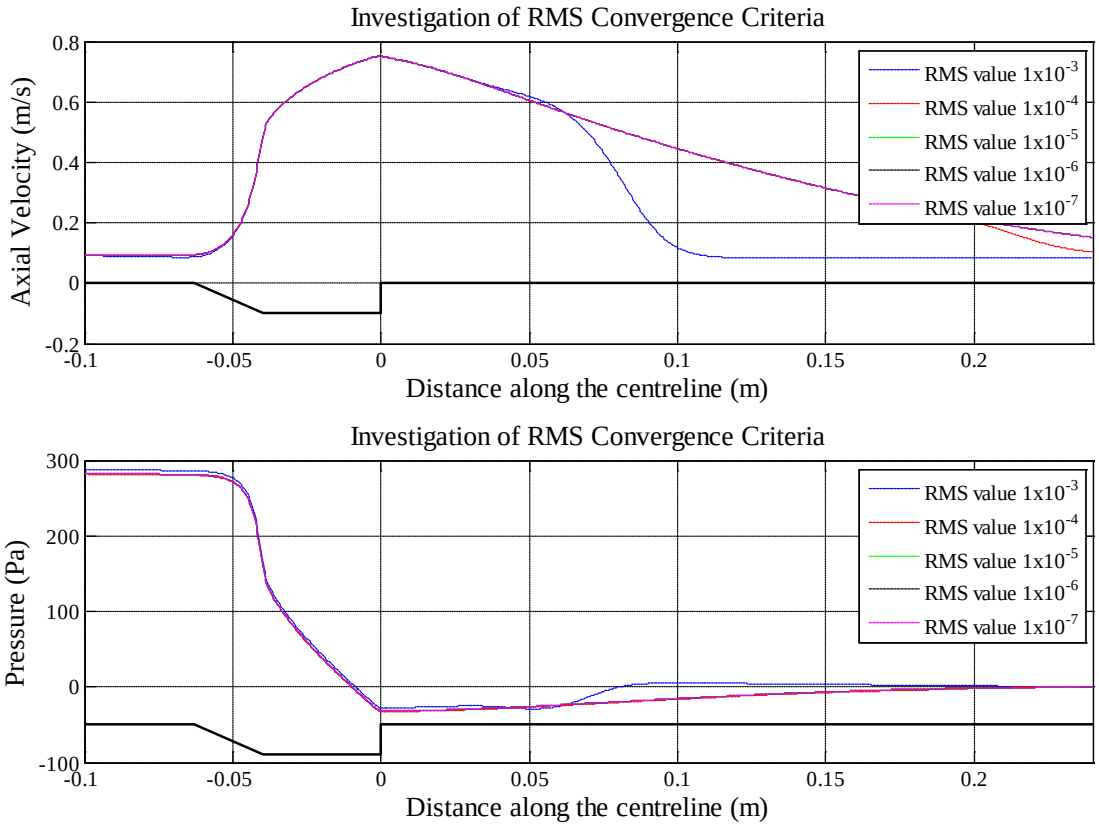

FIGURE 2-5 - ASSESSMENT OF CONVERGENCE CRITERIA:
AXIAL VELOCITY AND PRESSURE ALONG THE CENTRELINE

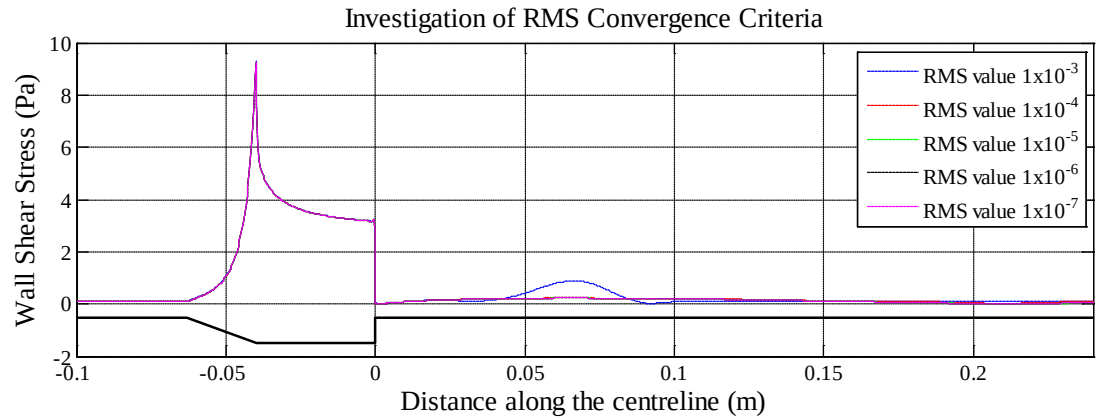

FIGURE 2-6 - ASSESSMENT OF CONVERGENCE CRITERIA:
SHEAR STRESS ALONG THE WALL

The computed axial velocities and pressures along the centreline and the computed shear stresses along the wall are identical for simulations with RMS residuals $\leq 1x10^{-5}$.

Based on these findings, all CFD simulations detailed in this thesis are assumed to have reached a converged solution once the RMS residuals of pressure and momentum reach a value of less than $1x10^{-5}$.

ASSESSMENT OF MESH CONVERGENCE 2.4.3

In all CFD simulations it is important to ensure that the computational mesh employed to discretise the spatial domain has no influence on the resulting flow field predictions. As such it is essential that a mesh sensitivity study be conducted to ensure the results are independent of this discretisation.

There are any number of methods for assessing mesh convergence, from evaluating the percentage change between different mesh densities, to '*eyeballing*' the variation. In this thesis a more formal method, known as Richardson's extrapolation [83, 84], is used to predict the error in the numerical solution. Richardson's extrapolation method requires the solution of a problem on at least three mesh densities [83]. The reference length (h_i) of each computational mesh and the numerical solutions (f_i) are then extrapolated to compute the solution, assuming a reference length of zero.

Consider a set of computational meshes, the refinement ratio of which is defined by:

$$r_{mesh} = \frac{h_2}{h_1} = \frac{h_3}{h_2}$$

EQUATION 2-27

Where $i = 1$ denotes the finest mesh density.

The order (p_{sol}) of the numerical solution is simply:

$$p_{sol} = \frac{\ln\{(f_3 - f_2)/(f_2 - f_1)\}}{\ln(r_{mesh})}$$

EQUATION 2-28

From these an estimate of the exact solution (f_{ex}) can be obtained and in turn a measure of the relative error associated with the numerical prediction.

$$f_{ex} = f_1 + \frac{(f_1 - f_2)}{{r_{mesh}}^{p_{sol}} - 1}$$

EQUATION 2-29

Due to the nature of the parameter values of interest (i.e. pressure, axial velocity etc) it is important to define a relative error that produces meaningful values. For example percentage error can be a good indicator of agreement if the values of interest are non-zero. However, when the real value of the parameter is zero compared to a non zero estimated parameter, the percentage error becomes infinite. As such a more reliable formulation of a relative error is used in this Chapter, the absolute error between the real and predicted parameter is normalised based on the mean amplitude of the real parameter (Equation 2-30).

$$Relative\ error = \frac{(f_i - f_{ex})}{\frac{1}{n}\sum_{j=1}^{n} f_{ex}} \times 100$$

EQUATION 2-30

Where n is the number of points in Richardson's exact solution.

A solution is said to be converged when the mean value of this relative error is less than 2 and the maximum error value in the computed pressure and velocity is less than 5. This method and the given criteria are used throughout this Chapter, unless otherwise stated, to ensure the accuracy of the computational results.

LAMINAR RESULTS 2.4.4

The flow rate within the benchmark, at a Reynolds number of 500, is clearly laminar. This value relates to the fluid moving through the constriction, which corresponds to a Reynolds number of 166 in the inlet and outlet regions. For this reason a steady laminar simulation was believed to be the most appropriate for computing the flow field.

An initial mesh sensitivity study was conducted that employed all four mesh densities reported in Table 2.2. The centreline axial velocity and pressures (Figure 2-7) showed good agreement and the more sensitive parameters of shear strain rate and wall shear stress also demonstrated good agreement (Figure 2-8). Application of Richardson's extrapolation method demonstrated that the results for all mesh densities had a mean relative error (Equation 2-30) of less than 1.8 and a maximum relative error of 4.68 (Table 2.3). These results clearly illustrate that the results of all the mesh densities are mesh independent.

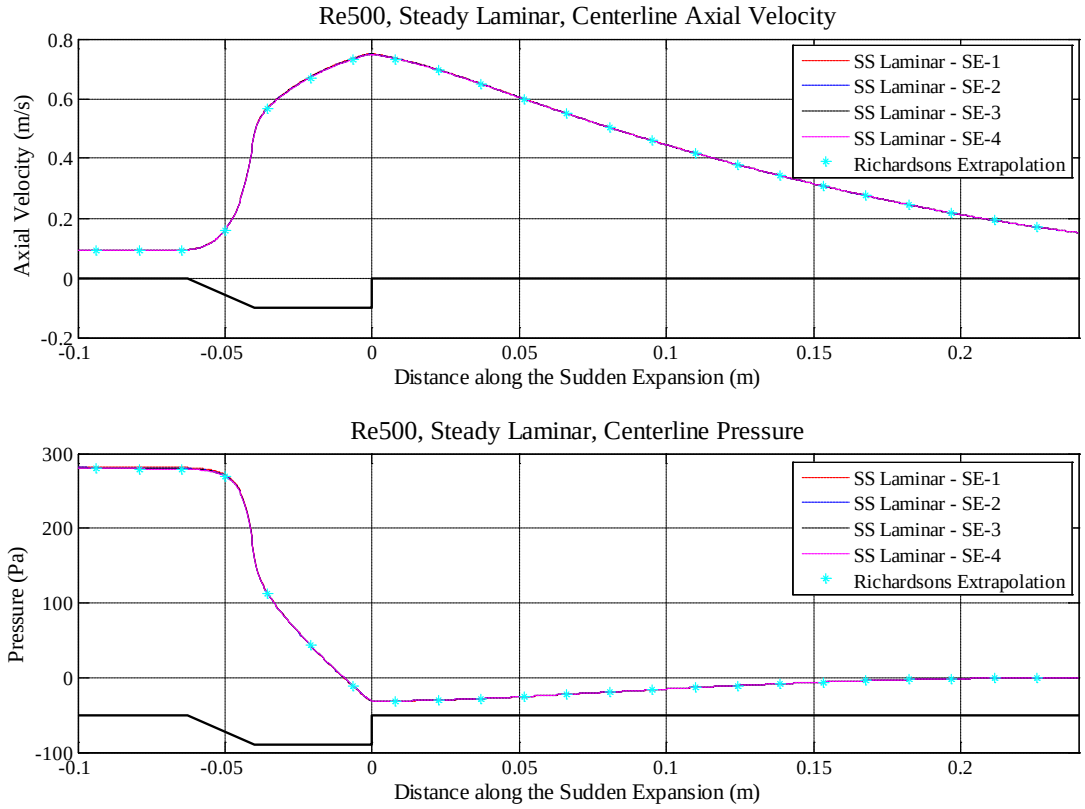

FIGURE 2-7 - COMPARISON OF CENTRELINE AXIAL VELOCITY AND PRESSURE COMPUTED ON A NUMBER OF MESH DENSITIES. STEADY LAMINAR SIMULATIONS AT RE500

The numerically computed pressure drop across the benchmark is 280.6 Pa, compared with the upper bound of the analytical prediction of 216 Pa. Although there is a variation in the predictions the combination of Bernoulli's and Poiseuille's principals support a reasonable first order approximation of the pressure drop.

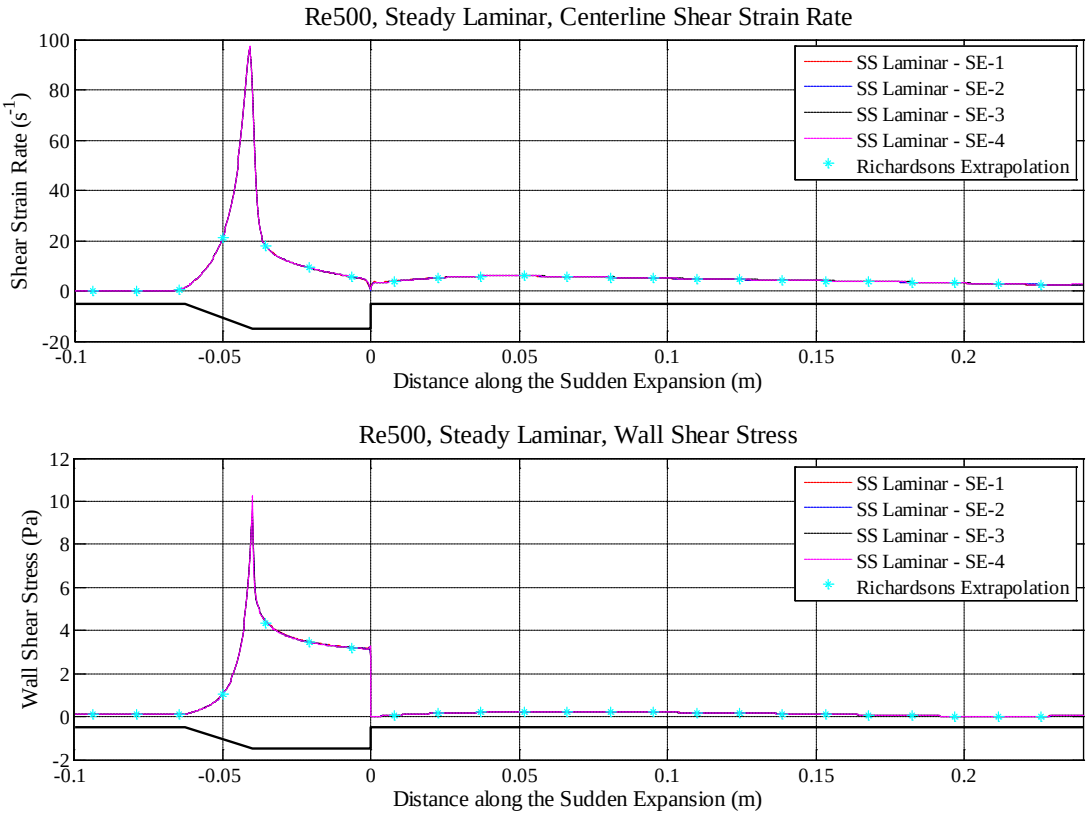

FIGURE 2-8 - COMPARISON OF CENTRELINE SHEAR STRAIN RATE AND WALL SHEAR STRESS COMPUTED ON A NUMBER OF MESH DENSITIES. STEADY LAMINAR SIMULATIONS AT RE500

	Mean (Max) Relative Error (ε)			
Mesh	**Axial Velocity**	**Pressure**	**Shear Strain Rate**	**Wall Shear Stress**
SE-1	0.25 (1.10)	1.16 (4.68)	1.20	1.73
SE-2	0.15 (0.64)	0.56 (2.30)	0.80	1.41
SE-3	0.11 (0.47)	0.41 (1.70)	1.17	1.21
SE-4	0.07 (0.27)	0.19 (0.79)	0.60	0.68

TABLE 2.3- EVALUATION OF THE MEAN AND MAX (SHOWN IN BRACKETS) RELATIVE ERROR (ε) FOR THE VARYING MESH DENSITIES AGAINST THE RICHARDSON'S PREDICTION. STEADY LAMINAR AT RE500

EXPERIMENTAL VS NUMERICAL RESULTS 2.4.5

Experimental results for the sudden expansion benchmark have been made available by the FDA, allowing detailed comparisons to be made between the numerical predictions and the experimental measurements. All comparisons have been made using the numerical results from mesh SE-1.

The range of experimental variation is interesting. All data sets demonstrate good agreement in terms of the centreline axial velocity, while the variation in the centreline pressure is far more significant (Figure 2-9).

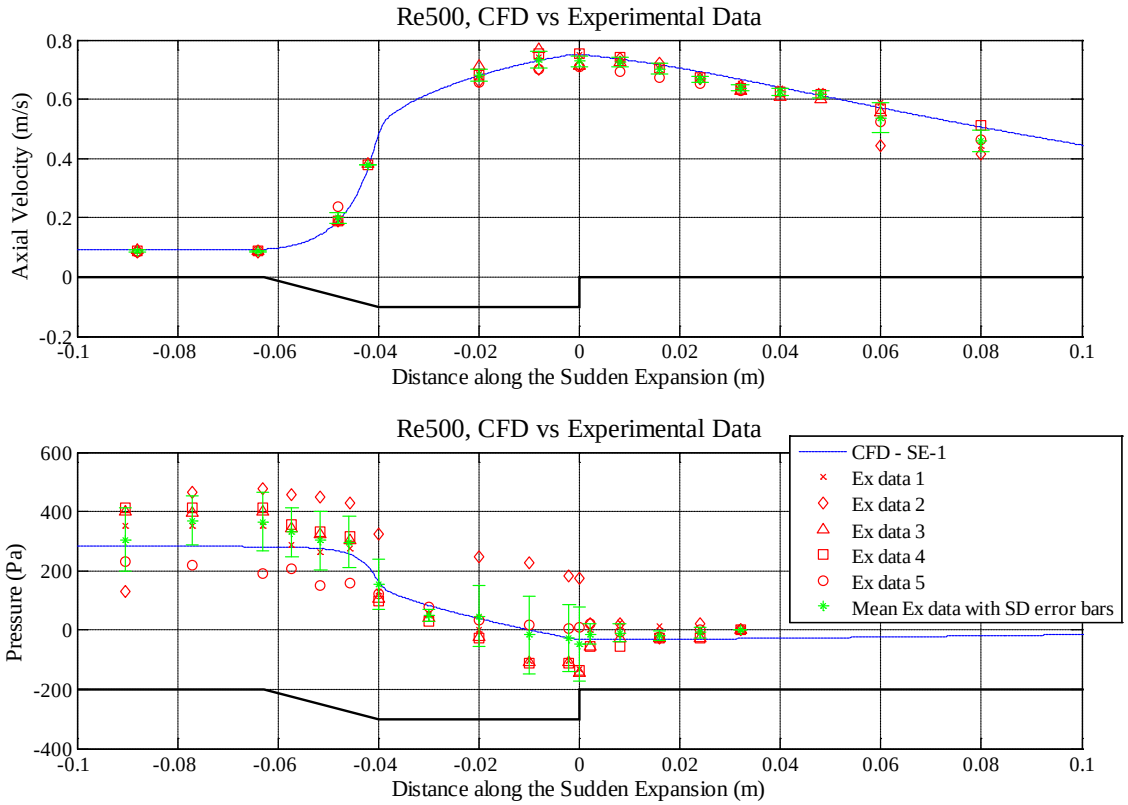

FIGURE 2-9 - COMPARISON OF CENTRELINE AXIAL VELOCITY AND PRESSURE, EXPERIMENTAL VS. NUMERICAL AT RE500.

The numerical results show extremely good agreement with the axial velocity, both in terms of the centreline velocity and the velocity profiles (Figure 2-9 and Figure 2-10). The CFD model predicts a slightly greater velocity in the inlet domain, which can be seen most clearly in the velocity profile at an axial position of -0.064 m (Figure 2-10). However, the numerical and experimental agreement through the

conical constrictor, the sudden expansion and in the outlet domain (z=-0.048 m, 0 m and 0.24 m respectively) are indicative of the numerical model's ability to accurately capture the flow field. The experimental data has a greater variation in the region where the fluid is developing within the outlet domain, suggesting that during this transition to a fully developed laminar profile the flow field is highly sensitive.

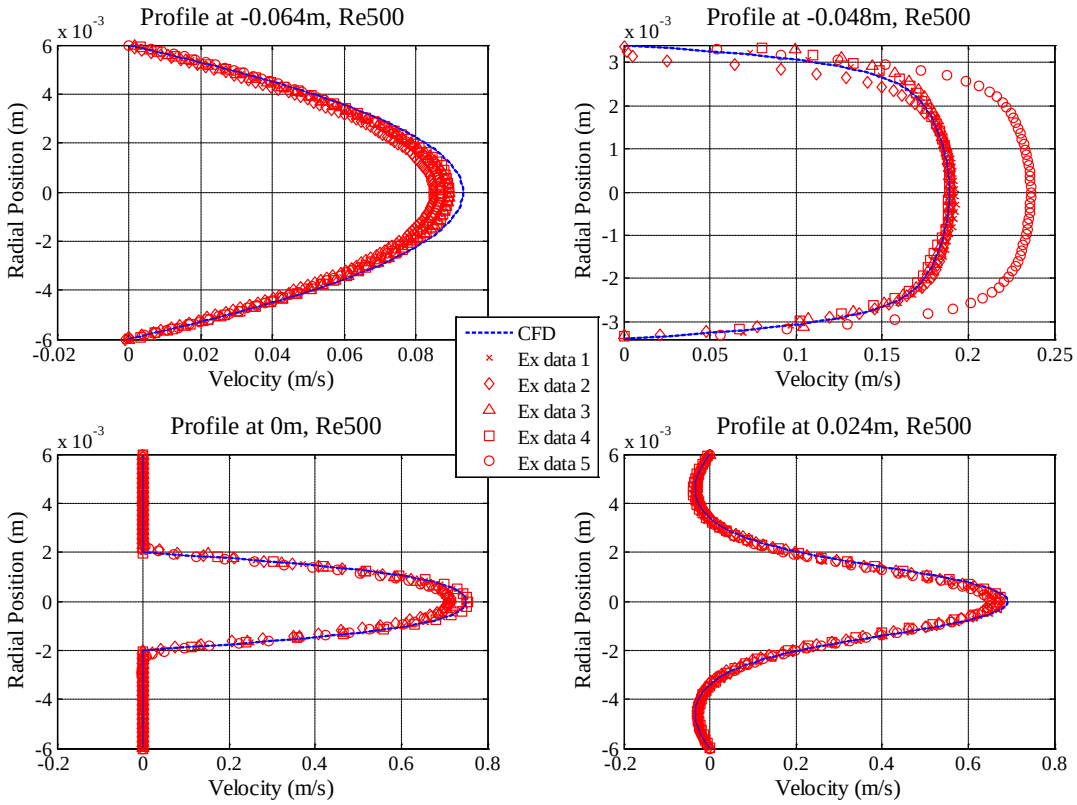

FIGURE 2-10 - COMPARISON OF AXIAL VELOCITY PROFILES AT A NUMBER OF LOCATIONS, EXPERIMENTAL VS. NUMERICAL AT RE500.

The mean experimental pressure drop is 305 Pa, with a range of 132 Pa to 413 Pa. Both the numerical and analytical approximations lie within this range, with the CFD model producing a close approximation to the mean experimental drop. The experimental results are in complete agreement that the pressure is fully recovered within the benchmark at an axial position of 0.032 m. The CFD simulation predicts the pressure is fully recovered at an axial position of 0.2 m, much further downstream than the experimental data suggests.

Finally a comparison between the experimental and numerical jet widths, as a function of axial position has been included (Figure 2-11). The jet width is defined

as the width of the profile, at the point where the axial velocity is half the peak. That is to say if the peak axial velocity is 1 ms^{-1} then the jet width is the width of the profile where the axial velocity is 0.5 ms^{-1} (Figure 2-12).

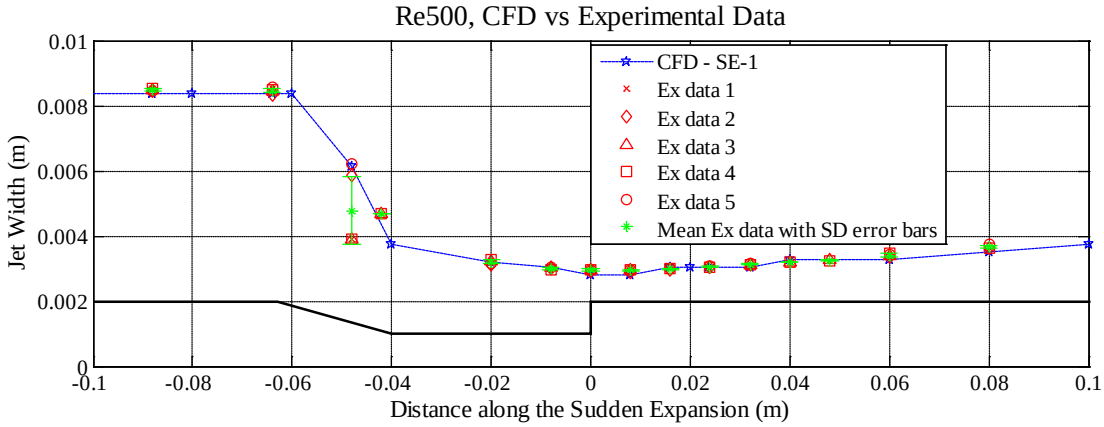

FIGURE 2-11 - COMPARISON OF JET WIDTH, EXPERIMENTAL VS. NUMERICAL AT RE500.

There is almost no variation in the experimental jet widths (Figure 2-11), with the exception of a point within the conical constrictor, where there appears to be a split in the experimental data. It would seem that it is not simply an anomalous result since three sets are in agreement. However, it may be that these three sets of results all come from the same experimental laboratory (the experimental data is anonymous) where the geometry may have been subtly different. It was reported that the benchmark geometries were within a 1% geometrical tolerance, but with highly sensitive flow rates these slight variations may be significant.

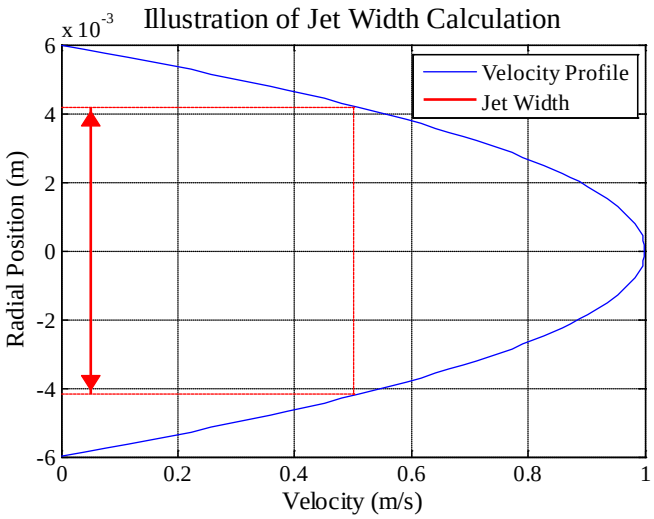

FIGURE 2-12 - ILLUSTRATION OF JET WIDTH CALCULATION

SUDDEN EXPANSION RE 3500: RESULTS AND DISCUSSION 2.5

ANALYTICAL SOLUTION 2.5.1

As in the previous case a gross first approximation of the pressure drop was computed using a combination of Poiseuille's and Bernoulli's principals. The calculated range of the total pressure drop was found to be between 881 Pa and 5273 Pa, with the pressure drop associated with each geometrical effect shown in Figure 2-13. The upper bound of the pressure recovery through the sudden expansion is known to be overestimated by Bernoulli, as discussed previously. The relative pressure drop associated with the conical constrictor is significantly larger at this Reynolds number when compared to the Reynolds number 500 case (Figure 2-4).

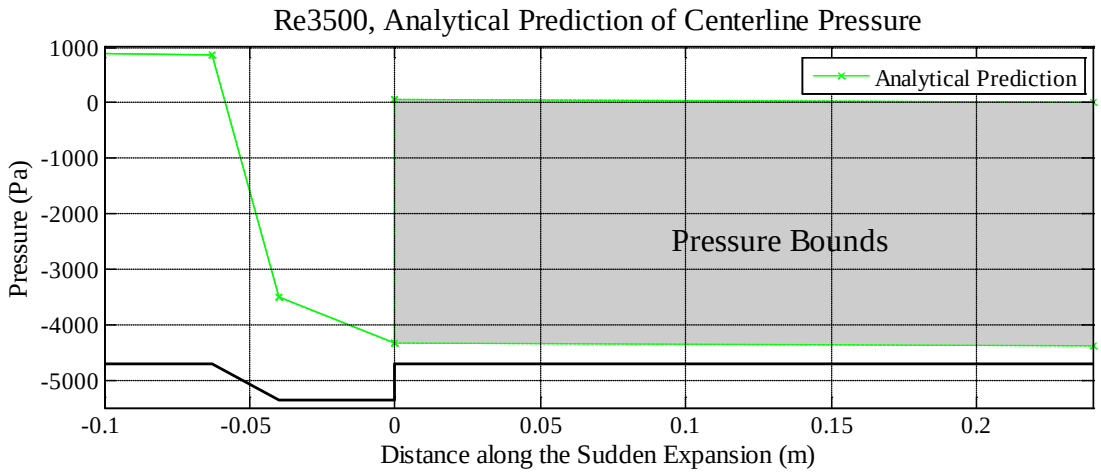

FIGURE 2-13 - ANALYTICAL PREDICTION OF PRESSURE AT RE3500

LAMINAR RESULTS 2.5.2

Although the Reynolds number in the constriction is 3500, suggesting turbulent flow (since 3500 > 2000), the Reynolds number in the larger, inlet and outlet, cylinders is approximately 1100, suggesting flow within the laminar regime.

As a first step a steady laminar simulation was conducted, on both SE-1 and SE-2 computational meshes. The simulations diverged in both cases.

Divergence of the steady laminar simulation implied that the flow field had significant temporal fluctuations. In an attempt to capture these temporal fluctuations a transient laminar simulation was conducted. The coarse computational mesh (SE-1) was used to conduct a simple time-step sensitivity test and it was identified that a very small time-step of $1x10^{-4}$s was required to ensure time accuracy.

Employing this time-step, transient laminar simulations were conducted on the three coarsest meshes (SE-1, SE-2 and SE-3). Unfortunately, due to the increased computational expense of a transient analysis, it was beyond the available computing power to conduct such a simulation on the finest mesh (SE-4).

The transient laminar analyses were run until the results became steady, i.e. not changing with time. This was found to occur after approximately 1.5 seconds of simulated physical time[1]. All simulations resolved temporal fluctuations in the flow

[1] Mesh SE-1 required 5 days, 10 hours and 49 minutes to simulate 1.5 seconds of physical time.

field, downstream of the sudden expansion. Figure 2-14 shows the instantaneous axial velocity (SE-2) on a planar cross-section through the length of the domain, at a number of instances in time. The flow shows strong fluctuation at the tip of the jet, identifying the cause of the divergent steady laminar simulations.

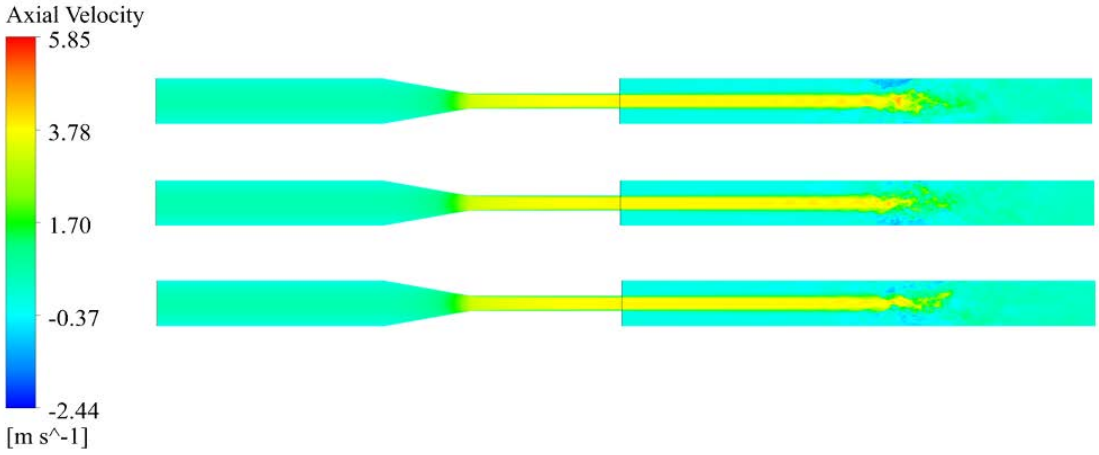

FIGURE 2-14 - INSTANTANEOUS AXIAL VELOCITY ON A PLANAR CROSS-SECTION THROUGH THE LENGTH OF THE BENCHMARK AT A NUMBER OF POINTS IN TIME (SE-2).

Evaluation of the time averaged axial velocity and pressure along the centreline illustrates the sensitivity of the transient laminar results to the mesh density (Figure 2-15). The coarse mesh predicts the onset of strong flow disturbance to occur at an axial location of approximately 0.022 m, while SE-2 and SE-3 predict the disturbance to occur around 0.05 m and 0.062 m respectively.

Mesh SE-2 required 12 days, 18 hours and 9 minutes to simulate 1.5 seconds of physical time.
Mesh SE-3 required 34 days, 22 hours and 18 minutes to simulate 1.5 seconds of physical time.
Simulations were solved on a Dell PowerEdge T710 using 4, 2.93 GHz Intel Xeon X5570 processors.

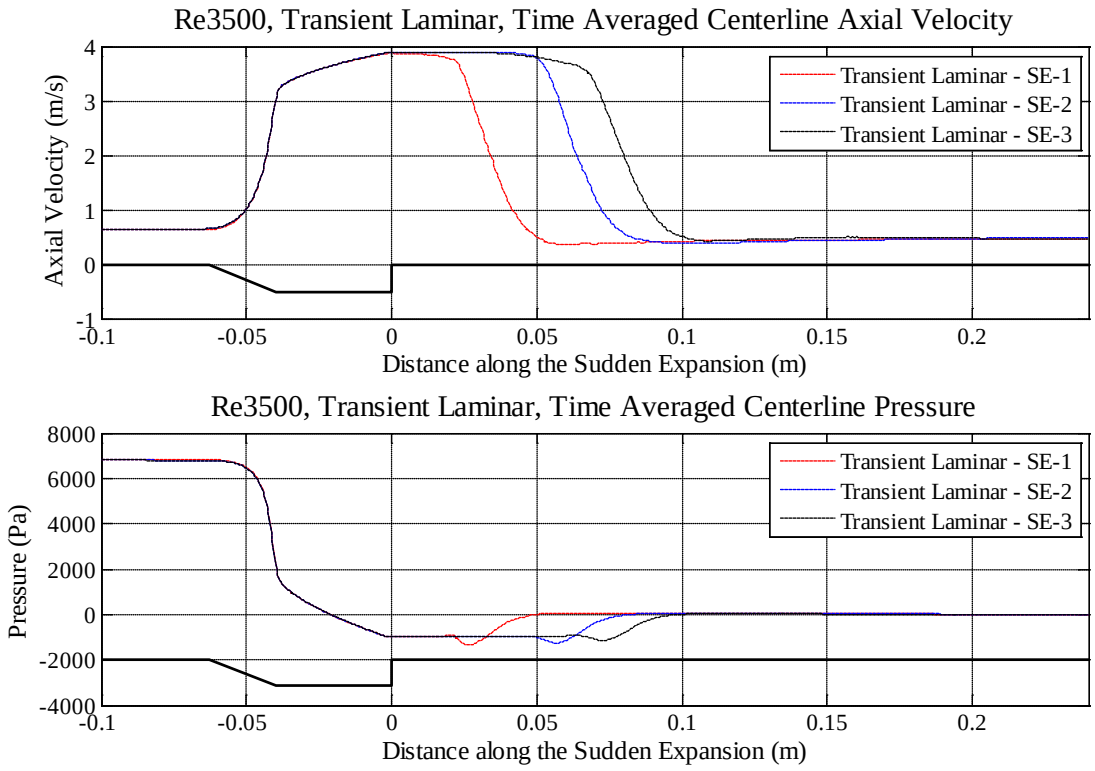

FIGURE 2-15 - COMPARISON OF TIME AVERAGED CENTRELINE AXIAL VELOCITY AND PRESSURE COMPUTED ON A NUMBER OF MESH DENSITIES. TRANSIENT LAMINAR SIMULATIONS AT RE3500

Clearly, without the ability to employ finer meshes, which approach the requirements for DNS the transient laminar simulation is unable to resolve the spatial length scales that contribute to the flow field at this Reynolds number. However, it is suggested that given the sensitivity of the flow even resolved DNS simulations may show a degree of statistical variation which may be described as a manifestation of the butterfly effect as defined in chaos theory.

STEADY STATE SHEAR STRESS TRANSPORT RESULTS 2.5.3

To fully close the governing equations of the SST model a turbulent intensity must be specified at the inlet and outlet boundaries of the computational domain. In ANSYS-CFX (ANSYS, Canonsburg, USA) there are a number of options as to how the intensity is defined. Since there was no experimental data available to indicate the degree of turbulent intensity within the benchmark, an assumption had to be made. The Reynolds number within the inlet cylinder was relatively low (1100) and so a low turbulent intensity (1%) was set. At the outlet a zero gradient turbulent

intensity condition was applied, which is appropriate for fully developed turbulent flows such as one might expect at the downstream boundary.

As in the Reynolds number 500 case, a mesh sensitivity study was conducted including each mesh density reported in Table 2.2. All the computational meshes show a good level of agreement in terms of the centreline axial velocity and pressure (Figure 2-16). This is also true for the wall shear stress and centreline shear strain rate (Figure 2-17), although there is a greater degree of variation in the shear strain rate as the fluid mores through the sudden expansion and the fluid becomes disturbed.

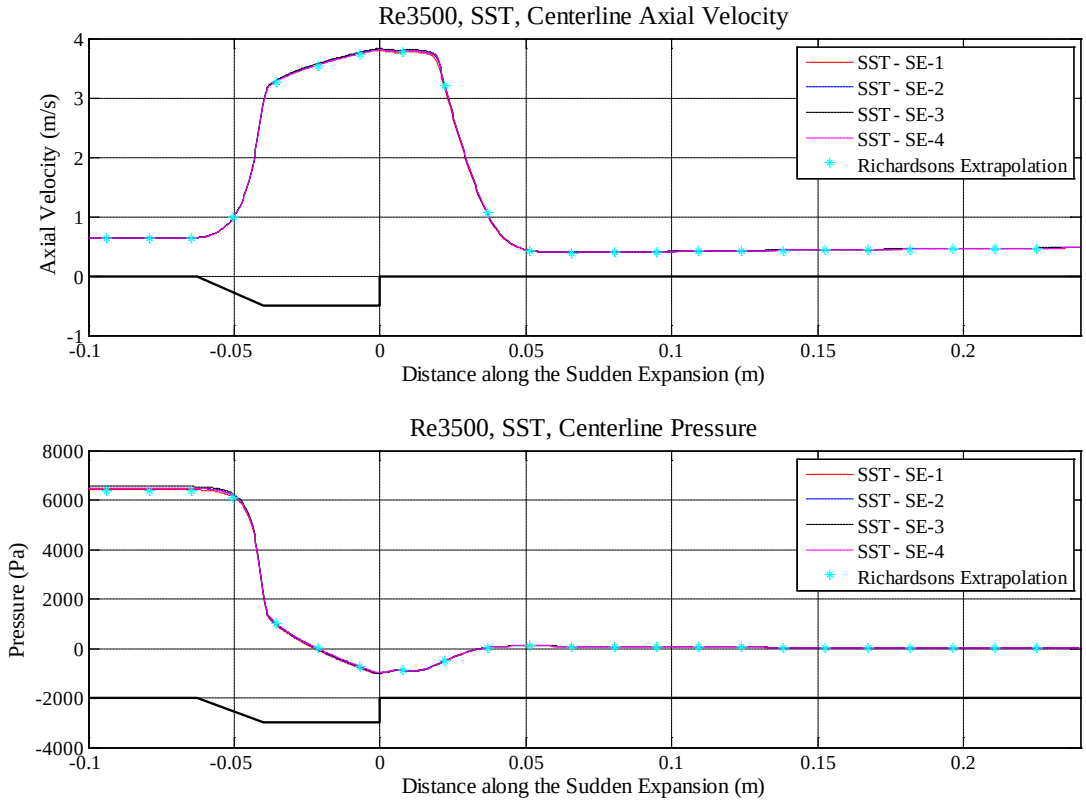

FIGURE 2-16 - COMPARISON OF CENTRELINE AXIAL VELOCITY AND PRESSURE COMPUTED ON A NUMBER OF MESH DENSITIES. SST SIMULATIONS AT RE3500

The centreline axial velocity has a much faster drop off after the sudden expansion than in the Reynolds 500 case (Figure 2-7). This is due to turbulence and the associated loss of energy which occurs at the higher flow rates. The turbulence is also responsible for the rapid recovery in pressure, which is seen in the higher Reynolds number flows (Figure 2-16). A further indication of the onset of turbulence

is the peak in the centreline shear strain rate, after the sudden expansion (Figure 2-17). After this peak the fluid rapidly becomes fully developed (i.e. the centreline shear strain rate returns to zero). This is not true in the Reynolds number 500 case, where the shear strain rate never truly returns to zero and as such the flow must not be fully developed even after such a long outlet domain.

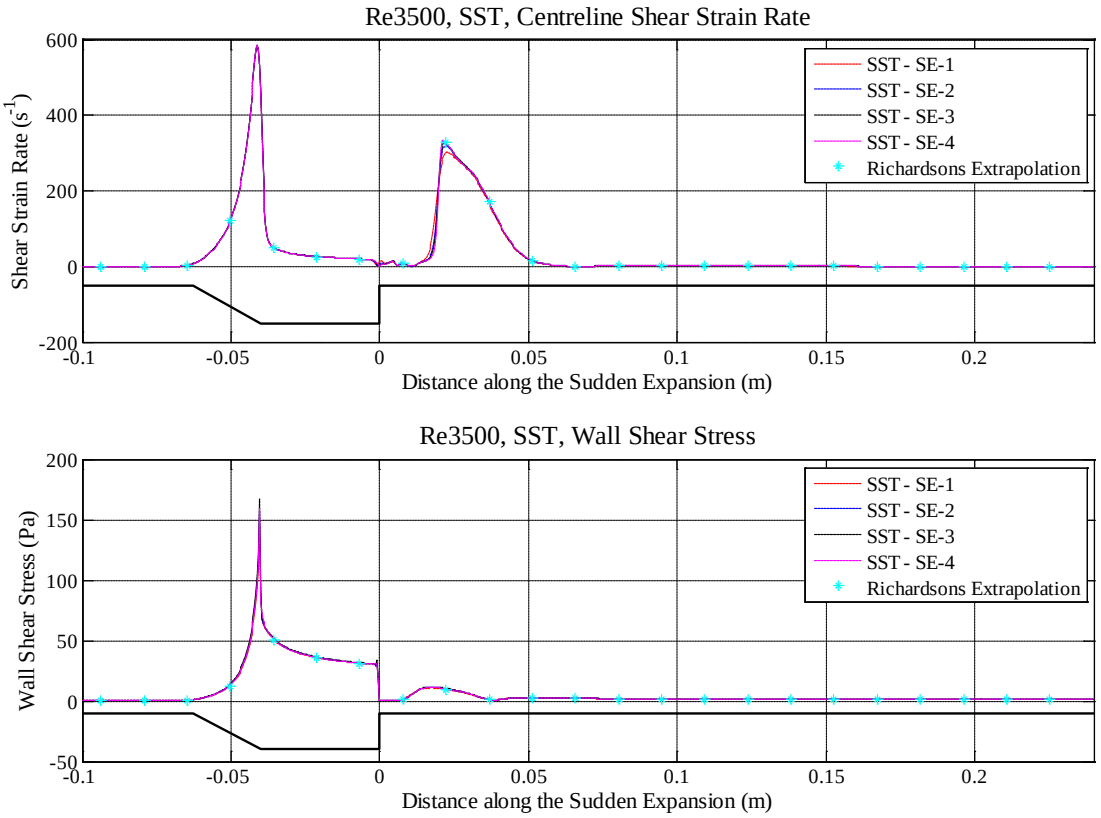

FIGURE 2-17 - COMPARISON OF CENTRELINE SHEAR STRAIN RATE AND WALL SHEAR STRESS COMPUTED ON A NUMBER OF MESH DENSITIES. SST SIMULATIONS AT RE3500

The dependence of the flow field solution on the computational mesh was assessed using Richardson's extrapolation method and the predicted solution for each variable of interest has been plotted (Figure 2-16 and Figure 2-17). The mean and maximum relative error associated with each computational mesh is summarised in Table 2.4.

	Mean (Max)		Relative Error	
Mesh	**Axial Velocity**	**Pressure**	**Shear Strain Rate**	**Wall Shear Stress**
SE-1	0.17 (2.71)	0.22 (1.48)	0.29	0.11
SE-2	0.17 (0.77)	0.42 (1.50)	0.17	0.19
SE-3	0.23 (1.04)	0.60 (2.41)	0.15	0.27
SE-4	0.09 (0.39)	0.30 (1.21)	0.08	0.14

TABLE 2.4 - EVALUATION OF THE MEAN AND MAXIMUM RELATIVE ERROR FOR THE VARYING MESH DENSITIES AGAINST THE RICHARDSON'S PREDICTION. SST AT RE3500

All meshes achieved the predefined criteria for mesh convergence. However, the coarsest mesh (SE-1) produced a maximum relative error in the centreline shear strain rate of 18.7, which is apparent in Figure 2-17. For this reason the comparisons between the experimental and numerical results have been made using mesh SE-2.

LARGE EDDY SIMULATION RESULTS 2.5.4

As discussed in Section 2.3.3 the Large Eddy Simulation solves the spatially filtered time varying Navier Stokes equations (Equation 2-19) employing the WALE SGS model. As in the transient laminar simulations the increase in computational expense required to conduct a transient analysis meant the finest mesh was not considered and after running the two coarse meshes the second finest mesh was also not employed since the time averaged plots of centreline velocity and pressure for the LES models (Figure 2-18) illustrate a similar trend to the transient laminar simulations.

The simulations predicted the onset of turbulence to occur further and further downstream of the sudden expansion as the mesh was refined producing results that are entirely dependent on the mesh density. This is perhaps not all that surprising since the underlying solution of the LES is a spatially filtered version of the equations which are solved in the transient laminar case.

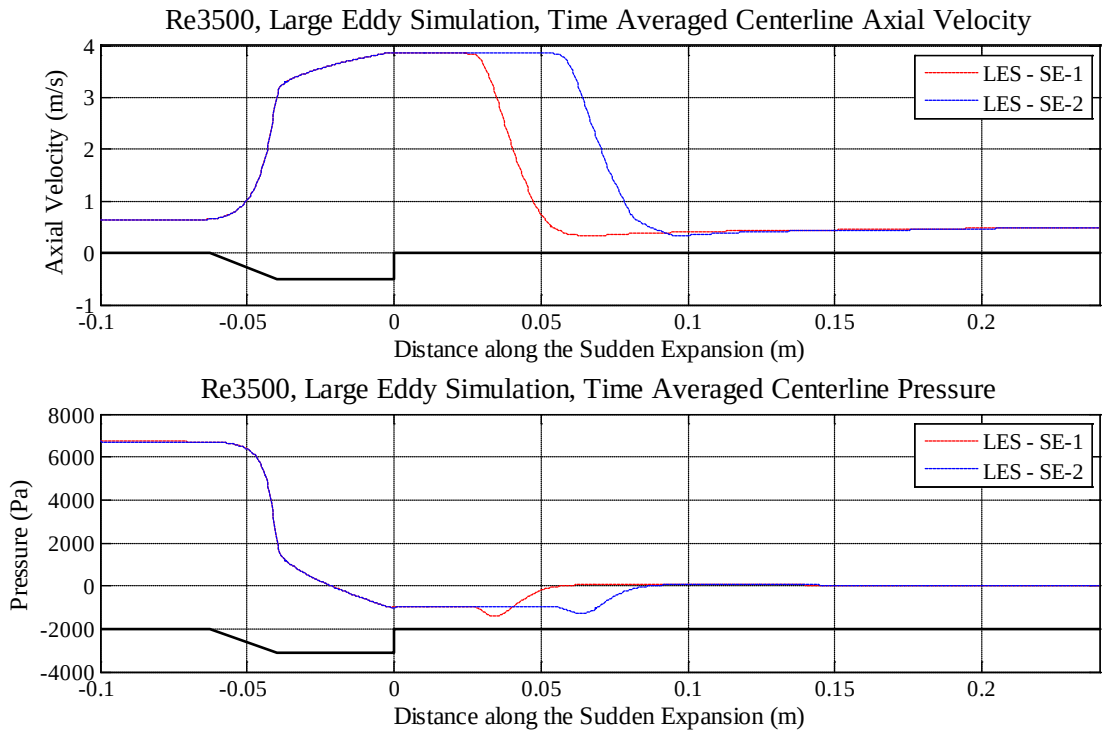

FIGURE 2-18 - COMPARISON OF TIME AVERAGED CENTRELINE AXIAL VELOCITY AND PRESSURE COMPUTED ON A NUMBER OF MESH DENSITIES. LES SIMULATIONS AT RE3500

SCALE ADAPTIVE SIMULATION – SST RESULTS 2.5.5

The SAS-SST model is a transient implementation of the SST model and so only the three coarsest meshes were considered. The SAS-SST simulations achieved a time averaged solution in approximately half the simulated physical time required for the transient laminar or LES simulations and required no additional computational effort[2]. This is believed to be because the SAS-SST model employs the SST (steady state turbulence model) to describe the steady components of the flow field.

The results of the different mesh densities (Figure 2-19 and Figure 2-20) demonstrate that unlike the transient laminar and LES models the SAS-SST simulations achieve mesh independence with the described meshes.

[2] Mesh SE-3 required 17 days, 4 hours and 36 minutes to simulate 0.8 seconds of physical time. Solved on a Dell PowerEdge T710 using 4, 2.93 GHz Intel Xeon X5570 processors.

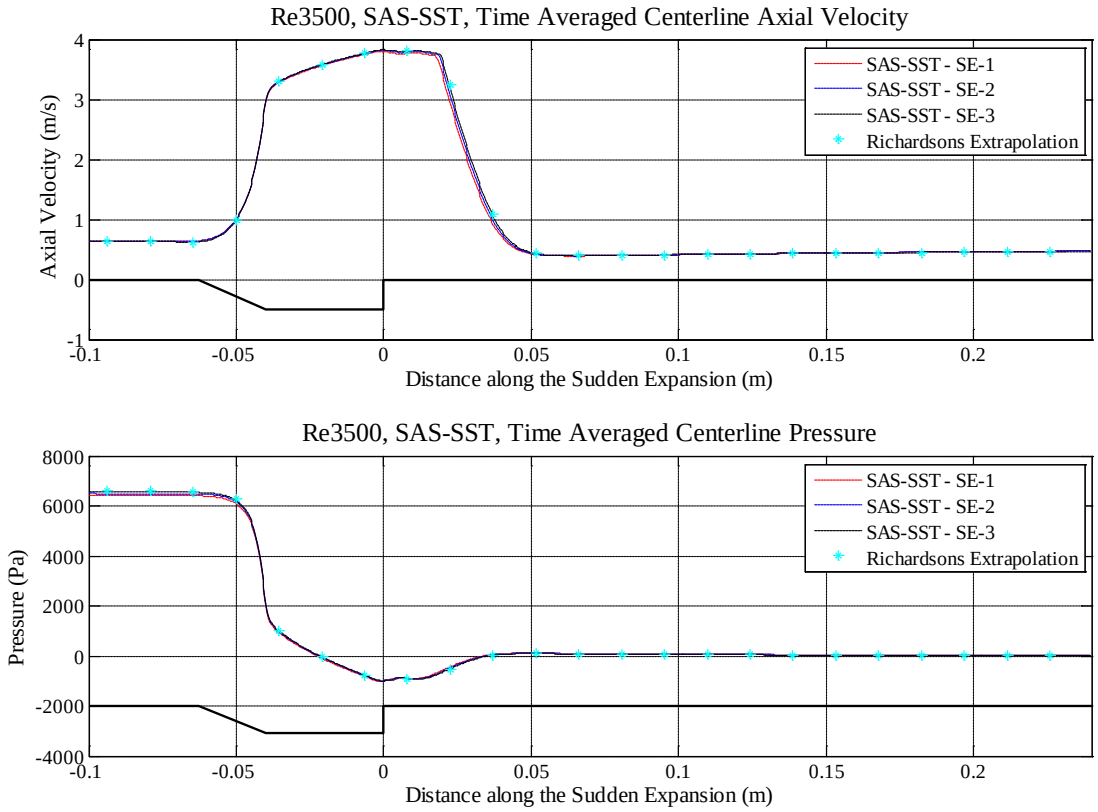

FIGURE 2-19 - COMPARISON OF TIME AVERAGED CENTRELINE AXIAL VELOCITY AND PRESSURE COMPUTED ON A NUMBER OF MESH DENSITIES. SAS-SST SIMULATIONS AT RE3500

The mean and maximum relative errors (Table 2.5) illustrate that all but the coarsest mesh achieves the pre-defined criteria of convergence for each variable of interest.

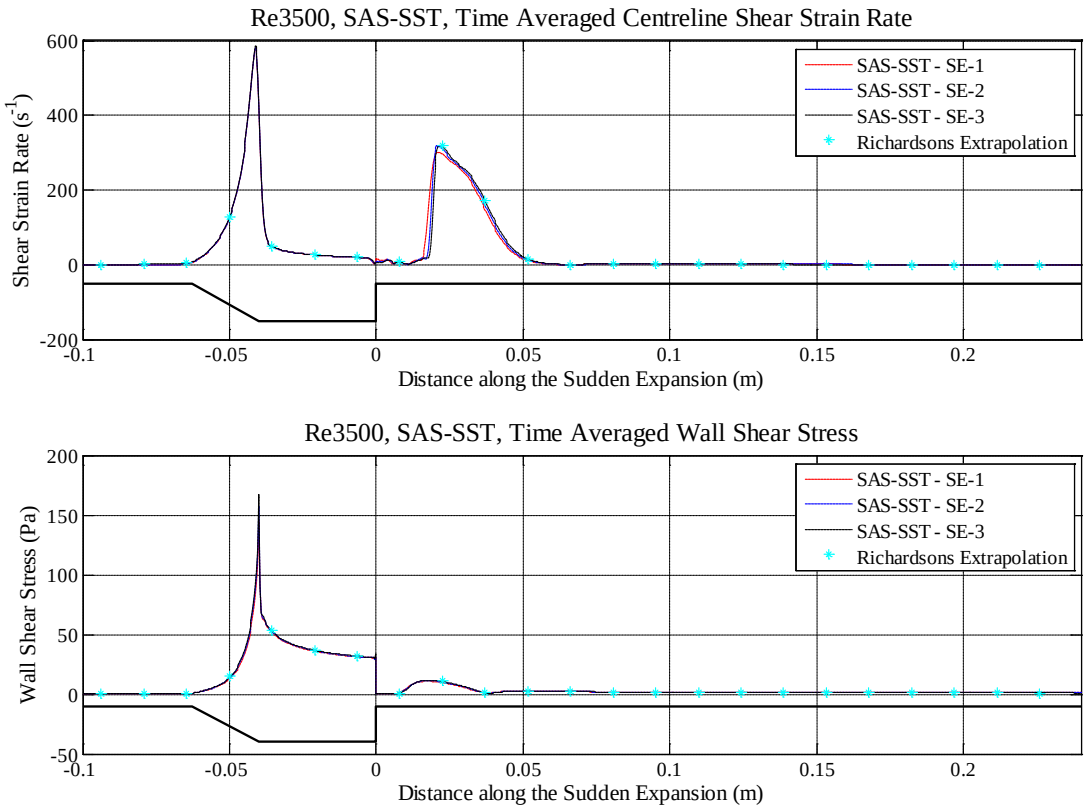

FIGURE 2-20 - COMPARISON OF TIME AVERAGED CENTRELINE SHEAR STRAIN RATE AND WALL SHEAR STRESS COMPUTED ON A NUMBER OF MESH DENSITIES. SAS-SST SIMULATIONS AT RE3500

		Mean (Max)	Relative Error	
Mesh	**Axial Velocity**	**Pressure**	**Shear Strain Rate**	**Wall Shear Stress**
SE-1	0.62 (8.31)	0.83 (2.69)	0.55	0.33
SE-2	0.39 (4.76)	0.48 (1.54)	0.31	0.24
SE-3	0.13 (1.56)	0.19 (0.63)	0.06	0.17

TABLE 2.5 - EVALUATION OF THE MEAN AND MAXIMUM RELATIVE ERROR FOR THE VARYING MESH DENSITIES AGAINST THE RICHARDSON'S PREDICTION. SAS-SST AT RE3500

Interestingly, in the steady SST model the coarsest mesh (SE-1) underestimated the centreline shear strain rate in the turbulent region downstream of the sudden expansion (Figure 2-17). This is not the case in the SAS-SST model where all the meshes are in good agreement as to the peak shear strain rate in this region (Figure

2-20). However, the coarsest SAS-SST simulation predicts the onset of turbulence to occur earlier than the finer meshes (Figure 2-19), which relates to a peak relative error in the centreline velocity of 8.31 (Table 2.5). In consequence, the mesh SE-2 has been used in the following comparison with the experimental data.

EXPERIMENTAL VS NUMERICAL RESULTS 2.5.6

When comparing the numerical predictions with the experimental results only the models with mesh converged solutions have been considered (i.e. SST and SAS-SST models).

The numerical and experimental centreline axial velocities and pressures have been compared in Figure 2-21. The spread in the experimental pressure data is far better than in the laminar case (Figure 2-9). The numerical models accurately predict the axial velocity in the inlet cylinder, the conical constrictor and through the constriction and sudden expansion. However, both the SST and SAS-SST models predict the onset of turbulence (and associated drop in axial velocity) to occur at a distance of approximately 0.02m downstream of the sudden expansion, whereas the experimental data shows it to occur at around 0.03m. This is believed to be because the numerical models overpredict the degree of turbulence and do not accurately capture the complex transitional flows that occur in this system.

The analytical (assuming no pressure recovery through the sudden expansion) and numerical pressure drops differ by approximately 20 percent in the Reynolds number 3500 case which is comparable to the percentage difference in the Reynolds number 500 case. The mean experimental pressure drop is 8260 Pa, with a range of 7671 Pa to 9568 Pa. Both the numerical and analytical solutions produce smaller pressure drops than those observed experimentally, with the numerical prediction varying from the mean experimental by approximately 20%. The simulation results also predict a region of negative pressure within the constriction and also as the fluid moves through the sudden expansion, while the experimental data are in agreement that the pressure remains positive through the constriction. The experimental pressures are seen to fully recover at an axial location of 0.032 m which is in agreement with the numerical results (Figure 2-21).

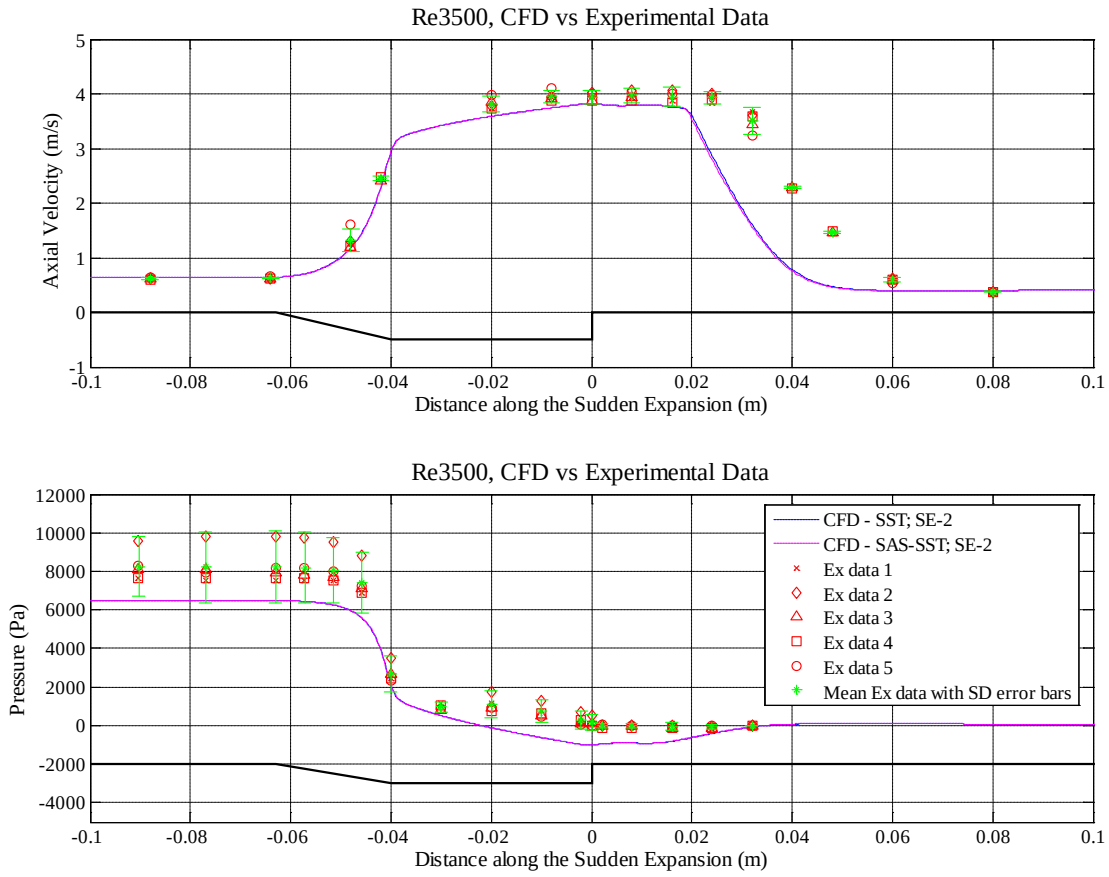

FIGURE 2-21 - COMPARISON OF CENTRELINE AXIAL VELOCITY AND PRESSURE, EXPERIMENTAL VS. NUMERICAL AT RE3500.

The numerical and experimental axial velocity profiles have been compared in Figure 2-22, at a number of points along the benchmark. The results confirm that the numerical models are in good agreement with the experimental data until the point where the turbulent structures are predicted in the outlet cylinder. This is further emphasised in Figure 2-23 where the experimental and numerical jet widths (as described in Figure 2-12) are compared along the length of the benchmark.

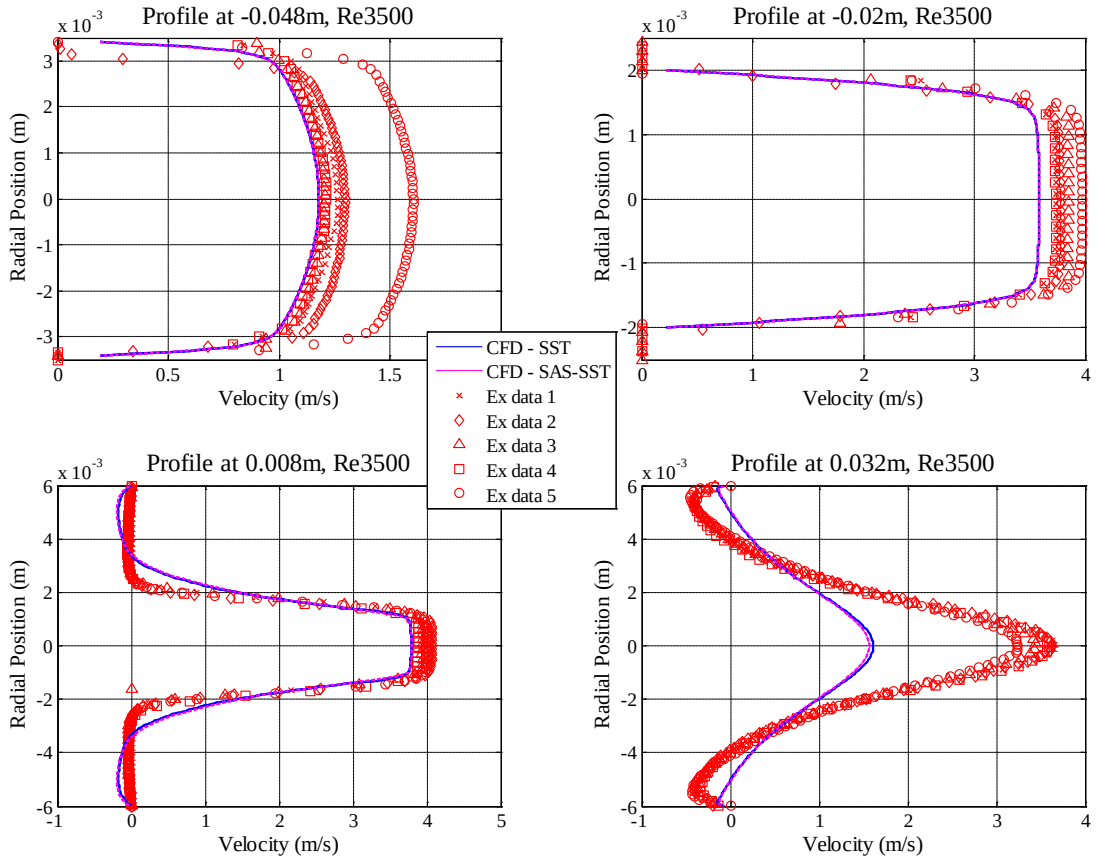

FIGURE 2-22 - COMPARISON OF AXIAL VELOCITY PROFILES AT A NUMBER OF LOCATIONS, EXPERIMENTAL VS. NUMERICAL AT RE3500.

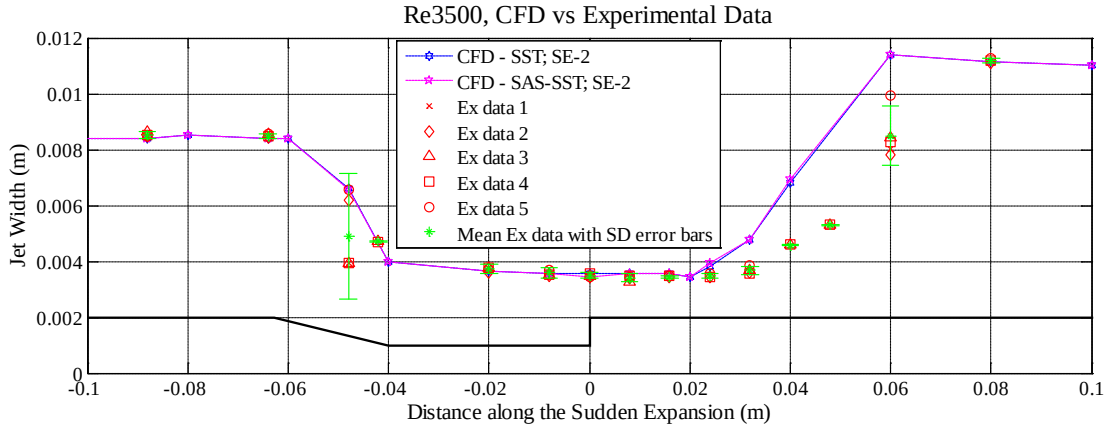

FIGURE 2-23 - COMPARISON OF JET WIDTH, EXPERIMENTAL VS. NUMERICAL AT RE3500.

It is also important to note that the SST and SAS-SST models are in near perfect agreement (Figure 2-21, Figure 2-22 and Figure 2-23), suggesting that the SST model is the most efficient and appropriate method for simulating highly sensitive steady flow fields of this type. The SAS-SST does not offer any advantages in this

steady flow system but could be of merit in transient flow fields such as those found in the aorta, which is a focus of the final half of this thesis.

RESULTS FROM THE CFD COMMUNITY

A number of figures published by the FDA [85] relating to this benchmark have been included, with permission, to demonstrate how important these validation studies are and how user-dependent CFD simulations can be.

The axial velocity profiles at a number of locations along the benchmark and the centreline axial velocity for the Reynolds number 500 case (Figure 2-24) and the Reynolds number 3500 case (Figure 2-25) are shown below.

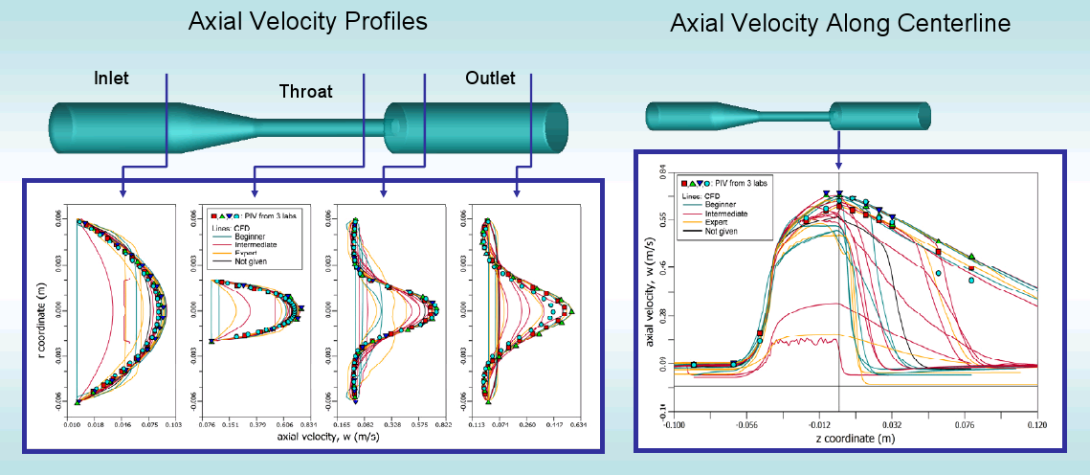

FIGURE 2-24 – AXIAL VELOCITY AT A NUMBER OF PROFILES AND ALONG THE CENTRELINE OF THE FDA BENCHMARK RE500. (THE LINES REPRESENT THE CFD RESULTS WITH THE LINE COLOUR CORRESPONDING TO THE SELF DEFINED USER LEVEL AND THE POINTS DENOTING THE EXPERIMENTAL DATA.)

The variation in the CFD results are quite shocking, with many alleged *"Expert"* and *"Intermediate"* users producing flow field predictions which deviate significantly from the experimental data and with what one might describe as very unusual and highly unlikely velocity profiles.

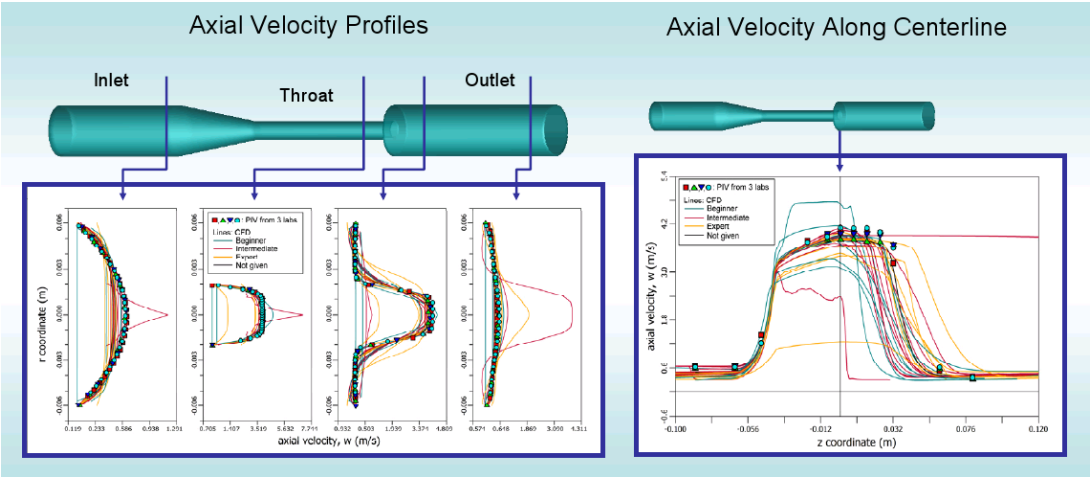

FIGURE 2-25 - AXIAL VELOCITY AT A NUMBER OF PROFILES AND ALONG THE CENTRELINE OF THE FDA BENCHMARK RE3500. (THE LINES REPRESENT THE CFD RESULTS WITH THE LINE COLOUR CORRESPONDING TO THE SELF DEFINED USER LEVEL AND THE POINTS DENOTING THE EXPERIMENTAL DATA.)

There is a very clear requirement for well validated CFD protocols before these techniques are likely to gain routine use in medical device certification.

CONCLUSIONS 2.7

An idealised benchmark described by the FDA has been studied at two Reynolds numbers. The first corresponds to a laminar flow field (Re500), while the second (Re3500) is considered transitional.

The steady Navier-Stokes and Continuity equations were shown to produce very good approximations for the laminar flow field when compared to the experimental data. The numerical pressure drop across the benchmark was within the range measured in the experimental studies, as was a first order approximation using a combination of Poiseuille's and Bernoulli's principals.

Five alternative numerical models were used to solve the more complex transitional flow field. The steady laminar simulation diverged due to temporal fluctuations and the spatial resolution of the transient laminar and LES models was not sufficient to capture the important turbulent length scales, producing mesh-dependent solutions. The steady SST and transient SAS-SST models produced the closest approximation

of the transitional flow field, although both models over-predicted the degree of turbulence and in turn energy losses within the system.

The importance of experimental validation of both a CFD code and a methodology is clearly demonstrated from the wide variation in numerical results both presented in this chapter and submitted to the FDA's CFD benchmark under the "*Critical Path Initiative*".

CHAPTER 3

TUNING STRATEGY FOR THE COUPLED WINDKESSEL

MOTIVATION 3.1

There is a strong drive within the cardiovascular engineering community to personalise computational models to an individual patient, thereby facilitating the use of simulations for intervention planning.

A challenge of this ambitious aim is the application of patient specific boundary conditions. The current state of the art is to couple complex 3D models to lower order 1D or 0D descriptions of the cardiovascular system, commonly termed *multi-scale* modelling. In doing this one incorporates an additional set of unknowns, associated with the lower order models. In the example of a 0D Windkessel element coupled to a 3D CFD model there are a number of 0D parameters which must be *tuned* to produce the desired response.

The following work documents an analytical strategy for this tuning process, which might otherwise be conducted in a trial and error manner. This becomes extremely computationally expensive since one must solve the fully coupled system at each iteration.

ANALYTICAL SOLUTIONS 3.2

To develop a strategy for tuning the parameters of a 0D Windkessel it is first important to understand the mathematics describing the isolated 0D system and subsequently the coupled system.

TWO ELEMENT WINDKESSEL 3.2.1

The two element Windkessel, as discussed in the introduction, comprises a resistive and a capacitance element (Figure 3-1).

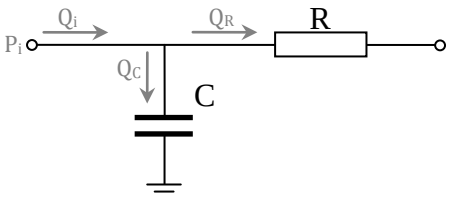

FIGURE 3-1 - TWO ELEMENT WINDKESSEL

The governing equation for this system is:

$$Q_i = Q_C + Q_R = C\frac{dP_i}{dt} + \frac{P_i}{R}$$

EQUATION 3-1

Where Q refers to flow, R is the value of resistance, C is the capacitance and P_i refers to the pressure (Figure 3-1).

THREE ELEMENT WINDKESSEL 3.2.2

The three element Windkessel has an additional resistor (Figure 3-2), referred to from here on in as the input resistance.

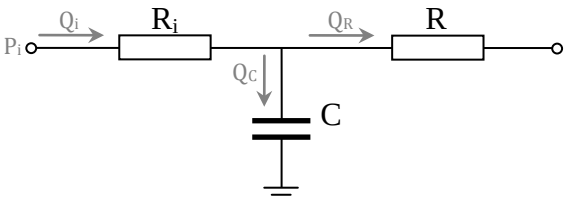

FIGURE 3-2 - THREE ELEMENT WINDKESSEL

The governing equation of the three element Windkessel is:

$$Q_i = Q_C + Q_R = C\frac{d(P_i - Q_i R_i)}{dt} + \frac{P_i - Q_i R_i}{R}$$

EQUATION 3-2

Where the input resistance is referred to as R_i.

WINDKESSEL COUPLED TO A TUBE - ALGEBRA 3.2.3

The latter part of this thesis focuses on the prediction and characterisation of flow in the human aorta, which in its simplest form is essentially a straight tube through which pressure information is transmitted. In the following work the algebra of the two and three element Windkessel are expanded upon to incorporate the description of a 1D tube at the upstream terminal of the Windkessel (Figure 3-3). By analytically studying this simplified system there is the potential to understand the fundamental behaviour and physics.

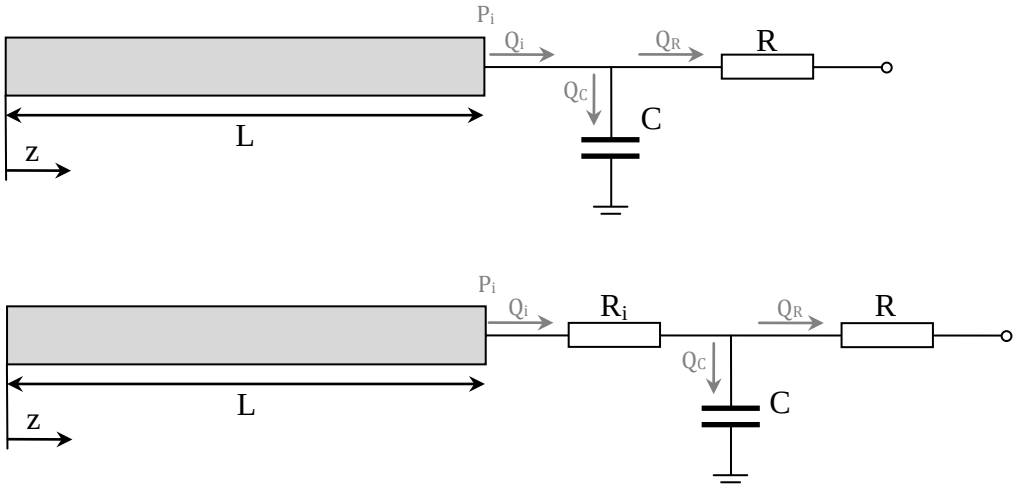

FIGURE 3-3 - ILLUSTRATION OF THE 1D TUBE COUPLED TO THE TWO AND THREE ELEMENT WINDKESSEL

It is necessary to consider initially the 1D domain in isolation. The inlet boundary condition (at z=0m) is assumed to be a harmonic flow wave of the form:

$$Q(0,t) = Q_{0c}cos(\omega t) + Q_{0s}sin(\omega t)$$

EQUATION 3-3

The solution throughout the 1D domain can be written in the following form in which the forward and backward travelling waves are fully described.

$$Q(z,t) = \{Q_1 cos(kz - \omega t) + Q_2 sin(kz - \omega t)\} + \{Q_3 cos(kz + \omega t) + Q_4 sin(kz + \omega t)\}$$

EQUATION 3-4

Note: $(Q_1 + Q_3) = Q_{0c}$ and $(-Q_2 + Q_4) = Q_{0s}$.

In Equation 3-4 k is the wave number which for an inviscid fluid, is defined as:

$$k = \frac{\omega}{c}$$

EQUATION 3-5

Where c is the wave speed, calculated from the Moens-Kortweg relation, modified for plane strain (assuming longitudinal tethering) (Equation 3-6).

$$c = \sqrt{\frac{Eh}{2\rho r_0(1 - v^2)}}$$

EQUATION 3-6

Where h is the thickness of the vessel wall, E is the Young's Modulus, ρ is the fluid density, r_0 is the initial radius and v is the Poisson's ratio of the vessel wall.

At the outlet of the 1D domain (z=L), Equation 3-4 expands to:

$$Q(L,t) = \{(Q_1 + Q_3)cos(kL) + (Q_2 + Q_4)sin(kL)\}cos(\omega t) + \{(Q_4 - Q_2)cos(kL) + (Q_1 - Q_3)sin(kL)\}sin(\omega t)$$

EQUATION 3-7

In the same way, the outlet pressure (z=L) can be described by:

$$P(L,t) = \{(P_1 + P_3)cos(kL) + (P_2 + P_4)sin(kL)\}cos(\omega t) + \{(P_4 - P_2)cos(kL) + (P_1 - P_3)sin(kL)\}sin(\omega t)$$

EQUATION 3-8

Now since:

$$\frac{P_1}{Q_1} = \frac{P_2}{Q_2} = -\frac{P_3}{Q_3} = -\frac{P_4}{Q_4} = \sqrt{\frac{L'}{C'}}$$

EQUATION 3-9

Where L' and C' represent the inertance and capacitance of the 1D domain, per unit length.

The pressure at the outlet can be written in terms of the flow components:

$$P(L,t) = \sqrt{\frac{L'}{C'}}\{\big((Q_1 - Q_3)cos(kL) + (Q_2 - Q_4)sin(kL)\big)cos(\omega t) + \big((-Q_2 - Q_4)cos(kL) + (Q_1 + Q_3)sin(kL)\big)sin(\omega t)\}$$

EQUATION 3-10

Consider now the inclusion of a two element Windkessel at the outlet of the 1D domain (Figure 3-3). If the boundary conditions are defined as:

$$Q(L,t) = Q_i = Q_{ic}cos(\omega t) + Q_{is}sin(\omega t) \;:\; P(L,t) = P_i = P_{ic}cos(\omega t) + P_{is}sin(\omega t)$$

Then from the governing equation (Equation 3-1) of the two element Windkessel it can be shown that under these boundary conditions the differential equation is satisfied if:

$$P_{ic} = \frac{R}{1 + R^2C^2\omega^2}(Q_{ic} - RC\omega Q_{is}) \quad : \quad P_{is} = \frac{R}{1 + R^2C^2\omega^2}(RC\omega Q_{ic} + Q_{is})$$

Substituting in the equations for flow and pressure, in terms of the flow components, at the outlet of the 1D domain (Equation 3-7 and Equation 3-10) and collecting like terms, one arrives at the following set of equations:

$$\begin{aligned}
&\left(\sqrt{\frac{L'}{C'}}cos(kL) + \frac{R}{1 + R^2C^2\omega^2}\left(-cos(kL) + RC\omega sin(kL)\right)\right)Q_1 \\
&\quad + \left(\sqrt{\frac{L'}{C'}}sin(kL) + \frac{R}{1 + R^2C^2\omega^2}\left(-sin(kL) - RC\omega cos(kL)\right)\right)Q_2 \\
&\quad + \left(-\sqrt{\frac{L'}{C'}}cos(kL) + \frac{R}{1 + R^2C^2\omega^2}\left(-cos(kL) - RC\omega sin(kL)\right)\right)Q_3 \\
&\quad + \left(-\sqrt{\frac{L'}{C'}}sin(kL) + \frac{R}{1 + R^2C^2\omega^2}\left(-sin(kL) + RC\omega cos(kL)\right)\right)Q_4 = 0
\end{aligned}$$

$$\begin{aligned}
&\left(\sqrt{\frac{L'}{C'}}sin(kL) + \frac{R}{1 + R^2C^2\omega^2}\left(-RC\omega cos(kL) - sin(kL)\right)\right)Q_1 \\
&\quad + \left(-\sqrt{\frac{L'}{C'}}cos(kL) + \frac{R}{1 + R^2C^2\omega^2}\left(-RC\omega sin(kL) + cos(kL)\right)\right)Q_2 \\
&\quad + \left(\sqrt{\frac{L'}{C'}}sin(kL) + \frac{R}{1 + R^2C^2\omega^2}\left(-RC\omega cos(kL) + sin(kL)\right)\right)Q_3 \\
&\quad + \left(-\sqrt{\frac{L'}{C'}}cos(kL) + \frac{R}{1 + R^2C^2\omega^2}\left(-RC\omega sin(kL) - cos(kL)\right)\right)Q_4 = 0
\end{aligned}$$

EQUATIONS 3-11

These, when combined with the conditions $(Q_1 + Q_3) = Q_{0c}$ and $(-Q_2 + Q_4) = Q_{0s}$, produce a solution for all components of the flow waveform. Which, when incorporated into Equation 3-4 and the equivalent description of pressure, fully

describes the forward and backward travelling pressure and flow waveforms within the coupled 1D-0D domain.

This same derivation process can be applied to the three element Windkessel with the resulting set of equations taking the form:

$$\left(\left\{\sqrt{\frac{L'}{C'}}-\mathrm{R_i}\right\}cos(kL)+\frac{R}{1+R^2C^2\omega^2}\left(-cos(kL)+RC\omega sin(kL)\right)\right)Q_1$$
$$+\left(\left\{\sqrt{\frac{L'}{C'}}-\mathrm{R_i}\right\}sin(kL)+\frac{R}{1+R^2C^2\omega^2}\left(-sin(kL)-RC\omega cos(kL)\right)\right)Q_2$$
$$+\left(\left\{-\sqrt{\frac{L'}{C'}}-\mathrm{R_i}\right\}cos(kL)+\frac{R}{1+R^2C^2\omega^2}\left(-cos(kL)-RC\omega sin(kL)\right)\right)Q_3$$
$$+\left(\left\{-\sqrt{\frac{L'}{C'}}-\mathrm{R_i}\right\}sin(kL)+\frac{R}{1+R^2C^2\omega^2}\left(-sin(kL)+RC\omega cos(kL)\right)\right)Q_4=0$$

$$\left(\left\{\sqrt{\frac{L'}{C'}}-\mathrm{R_i}\right\}sin(kL)+\frac{R}{1+R^2C^2\omega^2}\left(-RC\omega cos(kL)-sin(kL)\right)\right)Q_1$$
$$+\left(\left\{-\sqrt{\frac{L'}{C'}}-\mathrm{R_i}\right\}cos(kL)+\frac{R}{1+R^2C^2\omega^2}\left(-RC\omega sin(kL)+cos(kL)\right)\right)Q_2$$
$$+\left(\left\{\sqrt{\frac{L'}{C'}}-\mathrm{R_i}\right\}sin(kL)+\frac{R}{1+R^2C^2\omega^2}\left(-RC\omega cos(kL)+sin(kL)\right)\right)Q_3$$
$$+\left(\left\{-\sqrt{\frac{L'}{C'}}-\mathrm{R_i}\right\}cos(kL)+\frac{R}{1+R^2C^2\omega^2}\left(-RC\omega sin(kL)-cos(kL)\right)\right)Q_4=0$$

EQUATIONS 3-12

NUMERICAL COUPLING STRATEGY 3.3

Two coupling strategies have been implemented in the commercially available CFD software package ANSYS-CFX (ANSYS Inc, Canonsburg, USA), which is used throughout this thesis to solve the governing equations of the fluid. The 3D domain is coupled to a two or three element Windkessel model via a FORTRAN user subroutine (Figure 3-4). In both approaches the 3D domain passes flow (Q_{3D}) to the 0D domain and receives a value of pressure (P_{0D}) in return. The governing equations of the 0D model are solved in an implicit manner using a first order backward Euler algorithm.

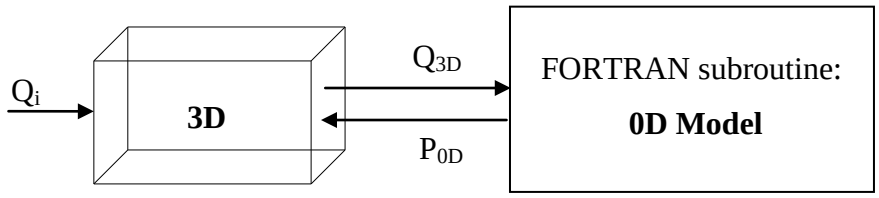

FIGURE 3-4 - ILLUSTRATION OF THE 0D-3D COUPLING,
Q_I IS THE INITIAL GUESS FROM ANSYS-CFX (ANSYS INC, CANONSBURG, USA)

The first coupling technique, from here on referred to as the *explicit coupling approach*, passes the 3D flow to the FORTRAN routine at the end of a time-step, at which point the governing equations of the 0D model are solved and the computed pressure is applied to the 3D domain for the next time-step calculation.

The second technique, from here on termed the *implicit coupling approach*, passes the 3D flow to the FORTRAN routine at the end of every iteration of the 3D solve (i.e. multiple times within a time-step). At each point the governing equations of the 0D model are solved and the calculated pressure is applied to the 3D domain.

In the explicit coupling approach the 3D boundary condition is essentially a time-step behind and so the size of the time-step becomes a limiting factor (if it is too large the resulting solution of the coupled system may be incorrect or unstable). However, an advantage to this approach is that it is simple to implement. In the implicit coupling approach there is no such dependence on the time-step which means in general the solution is more stable. A disadvantage is that since the

boundary conditions of the 3D domain are varying within each time-step the solution may require additional iteration loops to reach a converged solution.

Unless otherwise stated the explicit coupling approach is used throughout this thesis.

ANALYTICAL VS. NUMERICAL COUPLING 3.4

A comparison, between the derived analytical solutions (Equations 3-11 and Equations 3-12) and a 3D CFD model coupled to a 0D Windkessel termination, is conducted to check the validity of the analytical derivations and that of the numerical coupling strategy.

MODEL PARAMETERS 3.4.1

This thesis focuses on simulating aortic flow fields. As such the comparison employs an idealised vessel with dimensions and material properties similar to those of a healthy human aorta.

The idealised vessel has a length of 200 mm, a radius of 10 mm and a wall thickness of 0.8 mm (Figure 3-5). The wall is assumed to be linear elastic, with a Young's Modulus of $1x10^6$ Pa, a density of 1000 kgm^{-3} and a Poisson's ratio of 0.49.

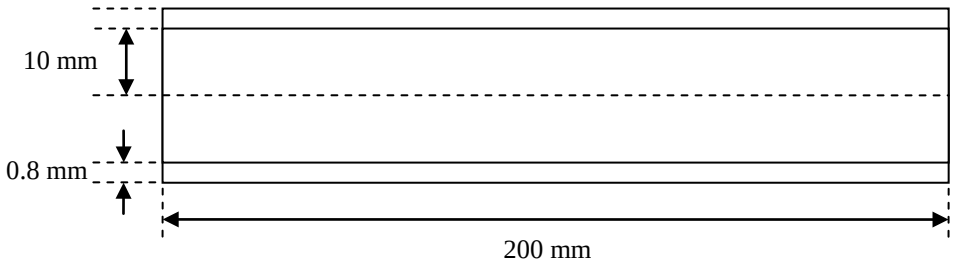

FIGURE 3-5 – ILLUSTRATION OF 3D/1D VESSEL GEOMETRY

The parameter values of the 2 and 3 element Windkessel models are documented in Table 3.1. These parameters are chosen to produce a comparable pressure magnitude and range to the clinical measurements, which are discussed presently. A single frequency (1 Hz), sinusoidal, flow waveform is applied at the inlet of the vessel with an amplitude of $5x10^{-4}$ m^3s^{-1}.

	R ($kgm^{-4}s^{-1}$)	C ($m^4s^2kg^{-1}$)	R_i ($kgm^{-4}s^{-1}$)
Parameter Value	$1.45x10^{8}$	$1.45x10^{-8}$	$1.1x10^{7}$

TABLE 3.1 – WINDKESSEL PARAMETER VALUES

COMPRESSIBLE FLUID METHODOLOGY 3.4.2

To allow comparisons to be made within a reasonable time scale the wave propagation effects, in the CFD model, are approximated using a compressible fluid. This methodology assumes that the compressibility of the fluid is analogous to the compliance of the vessel wall, thereby allowing investigation of wave propagation effects without the computational expense of a full FSI simulation [86, 87]. The accuracy of this assumption is the focus of Chapter 4.

The compressible fluid model employs the ideal gas law (Equation 3-13) to describe the density variation in the fluid. The wave speed can be defined as a function of pressure and density (Equation 3-14).

$$P = \frac{R_c T \rho}{M}$$

EQUATION 3-13

Where R_c is the universal gas constant, T is the temperature in Kelvin and M is the molar mass of the fluid.

$$c^2 = \gamma \frac{P}{\rho}$$

EQUATION 3-14

Combining Equation 3-13 and Equation 3-14 with the assumption of an isothermal process ($\gamma = 1$) a relationship between pressure and density (Equation 3-15) is reached, such that the values of temperature and molar mass can be altered to produce a wave speed and density analogous to the system of interest.

$$P = \frac{R_c T \rho}{M} = c^2 \rho$$

EQUATION 3-15

In the idealised aorta the temperature is set to a constant value of 310 K. The wave speed is calculated, using the Moens-Kortweg equation (Equation 3-6), to be 7.08 ms^{-1} and the corresponding molar mass is 51.71 kg mol^{-1}.

A time-step of 5 ms is employed and each time-step is assumed to be numerically converged once the RMS residuals are below a value of $1x10^{-5}$. This criterion was shown in Chapter 2 to result in numerically converged solutions.

The pressure within the 3D domain is initialised with the inlet pressure value from the analytical solution at time zero. This is done in an attempt to minimise the initialisation effects and reduce the computational time required to reach a periodic solution.

TWO ELEMENT WINDKESSEL RESULTS 4.4.3

Numerical analysis of the 3D vessel, coupled to the two element Windkessel, suffered from oscillations (Figure 3-6 - middle) that reduced in magnitude as the solution progressed. The underlying waveform is at the forcing frequency and is comparable, in its magnitude and form, to that of the analytical solution (Figure 3-6 - top). To ensure that the oscillations are a real phenomenon of the system, rather than a numerical oscillation caused by the explicit coupling approach, the implicit coupling scheme was developed and the system of interest is simulated (Figure 3-6 - bottom). The implicit coupling scheme, as in the explicit scheme, experienced high frequency oscillations which are damped over time. The use of an implicit coupling scheme increases the damping of the oscillations and achieves comparable results to the analytical solution after a shorter time period.

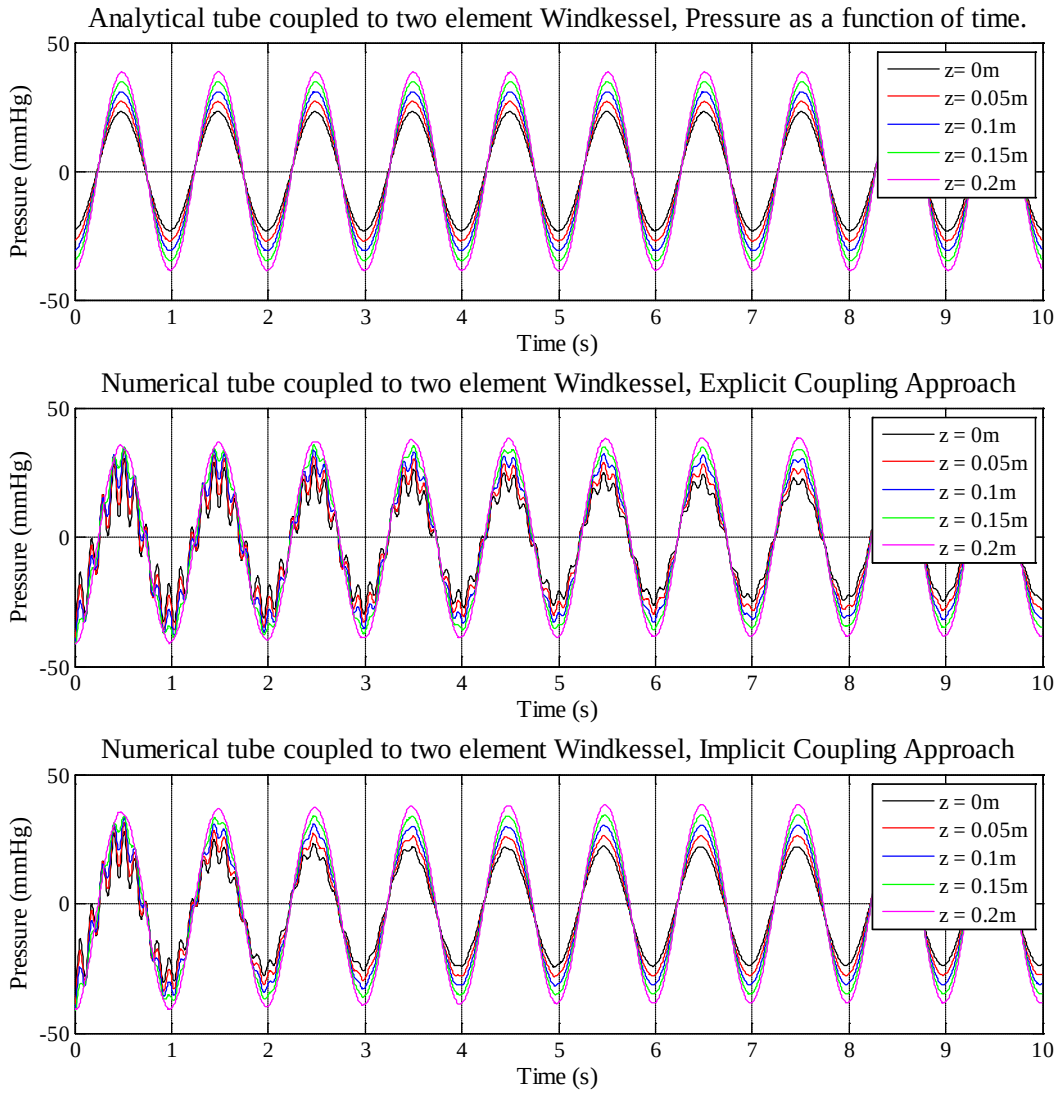

FIGURE 3-6 – PRESSURE AGAINST TIME AT A NUMBER OF AXIAL POSITIONS, ANALYTICAL AND NUMERICAL TUBE COUPLED TO A TWO ELEMENT WINDKESSEL USING AN EXPLICIT AND AN IMPLICIT COUPLING APPROACH

The oscillations are believed to be the result of the initial conditions, i.e. the assumption that the fluid is initially at rest and that the pressure is constant along the length of the domain. The reducing amplitude of the oscillations (with time) is due to the damping effect of the fluid viscosity. A time varying fluid viscosity, described by the exponential function in Equation 3-16 (and shown graphically in Figure 3-7), is applied in an attempt to reduce the magnitude of the initial oscillations.

$$\mu = 0.35e^{(-5t)} + 0.0035$$

EQUATION 3-16

The variable viscosity is applied to the explicitly coupled system, effectively damping the oscillations and producing smooth sinusoidal pressure variations in time (Figure 3-7). As the viscosity is reduced the oscillations do not return, further demonstrating that it is indeed the initial conditions that cause the oscillations.

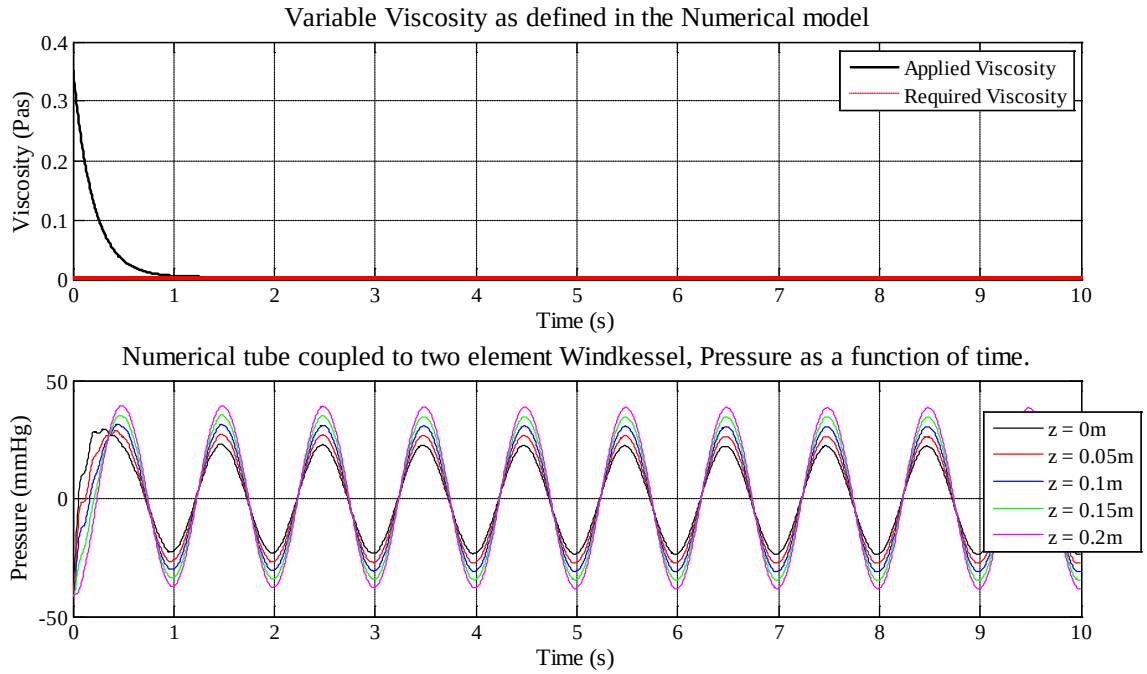

FIGURE 3-7 – VARIABLE VISCOSITY APPLIED TO THE COUPLED NUMERICAL SIMULATION AND THE RESULTING PRESSURE AGAINST TIME AT A NUMBER OF AXIAL POSITIONS.

The analytical and damped numerical solutions for the pressure variation, both along the vessel and in time, show good agreement (Figure 3-8). The peak variation occurs at the inlet with a relative error, normalised by the peak pressure, of 3.56. The use of this relative error is more appropriate than a percentage difference measure, for this case, since the pressure wave moves through the x-axis. The small differences seen in Figure 3-8 are attributed to the assumptions inherent in the analytical solution. The analytical solution assumes the fluid is inviscid and although the given system is predominantly governed by the inertial effects (with a Womersley number of 13.8) this approximation will introduce a degree of variation between the numerical and analytical solutions. However, the results clearly demonstrate not only the validity of the compressible fluid analogy, but also the coupling strategy adopted.

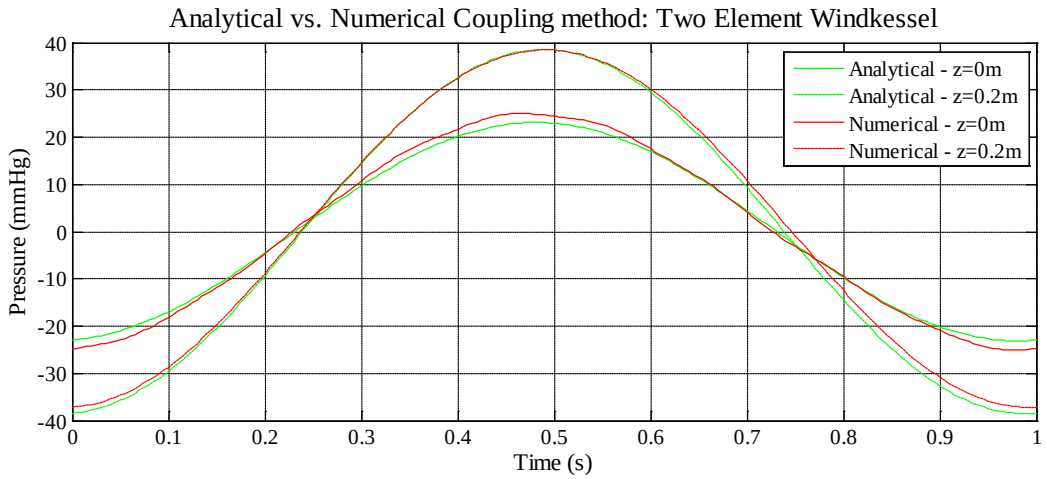

FIGURE 3-8 - ANALYTICAL VS. NUMERICAL COUPLING, TWO ELEMENT WINDKESSEL

Aortic flow and pressure waveforms are composed of multiple frequency components. The two element Windkessel is known to behave poorly at high frequencies, which may also introduce oscillations into the system. The use of a variable viscosity will damp the effects associated with the initial conditions but is not expected to remove oscillations due to high frequency signals.

This hypothesis is tested, with the sinusoidal flow waveform replaced by a clinical waveform extracted from 2D MRI flow data (Figure 3-9). The system is initially damped using the variable viscosity strategy to minimise the oscillations due to the initial conditions (Figure 3-7). The high frequency components give rise to significant oscillations in the system (Figure 3-9). This is perhaps not so surprising if we consider the frequency response of the two element Windkessel. At high frequencies the impedance modulus of the Windkessel approaches zero causing a significant mismatch in the impedance of the 3D/1D domain and the 0D domain [88]. As a quick check the analytical solution is modified, under the assumption that the flow and pressure waveforms can be expressed as a sum of their harmonic components, to consider a true cardiac waveform. The analytical solution also contained oscillations, at the same frequency as the numerical analysis (Figure 3-9). This approach is used to validate further the 3D solutions and coupling approach in Chapter 4. These findings identify a serious limitation in the use of two element Windkessel models as a downstream condition for CFD simulations: the interface

between the tube and the 0D termination produces strong pressure reflections in the domain.

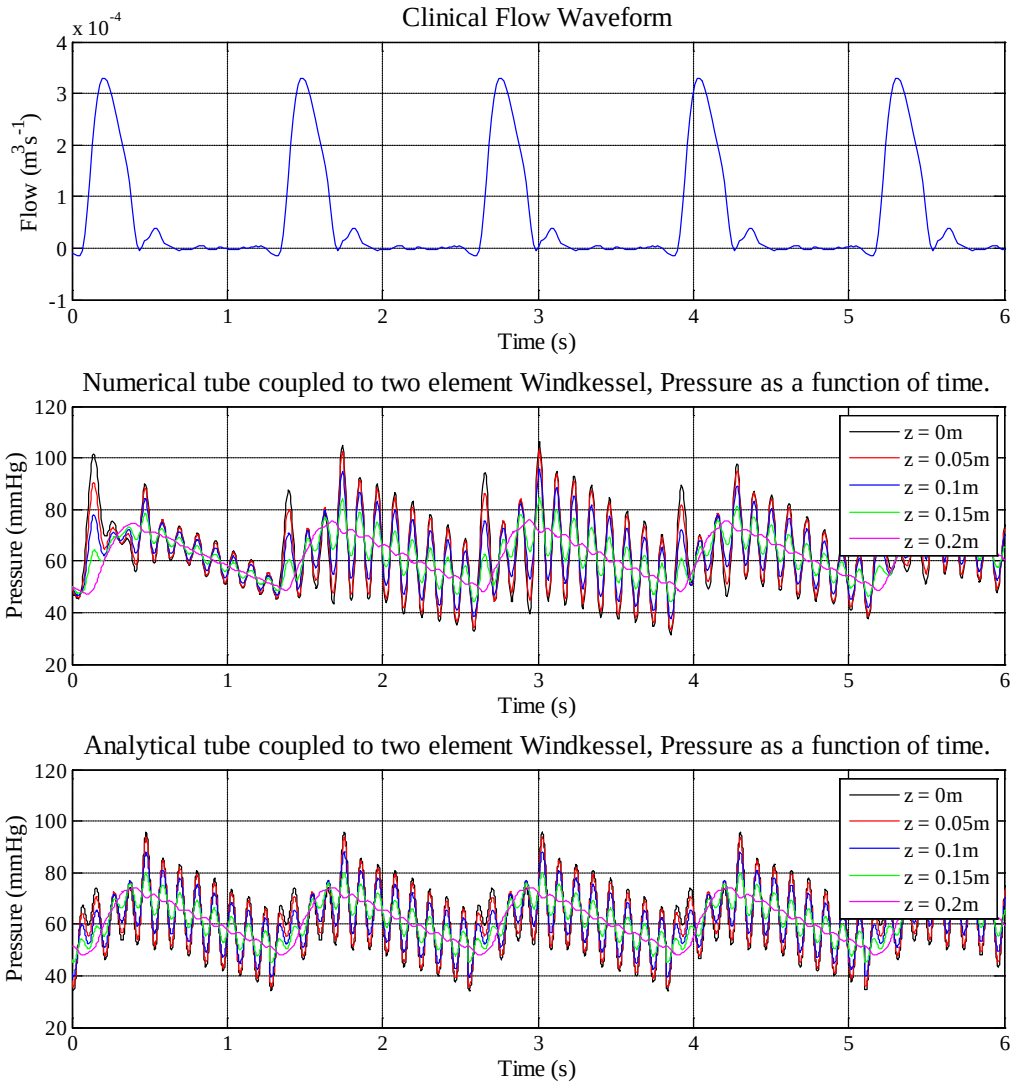

FIGURE 3-9 – PRESSURE AGAINST TIME AT A NUMBER OF AXIAL POSITIONS IN A TUBE COUPLED TO A TWO ELEMENT WINDKESSEL; NUMERICAL PREDICTION (MIDDLE), ANALYTICAL SOLUTION (BOTTOM) AND REAL CLINICAL FLOW WAVEFORM (TOP)

THREE ELEMENT WINDKESSEL RESULTS 3.4.4

Analytical and numerical analyses of the 1D/3D vessel, coupled to a three element Windkessel model, demonstrate good agreement (Figure 3-10). The inclusion of the input resistance has a damping effect on the system and prevents the oscillations, apparent in the numerical model with a two element Windkessel termination (Figure

3-6), due to the initial conditions. For completeness and to demonstrate that the additional resistance is able to stabilise the system, not only for a low frequency sinusoidal waveform, but also when the inlet signal contains higher frequencies, a numerical simulation is conducted with the same clinical flow wave shown in Figure 3-9. The resulting system has no unrealistic oscillations (Figure 3-10).

As with the two element Windkessel there is a small difference between the analytically and numerically calculated pressure plots (Figure 3-11). The greatest variation occurs at the outlet with a relative error, normalised to the maximum local pressure, of 3.55%. The source of the disparity has been discussed previously in relation to the two element model, these arguments also hold in the current comparison.

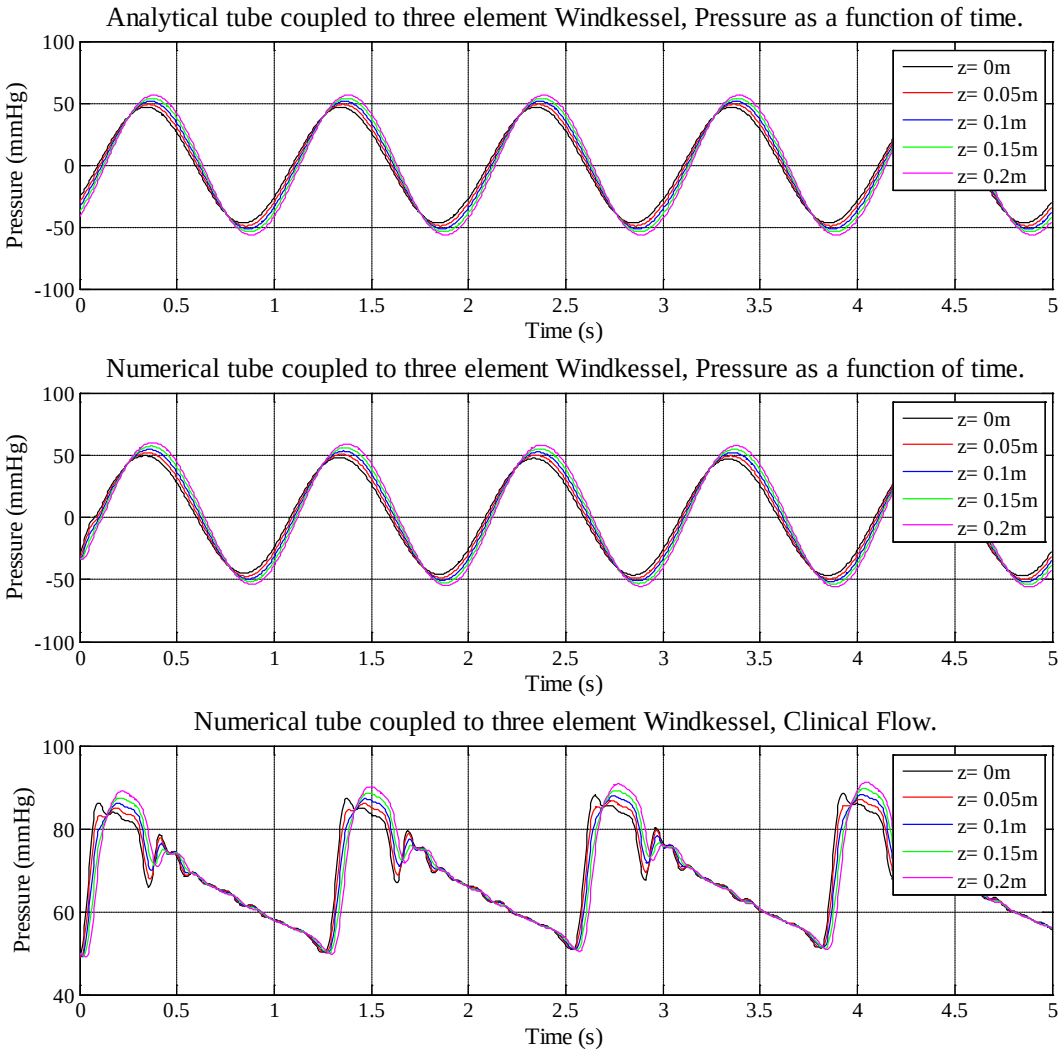

FIGURE 3-10 - PRESSURE AGAINST TIME AT A NUMBER OF AXIAL POSITIONS, ANALYTICAL AND NUMERICAL TUBE COUPLED TO A THREE ELEMENT WINDKESSEL AND THE NUMERICAL TUBE WITH A CLINICAL FLOW WAVEFORM APPLIED.

The predicted pressure waveforms for the low frequency inlet signal are similar in both the two and three element Windkessel terminations (Figure 3-8 and Figure 3-11). The inclusion of an input resistance produces a phase shift, with the peak inlet pressure occurring 0.14 seconds earlier than in the two element Windkessel. There is also an increase in the magnitude of the pressure wave. The two element Windkessel results in a peak inlet pressure of 22.21 mmHg compared to a peak value of 46.15 mmHg in the three element model. These effects are of course governed by the relative ratio of R_i/R and the parameters can be changed to elicit a desired response.

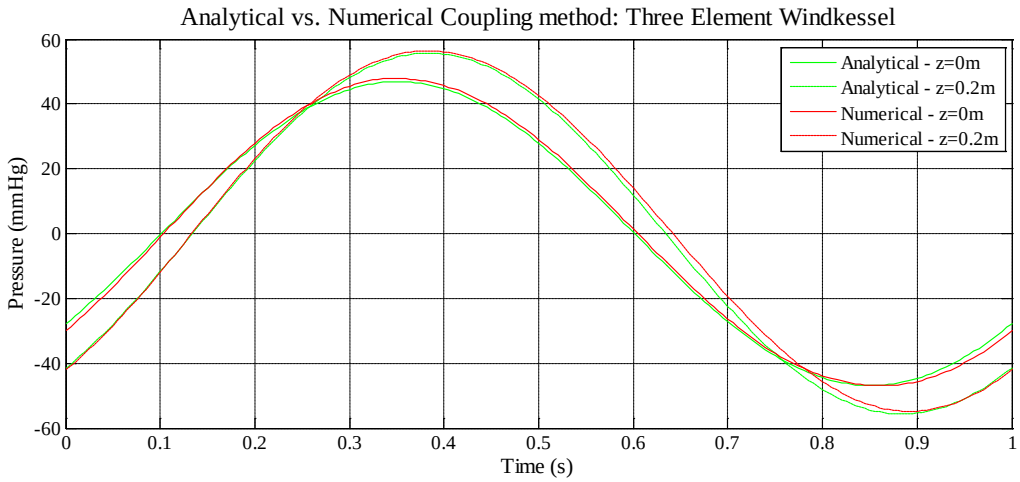

FIGURE 3-11 – ANALYTICAL VS. NUMERICAL COUPLING, THREE ELEMENT WINDKESSEL

CONCLUSIONS 3.4.5

The analytical solutions have been derived for a 1D vessel coupled to a two and three element Windkessel model. A methodology, that employs a compressible fluid to approximate the compliance of the vessel wall, has been presented and the results compared to the analytical solution. The results demonstrate that, at frequencies around 1Hz, the two element termination suffers from initialisation effects that result in oscillations which are damped with time by the viscosity of the fluid. Assuming the inlet flow waveform is smooth and continuous these oscillations can be removed by using a variable viscosity which prevents their formation and the system remains stable as the viscosity is subsequently reduced. However, if the inlet flow waveform contains high frequency components, such as in a real cardiac waveform, the system suffers from oscillations, caused by wave reflections from the 1D/3D-0D interface.

The inclusion of an input resistance (the three element Windkessel) produces similar pressure responses to the two element Windkessel, at low frequencies, but without the need to artificially damp oscillations associated with the initialisation of the system. More importantly the three element Windkessel does not suffer from oscillations (induced by wave reflections) when the input signal contains high frequency components.

As a result of these findings the work which follows focuses on the three element Windkessel as the downstream condition for the numerical simulations.

FURTHER CHARACTERISATION OF THE THREE ELEMENT WINDKESSEL 3.5

ANALYTICAL DERIVATION 3.5.1

It is possible to further characterise the dynamics of the three element Windkessel model in terms of the dimensionless parameters; $\frac{R_i}{R}$, $CR\omega$ and $\frac{1}{R}$. For the following derivation it is convenient to take the interface of the 1D and 0D domain as the reference position (Figure 3-12).

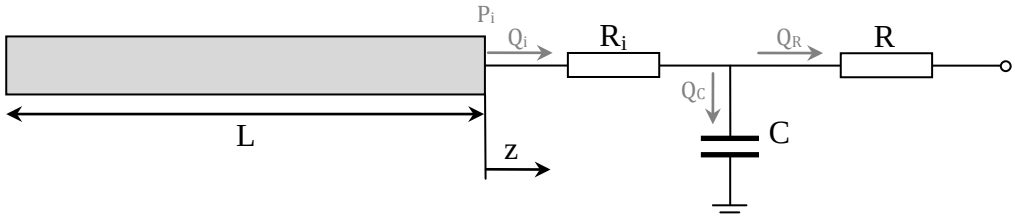

FIGURE 3-12 - COUPLED THREE ELEMENT WINDKESSEL, REFERENCE POINT (Z=0) AT THE INTERFACE

Substituting $P_i = P_{ic}cos(\omega t) + P_{is}sin(\omega t)$ and subsequently $Q_i = Q_{ic}cos(\omega t) + Q_{is}sin(\omega t)$, into the governing equation of the three element Windkessel (Equation 3-2) results in the following relations (Equation 3-17 and Equation 3-18 respectively):

$$CR_i\frac{dQ_i}{dt} + \left(\frac{R_i}{R} + 1\right)Q_i = \left(P_{is}C\omega + \frac{P_{ic}}{R}\right)cos(\omega t) + \left(-P_{ic}C\omega + \frac{P_{is}}{R}\right)sin(\omega t)$$

EQUATION 3-17

$$\left(CR_i\omega Q_{is} + \left(\frac{R_i}{R} + 1\right)Q_{ic}\right)cos(\omega t) + \left(-CR_i\omega Q_{ic} + \left(\frac{R_i}{R} + 1\right)Q_{is}\right)sin(\omega t) = \left(P_{is}C\omega + \frac{P_{ic}}{R}\right)cos(\omega t) + \left(-P_{ic}C\omega + \frac{P_{is}}{R}\right)sin(\omega t)$$

EQUATION 3-18

Equating coefficients produces a set of equations (Equations 3-19) for the Windkessel:

$$\left(\frac{R_i}{R}+1\right)Q_{ic}+CR_i\omega Q_{is}=\frac{P_{ic}}{R}+P_{is}C\omega \quad : \quad -CR_i\omega Q_{ic}+\left(\frac{R_i}{R}+1\right)Q_{is}=-P_{ic}C\omega+\frac{P_{is}}{R}$$

EQUATIONS 3-19

Solving Equations 3-19 for flow, in terms of the predefined parameters of interest gives:

$$Q_1+Q_3=Q_{ic}=\frac{\left[\left(\frac{1}{R}\left(\frac{R_i}{R}+1\right)+\frac{1}{R}\frac{R_i}{R}C^2R^2\omega^2\right)\cdot P_{ic}+\frac{1}{R}CR\omega\cdot P_{is}\right]}{\left[\left(\frac{R_i}{R}+1\right)^2+\left(\frac{R_i}{R}\right)^2C^2R^2\omega^2\right]}$$

$$-Q_2+Q_4=Q_{is}=\frac{\left[-\frac{1}{R}CR\omega\cdot P_{ic}+\left(\frac{1}{R}\left(\frac{R_i}{R}+1\right)+\frac{1}{R}\frac{R_i}{R}C^2R^2\omega^2\right)\cdot P_{is}\right]}{\left[\left(\frac{R_i}{R}+1\right)^2+\left(\frac{R_i}{R}\right)^2C^2R^2\omega^2\right]}$$

EQUATIONS 3-20

And then for pressure:

$$P_1+P_3=P_{ic}=\frac{\left[\left(\left(\frac{R_i}{R}+1\right)+C^2R^2\omega^2\frac{R_i}{R}\right)\cdot Q_{ic}+\left(CR\omega\frac{R_i}{R}-CR\omega\left(\frac{R_i}{R}+1\right)\right)\cdot Q_{is}\right]}{\left[\frac{1}{R}+C^2R^2\omega^2\frac{1}{R}\right]}$$

$$-P_2+P_4=P_{is}=\frac{\left[\left(CR\omega\cdot\left(\frac{R_i}{R}+1\right)-CR\omega\cdot\frac{R_i}{R}\right)\cdot Q_{ic}+\left(\left(\frac{R_i}{R}+1\right)+C^2R^2\omega^2\cdot\frac{R_i}{R}\right)\cdot Q_{is}\right]}{\left[\frac{1}{R}+C^2R^2\omega^2\frac{1}{R}\right]}$$

EQUATIONS 3-21

The amplitudes of the flow and pressure waveforms are then:

$$|Q_i|=\frac{1}{\left[\left(\frac{R_i}{R}+1\right)^2+\left(\frac{R_i}{R}\right)^2C^2R^2\omega^2\right]}\cdot\sqrt{\begin{array}{l}\left[\left(\frac{1}{R}\left(\frac{R_i}{R}+1\right)+\frac{1}{R}\frac{R_i}{R}C^2R^2\omega^2\right)\cdot P_{ic}+\frac{1}{R}CR\omega\cdot P_{is}\right]^2+\\ \left[-\frac{1}{R}CR\omega\cdot P_{ic}+\left(\frac{1}{R}\left(\frac{R_i}{R}+1\right)+\frac{1}{R}\frac{R_i}{R}C^2R^2\omega^2\right)\cdot P_{is}\right]^2\end{array}}$$

and

$$|P_i| = \frac{1}{\left[\frac{1}{R} + C^2R^2\omega^2 \cdot \frac{1}{R}\right]} \cdot \sqrt{\left[\left(\left(\frac{R_i}{R}+1\right) + C^2R^2\omega^2\frac{R_i}{R}\right)\cdot Q_{ic} + \left(CR\omega\frac{R_i}{R} - CR\omega\left(\frac{R_i}{R}+1\right)\right)\cdot Q_{is}\right]^2 + \left[\left(CR\omega\left(\frac{R_i}{R}+1\right) - CR\omega\frac{R_i}{R}\right)\cdot Q_{ic} + \left(\left(\frac{R_i}{R}+1\right) + C^2R^2\omega^2\frac{R_i}{R}\right)\cdot Q_{is}\right]^2}$$

EQUATIONS 3-22

The amplitude ratio of flow and pressure (also known as the admittance of the three element Windkessel) at the 1D-0D interface can then be calculated, in terms of the predefined parameters, from Equation.3-23.

$$\frac{|Q_i|}{|P_i|} = \frac{1}{R}\cdot\frac{\sqrt{\left[\left(\frac{R_i}{R}+1\right) + \frac{R_i}{R}C^2R^2\omega^2\right]^2 + C^2R^2\omega^2}}{\left[\left(\frac{R_i}{R}+1\right)^2 + \left(\frac{R_i}{R}\right)^2 C^2R^2\omega^2\right]}$$

EQUATION.3-23

The inverse of the admittance provides a solution for the impedance of the three element Windkessel.

Having described the pressure and flow amplitudes it is now possible to calculate the relative phase (ϕ_{QP}) of the waves. If we consider a purely cosine wave, such that:

$$P_i = |P_i|\cos(\omega t)$$

EQUATION 3-24

The relative phase of the travelling waves can be described by:

$$Q_i = |Q_i|\cos(\omega t - \phi_{QP}) = |Q_i|cos(\phi_{QP})cos(\omega t) + |Q_i|sin(\phi_{QP})sin(\omega t)$$

EQUATION 3-25

In terms of the predefined parameters:

$$|Q_i|cos(\phi_{QP}) = \frac{\left[\left(\frac{1}{R}\left(\frac{R_i}{R}+1\right)+\frac{1}{R}\frac{R_i}{R}C^2R^2\omega^2\right)\cdot P_{ic}\right]}{\left[\left(\frac{R_i}{R}+1\right)^2+\left(\frac{R_i}{R}\right)^2C^2R^2\omega^2\right]}$$

$$|Q_i|sin(\phi_{QP}) = \frac{\left[-\frac{1}{R}CR\omega\cdot P_{ic}\right]}{\left[\left(\frac{R_i}{R}+1\right)^2+\left(\frac{R_i}{R}\right)^2C^2R^2\omega^2\right]}$$

EQUATION 3-26

Then the relative phase is simply:

$$\phi_{QP} = tan^{-1}\left(\frac{-CR\omega}{\left(\frac{R_i}{R}+1\right)+\frac{R_i}{R}C^2R^2\omega^2}\right)$$

EQUATION 3-27

The relative phase shift between Q_i and P_i is entirely determined by the value of the dimensionless parameters $\frac{R_i}{R}$ and $CR\omega$. However, the magnitude ratio of the flow and pressure is also affected by the $\frac{1}{R}$ term. The effect of the $\frac{1}{R}$ term is purely a scaling factor on the response of the system (Equation.3-23).

ANALYTICAL RESULTS 3.5.2

Matlab (MathWorks, UK) is used to evaluate the influence of the dimensionless parameters $\left(\frac{R_i}{R}\text{ and }CR\omega\right)$ on the relative magnitude ratio and phase shift of the flow and pressure waveforms. The results are plotted as a 2D surface, representing the solution space of the admittance (Figure 3-13) and the relative phase shift (Figure 3-14).

The effect of increasing $\frac{R_i}{R}$ is to reduce the magnitude ratio at all frequencies, moving asymptotically towards a value close to zero (Figure 3-13). In contrast, increasing the value of this parameter results in a smaller, less negative, phase shift between the

flow and pressure waves (Figure 3-14). For values of $\frac{R_i}{R}$ greater than 0.1 the effect on the magnitude ratio and phase difference is minimal (Figure 3-13 and Figure 3-14).

There is a peak in the magnitude ratio of flow and pressure as $\frac{R_i}{R}$ becomes small and CRω becomes large (Figure 3-13). However, moving away from small values of $\frac{R_i}{R}$ it can be seen that there is only a small decline in the magnitude ratio as the value of CRω reduces.

There is a significant trough in the solution space of the relative phase shift, running along all values of $\frac{R_i}{R}$ when CRω is approximately 1.6. Moving away from this trough the variation in phase shift as a function of CRω is fairly small, although there is a general reduction (less negative) in the phase shift as CRω increases.

The solution space for the magnitude ratio and phase difference of the flow and pressure suggest that when it comes to tuning the 0D parameter values to elicit a specific response there may be a number of parameter sets ($\frac{R_i}{R}$ and CRω) that can produce the desired response. That is to say that the solution space is likely to be relatively flat.

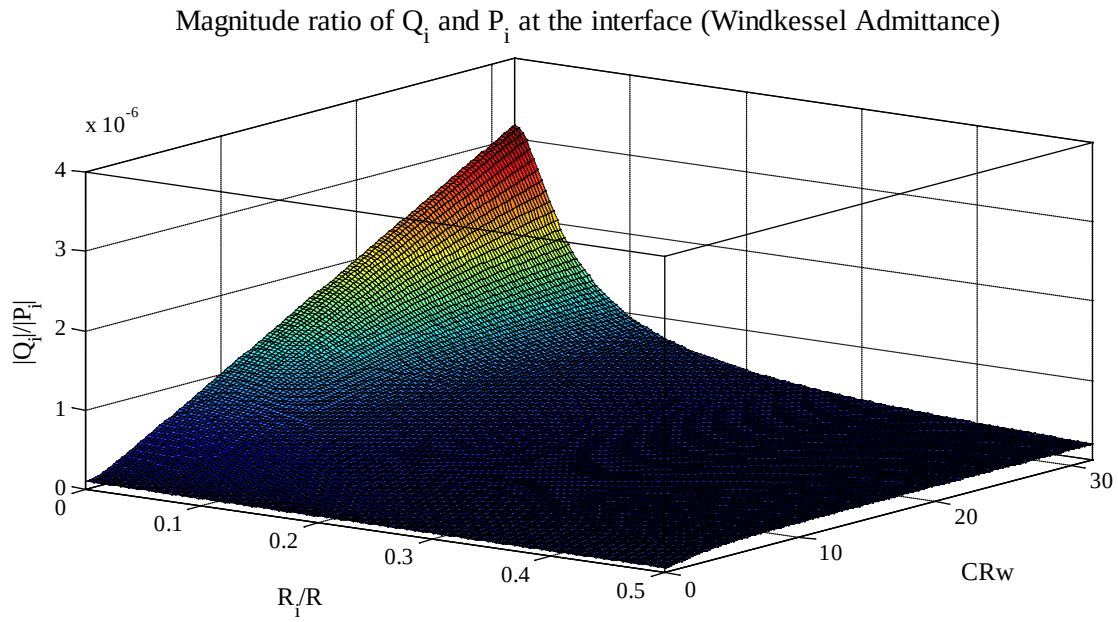

FIGURE 3-13 - ILLUSTRATION OF HOW |Q|/|P| (ADMITTANCE) VARIES WITH THE DIMENSIONLESS PARAMETERS R_I/R AND $CR\omega$

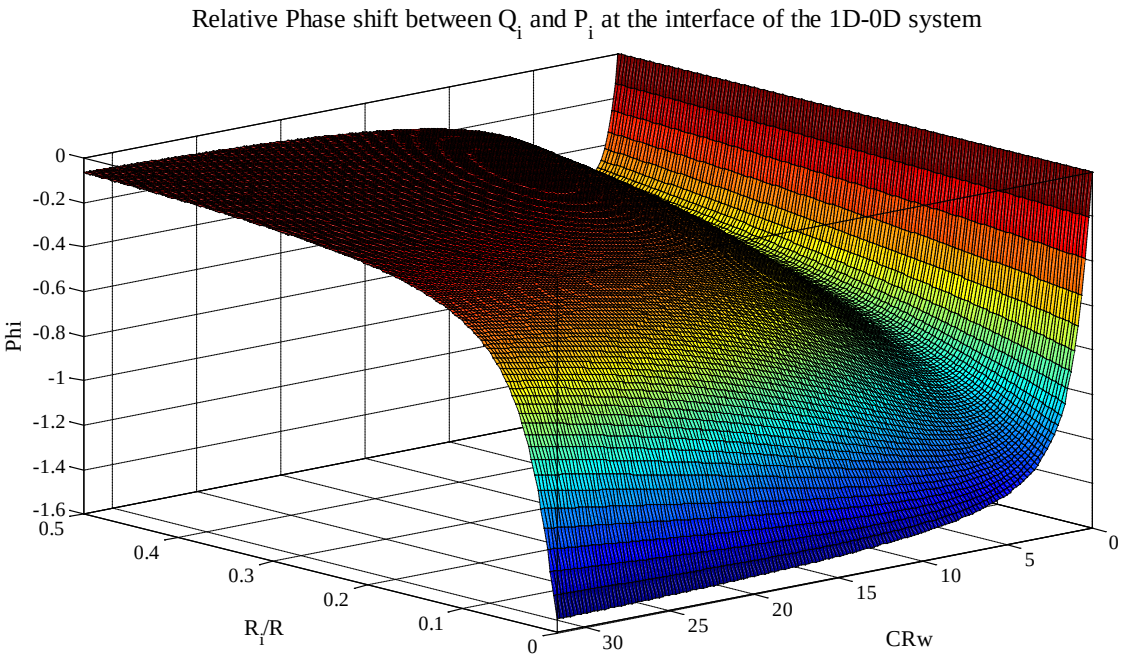

FIGURE 3-14 - ILLUSTRATION OF HOW ϕ_{QP} VARIES WITH THE DIMENSIONLESS PARAMETERS R_I/R AND $CR\omega$

TUNING STRATEGY 3.6

The application of lower order models as boundary conditions for higher order models is only useful if the lower order models elicit the desired response. In the case of the three element Windkessel there are three parameters that can be tuned to alter the given response. The tuning process may be approached on a trial and error basis but this would involve the solution of the coupled system for each new set of parameters, which is computationally expensive and extremely time consuming. An alternative approach is to approximate the parameters required to achieve a desired response based on some simple relations. The total value of resistance ($R_i + R$) can be approximated from:

$$R_i + R = \frac{P}{Q}$$

EQUATION 3-28

Where P is the average desired pressure and Q is the average flow.

The input resistance can be defined as the characteristic impedance of the 1D/3D vessel [88]:

$$R_i = \frac{\rho c}{A}$$

EQUATION 3-29

Where A is the cross-sectional area of the 1D/3D vessel.

While the compliance can be approximated from the diastolic pressure decay [88]:

$$\tau = RC$$

EQUATION 3-30

Where τ is the time constant associated with the diastolic pressure decay.

However, the most accurate approach to calculating the parameters required to elicit a desired response is to employ a formal optimisation strategy.

The following section describes the creation and implementation of an optimisation scheme, written within Matlab, using a number of the inbuilt algorithms, to compute a set of fitted values for; $\frac{R_i}{R}$, CR and $\frac{1}{R}$, given a desired response (Note that the parameter $CR\omega$ has been reduced to CR because for multiple frequency signals ω is not constant). When using clinical data to tune the Windkessel it is unlikely that there will be an exact solution and so the process must be approached as an optimisation problem.

TUNING METHODOLOGY 3.6.1

Given the desired flow and pressure as the input to the Windkessel, it is possible to write n equations that describe the pressure at n points in time, as a function of the predefined parameters of interest and the amplitude of the harmonic flow components. So long as n is greater or equal to the number of unknowns, in this case 3, then the solution is said to be fully determined (or over-determined).

Matlab (The MathsWorks Inc. USA) has a number of pre-defined algorithms, such as the *'Trust Region Reflective'* [89] and *'Levenberg-Marquardt'* [90] algorithms that use conjugate gradient techniques to approximate parameter values in such problems. In the following work the *'Trust Region Reflective'* algorithm is employed because it offers improved convergence for problems with a bounded solution space. In the following work the solutions of the fitted parameter values are constrained to be positive.

Starting from the governing equations of the three element Windkessel (Equations 3-19) one can write the solution to the pressure components in terms of the flow (Equations 3-21). Substituting these into $P_i(t) = P_{ic}cos(\omega t) + P_{is}sin(\omega t)$ gives the following relation which describes the time varying pressure at the Windkessel in terms of the harmonic flow amplitudes and the predefined parameters of interest.

$$P_i(t) = \frac{\left[\left(\left(\frac{R_i}{R}+1\right)+C^2R^2\omega^2\frac{R_i}{R}\right)\cdot Q_{ic}+\left(CR\omega\frac{R_i}{R}-CR\omega\left(\frac{R_i}{R}+1\right)\right)\cdot Q_{is}\right]}{\left[\frac{1}{R}+C^2R^2\omega^2\frac{1}{R}\right]}cos(\omega t) + \frac{\left[\left(CR\omega\cdot\left(\frac{R_i}{R}+1\right)-CR\omega\cdot\frac{R_i}{R}\right)\cdot Q_{ic}+\left(\left(\frac{R_i}{R}+1\right)+C^2R^2\omega^2\cdot\frac{R_i}{R}\right)\cdot Q_{is}\right]}{\left[\frac{1}{R}+C^2R^2\omega^2\frac{1}{R}\right]}sin(\omega t)$$

EQUATION 3-31

The optimisation code goes through a number of stages before arriving at a set of fitted parameter values (Figure 3-15). The first step involves decomposing the flow waveform into k harmonic frequencies, using the Fast Fourier Transform (FFT), and extracting the flow components (Q_{ic} and Q_{is}) for each harmonic. As a check the signal is then reconstructed and plotted against the original flow waveform. The pressure wave is then sampled at n points in time and the corresponding set of, n, algebraic equations are constructed (from Equation 3-31). An initial guess is then set for the parameters which are to be optimised. The choice of the initial guess is often a cause of divergence when using conjugate gradient methods and so must be carefully chosen. The minimisation algorithm is then run and finally the forward problem (using the fitted parameter values) is solved and the resulting pressure trace compared with the desired pressure response (Figure 3-15).

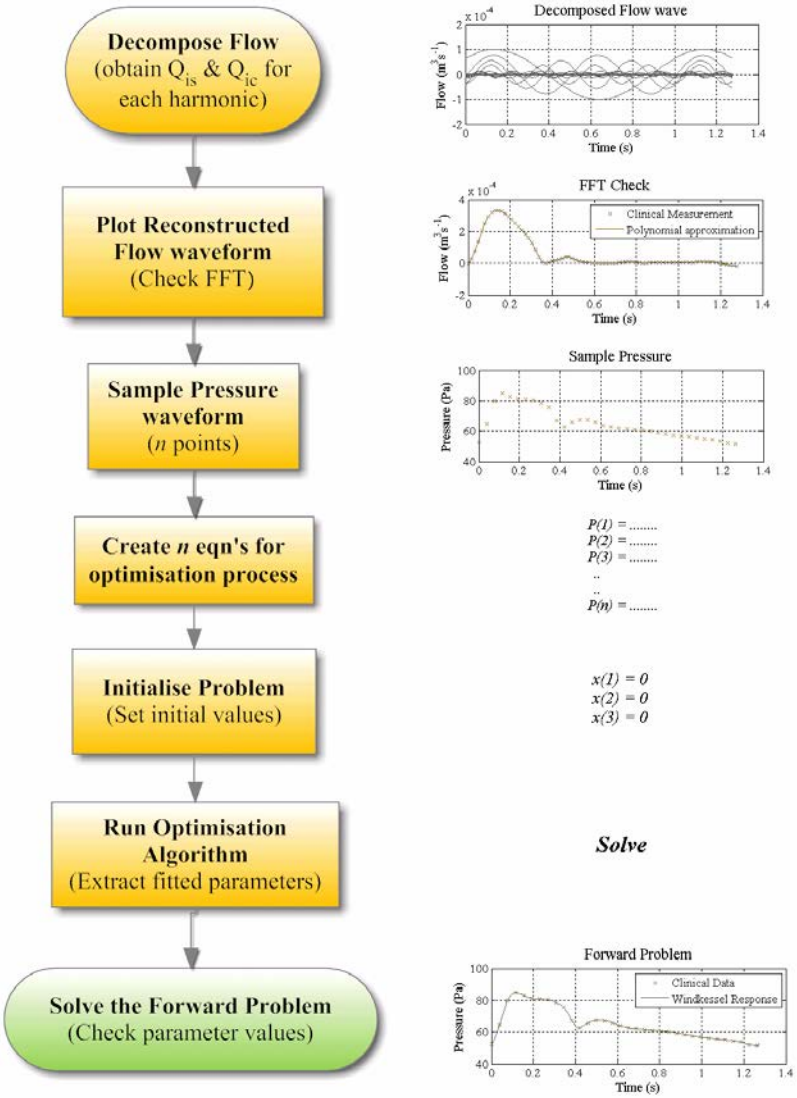

FIGURE 3-15 – FLOW CHART ILLUSTRATING THE OPTIMISATION STAGES

IDEALISED APPLICATION 3.6.2

The optimisation process is tested initially on a set of pressure and flow data produced from the numerical model coupled to a three element Windkessel. The simulation previously described (Section 3.4.4), which employed a clinical flow inlet boundary condition, is used (Figure 3-10) although with slightly different Windkessel parameters (Table 3.2). Since there is an exact solution to the set of equations constructed in the optimisation process it represents a problem with a minimum which is equal to zero.

As mentioned previously, initialisation of the parameters is critical. A poor initial guess can cause the conjugate gradient method to converge to a local minimum rather than the global minimum. In an attempt to avoid this problem an initialisation strategy was developed. A bounded region was defined for the initial guess of each parameter (Table 3.2) and a granularity for sampling the range was set. The optimisation code then ran the minimisation process for every possible combination of initial values and subsequently, based on the RMS residual, identified the set of fitted parameters which best approximated the desired pressure waveform.

Parameter	Bounds	Analytical Value	Simple Rules	Fitted Value
R_i/R	0.001-1	0.1	0.124	0.0925
1/R (m^4s/kg)	10^{-10} - 10^{-5}	$1x10^{-8}$	5.41 $x10^{-9}$	$9.92x10^{-9}$
CR (s)	0.01-10	0.5	0.675	0.497

TABLE 3.2 – BOUNDS OF INITIAL PARAMETER VALUES, ANALYTICAL WINDKESSEL VALUES AND THE CALCULATED WINDKESSEL VALUES FROM SIMPLE RULES AND THE OPTIMISATION APPROACH

The granularity of the initial guess range is set to a value of 4, that is to say 64 (4^3) initial value combinations are solved. The desired pressure trace is sampled at 200 instances in time, correlating to 200 equations of the form Equation 3-31. The resulting optimisation problem is solved and the minimum RMS residual of pressure is 0.377 mmHg. The optimised scheme produces a close approximation to the known parameter values, with the largest difference being the prediction for $\frac{R_i}{R}$ (Table 3.2). The parameter values are also calculated based on the simple relations (Equation 3-28 to Equation 3-30) and although they give a rough approximation of the true values the associated errors range from 24 % to 46 %.

The output of the optimisation procedure is shown in Figure 3-16. The reconstructed fast Fourier transformation (FFT), of the flow waveform demonstrates that the decomposition was accurate and the normalised spectral energy plot shows that it is the first 15 harmonics which most strongly contribute to both the flow and pressure signals (the first 20 harmonics are considered for the optimisation procedure). A comparison of the desired pressure response and that computed from the fitted

parameters show good agreement, although there is a slight variation in the rising edge and around the dicrotic notch. In general the results demonstrate that the optimisation strategy is capable of tuning the Windkessel parameters to elicit a specific response.

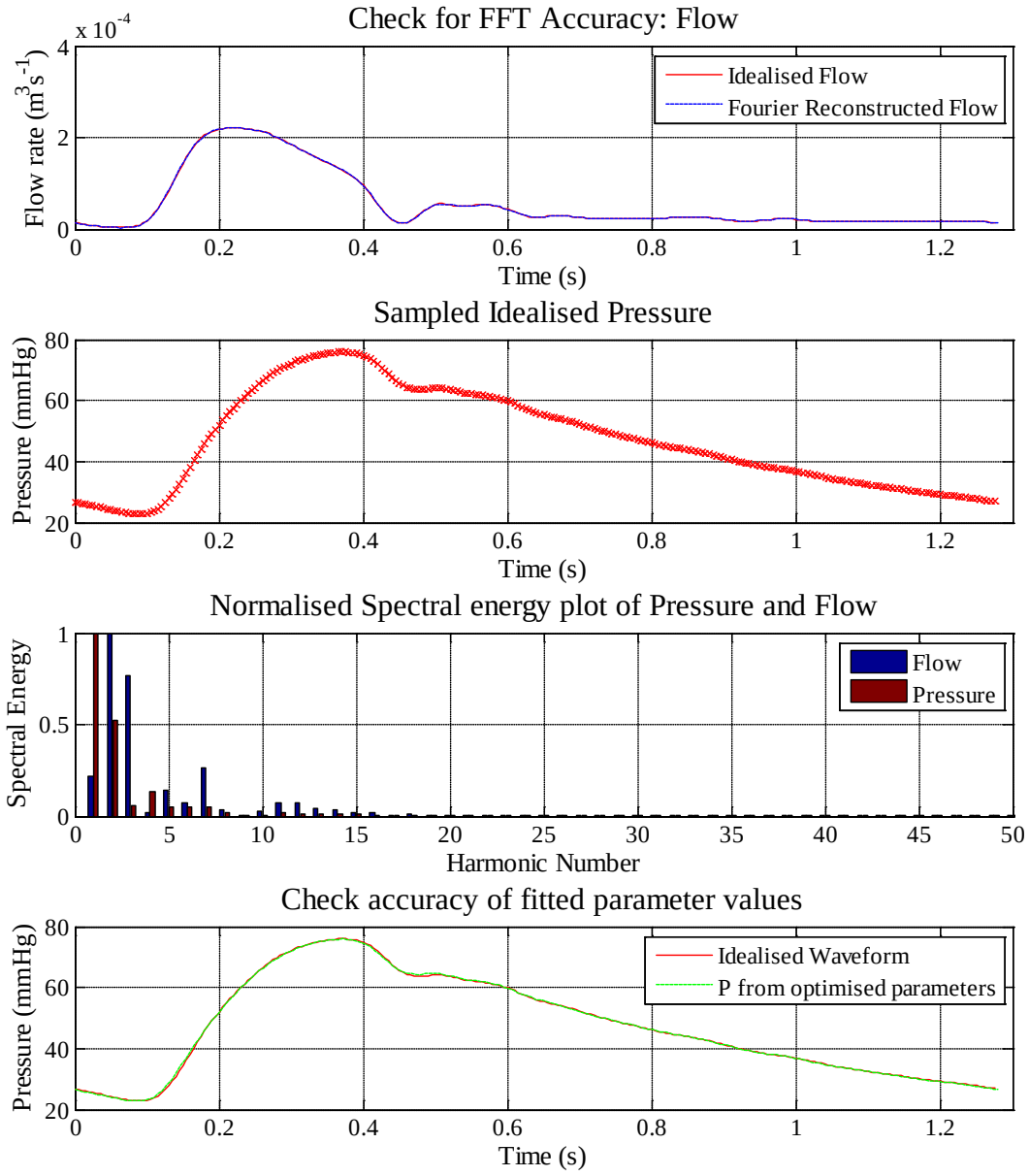

FIGURE 3-16 – OUTPUT FROM THE OPTIMISATION PROCEDURE

To investigate how the initial guess affects the corresponding fitted parameter values, a 3D plot of movement is included (Figure 3-17). The final fitted parameters are plotted as a solid red triangle. There is a clustering of the optimised parameters

around the correct values of $\frac{1}{R}$ and CR but there is a significant variation in the prediction of $\frac{R_i}{R}$. This may suggest that $\frac{R_i}{R}$ has a small effect on the resulting pressure waveform, or that the solution space around this region is relatively flat with numerous local minimums. Figure 3-17 clearly shows the presence of an additional local minimum (where $\frac{R_i}{R} \approx 1, CR \approx 0$ and $\frac{1}{R} \approx 0$), which is drawing a number of the initial guesses to converge within it, rather than to the global minima.

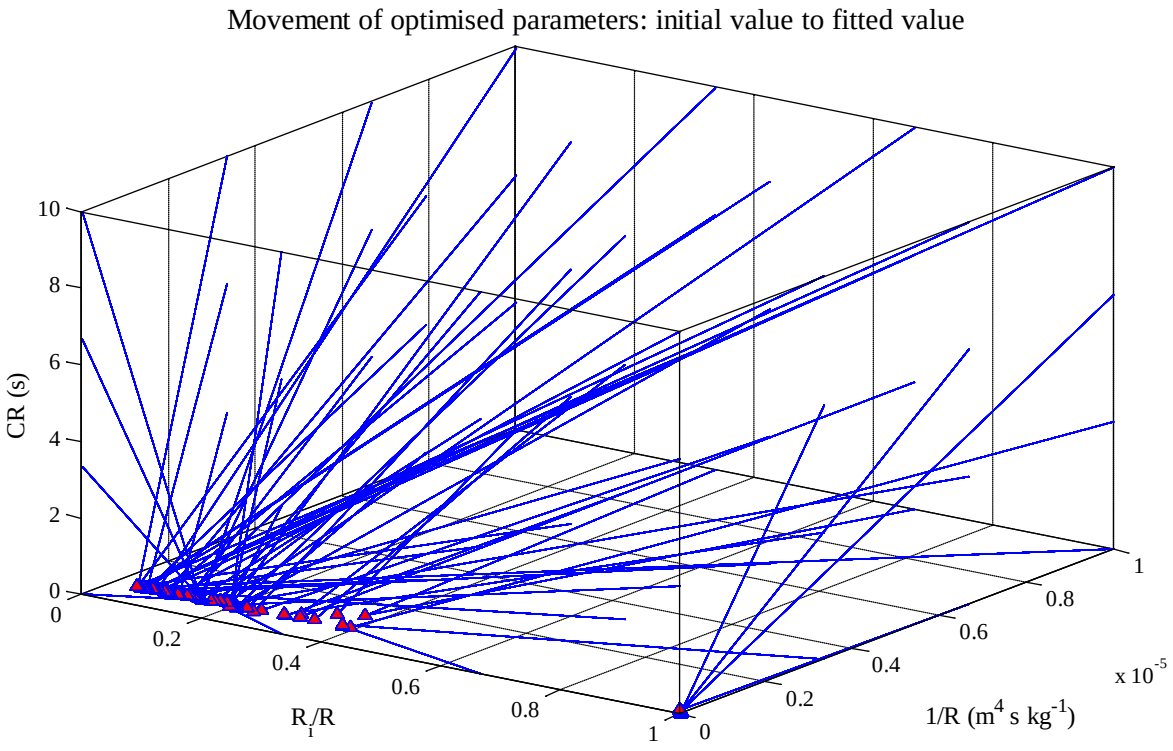

FIGURE 3-17 – ILLUSTRATION OF PARAMETER VALUE MOVEMENT: INITIAL VALUE TO FITTED VALUE (RED TRIANGLE) AFTER OPTIMISATION PROCESS

To identify whether the variation in $\frac{R_i}{R}$ is a result of numerous local minima, or an indication of its negligible effect on the pressure trace, the forward problem is solved for each set of fitted parameters. Figure 3-18 shows there are two distinct groups of wave shape, one far closer to the desired pressure response. These are found to correlate directly with the two areas of convergence apparent in Figure 3-17. The large cluster of waveforms (Figure 3-18), correlate directly to the group of fitted parameters which vary predominantly in $\frac{R_i}{R}$. Considering the significant variation of these waveforms it might be surmised that this area of the solution space is relatively

flat and populated by numerous local minima, rather than $\frac{R_i}{R}$ having a negligible effect on the pressure waveform.

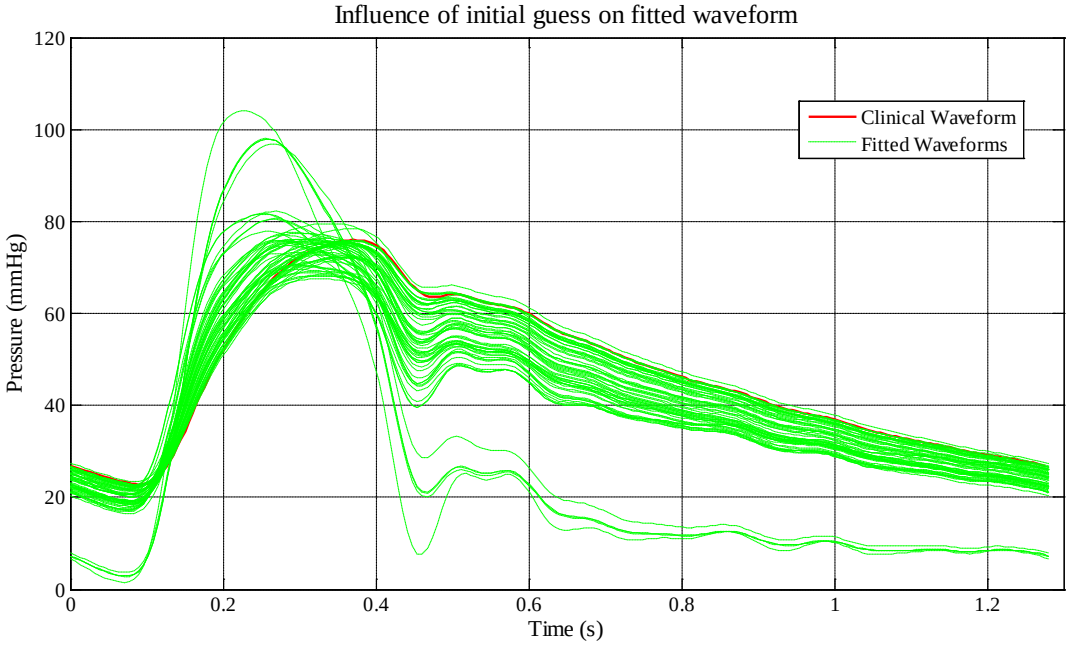

FIGURE 3-18 – INFLUENCE OF INITIAL GUESS ON THE PRESSURE WAVEFORM. COMPUTED FROM THE FITTED PARAMETER VALUES

The use of an idealised pressure and flow response has been used to demonstrate that the described optimisation strategy is able to accurately predict the Windkessel parameters required to produce a desired response. The work also identified the importance of the initial guess and demonstrates the usefulness of evaluating a matrix of initial values.

CLINICAL APPLICATION 3.6.3

Extending the optimisation process to a clinical application brings a number of additional challenges. The first and foremost is that very few clinical applications are single inlet-outlet systems. The aorta for example can have between three to five outlets, depending on the anatomy of the individual. This not only presents a challenge to elicit the desired response at each outlet but also the distribution/balance of flow is now governed entirely by the choice of Windkessel parameters. That is to say, a poor approximation of the pressure response at one branch will alter the flow distribution, and in turn the pressure distribution, throughout the entire domain. The

clinical application described below employs data from a patient with a mild aortic coarctation (Figure 3-19) and three supra-aortic vessels; the brachiocephalic (BCA), the left common carotid (LCC) and the left subclavian artery (LSUB) (Figure 3-19).

Ethical approval for use of this data was obtained in September 2009 from the Local Research Ethics Committee of the Guy's, King's and St Thomas' NHS Trust. The title of the approved protocol is "Patient-specific cardiovascular modelling and simulation in vascular and aortic disease" and the R&D REC number is 08/H0804/134. Informed consent was obtained from all patients according to the approved ethics. For obvious ethical reasons it is not possible to obtain invasive pressure measurements for a normal aorta.

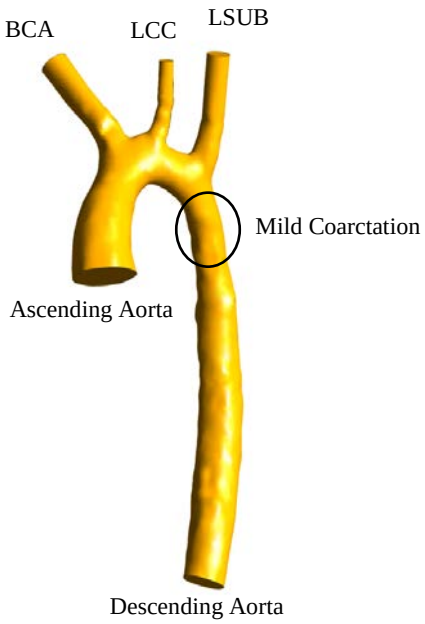

FIGURE 3-19 – GEOMETRY OF PATIENT-SPECIFIC AORTA USED IN THE CLINICAL APPLICATION OF THE TUNING METHODOLOGY

A second complication concerns the acquisition and accuracy of the clinical data. The pressure data used in the following work was taken from a patient under general anaesthetic. Pressure catheters were located in the ascending and descending aorta and recordings were made simultaneously for approximately 30 seconds. Even in an anaesthetised patient the peak, range and baseline pressures vary from cycle to cycle (Figure 3-20). For the purposes of the tuning and simulation work the pressure traces were cut, averaged and filtered, by Cristina Staicu, to ensure the pressure waveform

was periodic. The flow measurements were taken over a longer period of approximately 5 minutes and automatically extracted from 2D phase contrast MR sequences. The flow measurements were acquired at a different time to the pressure although the patient remained anaesthetised.

It is also worth noting that unlike the idealised application there is no guarantee that the cost function constructed for the clinical application will have a minimum that is zero, in fact it is highly unlikely.

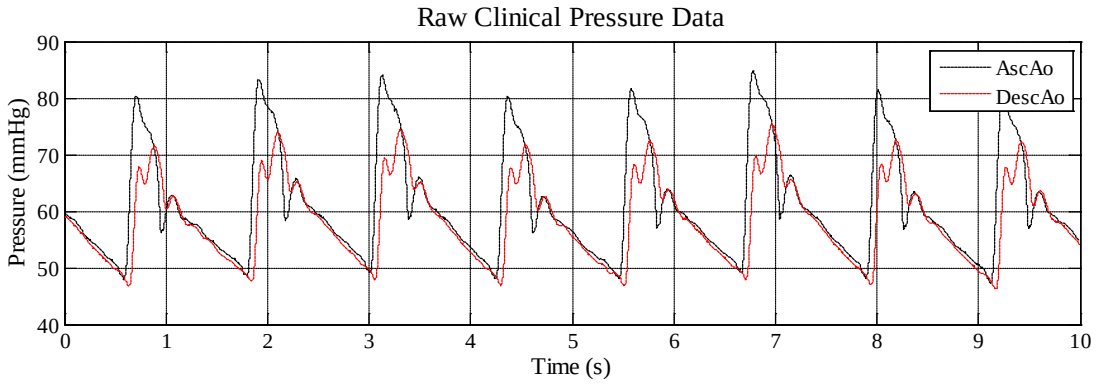

FIGURE 3-20 – RAW CLINICAL PRESSURE DATA FROM AN ANAESTHETISED PATIENT

Unfortunately the inconsistency in the data collection is unavoidable and, since there was no frame of reference (for example an ECG trace), the waveforms required manual alignment. The optimisation scheme assumes the pressure and flow are taken at a coincident point, with this in mind it was decided that waveforms should be aligned assuming that the rising edges occur simultaneously (Figure 3-21).

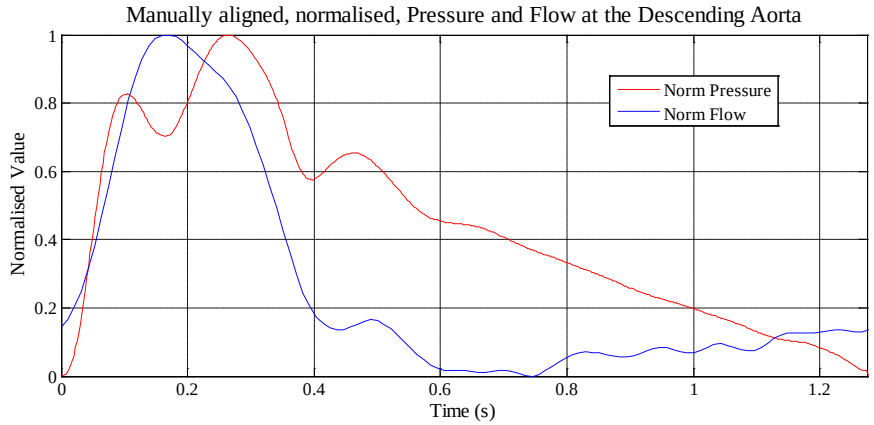

FIGURE 3-21 – MANUAL ALIGNMENT OF THE NORMALISED PRESSURE AND FLOW WAVEFORMS, AT THE DIAPHRAGM LEVEL IN THE DESCENDING AORTA

The clinical pressure recordings were made at only two points within the vessel; the ascending and descending aorta. The optimisation scheme requires the pressure and flow to be known at each of the outlets requiring a Windkessel termination. An assumption is made that the pressure at the outlets of the supra-aortic vessels are equal to that in the ascending aorta.

The Windkessel parameters for the descending aorta boundary are tuned employing the same optimisation settings, as described for the idealised application. Comparison of the clinical pressure and that predicted from the fitted parameter values is not so good, with the RMS residual computed as 8.89 mmHg. The corresponding plot of parameter value movement shows that in every case the fitted value of $\frac{1}{R}$ moves below $1x10^{-7}$, suggesting that the initial guess range is larger than necessary. The initial guess range, for $\frac{1}{R}$, is reset as $1x10^{-10}$ $m^4s\ kg^{-1}$ to $1x10^{-6}$ $m^4s\ kg^{-1}$ and the optimisation process rerun. The granularity of the initial guess matrix is also varied, following identification of the importance of the initial guess in the previous example (Figure 3-17 and Figure 3-18).

The resulting RMS residuals and solution times for the different initial guess granularities are summarised in Table 3.3. With the exception of the lowest granularity the trend, as one would expect, shows an improved RMS residual value as the granularity of the initial guess matrix is refined. The plots of parameter movement are similar to that of the previous, idealised problem, with the fitted values of $\frac{1}{R}$ and CR being relatively consistent while the values of $\frac{R_i}{R}$ vary significantly (Figure 3-22 - left, a matrix granularity of 5 was plotted as for higher values of granularity the individual lines of movement become hard to distinguish). Evaluation of the pressure waveforms, based on the given flow and fitted parameters, illustrates that the variation in $\frac{R_i}{R}$ is due to a relatively flat solution space, with numerous local minima which the optimisation scheme is converging to, rather than $\frac{R_i}{R}$ having a negligible effect on the shape and magnitude of the pressure wave (Figure 3-22 - right).

Granularity	Number of Initial Guesses	RMS residual (mmHg)	Solution time (s)
4	64	3.30	462
5	125	10.42	881
6	216	7.18	1171
7	343	3.20	1841
8	512	2.95	5039

TABLE 3.3 – SUMMARY OF THE OPTIMISATION RESULTS AS THE GRANULARITY OF THE INITIAL GUESS MATRIX WAS ALTERED. DESCENDING AORTA WINDKESSEL TUNING

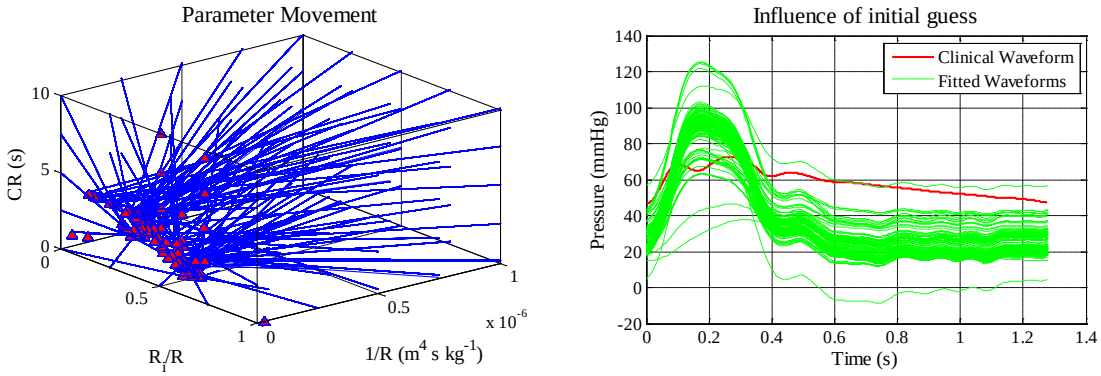

FIGURE 3-22 – PARAMETER MOVEMENT AND INFLUENCE OF INITIAL GUESS ON THE PRESSURE WAVEFORM, COMPUTED FROM THE FITTED PARAMETER VALUES (GRANULARITY 5). DESCENDING AORTA WINDKESSEL TUNING

The final output of the optimisation process is shown in Figure 3-23. The fitted pressure waveform is unable to capture the double peak in the clinical pressure. This phenomenon is common in patients with coarctation, but is not apparent in patients with normal aortae [75]. It is suggested that to accurately capture this feature one would need additional elements in the 0D model. However, for this work it is not deemed necessary to capture these complex features, but rather it is the gross response of the pressure wave that is important in this context. It is certainly true that the gross response, i.e. the baseline and pressure range, as well as the gradient of decay and to a degree the dicrotic notch, are all suitably captured by the fitted Windkessel model (Figure 3-23).

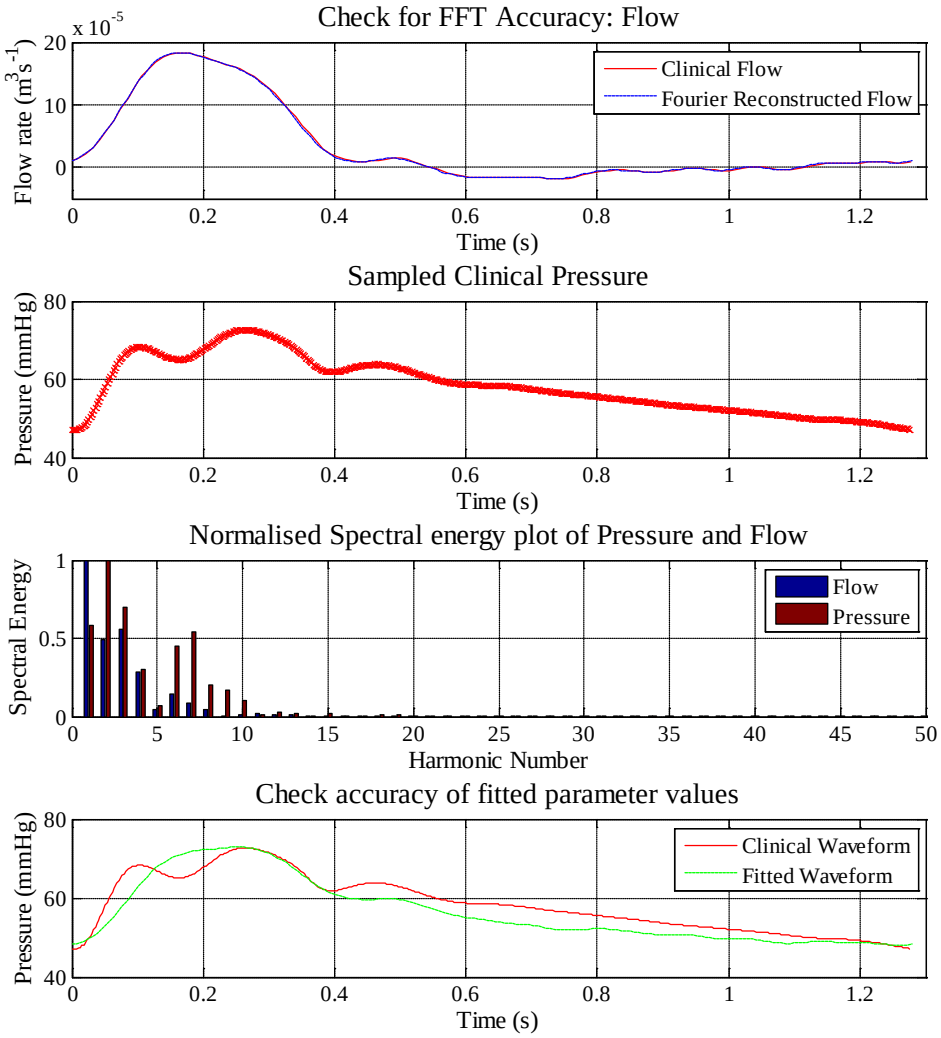

FIGURE 3-23 - OUTPUT FROM THE OPTIMISATION PROCEDURE (GRANULARITY 7). DESCENDING AORTA WINDKESSEL TUNING

The optimisation process is run for each set of pressure and flow data associated with the supra-aortic arteries. The resulting RMS residuals are shown in Table 3.4. An initial guess matrix granularity of 7 is used in each case since the apparent improvement in the fitted descending aorta waveform (difference in the RMS residual of 0.25 mmHg) is not sufficient to justify the additional solution time (Table 3.3). The parameter values for each optimised Windkessel boundary are documented in Table 3.5.

	RMS Residual (mmHg)	Solution time (s)
BCA	12.00	1926
LCC	13.38	1438
LSUB	21.65	1345

TABLE 3.4 – SUMMARY OF THE RMS RESIDUALS FOR THE FITTED PRESSURES AT THE SUPRA-AORTIC VESSELS

It is interesting to note that the optimisation scheme did not perform well for the supra-aortic arteries (Table 3.4). This is attributed to the poor resolution of the measured flow data at these boundaries and the lack of a corresponding pressure trace measured at the same location.

	$\frac{R_i}{R}$	$\frac{1}{R}$ $(\mathbf{m^4 s\ kg^{-1}})$	CR $(\mathbf{s})$
DescAo	0.06882	4.851×10^{-9}	4.100
BCA	0.05009	1.376×10^{-9}	0.7266
LCC	0.1279	4.286×10^{-10}	2.815
LSUB	0.0669	4.608×10^{-10}	3.480

TABLE 3.5 – SUMMARY OF THE FITTED PARAMETER VALUES

As discussed previously, an additional complication when using the prescribed tuning method in a multiple outlet model is that the Windkessel parameters directly determine the distribution of flow. Since the optimisation scheme tackles each boundary in isolation it is unable to ensure the resulting flow distributions are appropriate. In addition the poor resolution of the flow measurements cumulate in a significant error. For the case of interest there is a mismatch of approximately 16% in the measured flow moving into the aorta, when compared to the flow measured leaving the aorta (Table 3.6). Since the pressure described by the Windkessel element is intimately coupled to the flow (Equation 3-31) it is accepted that an

additional stage of tuning is required to achieve the desired pressure response in a full CFD simulation. For comparison purposes the error in the clinical outlet flows was assumed to be evenly distributed across all outlets (Table 3.6 – Corrected Data).

	Q_{BCA}	Q_{LCC}	Q_{LSUB}	Q_{DescAo}	Q_{AscAo}
Clinical Data	0.18	0.052	0.046	0.56	1
Corrected Data	0.22	0.093	0.087	0.60	1
CFD – Initial Opt	0.20	0.063	0.067	0.67	1
CFD – Final Opt	0.23	0.092	0.088	0.59	1

TABLE 3.6 – COMPARISON OF CLINICAL AND NUMERICAL FRACTIONAL FLOW DISTRIBUTION

The initial optimisation process achieves a reasonable first approximation of the Windkessel parameters. An iterative process is then started which involves solving a CFD simulation, using the compressible fluid methodology described previously, with the fitted Windkessel parameters (Figure 3-24 and Figure 3-25). Assuming the resulting flow distributions are approximately correct the optimisation process is repeated with the numerical flow waveforms and the resulting fitted parameters fed back into the CFD simulation. This process is repeated until a reasonable agreement between the numerical and clinical data is achieved. This process is illustrated in the flowchart shown in Figure 3-26.

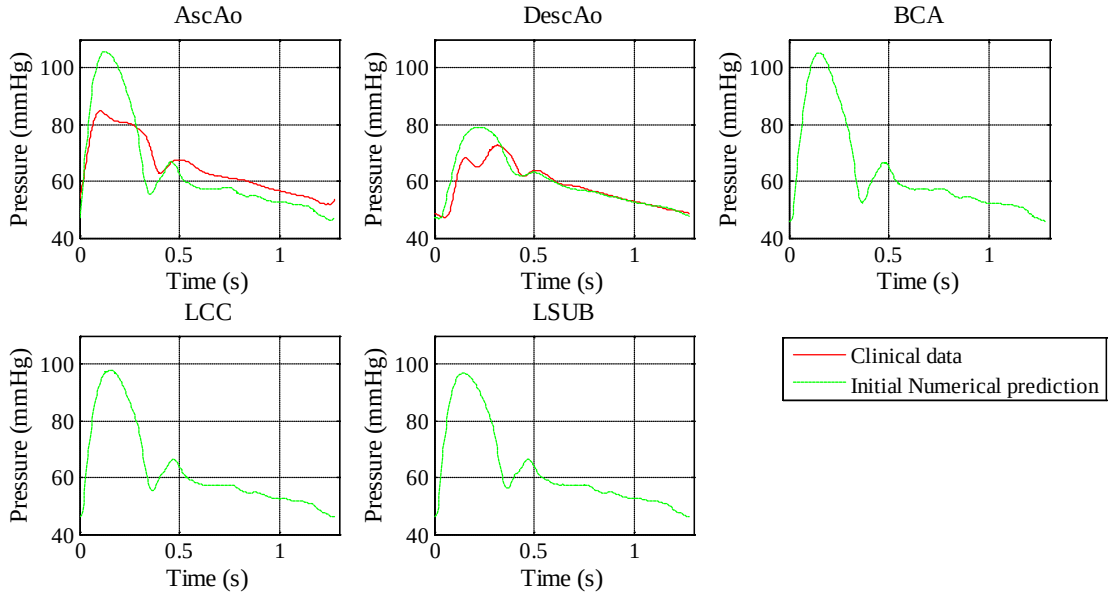

FIGURE 3-24 - COMPARISON OF CLINICAL PRESSURE DATA AND THE NUMERICAL PRESSURE RESPONSE. COMPUTED WITH THE INITIAL TUNED WINDKESSEL PARAMETERS

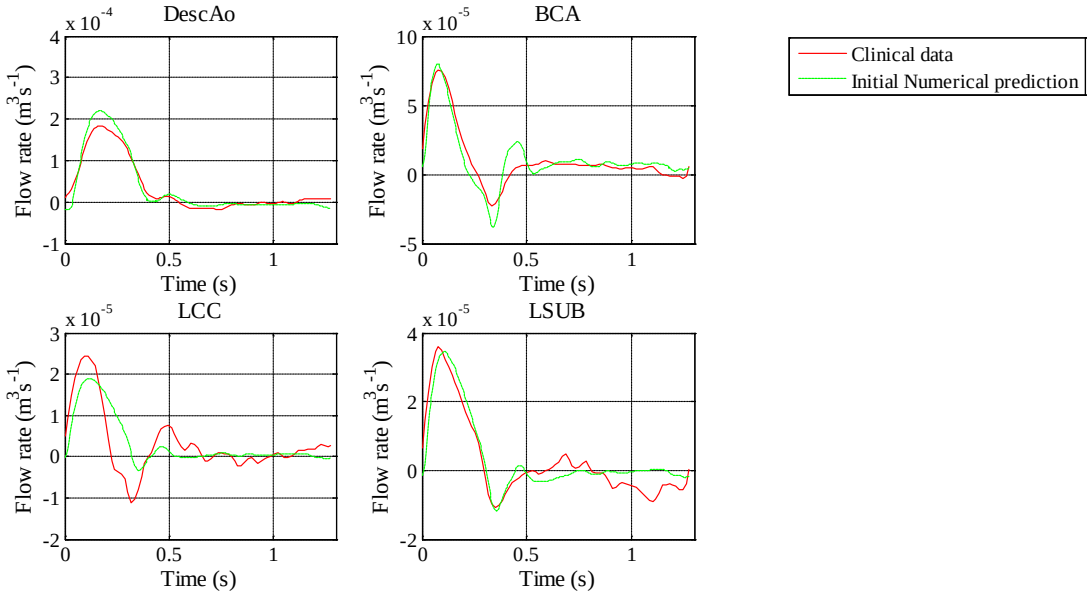

FIGURE 3-25 - COMPARISON OF CLINICAL FLOW DATA AND THE NUMERICAL FLOW DISTRIBUTION. COMPUTED WITH THE INITIAL TUNED WINDKESSEL PARAMETERS

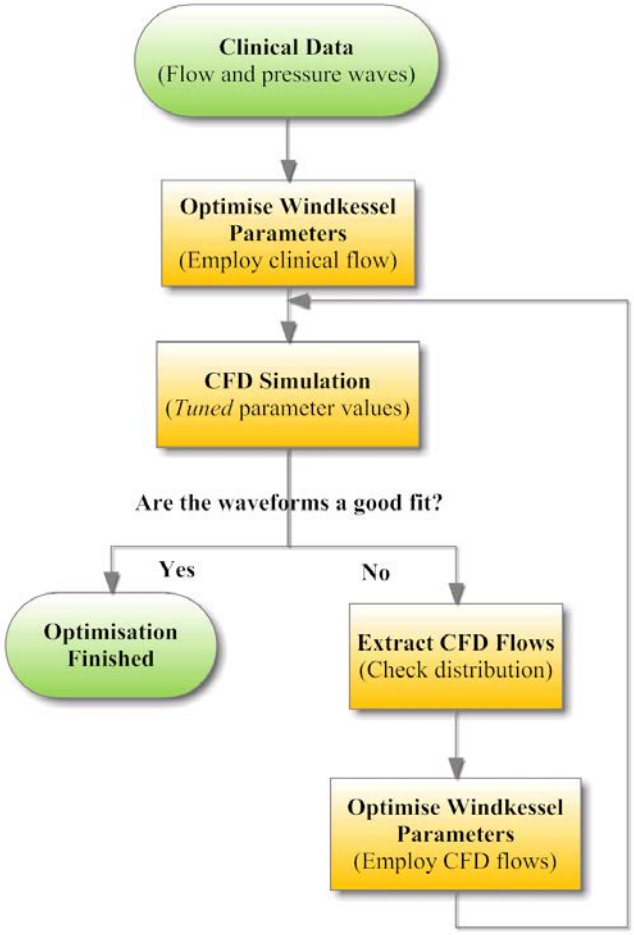

FIGURE 3-26 – FLOWCHART REPRESENTATION OF THE FINAL OPTIMISATION STRATEGY WHEN TUNING FOR CLINICAL DATA

The final sets of Windkessel parameters, for the presented aorta, are shown in Table 3.7. The numerical pressure and flow waveforms have been compared to the clinical data in Figure 3-27 and Figure 3-28, with the flow distributions included in Table 3.6.

	$\frac{R_i}{R}$	$\frac{1}{R}$ $(\mathbf{m^4 s\ kg^{-1}})$	CR $(\mathbf{s})$
DescAo	0.05889	4. 502x10^{-9}	3.578
BCA	0.02382	1.675x10^{-9}	2.060
LCC	0.1127	7.107 x10^{-10}	2.253
LSUB	0.03817	6.382x10^{-10}	3.308

TABLE 3.7 - SUMMARY OF THE FINAL FITTED PARAMETER VALUES

The numerically predicted pressure (Figure 3-27) and flow waveforms (Figure 3-28) are well matched to the clinical measurements. The increased flow rates apparent in the great arteries have been discussed in detail and are explained by the poor resolution of the clinical flow acquisition. A detailed analysis of the numerical results is presented in the following Chapter.

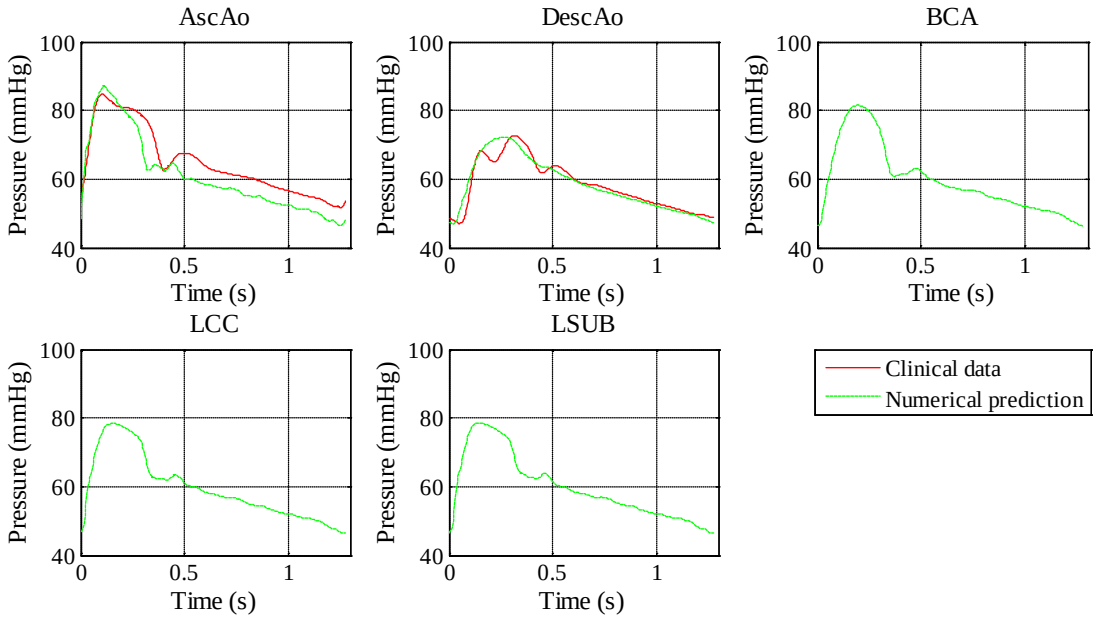

FIGURE 3-27 – COMPARISON OF CLINICAL PRESSURE DATA AND THE NUMERICAL PRESSURE RESPONSE. COMPUTED WITH THE FINAL TUNED WINDKESSEL PARAMETERS

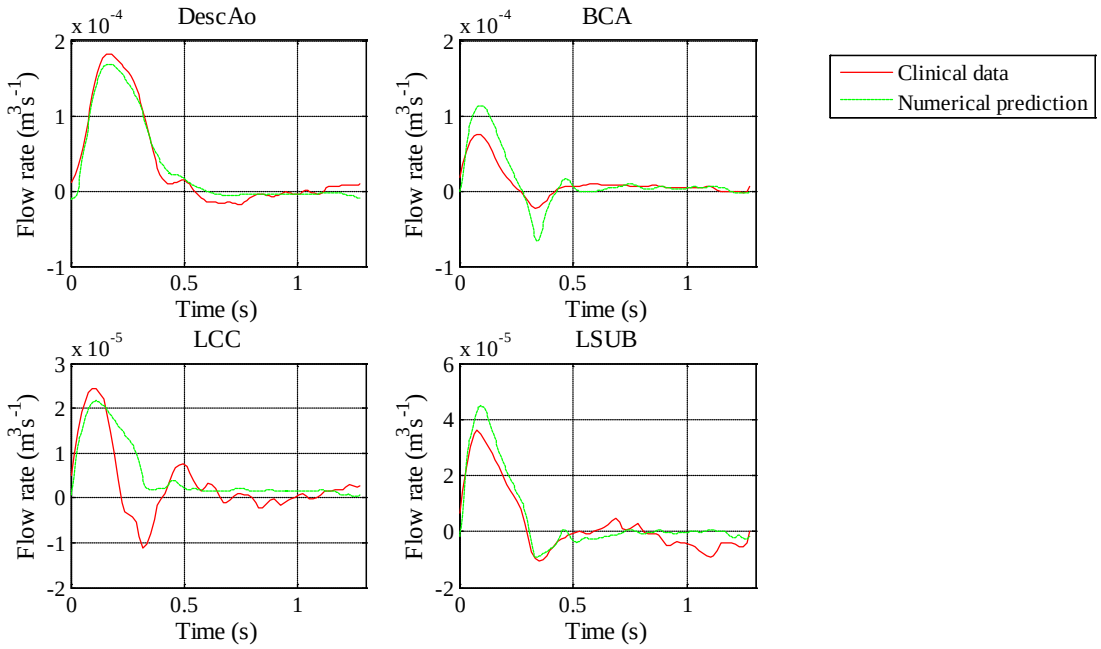

FIGURE 3-28 - COMPARISON OF CLINICAL FLOW DATA AND THE NUMERICAL FLOW DISTRIBUTION. COMPUTED WITH THE FINAL TUNED WINDKESSEL PARAMETERS

CONCLUSIONS 3.7

An analytical solution, which describes a 1D tube coupled to a 0D Windkessel model, was derived. The solution was used to validate the coupling approach employed to terminate 3D CFD simulations in a 0D Windkessel element. The use of a two and three element Windkessel model was investigated. The work demonstrates that the numerical analyses of a tube coupled to a two element Windkessel becomes unstable if there are high frequency components present in the applied flow wave (such as is found in real cardiac waveforms). The inclusion of an input resistance, producing a three element Windkessel, damps these oscillations and results in a more stable downstream condition for CFD simulations.

A minimisation scheme has been presented to tune the parameters of a three element Windkessel model to produce a desired pressure response under a known flow. The approach was applied to an idealised set of pressure and flow data where it performed well and converged to the correct parameter values. The method was subsequently tested on clinically acquired data from a patient specific aorta. The

clinical case was substantially more complex. Not only was there no analytical solution but there was the additional complication of multiple branches. To achieve reasonable predictions of the Windkessel parameters the optimisation strategy had to be revised to include a CFD simulation of the aorta and a feedback loop. However, with these alterations it was shown that, given a known flow and a required pressure response, a best fit set of Windkessel parameters could be calculated.

CHAPTER 4

ANALYSIS STRATEGIES

MOTIVATION 4.1

A major objective for the engineering simulation community is to translate its technologies into clinical application. The use of CFD to characterise haemodynamics in vascular systems has the potential to assist diagnostic and prognostic processes. However, any model that is intended for clinical application must capture the important physiological characteristics of the flow, but should be no more complex than necessary. State of the art simulations of aortic dynamics consider not only the motion of the fluid but also the motion of the vessel wall. These fluid-structure interaction (FSI) simulations are expensive in their computational requirements. The following chapter considers three cases; a uniform cylinder, a native patient-specific aorta and an assisted patient-specific aorta. The flow fields of these cases are predicted using three increasingly complex analysis strategies, namely:

1. Rigid Walled, Incompressible Fluid with Windkessel Outlets.
2. Rigid Walled, Compressible Fluid with Windkessel Outlets.

3. Fluid-Structure Interaction, Incompressible Fluid with Windkessel Outlets.

The subsequent results are analysed and compared with a focus on clinical translation.

Throughout this chapter it is assumed that the standard time-varying Navier-Stokes and Continuity equations are able to capture the flow fields of interest without the need for a turbulence model. The laminar assumption is investigated in Chapter 5. However, irrespective of the need for a turbulence model, the conclusions drawn from this chapter are believed to be valid since they offer a comparative study and hence the results are transferable to turbulent simulations.

FLUID-STRUCTURE INTERACTION METHODOLOGY 4.2

FSI simulations can be approached in a fully coupled or iterative manner [91-93]. In the fully coupled approach the equations that describe the motion of the fluid and the structure are solved simultaneously and the approach is often referred to as a monolithic technique. Following the iterative approach a fluid and a structural solver are dynamically coupled, with the equations of motion (for the fluid and for the structure) solved in isolation. In general, the fluid equations are solved for the initial geometry and the resulting pressures at the interface are passed to the structural solver which then computes the deformation of the geometry. The deformed geometry is passed back to the fluid solver to calculate the new pressure distribution. The process continues in this way until a predefined criterion of convergence is achieved, at which point the solution is said to be converged and the simulation moves on to the subsequent time-step (Figure 4-1).

The fluid structure interaction simulations presented in this thesis are conducted within ANSYS-CFX (ANSYS, Canonsburg, PA, USA) which employs an implicit, time marching iterative coupling approach to solving the FSI problem.

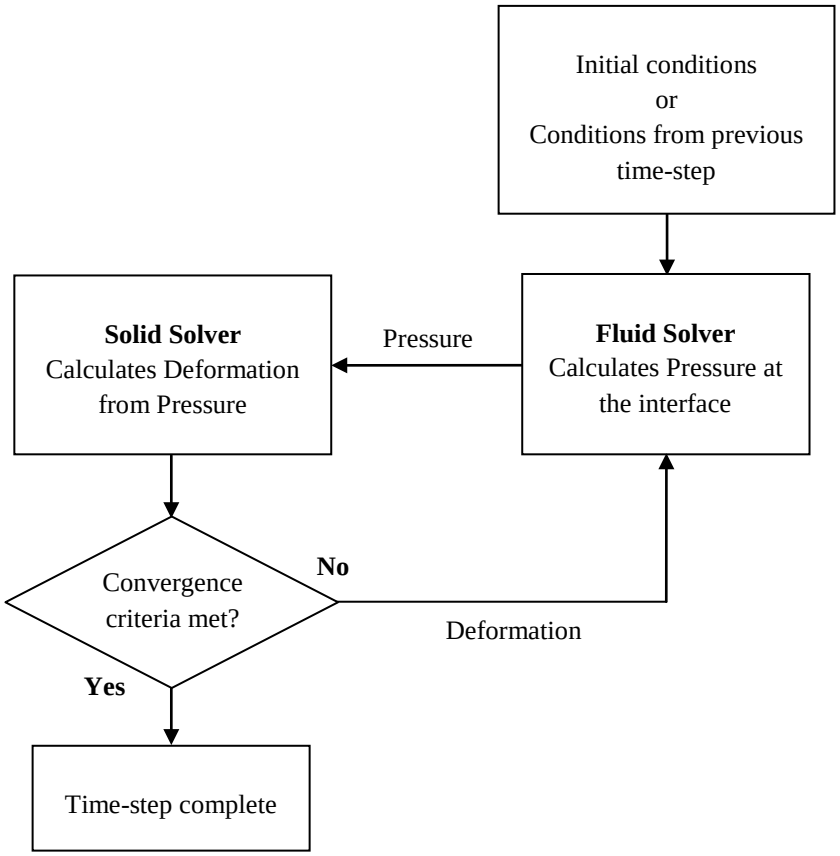

FIGURE 4-1 – ILLUSTRATION OF AN ITERATIVE FSI APPROACH.

FLUID STRUCTURE INTERACTION STABILITY CRITERIA 4.2.1

Causin et al identified an inherent numerical stability problem in the implicit, time marching, coupling scheme [94] such as is used in ANSYS-CFX (ANSYS, Canonsburg, PA, USA). The effect is known as the *"added mass effect"* and arises when modelling incompressible fluids within compliant structural domains. Causin et al derived, for a simple cylindrical system, a relation that identifies the necessary relaxation factor that must be applied to variables passed across the FSI interface to ensure numerical stability [94]. Surprisingly, the required relaxation factor is not only dependent on the time-step and material properties but also on the length of the domain. A discovery described by the authors as *"quite amazing"*. The analytical relaxation factor (ω) is described by Equation 4-1.

$$0 < \omega < \frac{2\left(\rho_s h + \left(\frac{Eh}{r_{max}{}^2(1-\nu^2)}\right)dt^2\right)}{\rho_s h + \rho\left(\frac{2L^2}{\pi^2 r_{max}}\right) + \left(\frac{Eh}{r_{max}{}^2(1-\nu^2)}\right)dt^2}$$

EQUATION 4-1

Where ρ_s is the density of the solid, h is the wall thickness, dt is the time-step, ρ is the fluid density, L is the length of the cylinder, r_{max} is the radius, E is the Young's Modulus of the wall and ν is its Poisson's ratio.

The application of a relaxation factor, to quantities passed across the FSI interface, results in a reduction in their magnitude. At each coupling iteration the given variable is increased by the difference in magnitude of the true and applied variable, multiplied by the relaxation factor. This process gives rise to an asymptotic approach to the true variable value as the number of coupling iterations increase. An example of this is shown in Figure 4-2, where a relaxation factor of 0.5 is applied to a variable of magnitude 1. By the seventh coupling iteration 99.2% of the true variable is applied at the FSI interface.

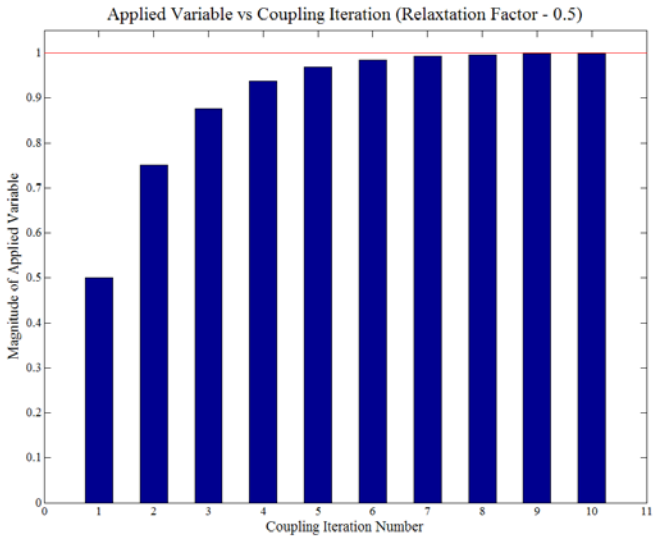

FIGURE 4-2 - ILLUSTRATION OF HOW A RELAXATION FACTOR AFFECTS THE VARIABLE BEING PASSED ACROSS THE FSI INTERFACE

To ensure that at the end of the time-step the true magnitude of the variable is passed across the FSI interface a minimum number of coupling iterations (which depends on the relaxation factor) must be specified. Equation 4-2 is used to calculate the number

of iterations needed and ensures that the difference between the applied and true variable value is less than 1%.

$$Minimum\ coupling\ iterations = \frac{-2}{\log_{10}(1-\omega)}$$

EQUATION 4-2

As well as defining the minimum number of coupling iterations, the ANSYS-CFX coupling code (MFX) assesses the convergence of each time-step via L2 norm residuals. The convergence criteria set for the MFX solver is a residual value, for each variable (Pressure and Displacement), of less than 0.005. This is equivalent to the variable value changing by a factor of less than 0.5% in consecutive coupling iterations.

FLUID STRUCTURE INTERACTION LIMITATION 4.2.2

In the current ANSYS-CFX FSI methodology it is not possible to reliably use a fluid mesh which contains prism elements at the wall. The problem arises from the way that the geometric deformation is applied to the fluid mesh and often results in the following error message:

```
"A negative ELEMENT volume has been detected. This is a fatal error
and execution will be terminated"
```

The deformation of the fluid mesh is determined by a Mesh Motion Model which essentially diffuses the nodal displacements at the boundary throughout the entire computational mesh [78]. This diffusion is described by Equation 4-3.

$$\nabla \cdot (\Gamma_{\text{stiff}} \nabla \delta) = 0$$

EQUATION 4-3

Where Γ_{stiff} is the local mesh stiffness and δ is the displacement relative to the previous mesh.

The method is designed to preserve the distribution of the mesh. However, in systems , such as in the human aorta, where there are large wall displacements that occur rapidly small elements at the wall can become inverted resulting in the error described above. A possible solution to this problem is to re-mesh the fluid domain

when the prism elements become inverted but at present this function is not implemented in the ANSYS-CFX FSI methodology.

Having identified the problem of using prism elements in an FSI simulation a pragmatic approach was taken in the analysis strategies employed in the work which follows. To allow fair comparisons to be made and conclusions to be drawn between the three methodologies proposed no prism elements were used in the simulations presented in this Chapter.

EVALUATION PARAMETERS 4.3

An important and challenging consideration when evaluating transient flow fields is the description of meaningful and informative parameters. The most simple and obvious comparisons consider the differences in the periodic pressure and flow waveforms. However, when comparing alternative analysis techniques and their ability to capture the important characteristics of the flow field it is not acceptable to consider these waveforms in isolation. It is also important to investigate how the predicted internal flow structures vary between the different modelling approaches. In an attempt to quantify the differences in the flow fields a number of parameters have been considered. The most commonly quoted evaluation parameters, in cardiovascular fluid mechanics, are the fluid velocity and wall shear stress (WSS) [63, 95, 96].

Another parameter which is less commonly used is the helical flow index (HFI). The HFI is a measure of the degree of helical flow within a fluid domain [97] and can be defined, in an Eulerian manner, as shown in Equation 4-4. Morbiducci *et al.* calculated the HFI of a healthy aorta from MR flow data [66]. The group computed the HFI in a Lagrangian sense, along a number of streamlines, and reported values ranging from 0.372 to 0.464 with a cycle averaged HFI of 0.414.

$$HFI = \int_V \left| \frac{\boldsymbol{U} \cdot (\nabla \times \boldsymbol{U})}{\boldsymbol{U} |\nabla \times \boldsymbol{U}|} \right| dV \qquad 0 \leq HFI \leq 1$$

EQUATION 4-4

Where $\boldsymbol{U}$ and $(\nabla \times \boldsymbol{U})$ are the vectors of velocity and vorticity and V is the fluid volume.

A further parameter, which is also useful in cardiovascular fluid mechanics, is residence time. This is the time that it takes a massless particle, released into the flow field at a given point, to move through the fluid domain. It can also be thought of as a representation of the 'age' of the fluid i.e. how long the fluid has resided in the computational domain. Ensight v9.1 (CEI Inc. USA) was used to compute the particle path-lines. In the following work a 30x30 grid of particles was released from a grid, superimposed on the inlet boundary, into the flow field at the start of a cardiac cycle and the residence times recorded. This method of particle tracking is a powerful post processing tool and clearly illustrates recirculation zones and other gross features or structures within a transient flow field.

UNIFORM CYLINDER 4.3

To appreciate fully the effect of the alternative methodologies on the characteristics of the flow field it is important to study their influence in both a simple and complex geometry.

The following section compares the different analysis strategies when applied to a uniform cylinder with dimensions similar to those of a human aorta (Figure 4-3).

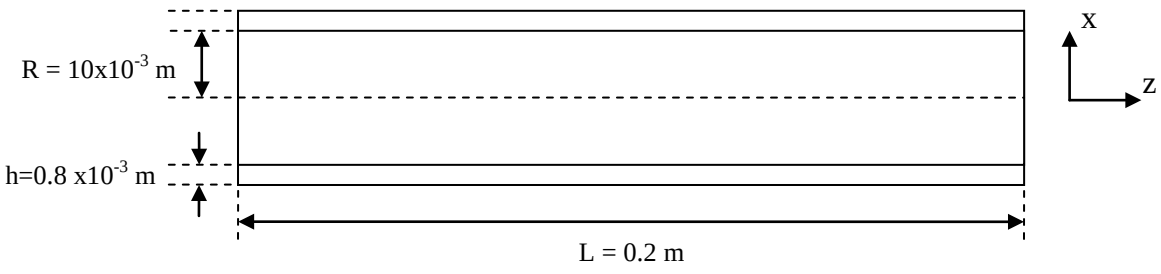

FIGURE 4-3 – DIMENSIONS OF THE UNIFORM CYLINDER

FLUID AND STRUCTURAL PROPERTIES 4.3.1

RIGID WALLED, INCOMPRESSIBLE FLUID PROPERTIES 4.3.1.1

The rigid walled, incompressible fluid properties are defined, as they have been throughout this thesis, as Newtonian, with a constant density and viscosity of 1056kgm^{-3} and 0.0035 Pas respectively.

RIGID WALLED, COMPRESSIBLE FLUID PROPERTIES 4.3.1.2

The compressible fluid model is tuned (as described in Chapter 3) to produce a realistic aortic wave speed of 6.83 ms^{-1} [98]. The temperature is set to a constant value of 310.15 K, which, when combined with the required wave speed and universal gas constant, results in a molar mass of 55.28 kg mol^{-1}.

FSI MECHANICAL AND FLUID PROPERTIES 4.3.1.3

The FSI fluid is defined as incompressible with properties identical to the rigid walled, incompressible fluid model (Section 4.3.1.1). In the following FSI simulations the wall is assumed to be linear elastic with a thickness of 0.8 mm, a density of 1000 kgm^{-3}, a Poisson's ratio of 0.49 and a Young's Modulus of 1x10^{6} Pa. This results in an analytical wave speed, calculated from the Moen-Kortweg equation, of 7.06 ms^{-1}. In truth the offset pressure value will dilate the vessel and thin the wall, thereby reducing the wave speed.

One can approximate the change in radius of a uniform cylinder, assuming plane strain, under a known pressure by Equation 4-5 [75].

$$\partial r = \frac{2P{r_a}^2(1-\nu^2)r_b}{E({r_b}^2-{r_a}^2)}$$

EQUATION 4-5

Where r_a is the inner radius, $r_b$is the outer radius, E is the Young's Modulus and ν is the Poisson's Ratio.

Assuming the change in wall thickness is negligible and predicting the offset pressure from the choice of Windkessel parameters ($P_{offset} \approx 65\, mmHg$) the corrected analytical wave speed is 6.83 ms^{-1}, the same as that for the compressible fluid solution.

FLUID AND MECHANICAL BOUNDARY CONDITIONS 4.3.2

FLUID BOUNDARY CONDITIONS 4.3.2.1

A flat velocity profile, which follows the flow waveform extracted from MR data in the ascending aorta (as described in Chapter 3), is applied to the inlet of the cylinder (Figure 4-4). The outlet pressure is described by a 3 element Windkessel model with parameters chosen to produce a physiological pressure response as in Chapter 3 (Table 4.1). In all simulations a non-slip condition is enforced at the wall.

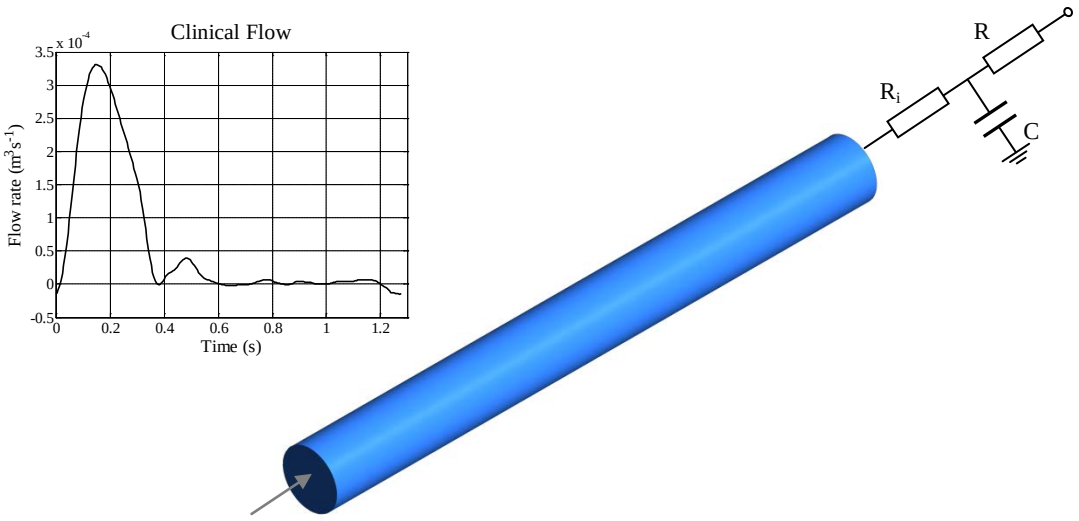

FIGURE 4-4 – ILLUSTRATION OF THE FLUID BOUNDARY CONDITIONS IN THE UNIFORM CYLINDER

	R_i [$kg \cdot m^{-4} \cdot s^{-1}$]	C [$m^4 \cdot s^2 \cdot kg^{-1}$]	R [$kg \cdot m^{-4} \cdot s^{-1}$]
Windkessel Parameters	1.1×10^7	1.45×10^{-8}	1.45×10^8

TABLE 4.1 – WINDKESSEL PARAMETERS FOR THE UNIFORM CYLINDER

FSI MECHANICAL CONSTRAINTS 4.3.2.2

The nodes at the inlet and outlet of the uniform cylinder are fixed in the axial (z) direction i.e. longitudinally tethered. Additional constraint equations are applied at the inlet and outlet boundaries to ensure that the average displacement in the planar x and y direction is zero i.e. the cylinder is free to dilate but unable to translate. To prevent the structure from spinning along its axis all nodes have a fixed z rotation.

MESH CONSTRUCTION 4.3.3

The cylinder is constructed and meshed in ICEM CFD (ANSYS Inc, Canonsburg, USA). As discussed previously the FSI implementation employed in ANSYS-CFX is unable to perform remeshing which restricts the use of prism elements at the wall. Due to this the fluid domain is discretised using only tetrahedral elements. A maximum element edge length of $1.5x10^{-3}$ m is prescribed and the resulting mesh contained approximately 260,000 elements.

The structural mesh is also created in ICEM CFD (ANSYS INC, CANONSBURG, USA) using tri noded shell elements. The same edge length is used and the resulting mesh contained approximately 16,000 elements.

SOLUTION SETTINGS 4.3.4

All simulations are solved with a time-step of 5 ms. The rigid walled incompressible and compressible simulations produced consistent results when compared to a run with a time-step of 1ms (the average percentage difference in the predicted pressure waveforms is less than 1%) and so the temporal discretisation is deemed accurate.

CFD VS. ANALYTICAL 4.3.5

The analytical solution for a 1D tube coupled to a 0D three element Windkessel model, presented in Chapter 3, is expanded upon, under the assumption that the flow and pressure waveforms can be expressed as a sum of their harmonic components, to consider a true cardiac waveform.

The flow waveform, shown in Figure 4-4, was decomposed and the normalised energy of each component was calculated in Chapter 3 (Figure 3-16) to identify the

number of harmonic frequencies that should be considered in the analytical solution. The main contribution to the flow wave comes from the first 15 harmonics. However, to ensure the waveform is accurately represented, the first 20 harmonics are considered. This choice is verified in Figure 4-5, Figure 4-6 and Figure 4-9 where the reconstructed analytical mass flow waveforms can be seen to match the waveform applied in the CFD simulations.

To approximate the rigid walled incompressible fluid the wave speed in the analytical solution is made large. A wave speed of 6.83×10^{7} ms^{-1} is found to produce exactly the same pressure and flow response as a wave speed of 6.83×10^{12} ms^{-1} and so the solution with the former is considered to represent the rigid walled incompressible fluid case.

The pressure and mass flow predictions for the incompressible fluid simulations are compared to the corresponding analytical solution in Figure 4-5. The inlet and outlet mass flow waveforms are identical, as they must be for a rigid walled system with an incompressible fluid. The peak pressure at the inlet is 90.31 mmHg in the CFD model compared to 88.83 mmHg in the analytical solution, a difference of 1.67%. Some variation is not unexpected since the analytical solution assumes the fluid is inviscid, while the CFD model considers the viscous effects. During periods of high acceleration one would expect the solutions to be in close agreement since the system is dominated by inertia, while during periods of low or zero acceleration (at peak flow for example) one would expect the viscous effects to be more dominant and hence the pressures in the CFD analyses to be elevated when compared to the analytical solution. These effects are clearly apparent in Figure 4-5. It is not surprising that the viscous effects are small in this system since the Womersley number is approximately 13, illustrating that the flow is dominated by inertial effects.

In an attempt to replicate more accurately the analytical solution the fluid viscosity is reduced to 1×10^{-6} Pas and the simulation rerun. The RMS residuals of the 'inviscid' CFD simulation are poorly converged with values reaching 1×10^{-4} during the deceleration region of the inlet flow waveform. However, the predicted pressure at the inlet and outlet are in very good agreement with the analytical solution (Figure

4-5) with a maximum pressure at the inlet of 89.13 mmHg compared to 88.83 mmHg in the analytical, a difference of just 0.34%.

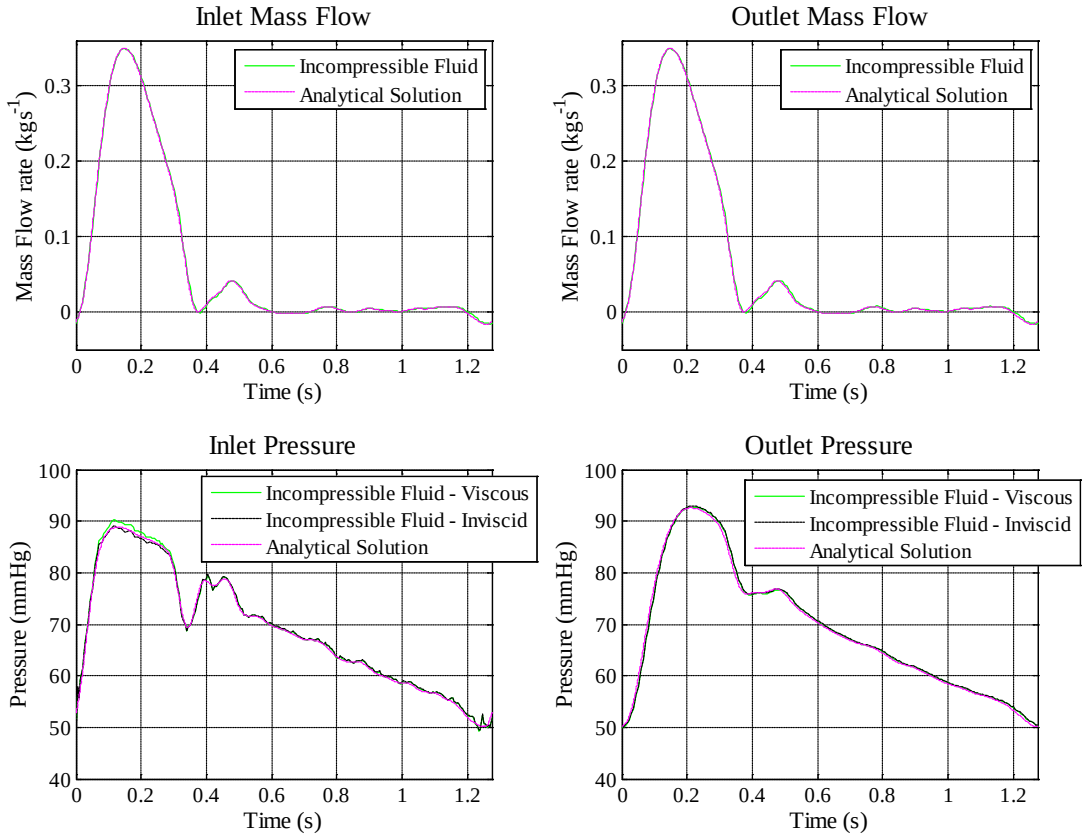

FIGURE 4-5 - INCOMPRESSIBLE FLUID CFD VS. ANALYTICAL SOLUTION: INLET AND OUTLET PRESSURE AND MASS FLOW WAVEFORMS

The pressure and mass flow predictions for the compressible fluid simulations are compared to the corresponding analytical solution in Figure 4-6. As in the incompressible fluid an 'inviscid' simulation is run to approximate better the analytical solution. Once again the numerical and analytical systems are in close agreement, demonstrating the accuracy of the CFD solution. The results also demonstrate that the compressible fluid model is able to capture the propagation of the travelling waves (which is not possible in the incompressible fluid model) and is in complete agreement with the analytical solution in terms of the time lag.

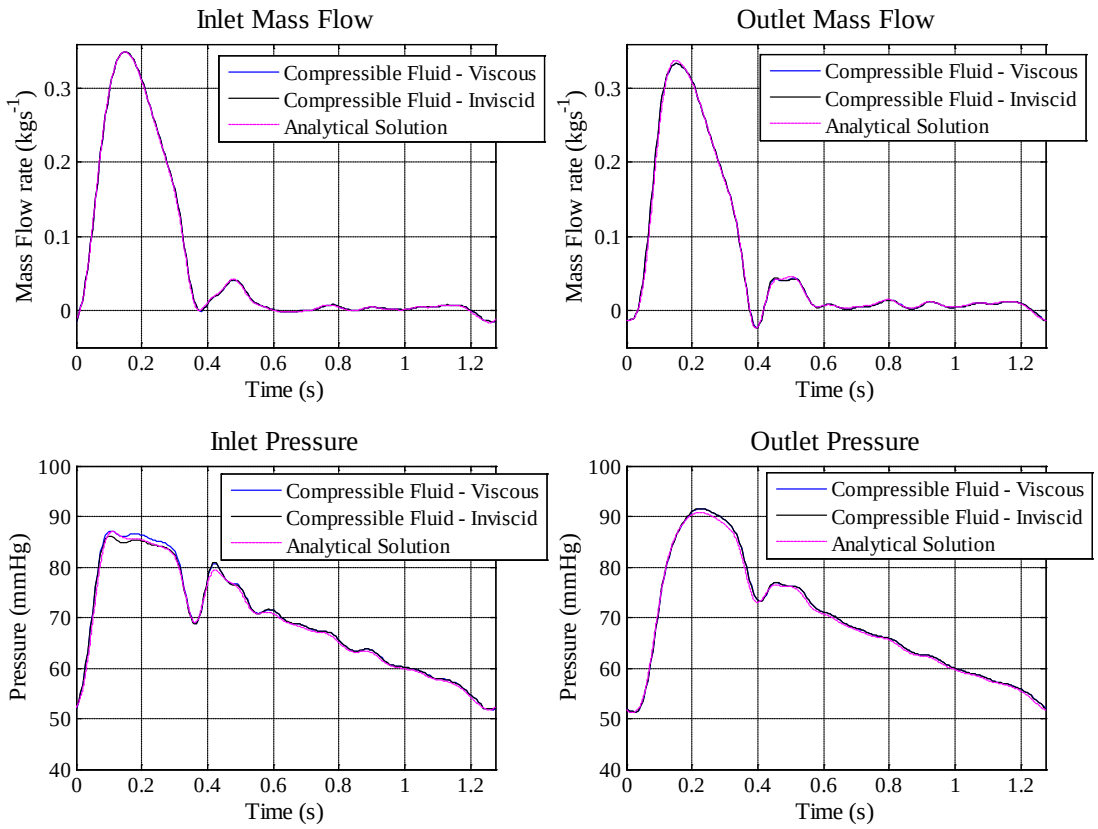

FIGURE 4-6 – COMPRESSIBLE FLUID CFD VS. ANALYTICAL SOLUTION: INLET AND OUTLET PRESSURE AND MASS FLOW WAVEFORMS

The apparent wave speed in the vessel is defined by Equation 4-6 as a function of the time (dt) it takes for the pressure wave to propagate a distance (dz) along the vessel. In the results of the analytical and numerical models shown in Figure 4-6 the apparent wave speed is approximately 4.5ms^{-1}, 34% slower than the Moens-Kortweg wave speed (6.83 ms^{-1}). However, if the outlet condition is described as the characteristic impedance of the 1D/3D domain (i.e. effectively a non-reflecting boundary condition) the apparent and the Moens-Kortweg wave speeds are in complete agreement. This indicates that the reduced apparent wave speed is a product of the backward travelling waves and suggests that in the presence of wave reflections the rate of propagation alone cannot be used to infer the material properties of the vessel wall.

$$c = \frac{dz}{dt}$$

EQUATION 4-6

To investigate this phenomenon further an equation for wave speed was derived based on the analytical description of pressure (Equation 3-8). For convenience it is included below.

$$P(z,t) = \{(P_1 + P_3)cos(kz) + (P_2 + P_4)sin(kz)\}cos(\omega t) + \{(P_1 - P_3)sin(kz) + (P_4 - P_2)cos(kz)\}sin(\omega t)$$

EQUATION 4-7

At time $(t + dt)$ the pressure is:

$$P(z,t+dt) = \{(P_1 + P_3)cos(kz) + (P_2 + P_4)sin(kz)\}cos\big(\omega(t+dt)\big) + \{(P_4 - P_2)cos(kz) + (P_1 - P_3)sin(kz)\}sin\big(\omega(t+dt)\big)$$

EQUATION 4-8

Assuming dt is small one can say $cos(\omega dt) \approx 1$ and $sin(\omega dt) \approx \omega dt$ so the expression for pressure can be simplified to:

$$P(z,t+dt) = \{(P_1 + P_3)cos(kz) + (P_2 + P_4)sin(kz)\}(cos\,\omega t - \omega dt.sin\,\omega t) + \{(P_4 - P_2)cos(kz) + (P_1 - P_3)sin(kz)\}(sin\,\omega t + \omega dt.cos\,\omega t)$$

EQUATION 4-9

The peak amplitude of the wave occurs at z when $\frac{dP}{dz} = 0$. By differentiation it can be shown at time t this occurs when:

$$tan(kz) = \frac{(P_2 + P_4)\,cos\,\omega t + (P_1 - P_3)\,sin\,\omega t}{(P_1 + P_3)\,cos\,\omega t - (P_2 - P_4)\,sin\,\omega t}$$

EQUATION 4-10

The peak pressure at time $(t + dt)$ occurs at $(z + dz)$ thus in the same manner it can be shown that:

$$tan(kz + kdz) = \frac{(P_2 + P_4)(cos\,\omega t - \omega dt.sin\,\omega t) + (P_1 - P_3)(sin\,\omega t + \omega dt.cos\,\omega t)}{(P_1 + P_3)(cos\,\omega t - \omega dt.sin\,\omega t) - (P_2 - P_4)(sin\,\omega t + \omega dt.cos\,\omega t)}$$

EQUATION 4-11

Assuming dz is small ($\tan(kdz) \approx kdz$) and applying a double angle formula then:

$$dz = \frac{1}{k} \frac{tan(kz + kdz) - tan(kz)}{1 + tan(kz)\, tan(kz + kdz)}$$

EQUATION 4-12

The apparent wave speed is then:

$$c = \frac{1}{kdt} \frac{tan(kz + kdz) - tan(kz)}{1 + tan(kz)\, tan(kz + kdz)}$$

EQUATION 4-13

Substituting in the two tan terms (Equation 4-9 and Equation 4-11) the apparent wave speed can be described, under the assumption that dt is vanishingly small, in terms of the forward and backward components of pressure:

$$c = \frac{\omega}{k} \cdot \frac{{P_1}^2 + {P_2}^2 - {P_3}^2 - {P_4}^2}{\left({P_1}^2 + {P_2}^2 + {P_3}^2 + {P_4}^2 + 2(P_1P_3 + P_2P_4)\, cos\, 2\omega t + 2(P_1P_4 - P_2P_3)\, sin\, 2\omega t\right)}$$

EQUATION 4-14

Equation 4-14 is a general solution for the apparent wave speed in a cylindrical vessel. In a system where there are no backward travelling waves ($P_3 = P_4 = 0$) the solution simplifies to $\frac{\omega}{k}$, the fundamental wave speed (i.e. Moens-Kortweg wave speed), and when the system has only backward travelling waves ($P_1 = P_2 = 0$) the solution simplifies to $-\frac{\omega}{k}$. Also in the special case that produces standing waves ($P_1 = P_2 = P_3 = P_4$) the apparent wave speed is zero.

Equation 4-14 demonstrates that the apparent velocity of a propagating wave is not only dependent on the characteristics of the forward and backward travelling waves but also on time. This result is by no means intuitive and has potentially far reaching implications.

Aortic wall stiffness is often extrapolated from the apparent wave speed (measured most commonly using the foot to foot method). However, Equation 4-14 suggests that the apparent wave speed is not only related to the material properties but also on

the reflection characteristics of the system and the positions at which the pressure is measured (since the apparent wave speed is dependent on time the wave does not appear to travel at a constant speed if measured by the transmission of the pressure trace). It also has implications in terms of FSI simulations. In models where the boundary conditions are described as pressure and flow waves a time lag must be incorporated into the outlet boundary condition to account for the propagation of the wave. In general this time lag will be approximated from the distance to the outlet and the fundamental wave speed in the given system. However, Equation 4-14 illustrates that this may not be a reasonable approach and could instead introduce spurious wave reflections into the computational domain, further illustrating the merits of reduced order boundary conditions.

In the system of interest it is important to understand whether the apparent wave speed is governed predominantly by the reflection characteristics, the effects of time or a combination of both. The relative energy and phase shift associated with the forward and backward travelling pressure waves, at the first 10 harmonics, are compared in Figure 4-7. The average magnitude ratio of the forward and backward travelling waves is 0.34 (Table 4.2). This corresponds to the relative decrease in the apparent wave speed when compared to the fundamental wave speed (34% reduction), suggesting that the apparent wave speed is strongly governed by the relative strength of the reflected waves. To investigate the influence of time on the apparent wave speed a pragmatic approach is taken. The pressure wave is plotted at five evenly spaced points along the cylindrical vessel (Figure 4-8) and the associated apparent wave speeds are compared. Qualitatively the wave appears to be moving at a constant speed, while a comparison of the apparent wave speeds gives a variation of approximately 6% along the length of the cylinder. This is deemed to be negligible and suggests that in the context of aortic fluid mechanics the apparent wave speed can be assumed to be constant with time.

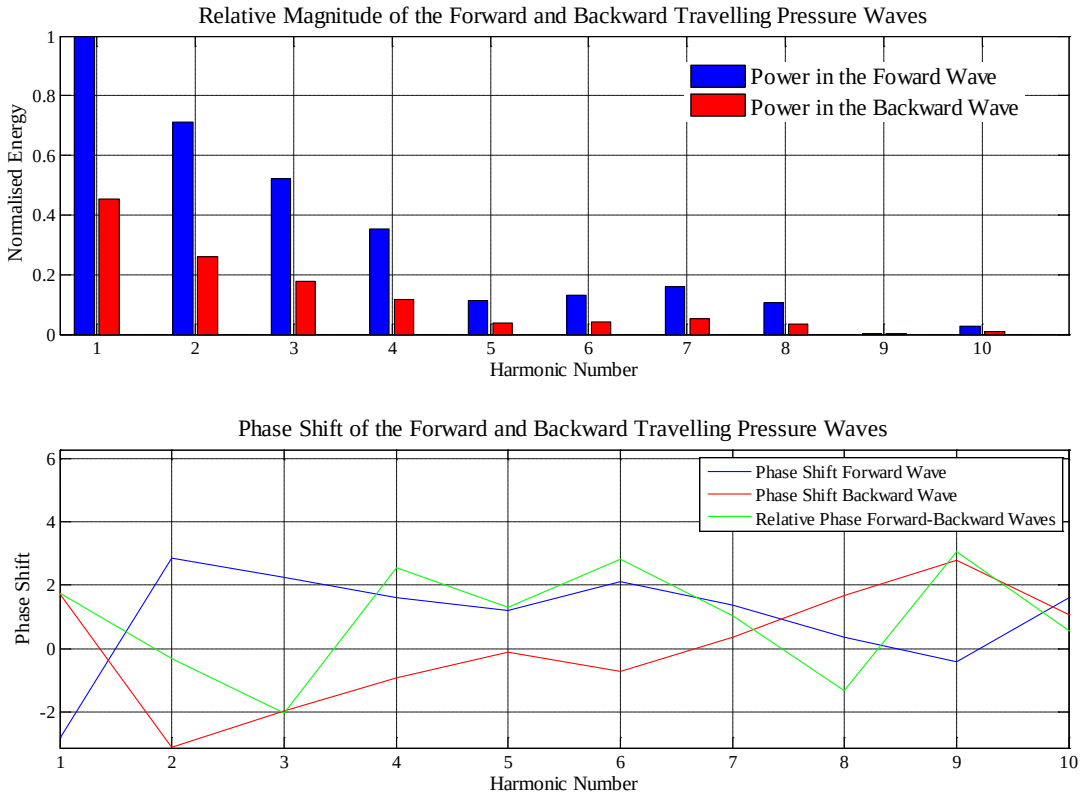

FIGURE 4-7 – COMPARISON OF THE NORMALISED ENERGY IN THE FORWARD AND BACKWARD TRAVELLING PRESSURE WAVES

Harmonic number	Magnitude Ratio	Harmonic number	Magnitude Ratio
1	0.455	6	0.320
2	0.363	7	0.319
3	0.339	8	0.319
4	0.328	9	n/a
5	0.325	10	0.318

TABLE 4.2 – RATIO OF ENERGY IN THE FORWARD AND BACKWARD TRAVELLING WAVES FOR THE FIRST 10 HARMONIC FREQUENCIES

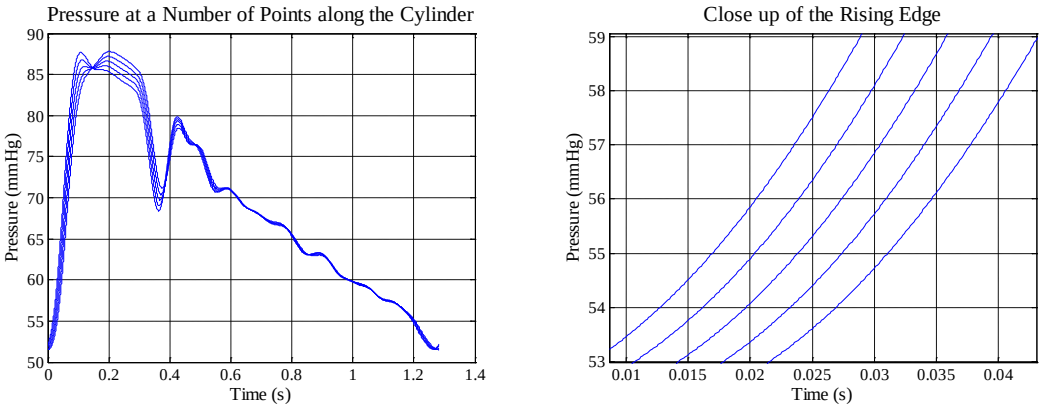

FIGURE 4-8 – ANALYTICAL PRESSURE WAVE AT A NUMBER OF EVENLY SPACED POINTS ALONG THE CYLINDER

The pressure and mass flow predictions for three FSI configurations are compared to the analytical solution in Figure 4-9. The first model (FSI-Real) aims to capture the true physics of the system, thereby including all non-linear geometrical effects. The second model (FSI-Ana) aims to replicate the analytical solution as closely as possible. The transient (inertial) effects and the bending stiffness of the structure are found to have a negligible impact on the solution. However, neglecting the non-linear geometrical effects produces a marked improvement in the agreement between the FSI and analytical solution. Thus the only difference between FSI-Real and FSI-Ana is that the non-linear geometrical effects are not considered in the latter. Finally the third model combined the FSI-Ana configuration with an apparent inviscid fluid (viscosity of $1x10^{-6}$ Pas, termed FSI-Ana-Inviscid). The results demonstrate good agreement with the analytical solution when the non-linear geometric effects are neglected but a greater variation is seen when these effects are considered (Figure 4-9). In both FSI models the inlet pressure wave form appears to be clipped, at approximately 0.07 s (Note: the clipping appears to occur later in the FSI-Real configuration), when compared to the analytical solution. It is proposed that this pressure clipping is the result of a wave reflection from the Windkessel termination. This would also explain why the clipping occurs later in FSI-Real as the wave speed in the system will be lower due to the effects of wall thinning. Considering FSI-Ana, the propagating wave must travel 0.4 m in approximately 0.07 s, relating to a wave speed of 4.44 ms^{-1}. The apparent wave speed (Equation 4-6) in the FSI cylinder, calculated from the transmission of the pressure waves, is 4.44 ms^{-1}. This variation in

the apparent and fundamental wave speeds has been discussed previously. One might argue that both the compressible and the analytical solutions capture the forward and backward travelling waves and thus should predict any pressure clipping associated with a reflected wave. However, the reflection characteristics at the outlet boundary are subtly different in the three systems. In both the compressible and analytical solution the characteristic impedance of the cylinder is constant (cross-sectional area and fundamental wave speed are constant in both models). In contrast the deformation of the wall, in the FSI simulations, changes the impedance of the vessel with time, thereby changing the reflection characteristics of the FSI-Windkessel interface.

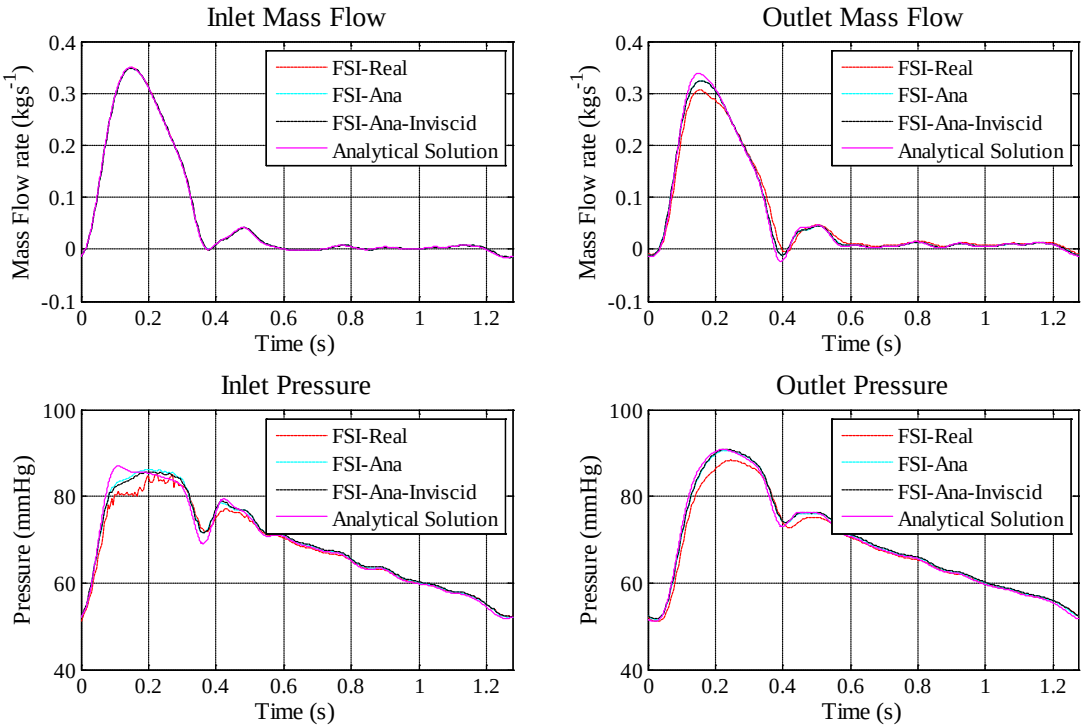

FIGURE 4-9 – FLUID STRUCTURE INTERACTION CFD VS. ANALYTICAL SOLUTION: INLET AND OUTLET PRESSURE AND MASS FLOW WAVEFORMS

Results demonstrate that the incompressible and compressible fluid simulations are performing as the analytical solution giving confidence in the CFD predictions in more complex geometries for which there is no analytical solution. The results also identify a possible limitation in the compressible fluid analogy as, in systems that undergo large deformations, it may not be able to accurately capture the reflection characteristics of a full FSI simulation.

COMPARISON OF ANALYSIS STRATEGIES 4.3.6

The flow field of a uniform cylinder, with dimensions similar to that of a human aorta (Figure 4-3), has been solved using three, increasingly complex, analysis strategies. The rigid walled simulations required 3 heart cycles[3] to reach a periodic solution while the FSI model required 2 cycles, which involved two simulations. The geometry was pressurised in an initial simulation, before being restarted with the appropriate inlet flow wave. The most complex methodology required approximately 30 times more computational time per cycle than the rigid walled models.

	FSI	Compressible Fluid	Incompressible Fluid
Number of Cycles to reach Periodicity	2	3	3
Computational Time to reach Periodicity	60hrs 24mins	3hrs 25mins[4]	2hrs 48mins

TABLE 4.3 - SUMMARY OF COMPUTATION EXPENSE FOR THE UNIFORM CYLINDER

The pressure and mass flow waveforms for each analysis method are compared in Figure 4-10. The results are for a fluid with a viscosity appropriate to blood and the FSI configuration is that which best captures the true physics of the system (FSI-Real). The greatest variation in the predicted pressures arise at the inlet, with the incompressible and compressible fluid models resulting in an over-prediction of 18.87% and an 11.05% respectively when compared to the FSI results. These differences occur at around 0.07 seconds when there is believed to be a wave reflection which is not fully captured by the rigid walled models (as discussed previously). The outlet mass flow and pressure waveforms have a similar form in all analysis methods but their peak magnitudes vary (Figure 4-10). The incompressible fluid model predicts the largest values of pressure, while the FSI model predicts the lowest and the compressible fluid model falls between the two.

[3] All simulations were solved on a Dell PowerEdge T710 with 2 quad core 2.93 GHz Intel Xeon X5570 processors.

[4] The speed up maybe somewhat exaggerated since the Incompressible and Compressible fluid models were run on 2 processors, while the FSI model was run on 4 processors. To account for this difference a linear scaling was applied to the solver time of the rigid models.

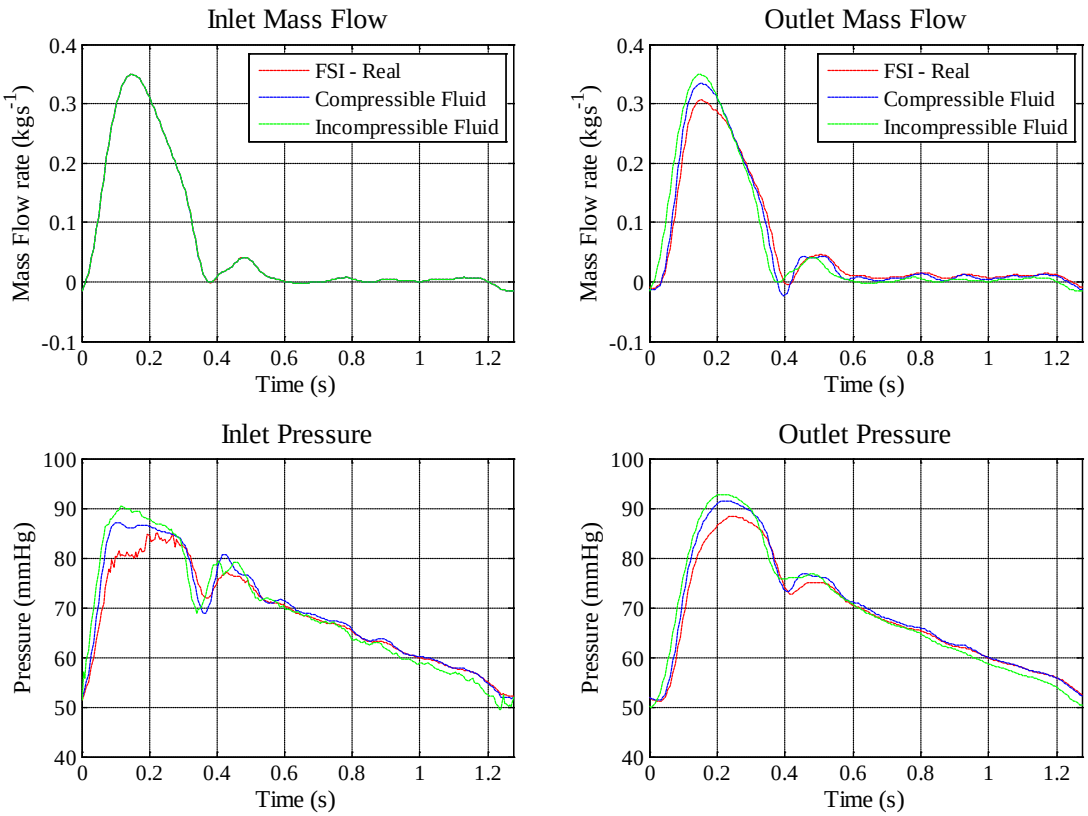

FIGURE 4-10 - COMPARISON OF PRESSURE AND MASS FLOW RATE AT THE INLET AND OUTLET, AS PREDICTED BY THE DIFFERENT CFD METHODOLOGIES

The trends seen in the pressure and mass flow curves (Figure 4-10) are also apparent in the peak and domain averaged velocities evaluated at a number of points across the cardiac cycle (Figure 4-11). As one would expect, the greatest variation is seen at peak systole when the volume of the FSI fluid domain is at its largest (Figure 4-11 - B) while during diastole the predicted velocities are in closer agreement.

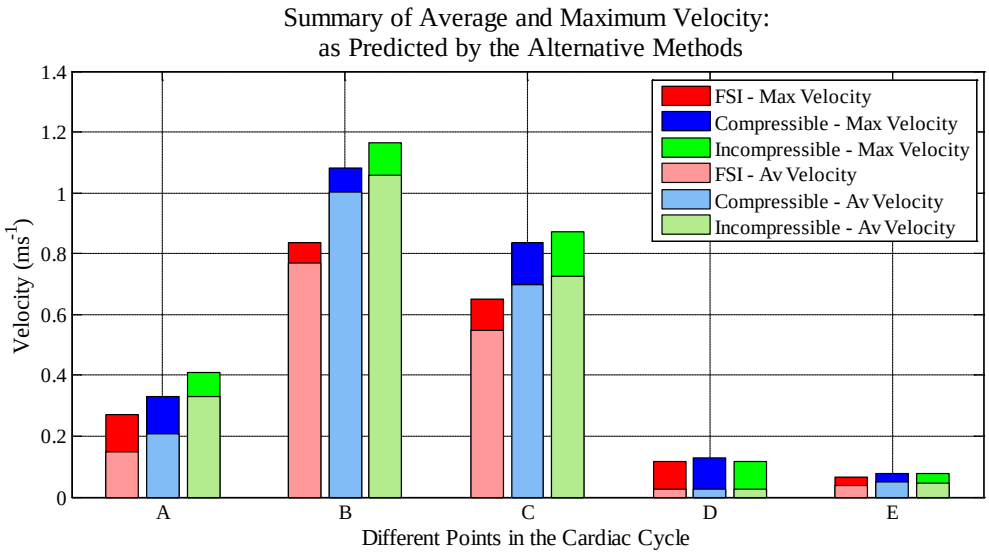

FIGURE 4-11 - COMPARISON OF MAXIMUM AND AVERAGE VELOCITY AS PREDICTED BY EACH CFD METHODOLOGY, AT A NUMBER OF POINTS IN THE CARDIAC CYCLE: (A = EARLY SYSTOLE, B = PEAK SYSTOLE, C = LATE SYSTOLE, D = MID DIASTOLE AND E = END DIASTOLE).

As one would expect analysis of the maximum and wall averaged WSS values across the cardiac cycle (Figure 4-12) have a similar trend to the velocity.

Although both rigid walled approaches overpredict the computed variables, compared to the FSI simulation, it has been demonstrated that the compressible fluid model is able to capture some of the wave propagation effects (such as accurately predicting the pressure lag) and, in doing so, offers an improved rigid walled analysis method.

It now remains to investigate these analysis strategies in realistic geometries with more complex flow structures.

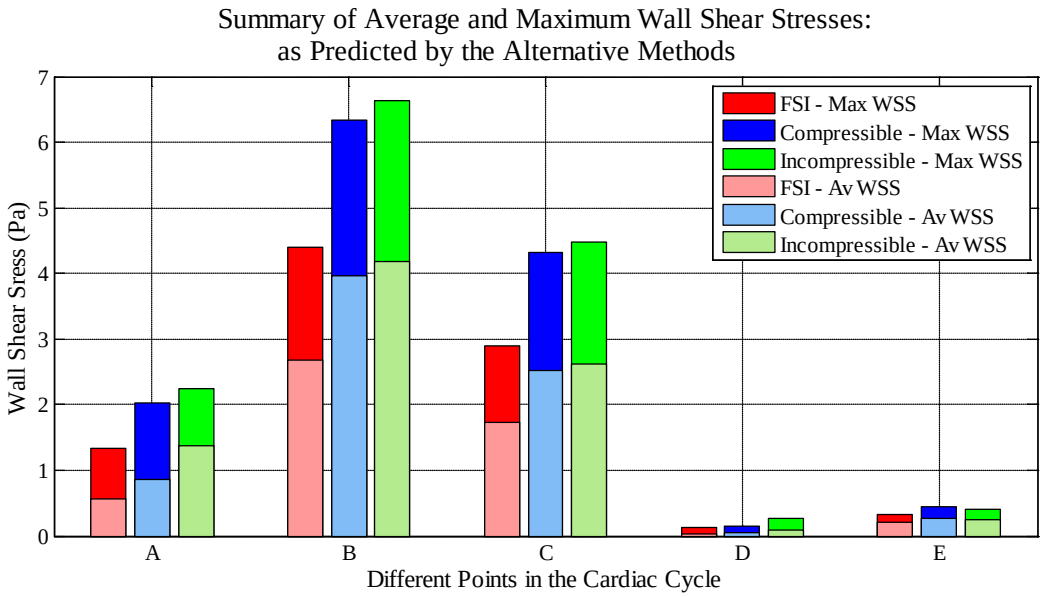

FIGURE 4-12 - COMPARISON OF MAXIMUM AND AVERAGE WALL SHEAR STRESS AS PREDICTED BY EACH CFD METHODOLOGY, AT A NUMBER OF POINTS IN THE CARDIAC CYCLE: (A = EARLY SYSTOLE, B = PEAK SYSTOLE, C = LATE SYSTOLE, D = MID DIASTOLE AND E = END DIASTOLE).

NATIVE AORTA 4.4

To investigate the influence of a complex geometry the patient-specific aorta, previously presented in Chapter 3, is employed in the following section to investigate the three methodologies described above.

All FSI implementations from here on consider nonlinear geometric effects such as wall thinning.

FLUID AND STRUCTURAL PROPERTIES 4.4.1

The incompressible fluid and structural material properties were kept the same as for the uniform cylinder.

RIGID WALLED, COMPRESSIBLE FLUID PROPERTIES 4.4.1.1

The compressible fluid model was tuned (as described in Chapter 3) to produce a wave speed of 7 ms^{-1} which is the same as the approximated average wave speed in

the FSI aorta model. The temperature was set to a constant value of 310.15 K, which when combined with the required wave speed and universal gas constant, resulted in a molar mass of 52.60 kg mol^{-1}.

FLUID AND MECHANICAL BOUNDARY CONDITIONS 4.4.2

FLUID BOUNDARY CONDITIONS 4.4.2.1

As for the cylinder, the patient-specific flow waveform is applied at the inlet as a flat velocity profile and the outlet pressures are described by 3 element Windkessel models. The Windkessel parameters (Table 4.4) are those tuned in Chapter 3 to match the patient specific clinical data.

	R_i [$kg \cdot m^{-4} \cdot s^{-1}$]	C [$m^4 \cdot s^2 \cdot kg^{-1}$]	R [$kg \cdot m^{-4} \cdot s^{-1}$]
BCA	1.422×10^{7}	5.970×10^{8}	3.451×10^{-9}
LCC	1.585×10^{8}	1.407×10^{9}	1.601×10^{-9}
LSUB	5.981×10^{7}	1.567×10^{9}	2.111×10^{-9}
DescAo	1.308×10^{7}	2.221×10^{8}	1.611×10^{-8}

TABLE 4.4 – WINDKESSEL PARAMETERS FOR THE PATIENT-SPECIFIC AORTA

FSI MECHANICAL CONSTRAINTS 4.4.2.2

The aorta is longitudinally tethered at each of the fluid boundaries, while a number of physiological constraints are applied to the inlet, outlets and at 3 additional rings, evenly distributed (and normal to the centreline) along the descending aorta (Figure 4-13). As for the cylinder the constraints ensure that the average displacement in the local x and y direction, on each constraint plane, is zero i.e. the aorta is free to pulse about the centreline but is not able to translate, which in reality would be prevented by the external tissue support. The ascending aorta and aortic arch are intentionally left free from such constraints, due to the reduced tissue support in these regions [60]. No attempt has been made to simulate the motion of the inlet plane due to the motion of the heart.

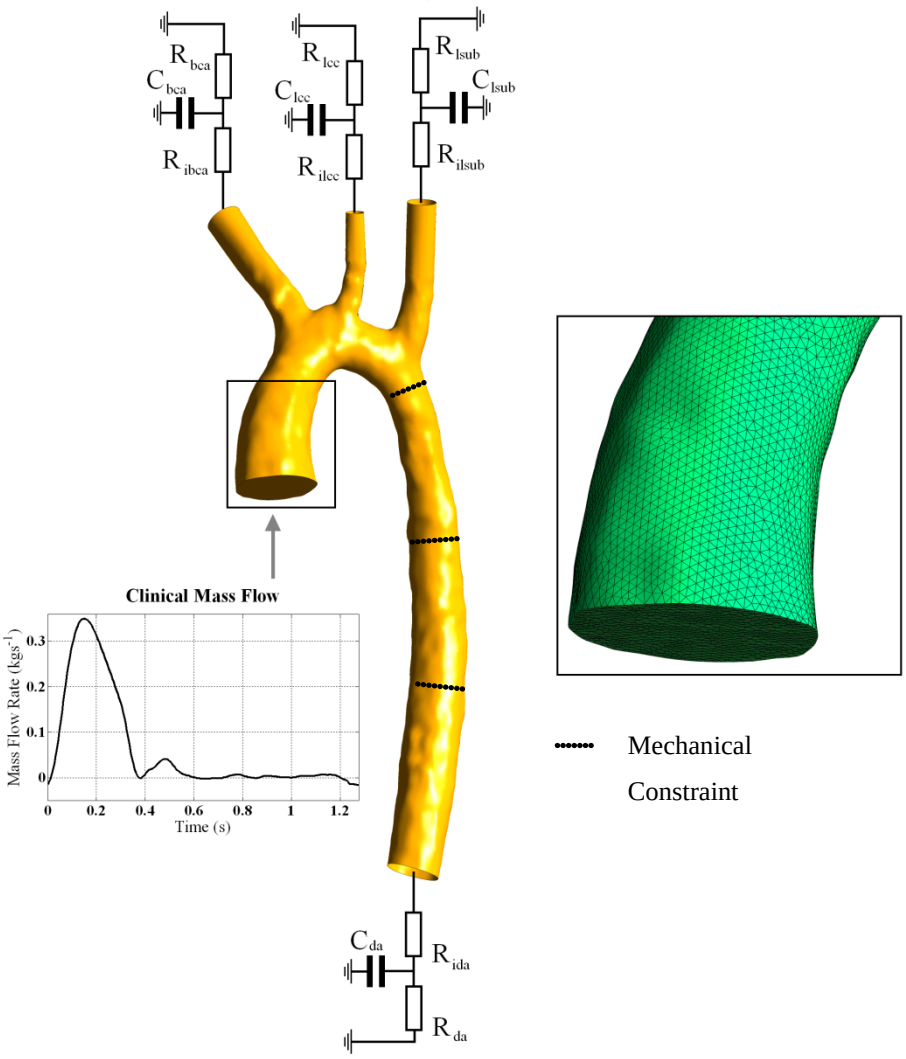

FIGURE 4-13 - ILLUSTRATION OF THE NATIVE AORTA MODEL WITH APPLIED BOUNDARY CONDITIONS AND MESH DENSITY

MESH CONSTRUCTION 4.4.3

As in the cylindrical geometry, the fluid domain is meshed with tetrahedral elements in ICEM CFD (ANSYS Inc, Canonsburg, USA). The maximum element edge length is set to $1x10^{-3}$ m resulting in a computational grid of approximately 500,000 elements (Figure 4-13).

The structural mesh has the same element edge length as the fluid domain and contains approximately 40,000 elements.

SOLUTION SETTINGS 4.4.4

A time-step of 5 ms is used and once again the results for the incompressible and compressible fluid analyses are consistent with those obtained using a smaller time-step of 1ms.

COMPARISON OF ANALYSIS STRATEGIES 4.4.5

The flow field of a patient-specific aorta is predicted using the three CFD methodologies discussed previously. As the focus of this chapter is on translation to the clinic Table 4.5 summarises the number of cardiac cycles required to reach a periodic state for each methodology and the corresponding run times. The most advanced methodology (FSI) requires 7 cycles to reach a period state or 145.5 hours, while the incompressible and compressible fluid models requires only 3 cycles and takes just 6.8 and 7.8 hours respectively (Table 4.5). It is clear immediately that for a clinical application the use of an FSI model is limited, by time constraints, for use in elective surgery cases. However, the computational and temporal expense of a compressible fluid or incompressible fluid model suggests they may be more feasible for clinical use.

	FSI	Compressible Fluid	Incompressible Fluid
Number of Cycles to reach Periodicity	7	3	3
Computational Time to reach Periodicity	145 hrs 30 mins	7 hrs 48 mins	6 hrs 48 mins

TABLE 4.5 – SUMMARY OF COMPUTATION EXPENSE FOR THE NATIVE AORTA

The computed pressures and mass flow rates for each of the methodologies are compared at the model boundaries, all give comparable results (Figure 4-14). This does not appear to support the commonly held belief that the propagation effects due to the compliance of the aortic wall have a significant effect on the form and magnitude of the travelling waves. The peak pressure in the ascending aorta of the rigid-walled incompressible fluid simulation is 85.13 mmHg, 3.8% higher than that

in the ‘gold-standard’ FSI simulation. The compressible fluid analogy, in capturing some of the wave transmission characteristics, reduces the error to 1.2%. There is a noticeable time-lag between the pressure and flow waveforms at the outlets, compared with those at the inlet, in both the FSI and compressible fluid methodologies. This is, of course, absent in the incompressible fluid methodology. The peaks of the pressure and flow waves in the branches (Figure 4-14 – B, C and D) in the FSI model occur marginally earlier than in the compressible fluid model. This is a known limitation of the compressible fluid methodology. The wave speed is related to the compressibility of the fluid, which is constant throughout the domain, while in the FSI case (and in reality) the wave speed will increase in the branches due to the reduction in vessel radius.

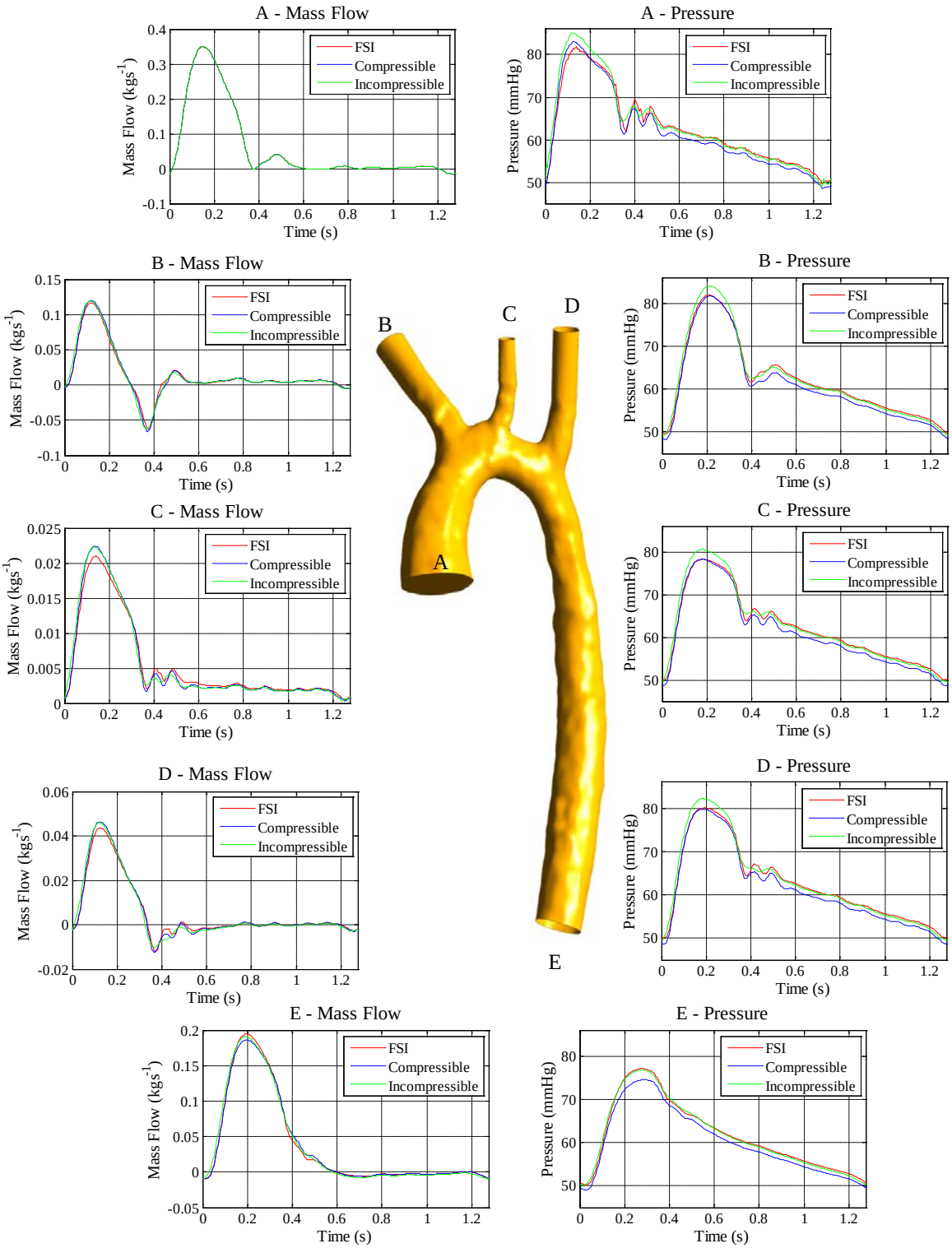

FIGURE 4-14 - COMPARISON OF PRESSURE AND MASS FLOW RATE AT THE BOUNDARIES, AS PREDICTED BY THE DIFFERENT CFD METHODOLOGIES

The FSI model gives a maximum change in radius of 0.6mm (corresponding to a 6% change in radius), while the analytical approximation (Equation 4-5) gives a change in radius of 0.58 mm. The agreement between analytical and numerical results suggest that the FSI deformations are accurate and reasonable.

It is important to not only understand whether the periodic forms of the flow and pressure waves are captured accurately by the alternative methodologies but also to know if the complex features within the flow field are accurately resolved by the simplified model. If the aim is to answer a clinical question one must fully understand each model's strengths and limitations in order to determine the most appropriate for a specific case. In an attempt to compare the more complex features of the flow field the fluid velocity, helical flow index (HFI), wall shear stress (WSS) and residence times are evaluated.

Figure 4-15 and Figure 4-16 summarise the maximum and average velocity and HFI at a number of points in the cycle.

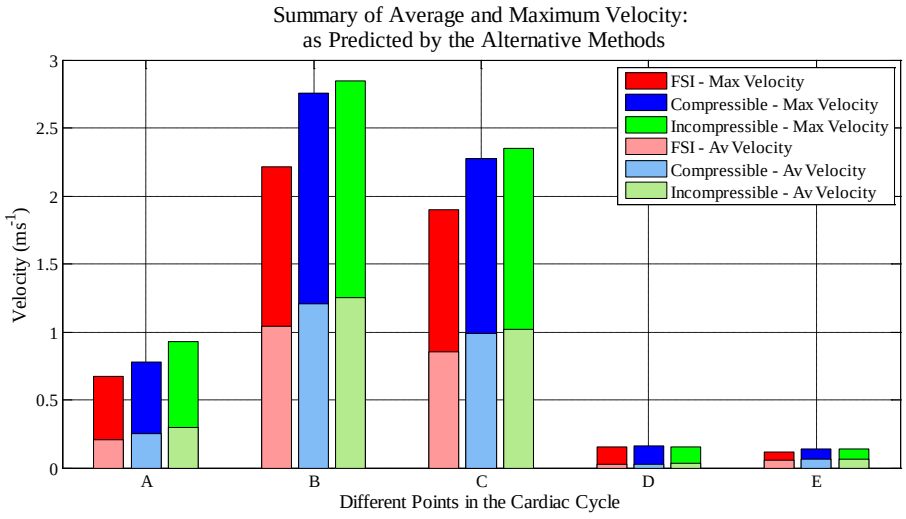

FIGURE 4-15 – COMPARISON OF MAXIMUM AND AVERAGE VELOCITY AS PREDICTED BY EACH CFD METHODOLOGY, AT A NUMBER OF POINTS IN THE CARDIAC CYCLE: (A = EARLY SYSTOLE, B = PEAK SYSTOLE, C = LATE SYSTOLE, D = MID DIASTOLE AND E = END DIASTOLE).

As one might expect, the simplified models over-predict the maximum velocities in the fluid domain during systole (Figure 4-15). This is a direct result of vessel dilation and the resulting increase in the volume of the FSI fluid domain. Both the

compressible and incompressible fluid models show good agreement with the peak velocities during diastole (when the difference in the fluid volume is minimised). In contrast the HFI shows better agreement during systole, which could be explained by the elastic recoil of the aorta producing increased helical flow during diastole (Figure 4-16).

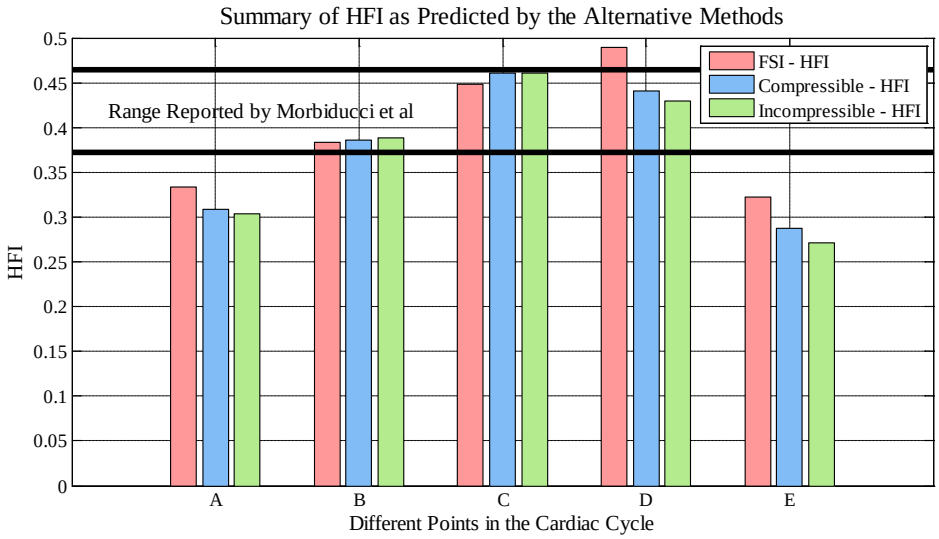

FIGURE 4-16 – COMPARISON OF HFI AS PREDICTED BY EACH CFD METHODOLOGY AT A NUMBER OF POINTS IN THE CARDIAC CYCLE: INCLUDING THE RANGE REPORTED FOR A HEALTHY AORTA BY MORBIBUCCI ET AL. (A = EARLY SYSTOLE, B = PEAK SYSTOLE, C = LATE SYSTOLE, D = MID DIASTOLE AND E = END DIASTOLE).

Table 4.6 summarises the maximum and average residence times for the different methodologies. The maximum residence time is less for the FSI model than for the rigid-walled simulations. However, the average residence time is greater in the FSI simulation when compared to the rigid walled models. There is a 33% and 36% difference in the average residence time predicted by the compressible and incompressible fluid simulations respectively compared to the FSI model. This is not surprising since both the average and peak velocities for the rigid models are greater than for the FSI simulation (Figure 4-15). What is surprising is that even though the maximum and average velocities are larger, suggesting that the particles should move through the domain faster, the maximum residence time in the rigid walled models is greater than the FSI simulation. One possible explanation for this is that

the motion of the wall in the FSI model prevents particles remaining in the near wall, low velocity, region.

	FSI	Compressible Fluid	Incompressible Fluid
Max Residence time (s)	1.537	2.116	2.108
Average Residence Time (s)	0.336	0.225	0.214

TABLE 4.6 – SUMMARY OF RESIDENCE TIME.
COMPARISON OF CFD METHODOLOGIES

In cardiovascular fluid dynamics, for reasons explained later, it is common to use wall shear stress (WSS) as an evaluation parameter in selecting alternative intervention options or in device design. Figure 4-17 evaluates the maximum and domain averaged WSS in each model at a number of points throughout the cardiac cycle, while Figure 4-18 and Figure 4-19 depict the distribution of WSS at peak systole, and end diastole, respectively. The magnitude of WSS in the FSI simulation differs from the alternative approaches by up to 29% at peak systole. However, the distribution of WSS peak systole is comparable in all three models, with regions of high WSS on the lesser curvature of the aortic arch and through the slight constriction (Figure 4-19 - Box) in the upper section of the descending aorta, whilst regions of low WSS are predicted at the entrance to the left subclavian artery (Figure 4-18). This region of low wall shear stress is also apparent at end diastole (Figure 4-19) suggesting the flow detaches from the wall in this area at peak systole and end diastole.

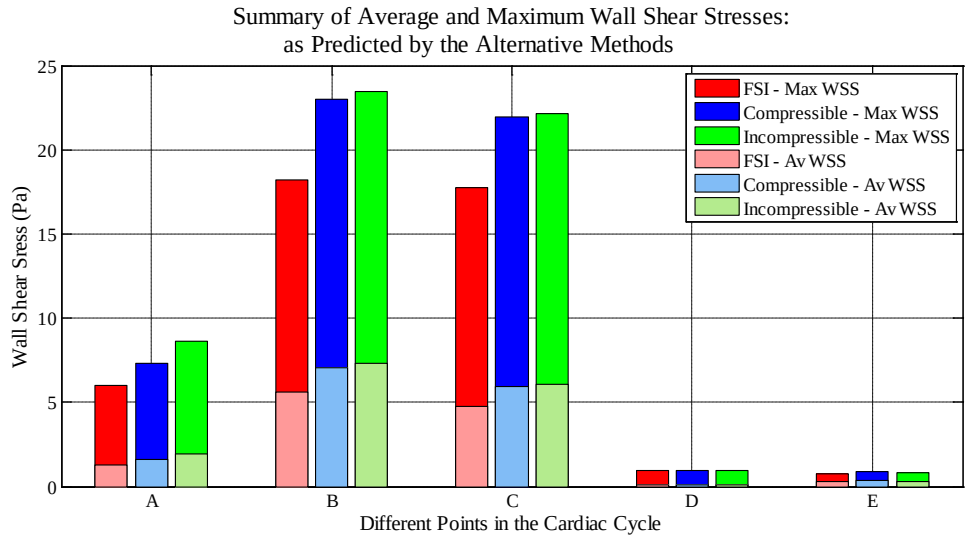

FIGURE 4-17 - COMPARISON OF MAXIMUM AND AVERAGE WALL SHEAR STRESS AS PREDICTED BY EACH CFD METHODOLOGY, AT A NUMBER OF POINTS IN THE CARDIAC CYCLE: (A = EARLY SYSTOLE, B = PEAK SYSTOLE, C = LATE SYSTOLE, D = MID DIASTOLE AND E = END DIASTOLE.)

Although errors in the absolute magnitudes of WSS in the rigid-walled models are as much as 29% for this specific patient geometry, this might nevertheless be within the bounds of our ability to interpret the results in the clinical context. It is likely that trends and changes, associated with prospective interventions for example, will be well-predicted by the simpler analyses, and this might be very important if simulations for a range of alternatives configurations need to be performed.

A particularly relevant example is identifying the optimal anastomotic location for the outflow cannula of an LVAD. In the following section the comparison of the three analysis methods is extended to a patient-specific aorta with the inclusion of an LVAD cannula.

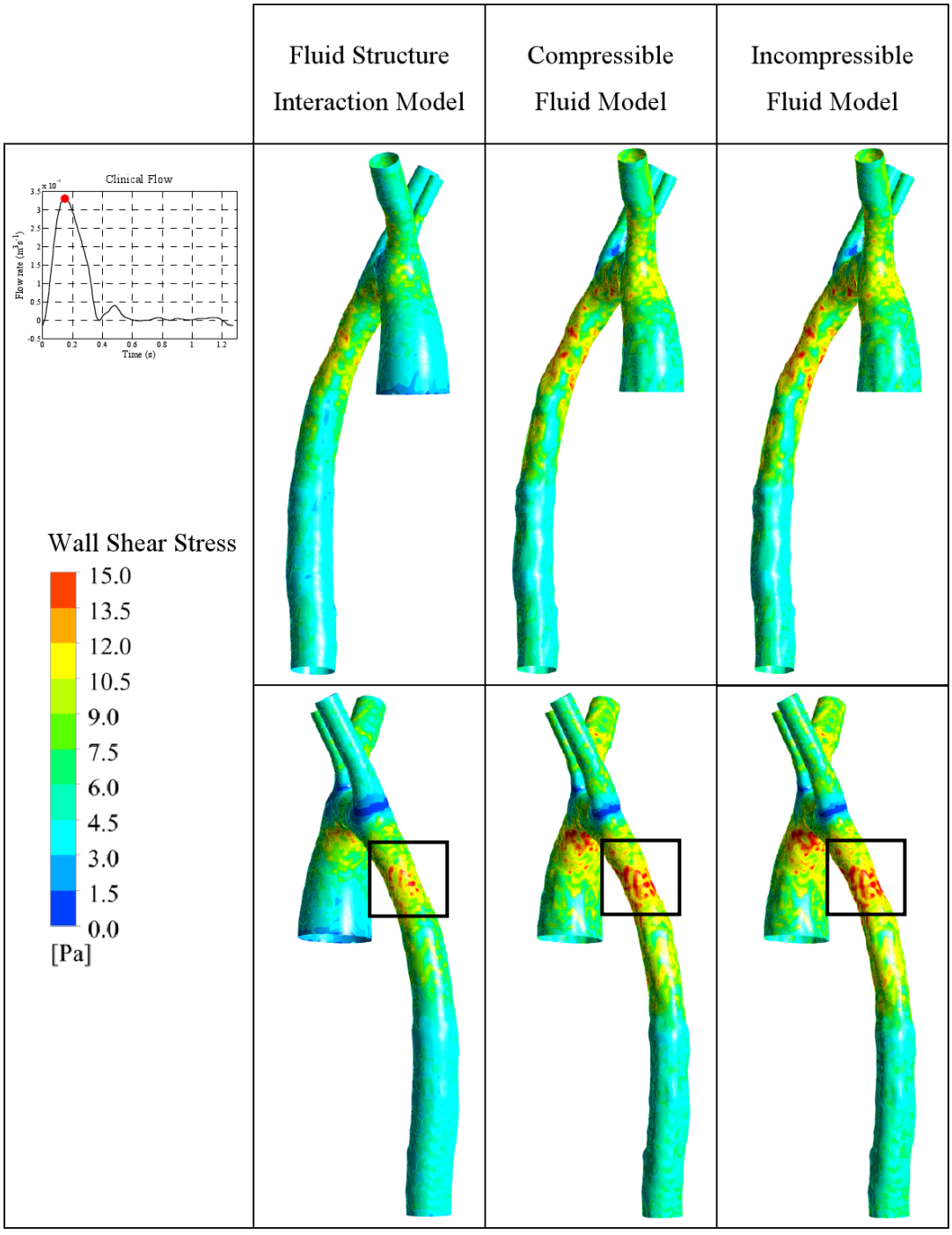

FIGURE 4-18 - COMPARISON OF WALL SHEAR STRESS AT PEAK SYSTOLE
(FSI – LEFT, COMPRESSIBLE FLUID – MIDDLE AND INCOMPRESSIBLE FLUID – RIGHT)

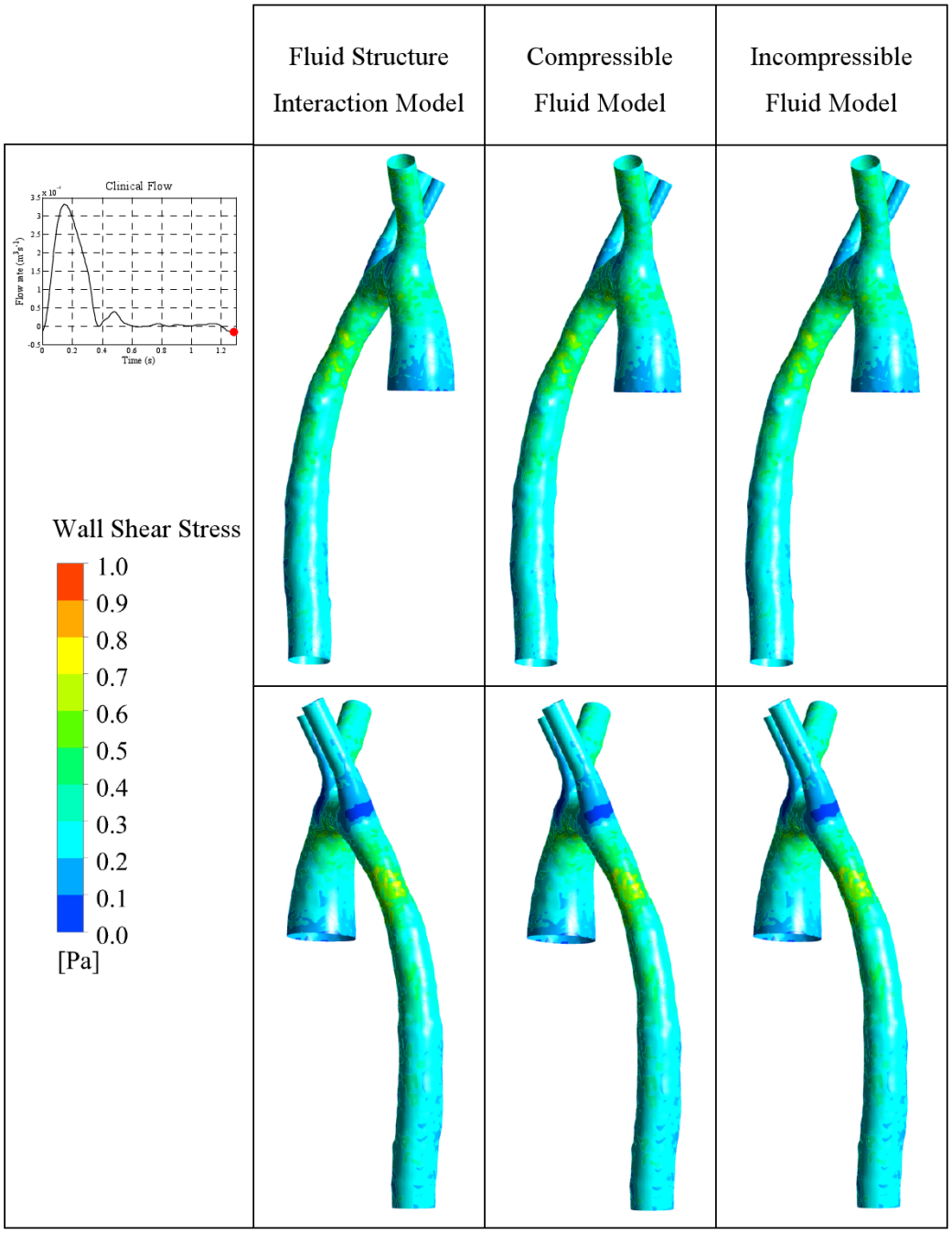

FIGURE 4-19 - COMPARISON OF WALL SHEAR STRESS AT END DIASTOLE
(FSI – LEFT, COMPRESSIBLE FLUID – MIDDLE AND INCOMPRESSIBLE FLUID – RIGHT)

ASSISTED AORTA 4.5

To simulate the flow field of an assisted aorta under the action of an LVAD (the Berlin Heart INCOR® LVAD) an idealised representation of the outflow cannula was created in ICEM CFD (ANSYS Inc., Cannonsburg, USA). The cannula was attached to the ascending aorta of the patient-specific aortic geometry, used in the previous section. The ascending aorta was chosen as the anastomotic site as this has been shown to be the most benficial location in both numerical and mock circulation models [11]. The assisted aortic geometry is shown in Figure 4-20.

All fluid and structural properties are chosen to be consistent with the native condition.

FLUID AND MECHANICAL BOUNDARY CONDITIONS 4.5.1

FLUID BOUNDARY CONDITIONS 4.5.1.1

The Windkessel parameter values are those used in the native condition (Table 4.4) and the inlet flow waveform (Figure 4-20) is taken from a previously validated 0D model of the cardiovascular system under support from the Berlin Heart INCOR® LVAD [53]. The LVAD rotating rate is tuned, using the 0D model, to produce the same integral volume flow rate as in the native case (ω=6500 rpm) and the scale used to plot the mass flow in Figure 4-20 is the same as that used in the native case to illustrate the near steady flow of the assisted aorta. The small degree of residual pulsatility is due to the weak contraction of the native heart.

In previously published work the author demonstrated the importance of applying a real LVAD velocity profile when evaluating the flow field of an assisted aorta [16]. For this reason the velocity profile of the INCOR® [23] is scaled to follow the given flow rate and is employed in all methodologies (Figure 4-20). The aortic valve is modelled as a wall, simulating a severely diseased left ventricle, as might apply immediately after LVAD implantation.

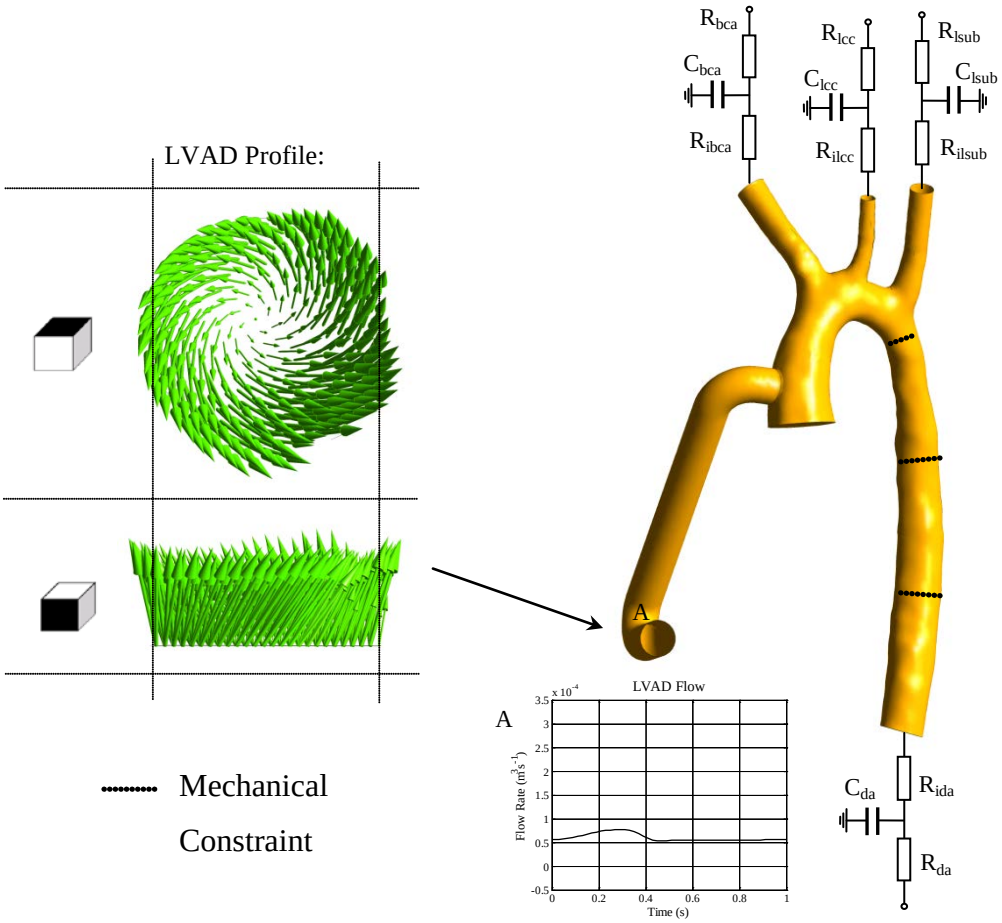

FIGURE 4-20 – ILLUSTRATION OF THE ASSISTED AORTIC GEOMETRY WITH APPLIED BOUNDARY CONDITIONS

FSI MECHANICAL CONSTRAINTS 4.5.1.2

The mechanical constraints applied at the inlet of the native aorta are not physiologically realistic for the assisted case. The fluid in the ascending aorta is no longer moving parallel to the aortic wall but instead is directed across the aorta and impacts on the inner wall. This flow direction results in a non-uniform displacement of the wall and hence the average displacement in the local x and y direction would not be expected to be zero. However, the application of average zero displacement constraints are believed to be realistic at the outlets and down the descending aorta (Figure 4-20) as the flow becomes more organised and develops a parabolic type profile. The LVAD cannula and the aortic inlet are fixed in space and time. Although this is not exactly physiological it is believed to be a reasonable approximation.

MESH CONSTRUCTION 4.5.2

The computational domain was discretised in the same manner as the native aorta, with the fluid domain consisting of approximately 750,000 tetrahedral elements and the structural domain composed of approximately 50,000 triangular shell elements.

COMPARISON OF ANALYSIS STRATEGIES 4.5.3

The assisted aortic flow field is solved using the three CFD methodologies described earlier in this chapter. A summary of the computational expense for each simulation method is tabulated in Table 4.7. The FSI methodology required more cycles to reach a periodic state, although the difference in the number of required cycles is reduced in the assist case when compared to the native case (Table 4.5). The FSI simulation requires approximately 20 times more computational time than the rigid models. The increased computational time of all assisted cases when compared to the native case, is due to the increased number of elements rather than any difficulties associated with numerical convergence.

	FSI	Compressible Fluid	Incompressible Fluid
Number of Cycles to reach Periodicity	8	6	6
Computational Time to reach Periodicity	288 hrs 12 mins	15 hrs 31 mins	10 hrs 58 mins

TABLE 4.7 - SUMMARY OF COMPUTATION EXPENSE FOR THE ASSISTED AORTA

The computed pressure and mass flow waveforms, at the model boundaries, are shown in Figure 4-21. The plot scales are preserved from the native case to illustrate the differences induced by the LVAD.

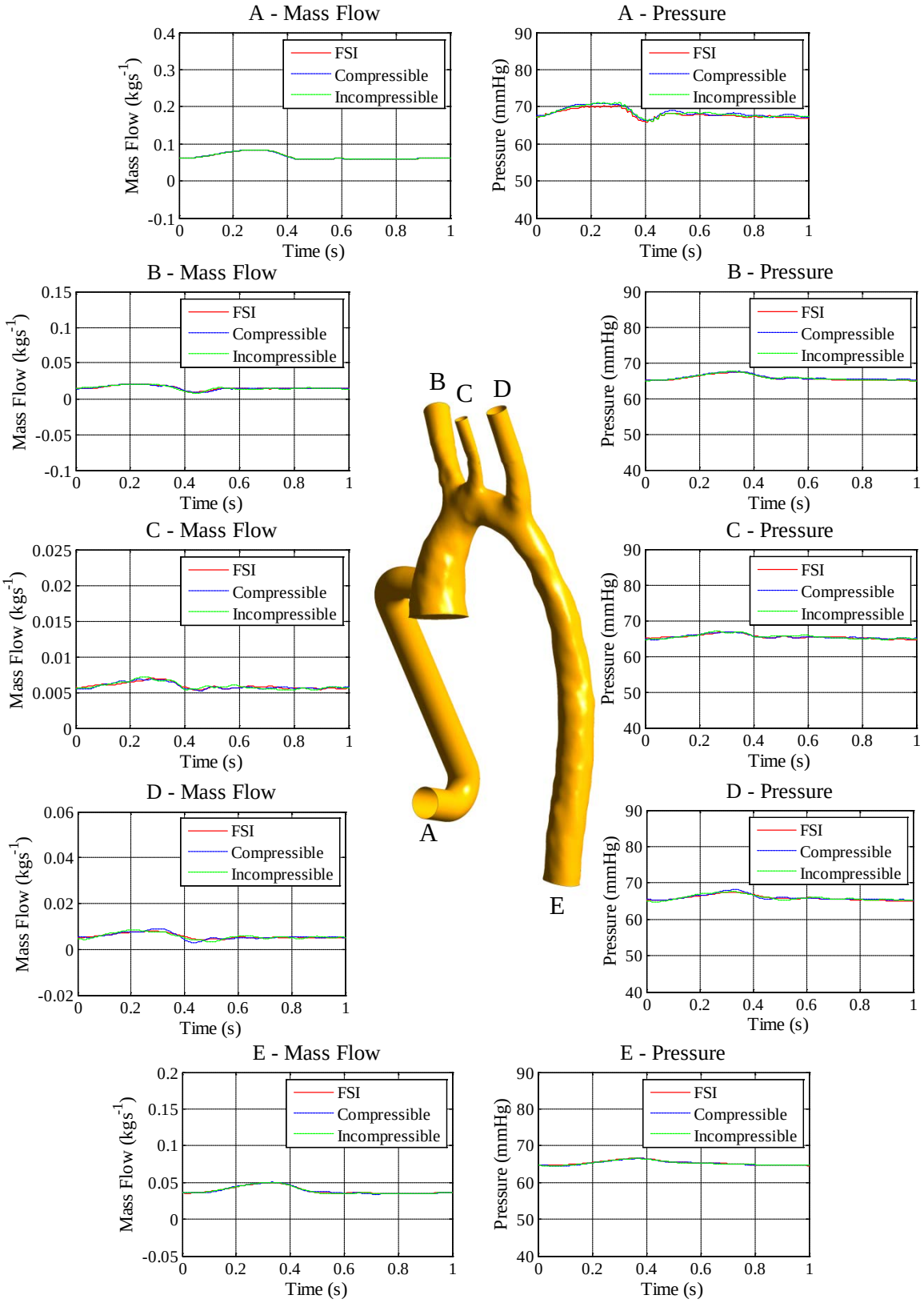

FIGURE 4-21 – COMPARISON OF PRESSURE AND MASS FLOW RATE IN THE ASSISTED AORTA (RED – FSI, BLUE – COMPRESSIBLE FLUID, GREEN – INCOMPRESSIBLE FLUID)

As one would expect in a system with minimal pulsatility the three methodologies produce very closely matched results (Figure 4-21). The largest differences appear in the predicted inlet pressure waveform with a maximum percentage difference of less than 2% when comparing the rigid walled models to the *'Gold Standard'* FSI simulation.

The maximum and domain averaged velocities and wall shear stresses are also closely matched in all three cases (Figure 4-22 and Figure 4-23). The largest variation in peak velocity occurs in the compressible fluid model at peak flow, where the percentage difference compared to the *'Gold Standard'* FSI model is 1.7% (Figure 4-22). Both incompressible and compressible fluid models over-predict the average velocity in the domain by maximum percentage differences of 10% and 11.4% respectively. These differences may appear large but they are in fact well within the range of physiological variation and, if one considers the magnitude of the velocities, it is apparent that the differences are small (maximum error in the mean velocity is approximately 0.03 ms^{-1}).

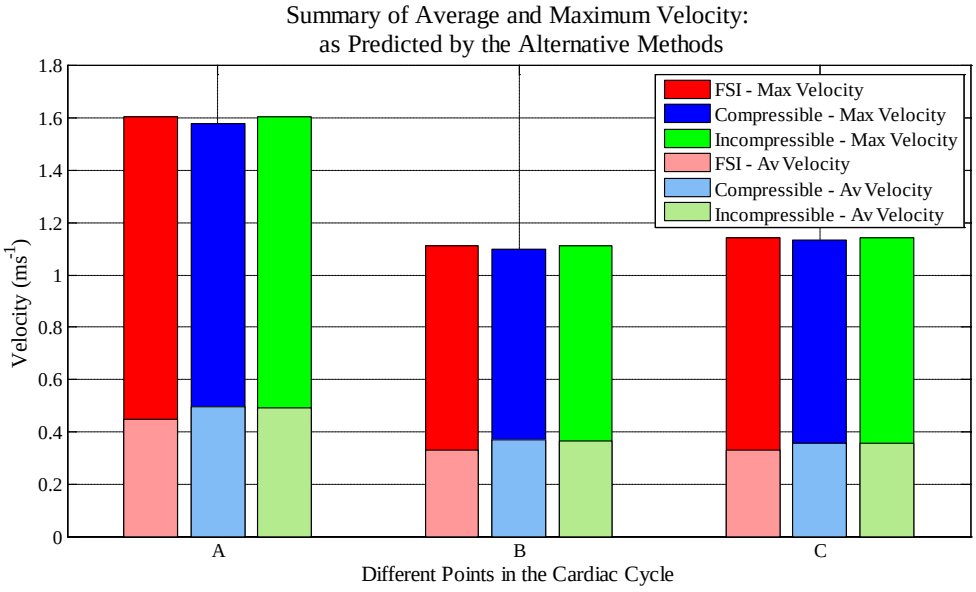

FIGURE 4-22 - COMPARISON OF MAXIMUM AND AVERAGE VELOCITY AS PREDICTED BY EACH CFD METHODOLOGY, AT A NUMBER OF POINTS IN THE CARDIAC CYCLE:
(A = PEAK FLOW, B = MINIMUM FLOW, C = END OF CYCLE.)

The peak and mean wall shear stresses demonstrate a similar trend, with peak values well-predicted by all the models and the rigid systems over-predicting the mean wall

shear stresses. However, the compressible fluid model produces consistently better approximations of the averaged wall shear stress. A maximum percentage difference in the peak wall shear stress, of 0.99%, occurs in the compressible fluid model at peak flow, while the maximum percentage difference in the mean wall shear stress of 13.1% occurs in the incompressible fluid model at minimum flow. Wall shear stress is an important parameter when considering the haemodynamics of an assisted aorta. It is a recognised factor associated with the development of atherosclerosis and could be important when considering the potential for endothelial cell or wall damage induced by continuous flow LVADs [25].

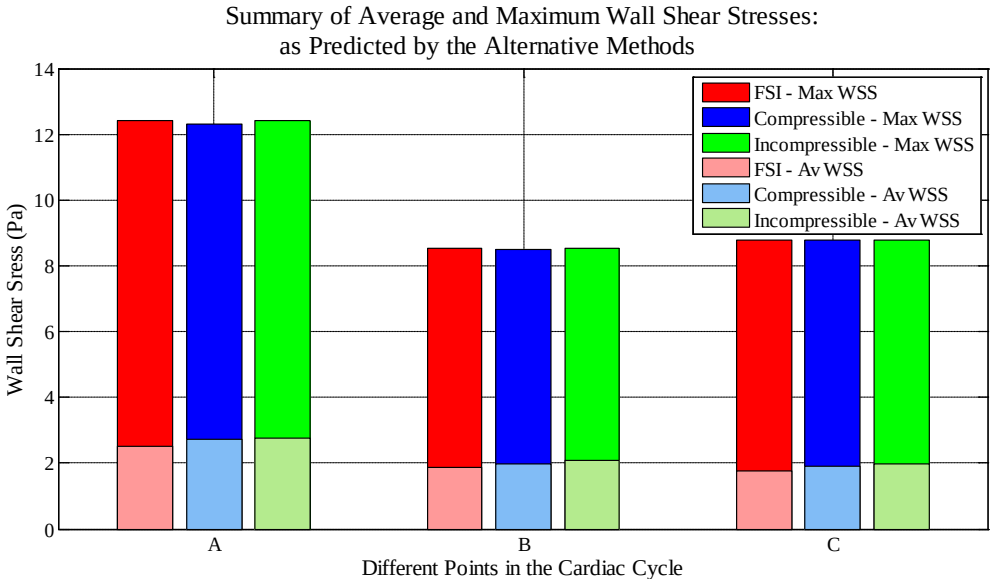

FIGURE 4-23 - COMPARISON OF MAXIMUM AND AVERAGE WALL SHEAR STRESS AS PREDICTED BY EACH CFD METHODOLOGY, AT A NUMBER OF POINTS IN THE CARDIAC CYCLE:
(A = PEAK FLOW, B = MINIMUM FLOW, C = END OF CYCLE.)

As well as reporting the average and maximum values of wall shear stress Figure 4-25 and Figure 4-24 compare the predicted distribution of wall shear stress both at peak flow and at the end of the cardiac cycle respectively. All models have a similar trend, with the highest wall shear stresses occurring in the ascending aorta and reducing in magnitude along the length of the aorta. The peak magnitudes of wall shear stress do not occur directly opposite the cannula anastomosis but instead occur slightly upstream on the lesser curvature of the aortic arch. This may be a result of applying a real LVAD profile which has a strong radial velocity component causing the fluid in the cannula to swirl.

All three methodologies illustrate there are regions of high wall shear stress in the ascending aorta, under the aortic arch and in the aortic valve region at the end of the cycle. However, the incompressible fluid model predicts the location of the high wall shear stress on the valve plane to occur at a different position compared to the alternative methodologies (Figure 4-25 - rectangles). Regions of low wall shear stress are apparent around the cannula anastomosis, at the branching point of the left common carotid and the left subclavian artery, and in the aortic valve region, at both points in the cardiac cycle. All three methodologies resolve these regions of low shear, which could be indicative of sites prone to the development of atherosclerosis (Figure 4-24 and Figure 4-25).

In general, the compressible fluid model results in a better approximation of the wall shear stress distribution, assuming the FSI model to be the *'Gold Standard'*.

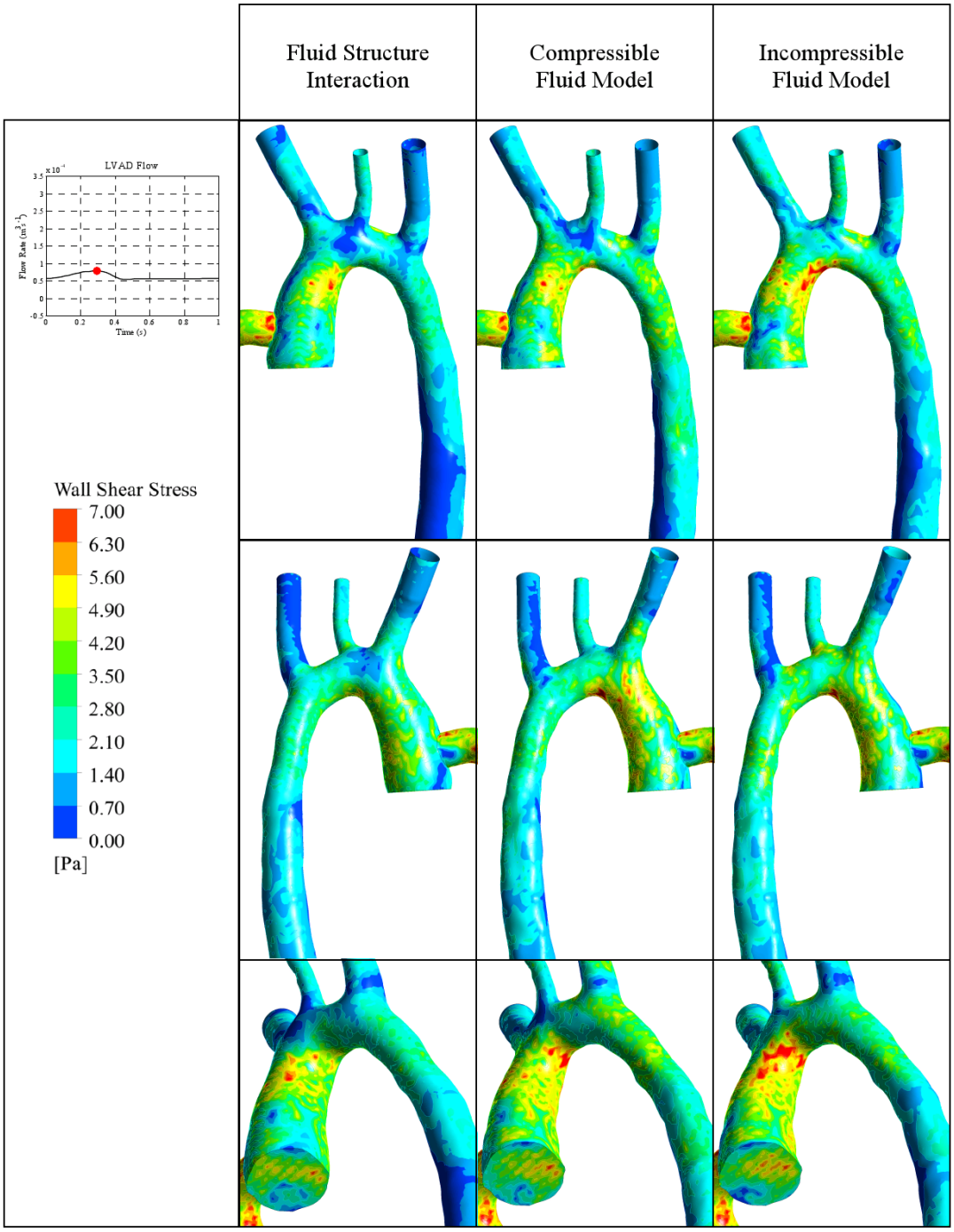

FIGURE 4-24 - COMPARISON OF WALL SHEAR STRESS AT PEAK FLOW
(FSI – LEFT, COMPRESSIBLE FLUID – MIDDLE AND INCOMPRESSIBLE FLUID – RIGHT)

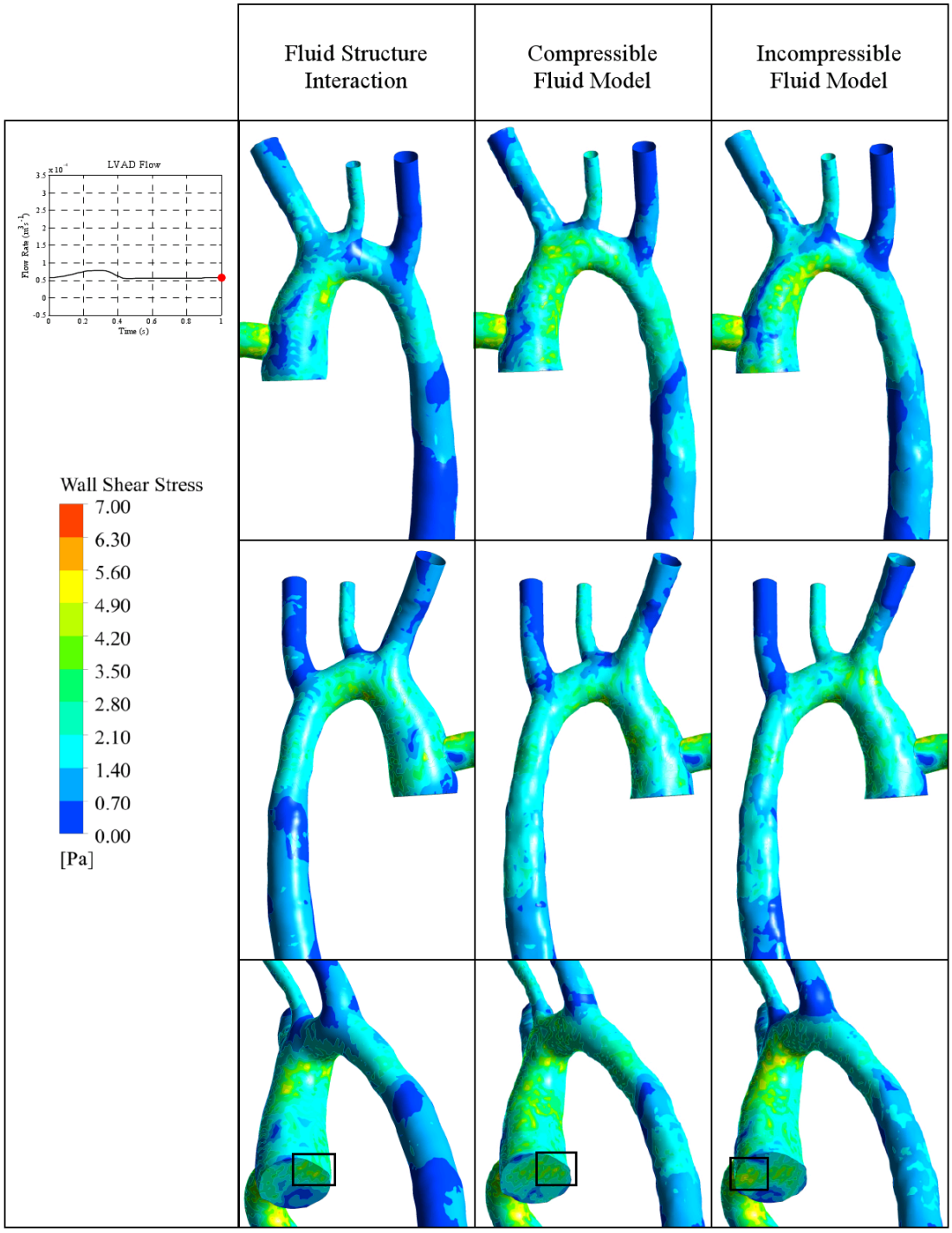

FIGURE 4-25 - COMPARISON OF WALL SHEAR STRESS AT THE END OF THE CARDIAC CYCLE (FSI – LEFT, COMPRESSIBLE FLUID – MIDDLE AND INCOMPRESSIBLE FLUID – RIGHT)

The HFI for each methodology, computed at three points in the cardiac cycle, is depicted in Figure 4-26. At each point in time, the HFI is greater than, or at the upper bound of, the range reported by Morbiducci *et al.* for healthy individuals [66]. This is perhaps unsurprising since there is a significant amount of swirl generated as the jet of blood leaving the cannula is propelled against the aortic wall. The compressible fluid model produces a better prediction of the FSI HFI than the incompressible fluid model, suggesting that the helical nature of the flow field is more accurately captured by the compressible fluid. Of course, a limitation of the HFI is that it is a domain averaged measure and so, although two systems may have the same value of HFI, they may have quite different internal flow structures.

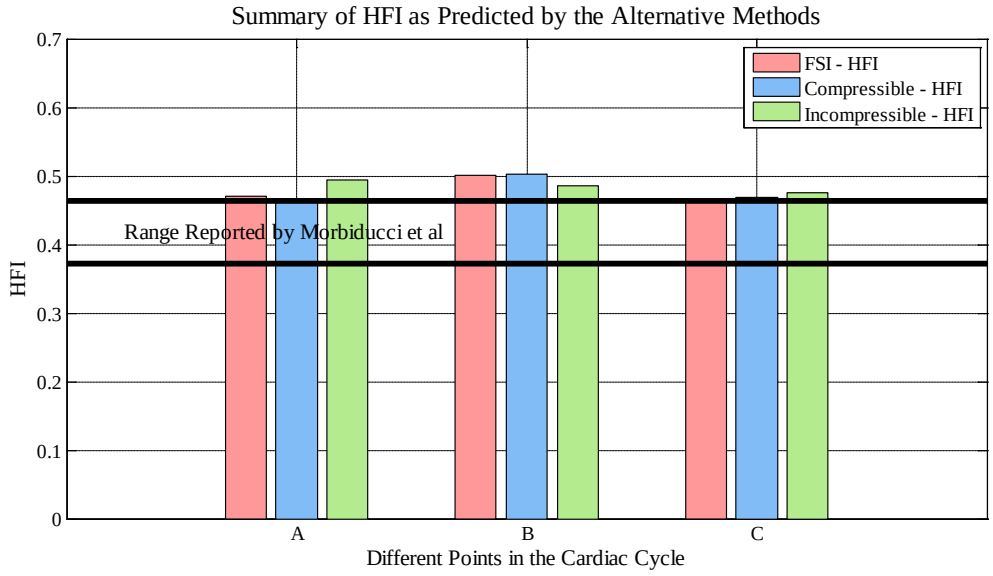

FIGURE 4-26 - COMPARISON OF HFI AS PREDICTED BY EACH CFD METHODOLOGY AT A NUMBER OF POINTS IN THE CARDIAC CYCLE: INCLUDING THE RANGE REPORTED FOR A HEALTHY AORTA BY MORBIBUCCI ET AL.
(A = PEAK FLOW, B = MINIMUM FLOW, C = END OF CYCLE.)

In an attempt to identify whether this is the case in the assisted aorta, a comparison of the particle path-lines is depicted in Figure 4-27. A grid of 10x10 massless particles were released from the cannula inlet at the start of a cardiac cycle and followed through the fluid domain over time. As one would expect, the path-lines demonstrate that all three methodologies predict similar structures within the flow field. A chaotic region is apparent in the ascending aorta where the blood impacts onto the aortic wall, while downstream, through the arch and in the descending aorta,

the flow becomes more ordered (Figure 4-27). It is also apparent from the path-lines that the compressible fluid model better approximates the distribution of particles to the upper branches.

The residence times for particles seeded from the inlet of the cannula (30x30 grid) are summarised in Table 4.8. All three methodologies are in close agreement, with a maximum difference of less than 2.5% in each case. The trends in residence time are consistent with those of velocity; the compressible fluid model generally under-predicted the peak velocities (Figure 4-22) and consequently the maximum residence time is greater.

	FSI	Compressible Fluid	Incompressible Fluid
Max Residence time (s)	1.918	1.962	1.952
Average Residence Time (s)	0.793	0.776	0.782

TABLE 4.8- SUMMARY OF RESIDENCE TIME.
COMPARISON OF CFD METHODOLOGIES

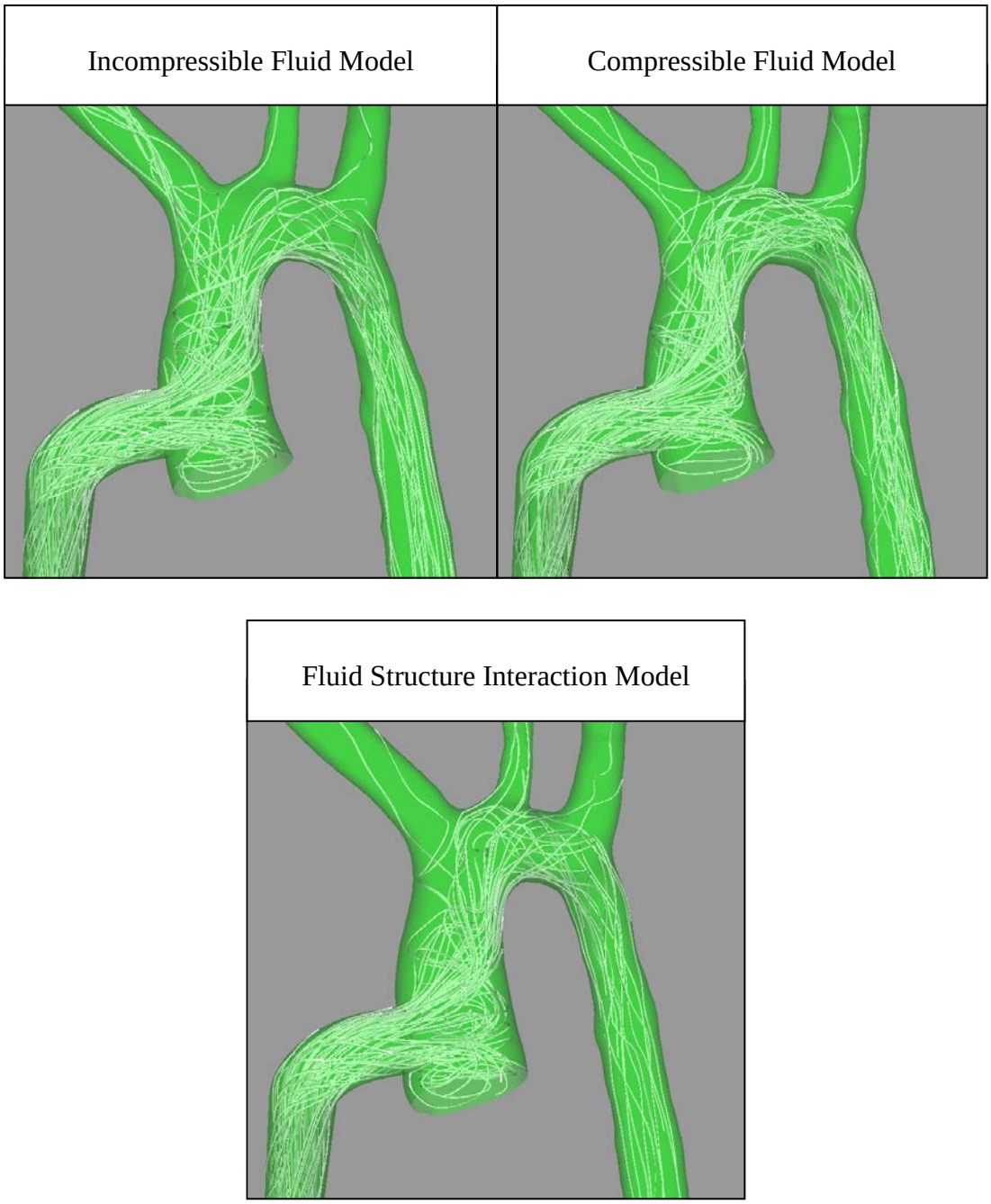

FIGURE 4-27 – COMPARISON OF MASSLESS PARTICLE PATH-LINES, RELEASED FROM THE CANNULA INLET, IN EACH OF THE METHODOLOGIES (10X10 GRID OF PARTICLES RELEASED).

A final comparison of the three methodologies employs an isosurface at peak flow (Figure 4-28). The isosurface illustrates regions of the flow field where the fluid velocity is $0.85\ ms^{-1}$. The surfaces are comparable in all cases, with the incompressible fluid predicting larger regions of high velocity fluid than the

compressible and FSI models. This is to be expected and further demonstrates that the compressible fluid model is a useful approximation for the more computationally demanding FSI simulation.

The isosurfaces also illustrate why the maximum values of wall shear stress are not located opposite the anastomosis. The fluid entering the aorta has a significant degree of swirl, causing the jet of blood to disperse and sending the higher fluid velocities towards the lesser curvature of the aortic arch (Figure 4-28). This effect is likely to be further enhanced by the fluid recirculating in the region of the aortic valve (Figure 4-27).

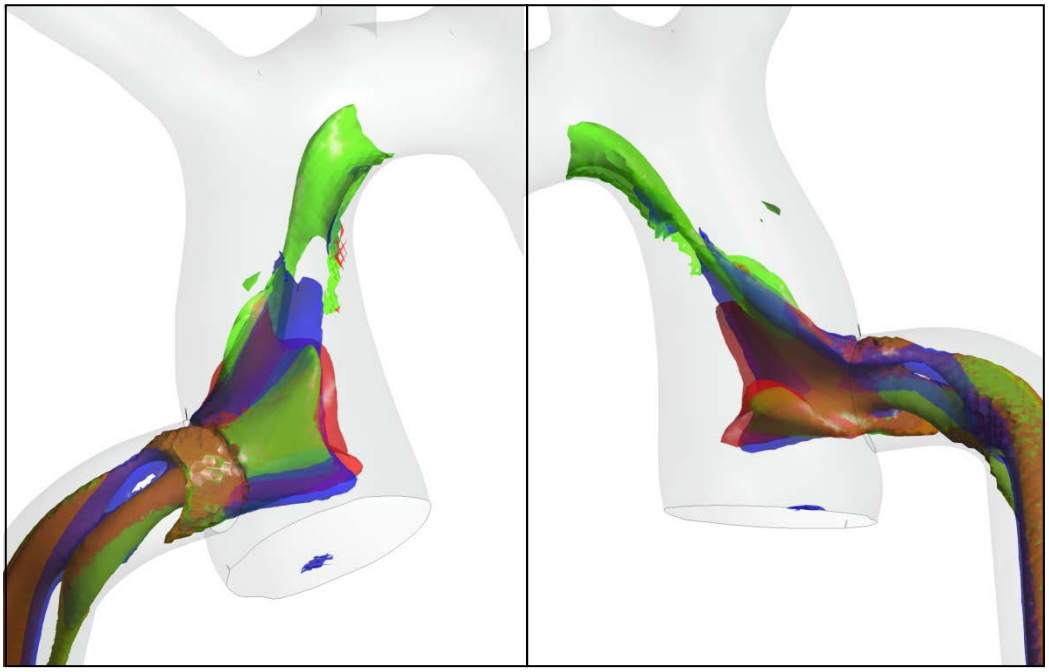

FIGURE 4-28- ISOSURFACE OF VELOCITIES GREATER THAN 0.85 MS^{-1} AT PEAK FLOW (RED – FSI, BLUE – COMPRESSIBLE FLUID AND GREEN – INCOMPRESSIBLE FLUID)

CONCLUSIONS 4.6

Three CFD methodologies, of varying levels of complexity, were evaluated in; a cylindrical vessel, a native patient-specific aorta and a patient-specific aorta under left ventricular support. The results were compared and considered for potential clinical practicality.

In all cases investigated the compressible fluid model, tuned to produce the desired wave speed, was able to capture the gross effects of the propagating waves that could not be predicted by the standard incompressible fluid simulation and with a much reduced computational overhead than a full FSI analysis.

In the cylindrical vessel, the compressible fluid model accurately predicted the time-lag associated with the propagating waves but was unable to capture fully the reflection characteristics of the FSI simulation. This resulted in different predicted forms for the inlet pressure wave. In both the compressible and FSI simulations the apparent wave speed, computed from the propagating pressure waves, was significantly lower than the fundamental wave speed. A brief analytical investigation demonstrated that the apparent wave speed is in fact dependent on not only the material properties of the vessel and the fluid but also on the relative magnitude of the backward travelling waves and on time. However, in the context of aortic simulations, where the wavelength is long compared to the length of the domain, it was shown that the apparent wave speed can be assumed constant throughout the domain.

In the patient-specific aorta all analysis strategies produced similar pressure and flow waves, suggesting that the magnitude and form of these waves are not significantly dependent on the compliance of the aortic wall. This is in contrast to the results from the cylindrical vessel and may be due to the curved and tapered geometry of the aorta. The predicted waveforms from the compressible fluid model were closer to those obtained from the full FSI analysis than to those produced by the more common incompressible fluid analysis. Both rigid walled models over-estimate the magnitude of the wall shear stress during systole but were able capture the relative distribution.

The assisted aortic flow field has a relatively small degree of pulsatility and as such the pressure and flow waveforms were extremely well-predicted by all three methodologies. However, the incompressible fluid was found to predict poorly the degree of helical flow within the domain, when compared to the FSI analysis. Peak values of wall shear stress were in close agreement for all models but the averaged wall shear stresses were over-estimated in the rigid walled simulations. As in the

native aorta the relative distribution of wall shear stress was captured by the rigid models with the compressible fluid analysis resulting in the closest approximation of the FSI simulation.

In general, the compressible fluid analyses, by capturing the gross dynamics of the propagating waves, were able to produce reasonable approximations of the pressure and flow waveforms when compared to the *'Gold Standard'* FSI results (especially in the physiological geometries). Although the magnitudes of peak and averaged wall shear stresses were generally over-estimated the relative distributions were well approximated. These results suggest the compressible fluid methodology may offer a computationally viable alternative to a full FSI model for diagnosis and, in particular, for interventional planning where the analysis of multiple options is required.

CHAPTER 5

LAMINAR VS. TURBULENT

MOTIVATION 5.1

A long-standing question, when considering the 3D simulation of aortic haemodynamics, is whether a turbulence model is required to predict accurately the flow field. If one considers the results presented in Chapter 2, where systems with a peak Reynolds number of 3500 are shown to require a turbulence model, it might be concluded that a turbulence model is important in the aorta where the Reynolds numbers fall above this threshold [75]. However, the FDA benchmark is an idealised geometry with features that are known to create complex flow structures (for example a sudden expansion), while the curvature of the aorta has a stabilising effect [99]. However, it is worth noting that if there is significant torsion in the aortic geometry, this will have a destabilising effect on the flow [100, 101]. Additionally, the flow waveform in a healthy aorta is pulsatile, whereas the FDA benchmark is a steady state system. Turbulence requires time to develop and so it is not clear

whether the turbulent structures would have time to form in a healthy aorta with pulsatile flow.

To illustrate the divided opinion within the scientific community Table 5.1 contains a summary of the most recently published papers that predict aortic haemodynamics for both healthy and diseased cases. Until 2009 no groups used a turbulence model to simulate aortic flows. Since then there has been a difference of opinion, with approximately one third of authors reporting the use of a turbulence model. Tan *et al.* conducted a detailed analysis of transient laminar and turbulent simulations, compared to *in vivo* flow measurements in an aortic aneurysm [102]. This group demonstrated that the transitional variant of the shear stress transport (SST) turbulence model gave a better correlation to the observed flow field than the laminar model. In an assisted aorta, Kaufmann *et al.* showed that a steady state SST model was able to capture the flow field to an accuracy of 10%, when compared to their *in vitro* study [103, 104]. The use of a turbulence model agrees with the experimental study published by Minakawa *et al.*, where different cardiopulmonary bypass cannula designs were compared and turbulence was always apparent in the aorta [17]. Feinstein *et al.* investigated alternative intervention options in a patient with aortic coarctation and were able to circumvent the potential requirement for a turbulence model by performing a direct numerical simulation [62]. The numerical results were compared to *in vivo* data of flow and area change, with the model producing a reasonable approximation. In truth, the application of a direct numerical simulation (DNS) is the ideal solution. However, to conduct a DNS Feinstein *et al.* employed 2,208 computational cores, this is far beyond the computing resources available to most researchers.

Table 5.1 includes information on the number of elements used to discretise the fluid domains. It is emphasised that this information be viewed with caution, since information as to the accuracy of the different element formulations was not always available in the literature and thus is not included.

Geometry	CFD Code	Steady/ Transient	Reynolds Number	Laminar/ Turbulent	Number of Elements	Author & Date
Assisted Aorta	ANSYS-CFX v12.0	Transient	2230 (mean) 2550 (peak)	SAS-SST	3.2 million	Brown et al. 2012
Thoracic Aorta	ANSYS-CFX v12.0	Transient	1037 (mean) 5833 (peak)	Laminar	500,000	Brown et al. 2012
Idealised Aorta: Healthy and assisted	Fluent v6.3	Both	1140 (mean healthy) 6155 (mean assisted)	SST	350,000	Benim *et al.* [105] 2011
Assisted Aorta: Cardio bypass	ANSYS-CFX v12.0	Steady	10^3	SST	700,000	Stühle et al. [18] 2011
Aortic Coarctation: Pre and Post surgery	Non-commercial	Transient	Not stated	DNS	2 million	Feinstein *et al.* [62] 2011
Idealised: Aortic Coarctation	Fluent v6.3	Both	Not stated	k-ω model	450,000	Kadem *et al.* [106] 2011
Aortic Dissection	ADINA v8.6	Transient	2866 (peak)	Laminar	115,000	Tse *et al.* [107] 2011
Assisted Aorta	ANSYS-CFX v12.0	Transient	970 (peak asc) 1582 (peak desc)	Laminar	1.6 million	Brown *et al.* [16] 2011
Healthy Aorta	Fluent	Both	Not stated	Laminar	Not stated	Liu *et al.[108]* 2011
Aortic Dissection:	Fluent	Transient	Not stated	Laminar	Not stated	Karmonik *et al.* [109]

Pre and Post Stent Graft						2011
Thoracic Aorta	Non - commercial	Transient	Not stated	Laminar	110,000	Moireau *et al.* [60] 2011
Thoracic Aorta	ACE +	Transient	1315 (mean)	Laminar	98,000	Wen *et al* [95] 2010
Aortic Dissection	ANSYS-CFX v11	Transient	3150 (peak) 1230 (mean)	SST	2.7 million	Xu *et al.* [110] 2010
Assisted Aorta	Star CCM+ v3.04	Steady	Not Stated	Laminar	Not stated	Osorio *et al.* [111] 2010
Thoracic Aortic Aneurysm	ANSYS-CFX v11	Transient	400-4000 (mean 1000)	Laminar & SST	1.9 million	Tan *et al.* [102] 2009
Assisted Aorta	ANSYS-CFX v11	Steady	Not Stated	SST	4.5 million	Kaufmann *et al.* [104] 2009
Healthy Aorta and Aortic Coarctation	Non-commercial	Transient	Not Stated	Laminar	1.9 million 2.6 million	Kim *et al* [61] 2009
Assisted Aorta	Non-commercial	Transient	Not Stated	Laminar	45,000	Bazilevs *et al.* [63] 2009
Thoracic Aorta	ADINA	Transient	Not Stated	Laminar	77,000	Markl *et al.* [112] 2008
Assisted Aorta	Acusolve	Steady	Not Stated	Laminar	1.5 million	Tokuda *et al.*[113] 2008

TABLE 5.1 – SUMMARY OF AORTIC SIMULATIONS PUBLISHED IN THE LAST 3 YEARS

In the following chapter the turbulent question is explored in both a native and an assisted aortic geometry. Steady state simulations are employed to conduct mesh sensitivity studies under peak flow conditions, with the understanding that this is a 'worst case' scenario. The converged meshes are subsequently used in a transient analysis to evaluate the influence of a turbulence model on a pulsatile flow field.

This approach is clearly valid in the assisted case where the LVAD flow waveform is close to steady state. However, it is acknowledged that the use of a steady state simulation is a simplification in the native case, where the period of turbulence, if present, is likely to be short.

All steady state turbulent simulations employ the transitional variant of the SST which was shown in Chapter 2 to produce good approximations for flows with similar Reynolds numbers. It is also the turbulence model of choice for aortic simulation (Table 5.1). The transient turbulent simulations all employ the SAS version of the transitional SST model. Once again, this model performed well in the FDA benchmark (Chapter 2) and has been shown to produce good agreement with experimental data when used to solve the flow field in a stenosed vessel [114].

NATIVE AORTA – STEADY STATE 5.2

The patient-specific aortic geometry, described in Chapters 3 and 4, is employed in the following work. In an attempt to isolate the effects of the chosen numerical model the simplest CFD methodology, a rigid walled incompressible fluid simulation, is used. The rigid walled assumption was shown, in Chapter 4, to have a relatively small effect in the native aorta model and an even smaller influence in the assisted case.

MODEL CONSTRUCTION 5.2.1

Steady state simulations are performed at peak flow with an evenly distributed velocity profile applied at the inlet, corresponding to a mass flow rate of 0.349 kg/s. Flow boundary conditions are applied to the outlets of the supra-aortic arteries, with the distribution extracted from clinical flow data (Table 5.2). To ensure the problem

is not over constrained a constant pressure of 65.12 mmHg (corresponding to the clinical pressure at peak flow) is applied at the descending aorta outlet.

	BCA	LCC	LSUB
Flow Distribution	0.24	0.08	0.12

TABLE 5.2 – FRACTION OF FLOW DISTRIBUTION TO THE UPPER BRANCHES

The peak Reynolds number in the system is approximately 5800 and occurs in the ascending aorta.

MESH CONSTRUCTION 5.2.2

ICEM CFD (ANSYS, Canonsburg, PA, USA) is used to spatially discretise the fluid domain. Tetrahedral elements are used in the core of the fluid domain with prism elements employed at the wall, to improve the resolution of the boundary layer.

Three computational meshes are created using a global scaling factor, which altered the maximum element edge length but did not affect the thickness, perpendicular to the wall, of the prism layer. A summary of the native aorta meshes is shown in Table 5.3.

Mesh Name	Number of Elements	Max Element Edge Length (m)	Max Element Volume (m^3)
NA-1	236,234	$1.5x10^{-3}$	$2.43x10^{-9}$
NA-2	1,418,809	$0.75x10^{-3}$	$3.81x10^{-10}$
NA-3	9,782,501	$0.375x10^{-3}$	$8.28x10^{-11}$

TABLE 5.3 – MESH INFORMATION FOR THE NATIVE AORTA

As in the FDA benchmark the distance from the aortic wall to the first computational node (y) is defined such that the y^+ value is less than 2 (in the native aorta y = 0.097 mm), thereby ensuring the requirements of the turbulent wall functions are met. Six prism layers were defined with an expansion ratio of 1.2. The number of

layers and the expansion ratio are chosen to ensure that the tetrahedral mesh does not become overly distorted in the branching vessels where the radius is small.

STEADY STATE LAMINAR 5.2.3

The two finest steady state laminar simulations failed to achieve the pre-defined convergence criteria. This phenomenon was also seen in the FDA benchmark and is attributed to transient features developing in the flow field, which are not resolved by the spatial resolution of NA-1.

STEADY STATE SHEAR STRESS TRANSPORT 5.2.4

All computational meshes achieved the required convergence criteria when solved using the steady state SST model. The centreline pressures and resulting solution of the Richardson's extrapolation method are compared in Figure 5-1. The largest deviation from the Richardson's solution is apparent in NA-1, with a mean and maximum relative error of 0.60 and 2.82. This demonstrates that all simulations produce mesh converged results in terms of the pressure distribution.

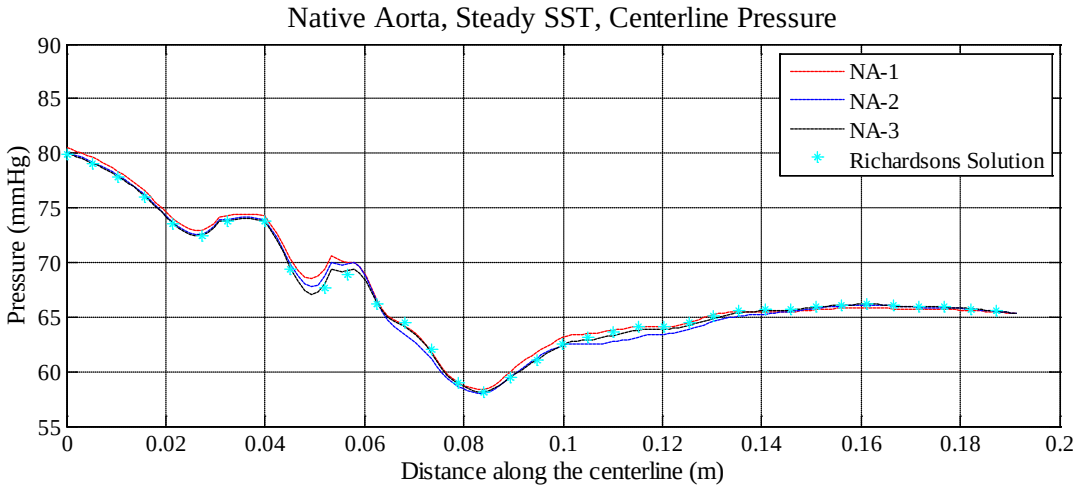

FIGURE 5-1 – CENTRELINE PRESSURE, NATIVE AORTA, STEADY SST

The peak and domain averaged values of velocity vary by a maximum of 4.41%, while the peak magnitudes of wall shear stress show more significant variation (Figure 5-2). The coarse meshes under-predict the peak wall shear stress by 36.9% and 23.8%, illustrating that although NA-1 and NA-2 accurately capture the pressure and general trends of velocity they cannot be considered converged if the parameter

of interest is the maximum value of wall shear stress (Figure 5-2). Analysis of the wall shear stress distribution, in NA-3, illustrates a local region of high wall shear on the inner curvature of the aortic arch, which is not accurately captured by NA-1 or NA-2 (Figure 5-3). However, neglecting this region, NA-2 produces comparable magnitudes and distributions of wall shear stress, while NA-1 shows larger discrepancies, especially in the descending aorta, on the inner curvature of the aortic arch and around the bifurcation to the left subclavian artery. In the context of this thesis mesh NA-2 is considered to be mesh converged and is used in the transient comparisons.

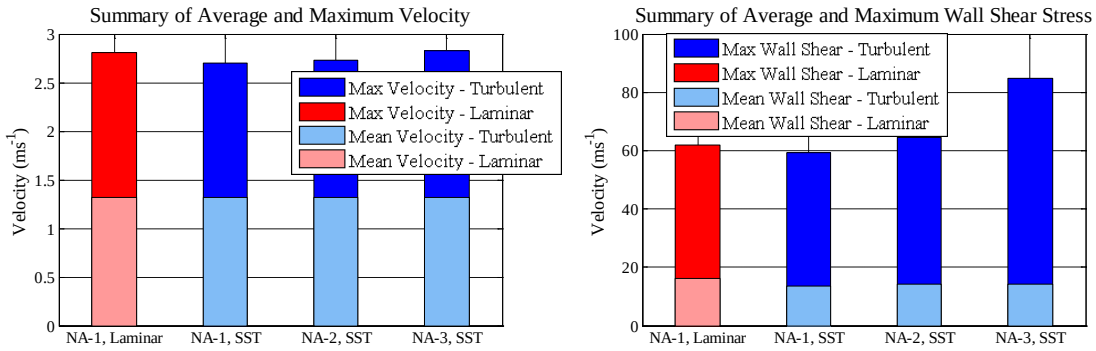

FIGURE 5-2 - COMPARISON OF THE MEAN AND MAXIMUM VELOCITY AND WALL SHEAR STRESS, AS COMPUTED BY THE DIFFERENT MESHES AND MODELS IN THE NATIVE AORTA.

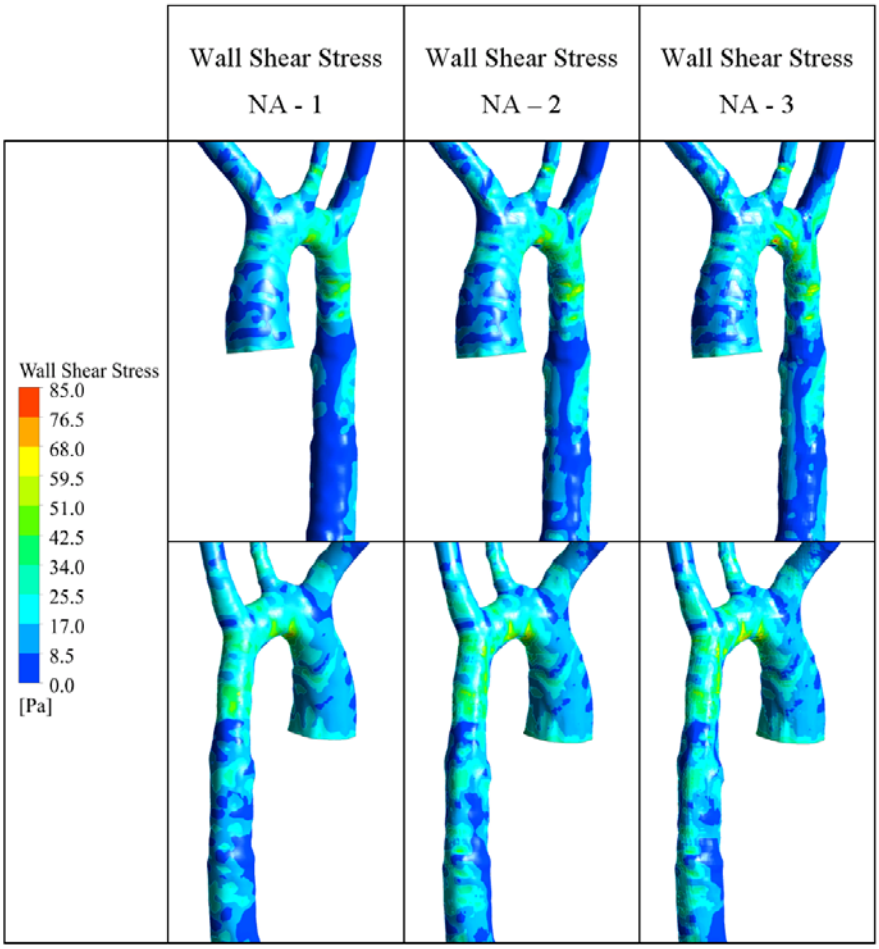

FIGURE 5-3 - COMPARISON OF WALL SHEAR STRESS DISTRIBUTION, NATIVE AORTA, SST (THE POOR RENDERING OF NA-3 OCCURS DUE TO THE LARGE NUMBER OF ELEMENTS)

STEADY STATE: LAMINAR VS. TURBULENT 5.2.5

Although only the coarse mesh produced numerically converged results when using the steady laminar model, a comparison of the laminar and turbulent results is included (Figure 5-2, Figure 5-4 and Figure 5-5). Both models predict a similar trend in the centreline pressure (Figure 5-4).

The laminar model predicts a pressure in the ascending aorta of 83.86 mmHg compared to 80.1 mmHg in the turbulent simulation; a difference of 4.5%. However, since the outlet pressure is prescribed and has no influence on the flow field (except to act as a reference pressure), a more realistic comparison of the methods is to consider the pressure drop across the domain, in which case the discrepancy is larger with the laminar model predicting a 25% greater pressure drop. The peak and

domain averaged velocities are more closely matched with a maximum difference of 3.7% (Figure 5-2).

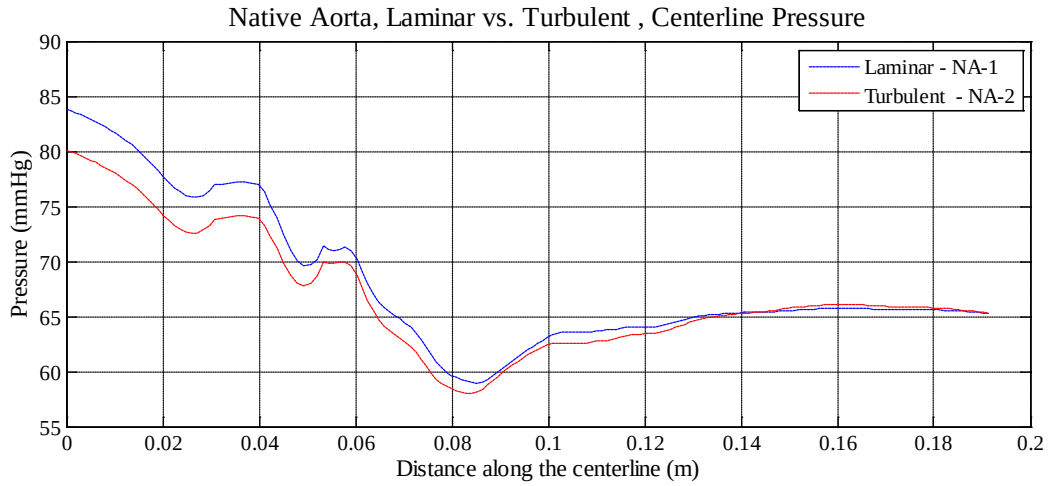

FIGURE 5-4 – COMPARISON OF LAMINAR AND TURBULENT CENTRELINE PRESSURE, NATIVE AORTA

Comparison of the velocity contours (Figure 5-5), at a number of planes along the aorta, show that both the laminar and turbulent simulations are in agreement as the fluid moves through the ascending aorta but the flow field predictions begin to diverge in the descending aorta. The contours are orientated such that the right hand side of the plane corresponds to the inner surface of the aortic arch. At plane H the turbulence model predicts the development of two secondary flow structures, while the laminar model resolves only one structure. Further investigation shows that this is due to the spatial resolution of NA-1 (only one secondary structure is observed in NA-1 when using the SST model) and it could be these complex structures that result in the laminar models, with a finer spatial resolution, failing to converge.

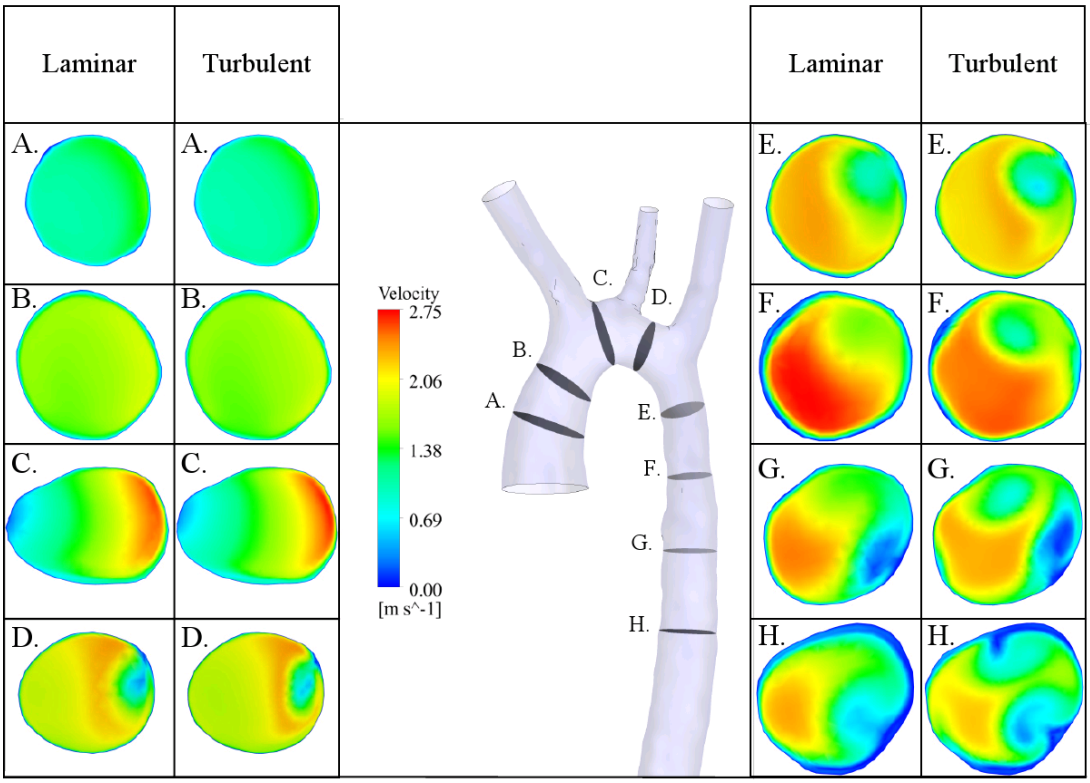

FIGURE 5-5 - COMPARISON OF PLANAR VELOCITY CONTOURS AS PREDICTED BY THE STEADY STATE LAMINAR (NA-1) AND TURBULENT (NA-2) SIMULATIONS, AT PEAK FLOW.

At this point it is important to remind oneself that these results consider the worst case scenario and in truth these flow rates only occur for a short period during systole. It is suggested that there are two important questions that remain unanswered:

1. Under pulsatile conditions is the period of high flow sufficient for transitional or turbulent structures to develop in the aorta?
2. Is a turbulence model appropriate for the periods of the cardiac cycle when the flow is in the laminar regime?

In an attempt to address the second point, i.e. whether the SST model is able to accurately capture a laminar flow field, a steady state simulation was performed at a peak Reynolds number of approximately 1150. This corresponds to one fifth of the peak cardiac flow rate and is within 10% of the average flow rate over the cardiac cycle. Mesh NA-2, which was shown to produce mesh independent results at peak flow, was used. In this case the laminar model converged and is considered the

'correct' solution, enabling us to quantify the error associated with using the SST model to compute a laminar flow field.

The centreline pressures are compared in Figure 5-6. The greatest variation is apparent in the ascending aorta. The difference in the predicted pressure drop across the aorta is 0.1mmHg (less than 10% of the total pressure drop). The centreline pressures show the same trend in the ascending aorta and become overlaid at approximately 0.08m along the aorta.

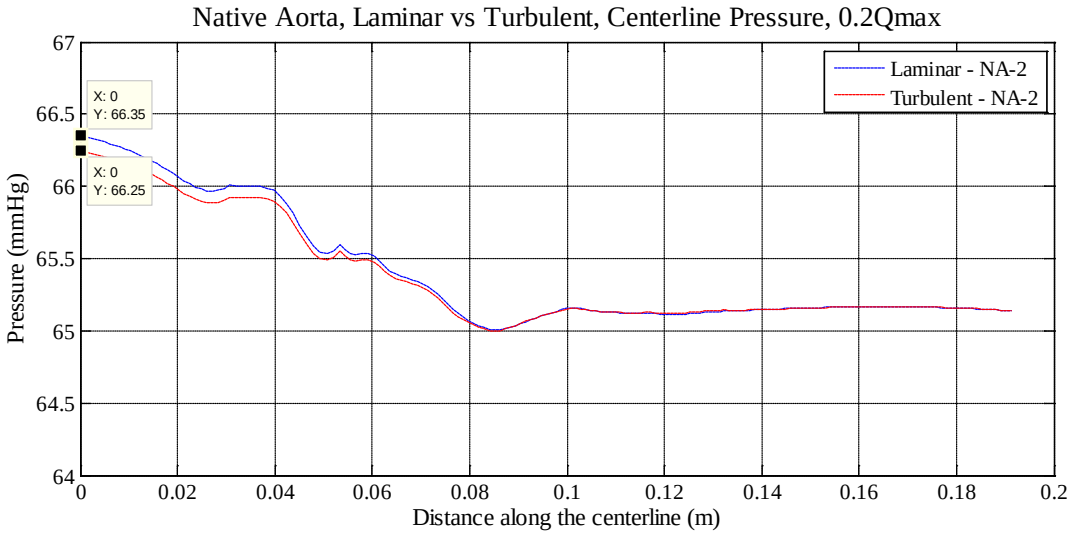

FIGURE 5-6- COMPARISON OF LAMINAR AND TURBULENT CENTRELINE PRESSURE, NATIVE AORTA AT ONE FIFTH THE PEAK FLOW RATE

Contours of velocity, at cross-sections along the aorta, are compared for the laminar and turbulent predictions under the reduced flow condition (Figure 5-7). The results clearly illustrate that, unlike the steady state simulations at peak flow, the laminar and turbulent model predict the same structures to occur at all points throughout the flow field. This clearly shows that the SST turbulence model is capable of capturing the characteristics of a laminar flow field as well as resolving any turbulent structures, as shown in Chapter 2 for the FDA benchmark case.

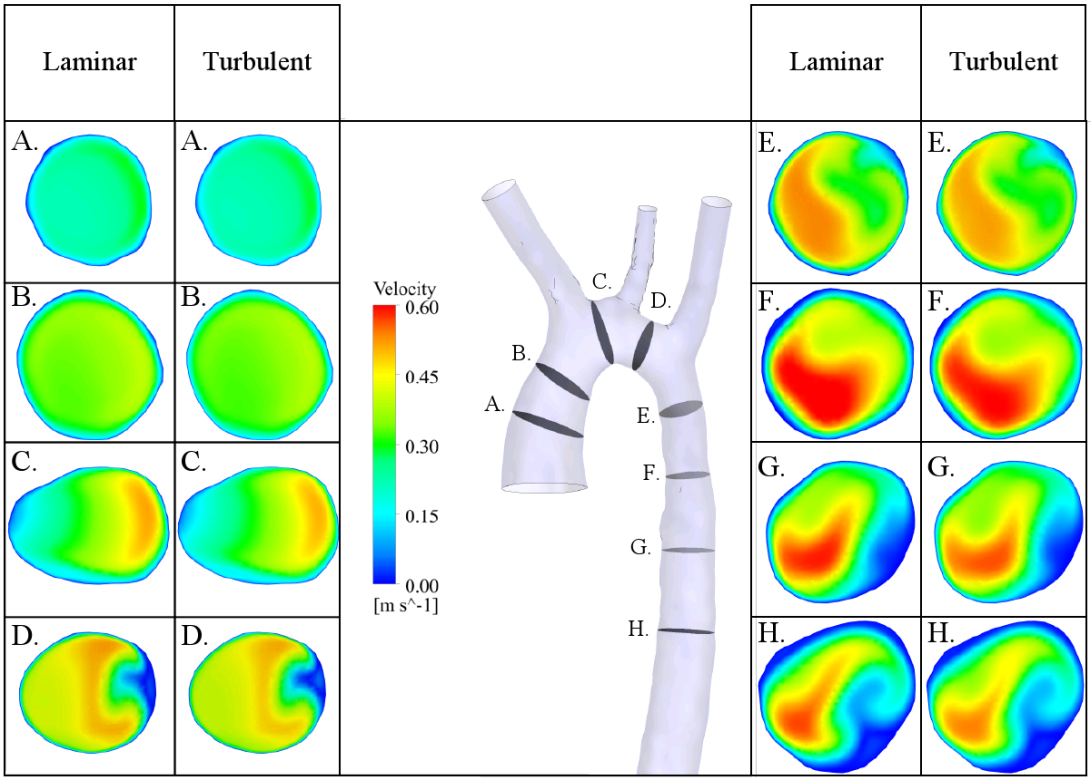

FIGURE 5-7 - COMPARISON OF PLANAR VELOCITY CONTOURS AS PREDICTED BY THE STEADY STATE LAMINAR AND TURBULENT SIMULATIONS, AT ONE FIFTH OF THE PEAK FLOW (NA-2).

NATIVE AORTA – TRANSIENT 5.3

It has been shown that under steady state conditions, the SST model is able to capture the characteristics of a laminar flow field (maximum Reynolds number of 1150) and that at peak aortic flow a turbulence model is required to produce numerically converged results. However, it is certainly not clear whether, in the physiological case, the period over which these large flow rates occur is sufficient for the development of transitional or turbulent structures.

MODEL CONSTRUCTION 5.3.1

To investigate this question the transient flow field was solved using the standard time-varying Navier-Stokes equations and the SAS-SST model described in Chapter 2. NA-2, which was shown to produce mesh independent results in the steady state analyses, is employed in the following investigation.

The transient models are setup as described in Chapter 4, with a prescribed flow rate enforced at the inlet and the outlet boundary conditions determined by tuned three element Windkessel models. An incompressible, rigid walled simulation with a time-step of 5ms is used.

TRANSIENT: LAMINAR VS. TURBULENT 5.3.2

Pressure and mass flow rates, at the model boundaries, are compared for the laminar and turbulent simulations (Figure 5-8). In general the magnitude and form of the pressure and mass flow waves are very closely matched, with the greatest variation apparent in the ascending aortic pressure. As demonstrated in the steady state case this does not mean that the computed internal flow structures are the same in both the laminar and turbulent simulations. Velocity contours, at three points in time, on planes along the aorta (located as shown in Figure 5-5 and Figure 5-7) have been compared in Figure 5-9.

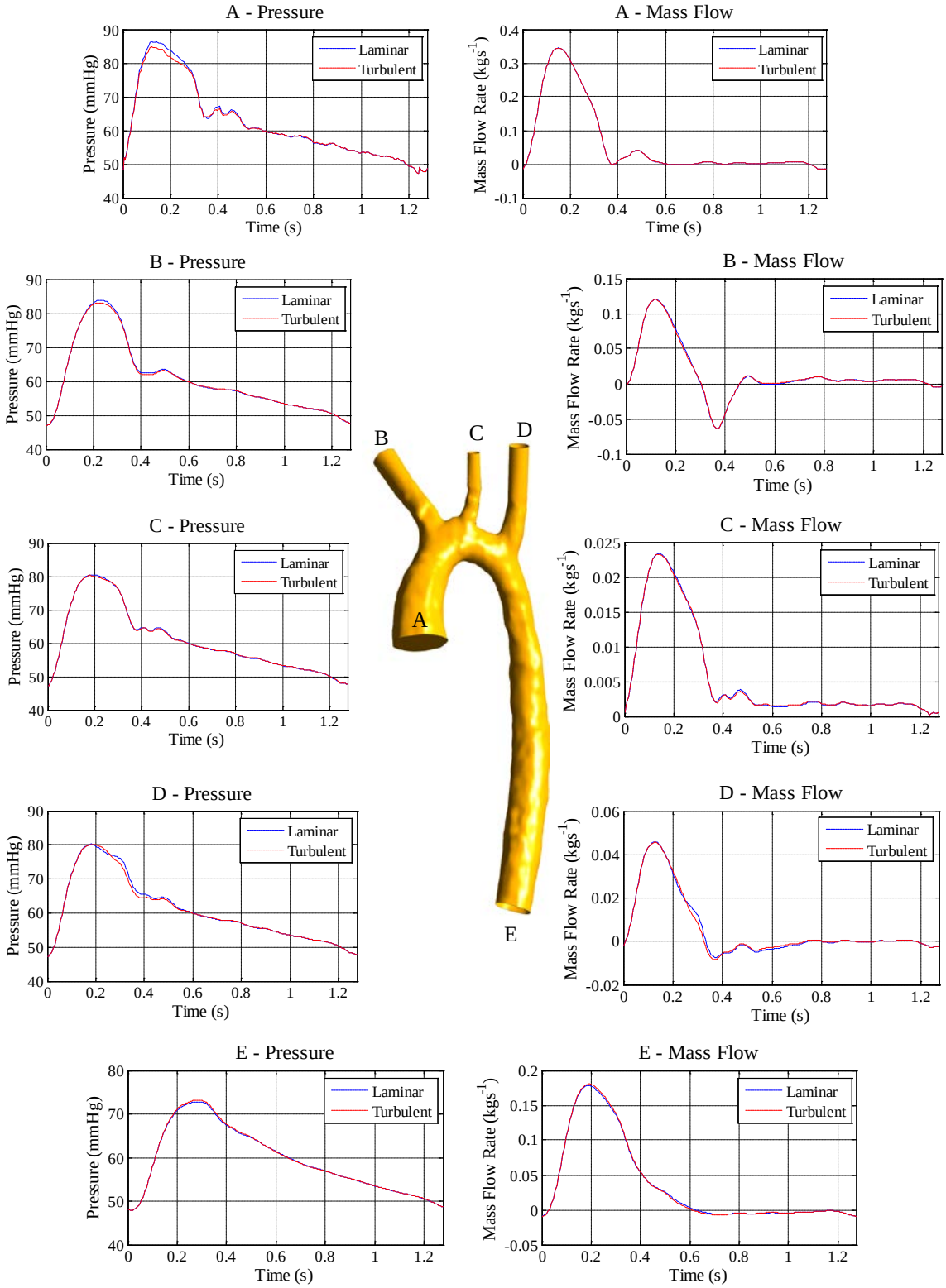

FIGURE 5-8 - COMPARISON OF PRESSURE AND MASS FLOW RATE IN THE NATIVE AORTA (BLUE – LAMINAR SIMULATION, RED – TURBULENT SIMULATION)

At peak systole the two numerical models are in close agreement, with high velocities predicted along the inner wall of the arch (Figure 5-9 – C) before the fluid detaches from the wall around the ductus diverticulum, resulting in a region of low velocity, recirculating fluid (Figure 5-9 - D). The laminar model computes a slightly larger region of low velocity fluid in this area when compared to the turbulent prediction. At late systole (0.3s), during the deceleration phase, the flow fields of the laminar and turbulent simulations show a slight variation as the fluid enters the descending aorta but in general the structures are comparable. The largest variation is apparent at mid diastole (0.95s). Plane A is the only contour which shows similar structures in both the laminar and turbulent simulation at this point in time. In the upper region of the descending aorta the laminar model computes an annulus of high velocity fluid with a low velocity core, while the turbulent model predicts a more evenly distributed profile (Figure 5-9 - E). Further downstream, the turbulence model computes a high velocity region near the centre of the cross-section, while the laminar model predicts a localised region of low velocity fluid (Figure 5-9 - G). It is worth noting that these differences are accentuated in the figure by the small velocity scale used to illustrate the velocity distribution at mid diastole.

To investigate the influence of this variation in the computed velocity fields during diastole the cycle averaged wall shear stress was calculated (Figure 5-10).

The use of a turbulence model results in a lower estimation of the peak cycle averaged wall shear stress by 18.6%, when compared to the laminar results. However, if the predicted distributions are considered, both the laminar and SAS-SST model produce very similar results. This is reinforced by a close agreement of the planar velocity contours during systole (Figure 5-9). As has been suggested throughout this thesis it is the accurate computation of the wall shear stress distribution which is considered to be of greatest importance, rather than the absolute values which we are arguably unable to draw meaningful conclusions from.

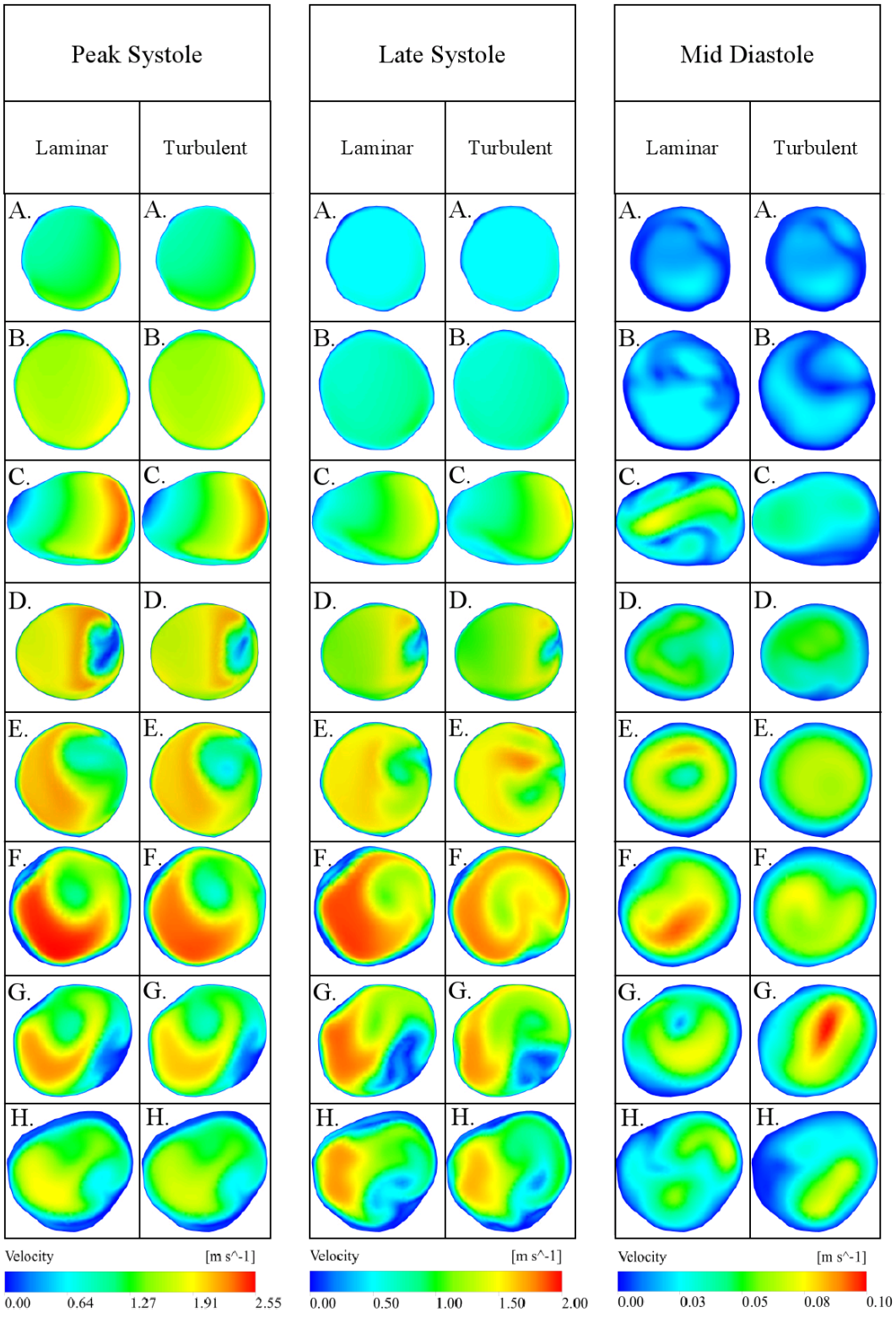

FIGURE 5-9 – COMPARISON OF PLANAR VELOCITY CONTOURS AS PREDICTED BY THE LAMINAR AND TURBULENT SIMULATIONS AT PEAK SYSTOLE (0.15S), LATE SYSTOLE (0.3S) AND MID DIASTOLE (0.95S).

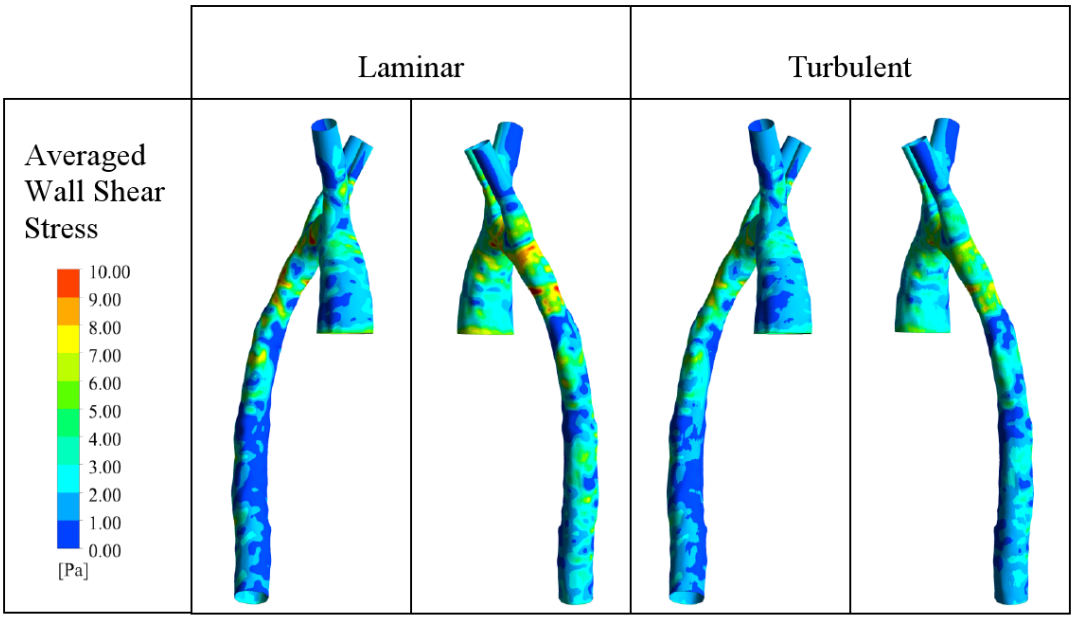

FIGURE 5-10 – CYCLE AVERAGED WALL SHEAR STRESS AS PREDICTED BY THE LAMINAR (LEFT) AND TURBULENT (RIGHT) NUMERICAL MODELS, NATIVE AORTA, NA-2.

Considering the results presented in Section 5.3 it is proposed that, when simulating aortic flow fields the SAS-SST turbulence model should be used. This model is able to capture the important characteristics of a laminar flow field, but more importantly, is able to compute the onset, if indeed there is an onset, of turbulence. This is extremely important in patients with high flow rates, geometrical abnormalities and under exercise conditions when the use of a numerical model which can span the laminar and turbulent regimes is vital.

ASSISTED AORTA – STEADY STATE 5.4

MODEL CONSTRUCTION 5.4.1

Unfortunately there is no clinical data available to inform the boundary conditions of the assisted aorta case. A pragmatic approach is taken, which uses the computational results from Chapter 4 to identify the relative distribution at peak flow. The resulting flow distributions (Table 5.4) are similar to those observed clinically (Table 5.2), which suggests that the use of Windkessel parameters, tuned to capture the correct flow distributions in the native system, is a valid method of describing the boundary

conditions in the assisted case. If the flow distributions were significantly altered *in vivo* one might expect the body's homeostatic systems, such as the cerebral autoregulation mechanism, to alter the downstream vessel impedance in an attempt to recover the required flow distribution.

	BCA	LCC	LSUB
CFD Flow Distribution	0.25	0.082	0.085

TABLE 5.4 - FLOW DISTRIBUTION TO THE UPPER BRANCHES, EXTRACTED FROM CFD RESULTS IN CHAPTER 4

Steady state simulations are performed at peak flow with the real INCOR LVAD velocity profile applied at the cannula inlet, corresponding to a mass flow rate of 0.084 kg/s. Flow boundary conditions are applied to the outlets of the great arteries, with the distributions computed as described previously (Table 5.4). The reference pressure, applied at the descending aorta boundary, is equal to the value used in the native case since it has only an additive effect on the computed pressure and does not influence the flow field.

The peak Reynolds number in the cannula is approximately 2550.

MESH CONSTRUCTION 5.4.2

Meshes for the assisted aorta are constructed as for the native aorta, with the distance to the first node, to ensure a y^+ value of less than 2, calculated as 0.075 mm. A summary of the computational meshes is included in Table 5.5.

Mesh Name	Number of Elements	Max Element Edge Length (m)	Max Element Volume (m^3)
AA-1	380,999	$1.5x10^{-3}$	$2.633x10^{-9}$
AA-2	2,163,443	$0.75x10^{-3}$	$4.915x10^{-10}$
AA-3	14,132,236	$0.375x10^{-3}$	$1.178x10^{-10}$
AA-2.5	4,651,197	$0.5625x10^{-3}$	$2.427x10^{-10}$

TABLE 5.5 – MESH INFORMATION FOR THE ASSISTED AORTA

STEADY STATE LAMINAR 5.4.3

None of the steady state laminar simulations achieved the pre-defined convergence criteria, suggesting that the steady laminar model is not appropriate for the assisted aortic flow field.

STEADY STATE SHEAR STRESS TRANSPORT 5.4.4

The coarsest mesh, AA-1, failed to reach the pre-defined convergence criteria, with the RMS residuals of momentum in all three dimensions reaching a plateau at a value of $1x10^{-4}$. The two finer meshes did achieve the required criteria, suggesting that the spatial resolution of the coarse mesh is not sufficient to capture the complex features of the flow field.

In ANSYS-CFX it is possible to output the maximum residual values, which are visualised as an isosurface in Figure 5-11 (left – AA-1: SST, left and inset AA-1: Laminar). The regions encapsulated by the surfaces represent areas which did not reach the convergence criteria, with the different colours denoting the three directions of the momentum residuals. As might be intuitively expected, the problematic area is as the fluid moves through the anastomosis and encounters a feature similar to a sudden expansion (as seen in the FDA benchmark – Chapter 2). Velocity vectors, on a plane through the anastomosis, are compared in the unconverged (AA-1: SST) and converged (AA-2: SST) solutions (Figure 5-11). It is

apparent that the large residual values in AA-1 occur primarily in a region where two recirculation zones interact, which is an area of high velocity gradients.

If a set of residual isosurfaces are created for the steady state laminar simulation on mesh AA-1 the entire ascending aorta and aortic arch are filled with regions of unconverged momentum residuals (Figure 5-11 – left inset), providing further evidence against the use of a steady state laminar simulation to compute the flow field of an assisted aorta.

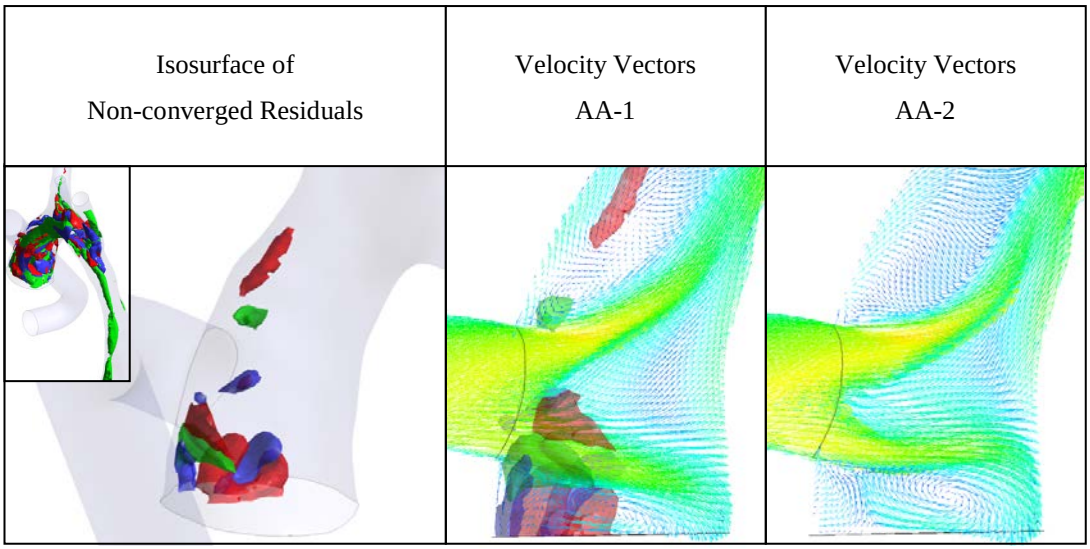

FIGURE 5-11 – ILLUSTRATION OF UNCONVERGED REGIONS OF THE SST (AND LAMINAR - INSET) AA-1 FLOW FIELD (LEFT) AND A COMPARISON OF THE VELOCITY VECTORS ON A PLANE THROUGH THE ANASTOMOSIS WITH AA-2 (RED = U-MOMENTUM, BLUE = V-MOMENTUM AND GREEN = W-MOMENTUM RESIDUAL)

The Richardson's extrapolation method requires the flow field solution for at least three mesh densities. In order to apply this method to the steady state SST model an additional mesh was produced with a maximum edge length of 0.5625 mm (halfway between that of AA-2 and AA-3). The mesh contained approximately 4.6 million elements (Table 5.5) and resulted in a numerically converged solution. The centreline pressures, predicted by the different meshes and the resulting Richardson's solution are compared in Figure 5-12. The maximum relative error was apparent in AA-2 with a value of 0.228, illustrating that all meshes are converged in terms of centreline pressures.

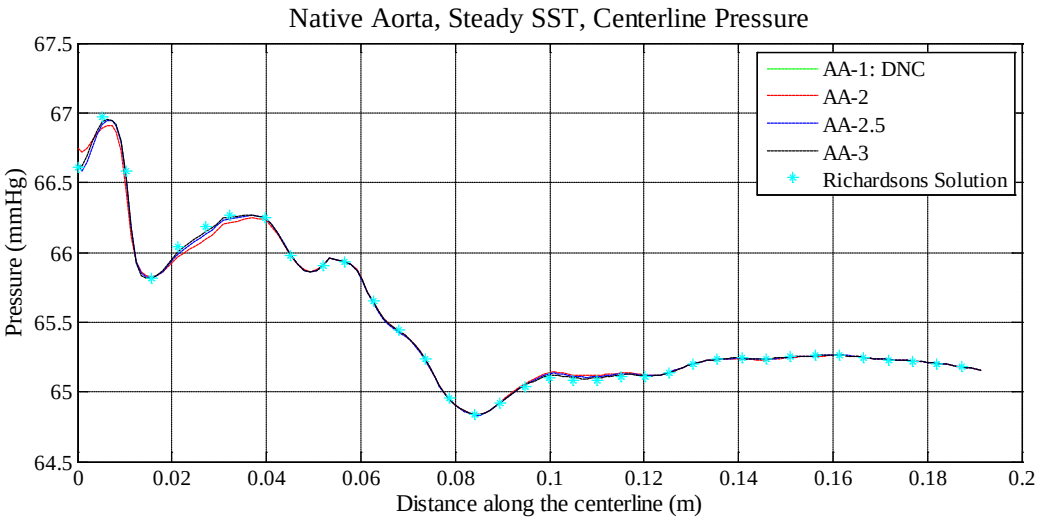

FIGURE 5-12 - CENTRELINE PRESSURE, ASSISTED AORTA, STEADY SST

The peak and domain averaged velocities are depicted in Figure 5-13 and demonstrates a good agreement across all the models, with a maximum percentage error of 0.98%. In the assisted aorta a key parameter of interest is wall shear stress, due to its role in the development of atheroma and vessel wall lesions. The peak and wall averaged shear stresses (Figure 5-13) and the predicted distribution, in the region of the anastomosis, are evaluated (Figure 5-14). Mesh AA-2 over predicts the peak wall shear stress by 6.53%, while the error in mesh AA-2.5 is just 0.53%.

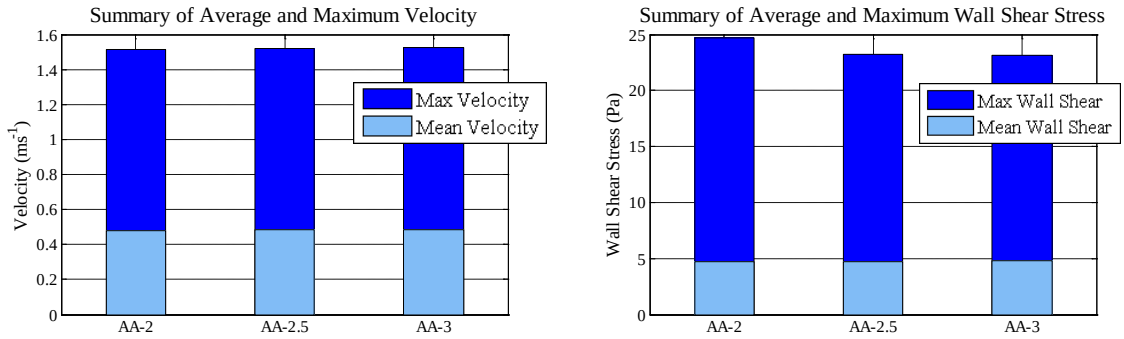

FIGURE 5-13 - COMPARISON OF THE MEAN AND MAXIMUM VELOCITY AND WALL SHEAR STRESS, AS COMPUTED BY THE DIFFERENT MESHES IN THE ASSISTED AORTA.

Analysis of the wall shear stress distribution shows that, although AA-2 over-predicts the peak wall shear stress, the general agreement between the three meshes is good (Figure 5-14). There are a number of low wall shear stress regions apparent around the aortic valve and in the ascending aorta, suggesting areas of flow

detachment which could be prone to atherosclerosis. However, it is worth noting that the real system is transient and so these regions of low wall shear stress may move throughout the cardiac cycle. If this is the case, parameters which capture this transient variation, such as the cycle averaged wall shear stress and oscillatory shear index (OSI), become important. OSI is not considered in this thesis as the primary focus is to simulate aortic haemodynamics in the presence of an LVAD, in which the flow field is relatively steady. However, for interest, OSI can be conceptualised as the period of the cardiac cycle during which the orientation of the instantaneous WSS is different from the average [16, 115].

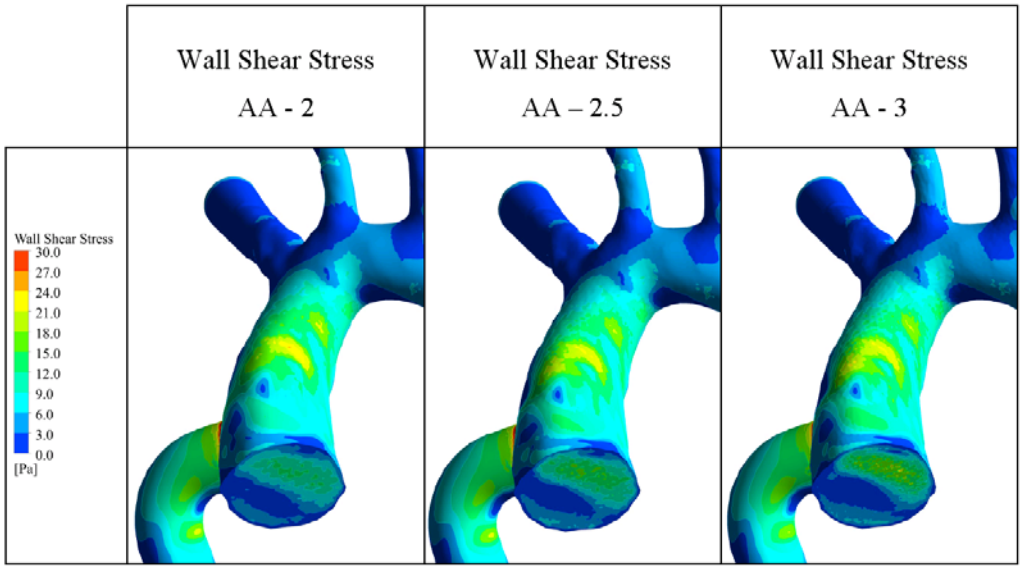

FIGURE 5-14 – COMPARISON OF WALL SHEAR STRESS DISTRIBUTION, ASSISTED AORTA, SST (THE POOR RENDERING OF AA-3 OCCURS DUE TO THE LARGE NUMBER OF ELEMENTS)

All numerically converged results accurately capture the centreline pressure, the global trends in velocity and the distribution of wall shear stress. Although AA-2 over predicts the peak value of wall shear stress by 6.53%, it is considered that all the numerically converged meshes accurately capture the flow field to a higher level of detail than with which we are currently able to analyse the results. Thereby all the meshes, excluding AA-1, are considered mesh converged and AA-2 will be used in the transient comparisons.

ASSISTED AORTA – TRANSIENT 5.5

MODEL CONSTRUCTION 5.5.1

The following transient simulations were conducted as described in Chapter 4. Windkessel elements describe the pressure at the outlet boundaries and a prescribed flow wave, in the form of a real LVAD velocity profile, is applied at the cannula inlet. An incompressible, rigid walled model is solved on mesh AA-2 and the predicted flow fields, when using a transient laminar and SAS-SST model, are analysed.

TRANSIENT: LAMINAR VS. TURBULENT 5.5.2

The predicted pressure and mass flow rates at the model boundaries are shown in Figure 5-15. The laminar model produces a greater amplitude and peak pressure at the inlet of the cannula, when compared to the turbulent simulation, with a peak and mean relative error (as described in Chapter 2) of 1.64 and 0.593, while the pressures at the descending aorta outlet are in closer agreement, with a peak and mean relative error of 0.154 and 0.003. The mass flow rate and pressure waveforms in the laminar case have an oscillating component which is most noticeable at the boundary to the LCC. The source of these oscillations is believed to be a result by the high Reynolds number flow. The grid resolution is such that the laminar model resolves some of the larger turbulent structures, producing what appears to be chaotic flow in the aorta. This is further support of the results presented in Chapter 4, where the flow field predictions on a mesh of lower spatial resolution have no such oscillations. It is suggested that the LCC suffers most noticeably because there is a smaller volume of fluid in the branch and so the inertia of the fluid is smaller resulting in more apparent oscillations. However, it is felt that the general agreement, in terms of pressure and mass flow rate, is reasonable.

The maximum and domain averaged velocities are evaluated at three points in the cardiac cycle; the start of the cardiac cycle, at peak flow and at minimum flow (Figure 5-16). The laminar and turbulent simulations produce similar trends in velocity with a maximum variation of less than 5% occurring in the mean velocity at

peak flow. The variation in wall shear stress is more pronounced, with a difference of 17.5% at peak flow. As discussed previously this may be within the limits of our ability to interpret these results (Figure 5-16). However, evaluation of the wall shear stress distribution, at peak flow (Figure 5-17), demonstrates that it is not just a difference in the maximum value, but that the predicted distributions are also different when using a laminar or turbulent numerical model.

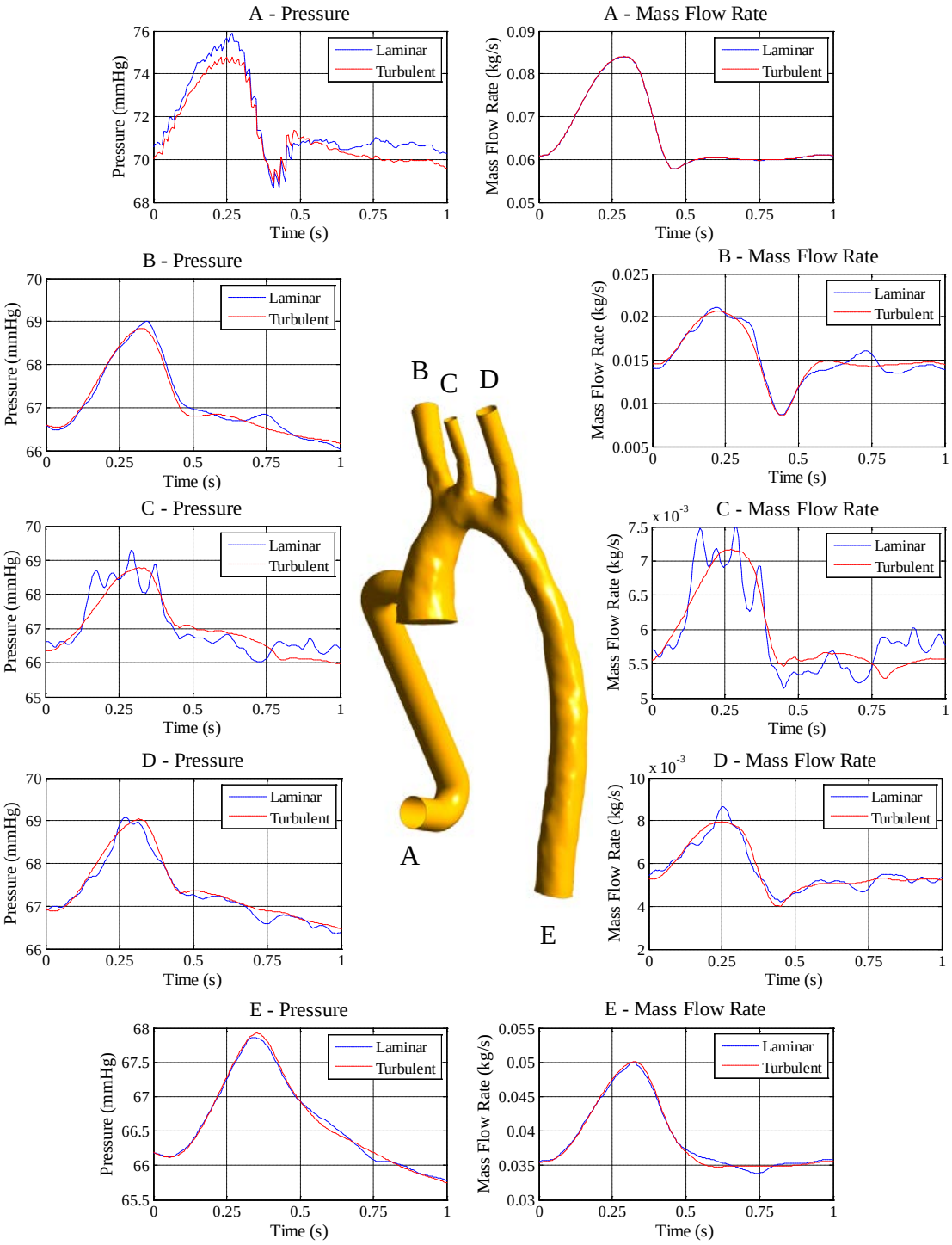

FIGURE 5-15 – COMPARISON OF PRESSURE AND MASS FLOW RATE IN THE ASSISTED AORTA (BLUE – LAMINAR SIMULATION, RED – TURBULENT SIMULATION)

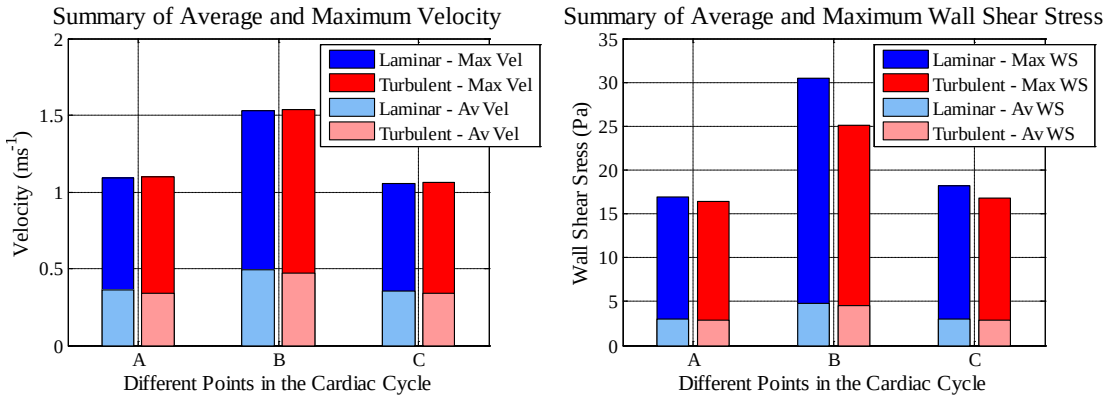

FIGURE 5-16 - COMPARISON OF MAXIMUM AND AVERAGE VELOCITY (LEFT) AND WALL SHEAR STRESS (RIGHT) AS PREDICTED BY THE LAMINAR AND TURBULENT SIMULATIONS, AT A NUMBER OF POINTS IN THE CARDIAC CYCLE (A = START OF CYCLE, B = PEAK FLOW, C = MINIMUM FLOW.)

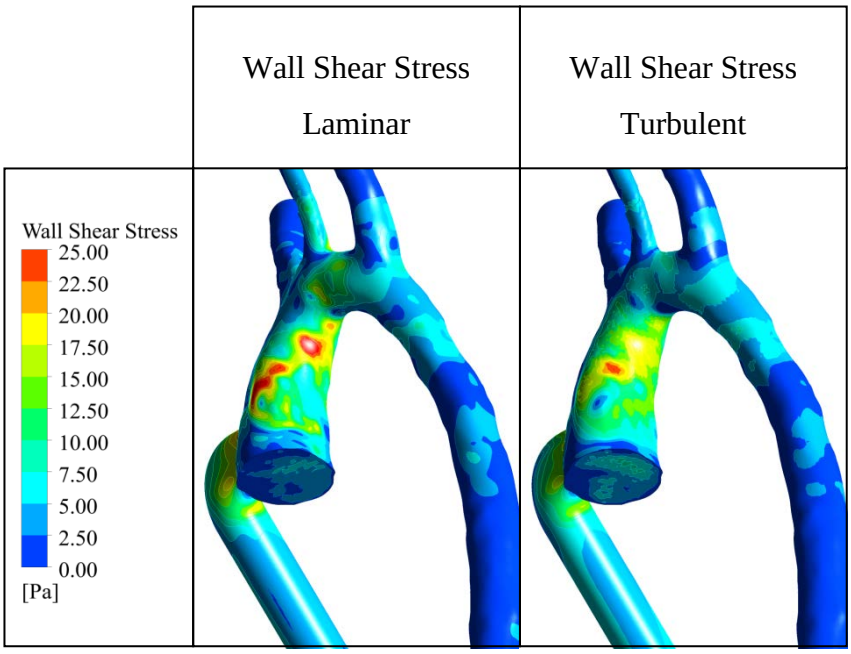

FIGURE 5-17 - COMPARISON OF WALL SHEAR STRESS DISTRIBUTION AT PEAK FLOW AS PREDICTED BY THE TRANSIENT LAMINAR AND TURBULENT SIMULATIONS

The Helical Flow Index is also calculated for the two models, with the laminar simulation predicting greater helical flow within the domain at all three given instances in time (Figure 5-18). These results, combined with the variation in the predicted wall shear stress distributions and previous experience in the native aorta case, suggest that the internal flow structures computed by the laminar and turbulent models are likely to be different.

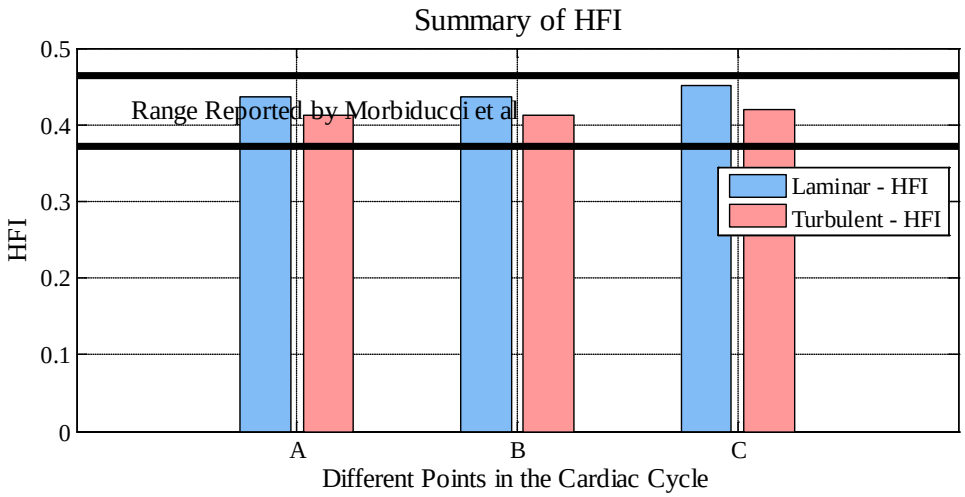

FIGURE 5-18 - COMPARISON OF HFI AS PREDICTED BY THE LAMINAR (BLUE) AND TURBULENT (RED) SIMULATIONS, AT A NUMBER OF POINTS IN THE CARDIAC CYCLE (A = START OF CYCLE, B = PEAK FLOW AND C = MINIMUM FLOW).

To investigate these claims, velocity contours, on planes normal to the centreline, are compared for the laminar and turbulent simulations at peak and minimum flow (Figure 5-19). The velocity contours show completely different flow patterns occurring in the two simulations. The laminar simulation predicts regions of high velocity in the ascending aorta which extend into the aortic arch, while the turbulent simulation has smaller regions of high velocity in the ascending aorta which reduce in magnitude more rapidly as it moves along the aortic arch. This is of course unsurprising since the turbulence model includes a turbulent viscosity which acts to further damp the system, thereby simulating the energy loss due to the turbulence. The greatest variation in the predicted flow fields can be seen within the aortic arch on planes D and E. At peak flow the turbulence model predicts regions of low fluid velocity near the greater curvature of the aortic arch (Figure 5-19 - D), which are not seen in the laminar case. On plane E, at both peak and minimum flow, the turbulent simulation shows a small region of low velocity fluid that is associated with flow detachment as the fluid moves around the arch and into the descending aorta. In contrast the laminar simulation shows regions of high velocity close to the minor curvature of the arch, suggesting the fluid remains attached, with a further region of high fluid velocity in the centre of the cross-section. At minimum flow the fluid appears detached (as in the turbulent model) but there is also a low velocity region in the centre of the vessel.

As a consequence of the steady state laminar model being unable to achieve numerical convergence in neither the assisted aorta nor the FDA benchmark (at a Reynolds number of 3500), it is proposed that the use of turbulence model is essential to accurately simulate aorta flow fields in the presence of a left ventricular assist device.

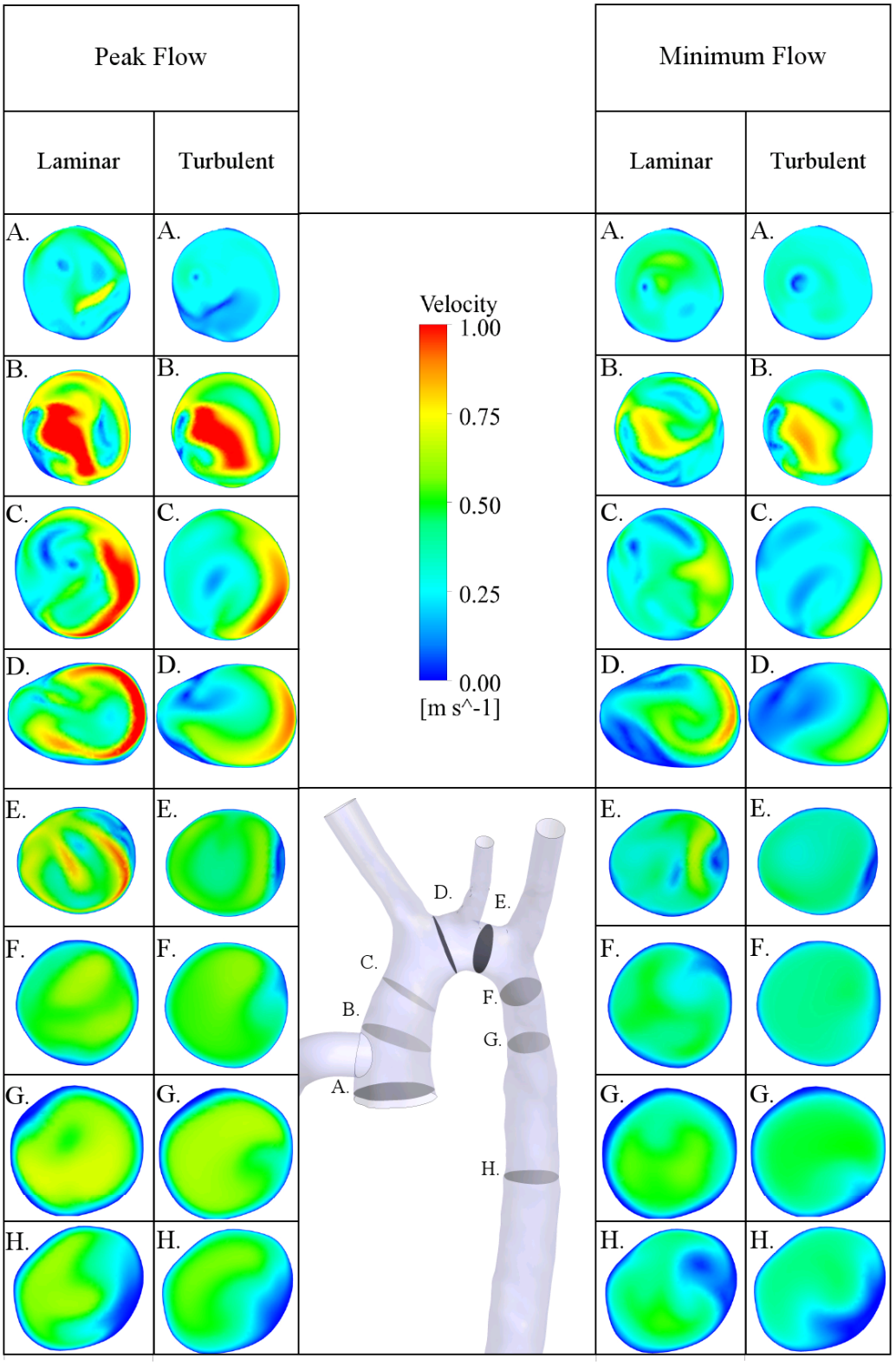

FIGURE 5-19 – COMPARISON OF PLANAR VELOCITY CONTOURS AS PREDICTED BY THE LAMINAR AND TURBULENT SIMULATIONS, AT PEAK (0.3S) AND MINIMUM FLOW (0.5S).

CONCLUSIONS 5.6

The requirement of a turbulence model has been investigated in a healthy and assisted aortic geometry under both steady state and transient conditions.

In the native aorta at peak flow, the steady state laminar model was unable to achieve numerical convergence in the finer meshes. This is believed to be due to transient vortex shedding in the flow field. All the steady state SST models achieved numerical convergence, with NA-2 producing mesh converged results. The converged laminar solution predicted a 25% greater pressure drop across the aorta than the SST model and analysis of the velocity contours showed significant variation in the internal flow field structures in the descending aorta.

Physiological flow in the aorta is pulsatile and so it is important that any numerical model chosen to predict aortic haemodynamics is able to capture laminar, transitional and potentially turbulent flow fields. Steady laminar simulations at peak flow were unable to achieve numerical convergence, while the SST model converged at high Reynolds numbers and was shown to give results that were in agreement with the steady state laminar simulation at a low Reynolds number of 1150. However, it is known that turbulence requires time to develop and this effect is not captured with a steady state simulation. Thus, a transient analysis was conducted to compare the laminar and SAS-SST models under physiological conditions. The laminar and turbulent simulations showed close agreement, especially during systole, suggesting that, in this case, the laminar model is sufficient to capture the important characteristics of the flow field. However, since the SAS-SST model also captured the important features and is able to resolve turbulent structures, which may occur in patients with higher flow rates, abnormal geometries or under exercise conditions, it is clearly the solution method of choice.

The steady state laminar model was unable to produce numerically converged results in the assisted aorta and it was found that a high spatial resolution was required for numerical convergence of the steady SST model. These results are due to the complex flow features that occur in the system as the fluid moves through the anastomosis. The near steady state environment of the physiological condition

suggests that, if the steady state laminar model is unable to converge, it is unlikely to be able to produce accurate results in the transient system. Although there is no experimental data to confirm this in the current geometry, the results presented in Chapter 2 agree with this statement.

The SAS-SST model is able to capture both the turbulent and laminar features of the native aortic flow field and, based on the results presented here and in Chapter 2, it is also believed to be the correct model to compute an assisted aortic flow field.

CHAPTER 6

ANASTOMOSIS DESIGN

MOTIVATION 6.1

The work up until this point has been carried out in order to describe and justify the use of certain models and modelling techniques to predict the aortic flow field in both a native and assisted vasculature. The following chapter applies these models to a real engineering problem and, by doing so, demonstrates their potential.

The interaction between an LVAD and the cardiovascular system is a complex problem but is essentially governed by two factors; the characteristics of the LVAD and the physiology of the patient. Clearly there is no way, from a design perspective, to alter the physiology of the patient and so one must concentrate on the LVAD. The characteristics of an LVAD are governed by:

1. Pump design
2. Operating condition
3. Cannula design
4. Anastomosis design

The design of the INCOR pump investigated in this work has been carefully engineered (by Berlin Heart GmbH, Germany) to minimise the fluid shear stresses, while maintaining a clinically appropriate cardiac output and is not a parameter that should be altered. The operating condition (assuming the pump is run in continuous mode, which is the current clinical operation mode) depends entirely on the output requirements of the patient, therefore cannot be varied. The design of the cannula is an important factor that could be optimised to improve the interaction of the LVAD and the native vasculature. However, this is not within the scope of the current work and has not been attempted. Finally we have the configuration of the anastomosis. This will be the focus of the current chapter.

The configuration of the anastomosis is essentially governed by three degrees of freedom (any variation of the insertion angle would require a redesign of the cannula):

1. Anatomical location
2. Radial position
3. Planar position

Constraints of the surgical approach mean there are only two regions of the aorta that are practical for the anastomosis; the ascending aorta and a region of the descending aorta. As discussed in Chapter 1, experimental and numerical studies have demonstrated that the ascending aorta is the optimal anatomical location as it prevents stagnant regions of fluid in the aortic root [13, 16]. Further anatomical constraints, namely the location of the pulmonary artery and the heart itself, mean that only a very small degree of radial variation is possible for the ascending aortic anastomosis and thus for the purposes of this chapter any variation in the radial angle has been neglected. Local positioning of the cannula has received very little attention in the literature and the work conducted has employed either simplified geometries [14] (two intersecting pipes) or non-physiological boundary conditions [15] (steady flow with uniform outlet pressures).

The following work aims to build on these initial studies, investigating the effects of planar anastomosis position in two aortic geometries; the first model (Figure 6-1 – Aorta A) is that used in previous Chapters, while the second model represents the

geometry from a healthy volunteer. This only became available in the latter stages of this project (Figure 6-1 – Aorta B). Although no invasive pressure data is available for the healthy geometry, for obvious ethical reasons, there is non-invasive flow data obtained in the ascending and descending aorta. The clinical data will be used to ensure that the distribution of flow, resulting from the choice of Windkessel parameters, is reasonable.

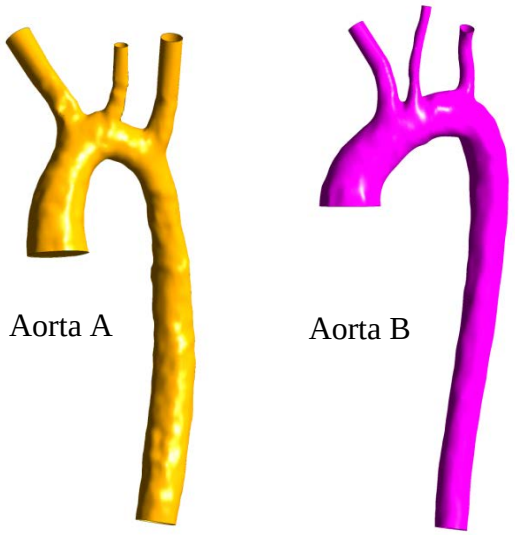

FIGURE 6-1 – ILLUSTRATION OF THE TWO AORTIC GEOMETRIES

To analyse the results a technique to visualise and quantify the degree of mixing in the assisted aorta, through the use of an information entropy measure, is employed. The approach was developed initially for chaotic micromixers [116] and has more recently been applied to blood flowing in helical geometries [117, 118]. This approach is used to offer an additional means for quantitatively evaluating transient flow fields, which in the author's opinion is a complex and much neglected problem.

METHODOLOGY 6.2

MODEL CONFIGURATION 6.2.1

The model setup combines the work documented in Chapters 4 and 5, utilising the compressible fluid model and the SAS-SST turbulence model to produce what is believed to be the most efficient and accurate modelling strategy described in this thesis, for the assisted aorta.

A representation of the Berlin Heart INCOR cannula is connected to the aortic geometries at a number of planar locations on a cross-section through the ascending aorta (Figure 6-2). The flow waveform, applied at the inlet of the cannula, is calculated (using a standalone 0D compartment model of the assisted vasculature [53]) to represent the VAD operating at 7300 rpm, matched to a clinical case. The resulting waveform supplies a flow rate of 4.56 L/min. Once again the real INCOR velocity profile is scaled to follow the inlet flow rate [16]. The outlet pressure conditions are described by Windkessel elements with the parameters used throughout this thesis. Before conducting this work it was believed that the parameters would require tuning for the new patient-specific case, to ensure the native flow distribution was preserved. However, after running some preliminary studies it was discovered that the current parameter values produced comparable distributions of flow to the clinically acquired data (within a 2.7% error range), which was deemed appropriate for the current research question.

The compressible fluid properties are the same as those used in Chapter 4, producing a uniform wave speed of 7 ms^{-1}.

The computational mesh is constructed as described in Chapter 5, with tetrahedral elements in the core and prism elements at the wall to improve the near wall resolution and ensure the requirements of the turbulence model are met. The distance to the first computational node, to achieve a $y^+ < 2$, is 0.11 mm. A maximum edge length of 0.75 mm, shown in Chapter 5 to produce mesh converged solutions in the assisted aorta, is also employed here.

As throughout this thesis a time-step of 5 ms is used in all simulations.

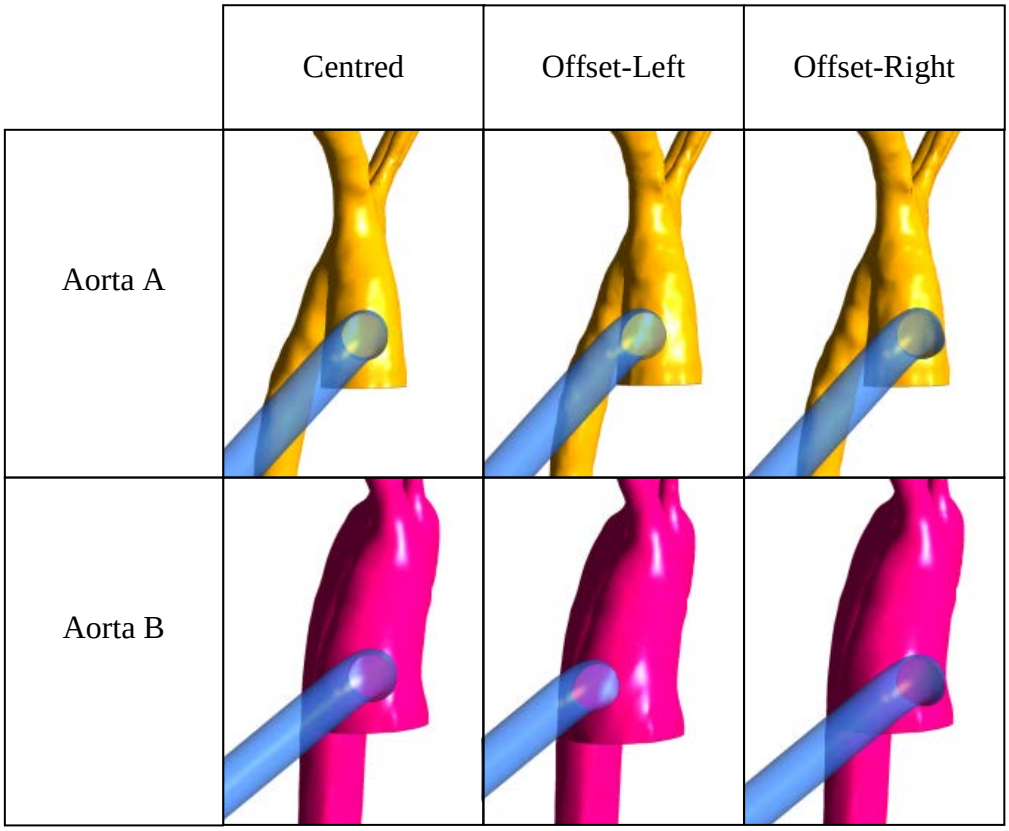

FIGURE 6-2 – ILLUSTRATION OF THE ANASTOMOSIS LOCATIONS INVESTIGATED IN THE TWO AORTIC GEOMETRIES

ENTROPIC MEASURE OF MIXING 6.2.2

In 1948 Shannon first proposed the concept of information entropy, which is essentially a measure of disorder [119]. An interesting implementation of this was described by Kang and Kwon [116] to quantify the degree of particle mixing in a micromixer and was later used by Cookson *et al.* [117, 118] when modelling blood flow in a helical geometry. The process involves three stages:

1. Computation of the periodic flow field of interest,
2. Computation of the trajectory of a number of species (e.g. different colours) of massless particles, through the flow field, and
3. Superimposing a uniform grid at a cross-section within the flow field and using Equation 6-1 to calculate the information entropy due to mixing.

$$S = \sum_{i=1}^{N_c} \left[w_i \sum_{k=1}^{N_s} (n_{i,k} log n_{i,k}) \right]$$

EQUATION 6-1

Where i is the cell index, k is the species index, w_i is the weighting factor for each cell, N_c is the number of cells, N_s is the number of species and $n_{i,k}$ is the particle number fraction of the k^{th} species in the i^{th} cell. The weighting factor is set such that it becomes zero if the cell contains no particles or only particles of a single species and one if there are multiple species in a single cell i.e. indicating that mixing has occurred.

The computed value of entropy is, on its own, rather meaningless and so Kang and Kwong defined a relative entropy (Equation 6-2) which quantifies the increase or decrease in information entropy at the cross-section of interest in relation to the initial distribution of the particle species and the maximum possible value of information entropy (i.e. perfect mixing).

$$\kappa = \frac{S - S_0}{S_{max} - S_0}$$

EQUATION 6-2

Where S_0 is the entropy of the initial particle distribution, S_{max} is the entropy assuming perfect mixing and S is the entropy at the region of interest.

As discussed by Cookson *et al.* [117, 118] care must be taken when selecting the number of particles and cells used in this analysis method. The value of entropy is strongly governed by N_c and in fact as $N_c \to \infty$ the calculated entropy goes to zero. In the following work approximately 20,000 particles are released from a planar cross-section at the start of an LVAD-cardiac cycle and 225 cells of uniform size are used to evaluate the information entropy at any given cross-section. Two particle species are used, which for the purposes of graphical representation have been coloured red and blue. The initial distribution of particles is defined such that a central circular area within the cross-section contains half the released particles, which are coloured blue. While the outer annulus contains the remaining particles,

coloured red. An idealised representation of the initial distribution for a cylindrical tube, including a uniform grid of cells used in the computation of the information entropy measure (the number of cells have been reduced for illustration purposes), is shown in Figure 6-3.

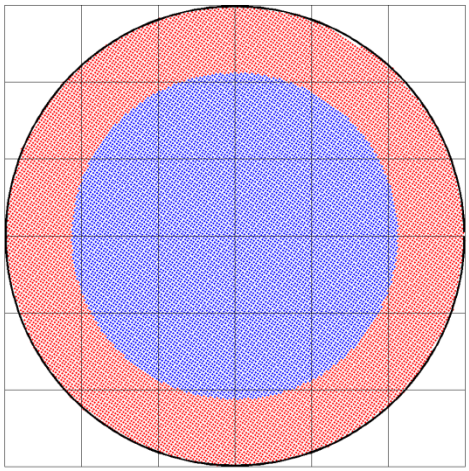

FIGURE 6-3 – ILLUSTRATION OF INITIAL PARTICLE DISTRIBUTION, WITH A REDUCED NUMBER OF CELLS OVERLAID

For the present investigation the particle release plane is located in the aortic valve region as it is an area prone to regions of fluid stagnation, and therefore the influence of cannula position on the mixing of these particles is of particular interest.

RESIDENCE TIME VIA SPECIES TRANSPORT 6.2.3

In previous chapters the average and maximum residence times were computed as a post-processing operation by solving the advection of massless particles through the flow field. In the following work an alternative approach is adopted, which results in a more informative representation of the fluid residence time. At the start of the simulation a massless, non-reacting species is defined throughout the fluid domain and given an initial value of 0. An additional transport equation (Equation 6-3) is solved, during the solution process, to describe the advection of the species (residence time) through the flow field. A volumetric source term of $1s^{-1}$ is defined throughout the domain to describe the age of the fluid and all new fluid entering the domain is assigned an initial species value of 0.

$$\frac{\partial(\rho\emptyset)}{\partial t} + \nabla \cdot (\rho \boldsymbol{U}\emptyset) = S_{\emptyset}$$

EQUATION 6-3

Where $\emptyset$ is the additional species and $S_{\emptyset}$ is the volumetric source term.

In turbulent simulations, such as employed in the current chapter, the additional transport equation, which describes the residence time, must be written in terms of the Reynolds-averaged quantities (Equation 6-4).

$$\frac{\partial(\rho\emptyset)}{\partial t} + \nabla \cdot (\rho \bar{\boldsymbol{U}}\emptyset) = S_{\emptyset}$$

EQUATION 6-4

Where $\bar{\boldsymbol{U}}$ is the averaged velocity components.

As well as the described measure of mixing and the new approach to computing residence time, mass flow distributions, velocity contours, the HFI and wall shear stress distributions are presented to evaluate the influence of planar cannula location on the assisted flow field.

RESULTS AND DISCUSSION: 6.3

The predicted mass flow waveforms, for each of the cannula configurations of Aorta A and Aorta B are shown in Figure 6-4 and Figure 6-5 respectively. The form of the mass flow waves are similar for all configurations, with the greatest variation seen in the left common carotid artery of Aorta A (Figure 6-4 – B). It is worth noting that the individual plots have different scales to clearly demonstrate the local variation at each boundary. The use of three element Windkessel models as the downstream termination ensures that the distribution of flow is within 2.7% of the clinical data in both cases and importantly maintains this distribution in all three configurations (Figure 6-4 and Figure 6-5). If the predicted distribution of flow was significantly altered by the position of the cannula this would suggest the model had inappropriate boundary conditions and was not faithfully representing the physiological condition.

In the human cardiovascular system homeostatic mechanisms, such as cerebral autoregulation, are in place to preserve the required flow rates.

The maximum difference in the predicted flow distributions in Aorta A and Aorta B is just 0.5%, suggesting that the aortic geometry has a negligible influence and is instead governed by the Windkessel parameters. This statement is only valid for relatively normal aortic geometries. Aortas suffering from severe geometrical malformations are likely to have a more significant effect on the flow distribution.

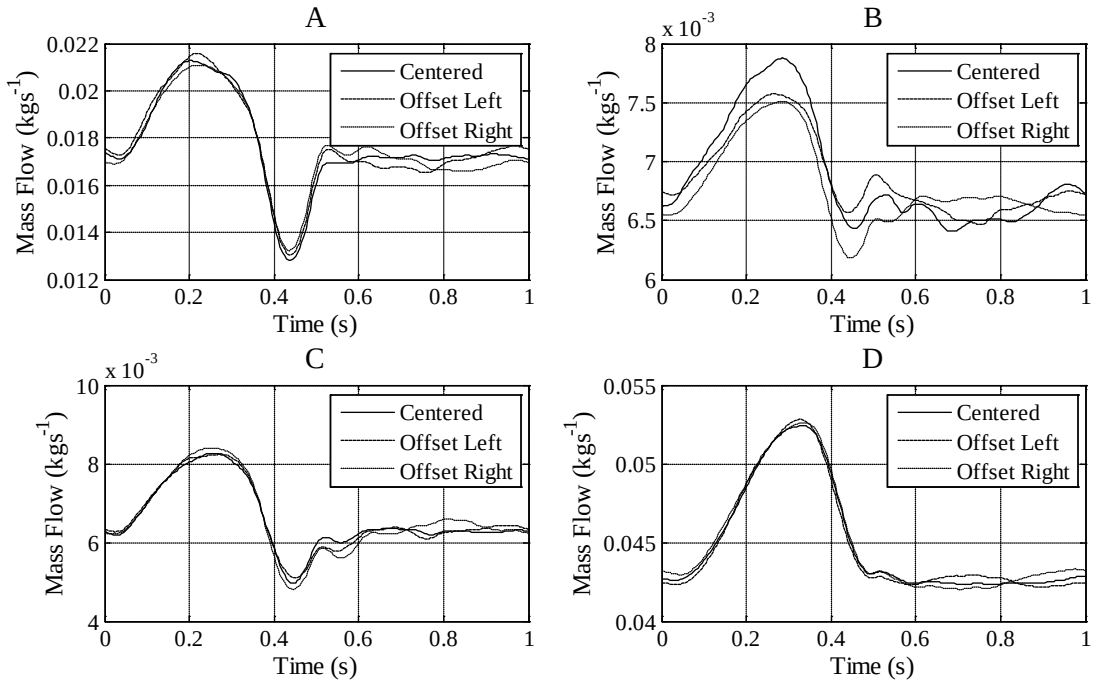

	A	B	C	D
Centred	0.233	0.090	0.087	0.590
Off-Right	0.232	0.090	0.087	0.590
Off-Left	0.233	0.089	0.087	0.590
Clinical	0.219	0.093	0.087	0.601

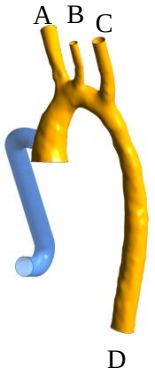

FIGURE 6-4 – INFLUENCE OF CANNULA LOCATION ON THE MASS FLOW WAVEFORMS AND FRACTIONAL DISTRIBUTION, AORTA A

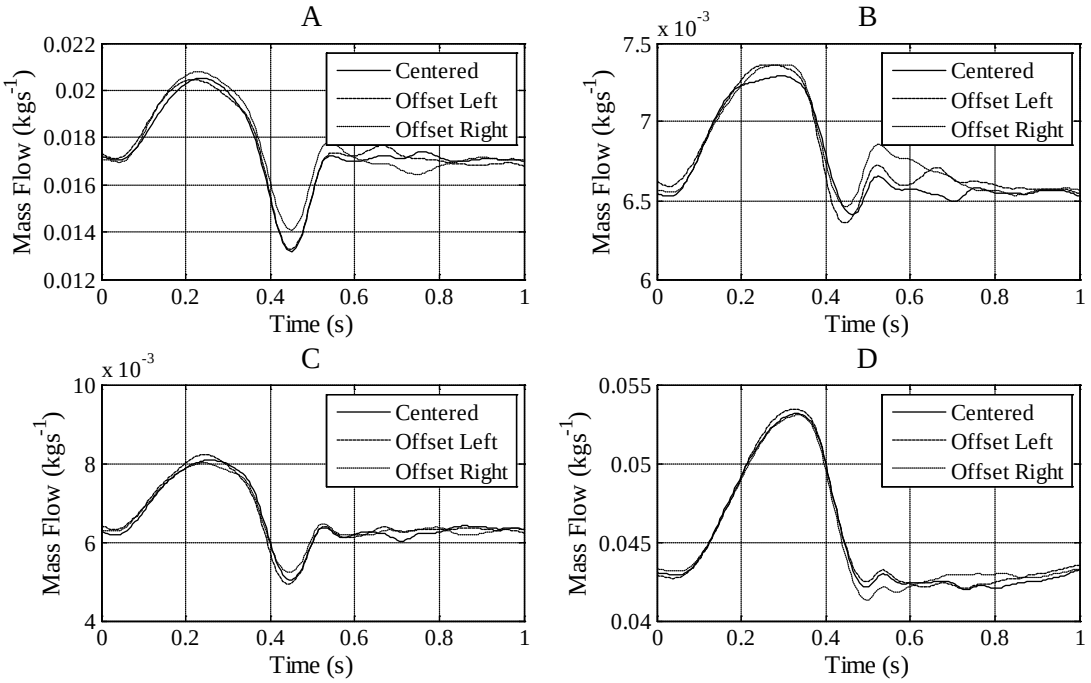

	A	B	C	D
Centred	0.230	0.089	0.086	0.595
Off-Right	0.232	0.089	0.086	0.593
Off-Left	0.230	0.089	0.086	0.595
Clinical	n/a	n/a	n/a	0.619

FIGURE 6-5 – INFLUENCE OF CANNULA LOCATION ON THE MASS FLOW WAVEFORMS AND FRACTIONAL DISTRIBUTION, AORTA B

Cycle averaged velocity contours, with vectors overlaid, have been plotted at a number of cross-sections along the length of the aortic geometries (Figure 6-6). As is the case throughout this thesis, the orientation of the cross-sections are such that the right hand side of each plane is associated with the lesser curvature of the aortic arch.

The position of the cannula is shown to significantly alter the structures within the flow field, in both Aorta A and Aorta B. Offsetting the cannula to the right results in higher fluid velocities in the region of the aortic valve (Figure 6-6 – Plane A) and is likely to produce a more complete washout of the valve region. In the Offset-Left

configuration both aortic models result in the peak velocities in the region of the anastomosis to be located within the centre of the aortic cross-section (Figure 6-6 – Plane B). This is in contrast to the Offset-Right configuration where, as one might expect, the peak velocities are offset to the right. The INCOR VAD imparts a rotational velocity to the fluid in a clockwise direction (see Chapter 4 and Chapter 5). This swirling motion is maintained through the cannula, although it is significantly distorted by the geometry of the cannula (see isosurfaces shown in Chapter 4). As the fluid enters the aorta it retains a clockwise swirling motion with the distorted profile having greater velocities to the right hand side. In the Offset-Right configuration this promotes the fluid to attach to the aortic wall where its momentum propels the fluid around the circumference of the aorta. The distorted profile has the opposite effect in the Offset-Left configuration, directing the high velocity fluid into the centre of the aorta inhibiting attachment to the wall. This effect is also seen in the Centred configuration (most noticeably in Aorta A) where the region of high velocity fluid is shifted towards the posterior wall of the aorta (Figure 6-6 – Plane B). Flow attachment is advantageous and certainly to be encouraged in cardiovascular flow fields as it reduces regions of stagnant fluid and areas of low wall shear stress, both of which should be avoided to maintain cardiovascular health.

In the Offset-Right configuration the fluid in the descending aorta maintains the anti-clockwise rotation apparent in the ascending aorta. This is consistent with *in vivo* studies of human blood flow where there is predominantly a right handed helix which forms in the ascending aorta and is maintained in the descending aorta [64]. This is also apparent in the Centred configuration of Aorta B, although the magnitudes of the rotational velocities are significantly smaller. In the Offset-Left configuration of Aorta B the fluid in the ascending and descending aorta have a clockwise rotation, producing left handed helical structures throughout the aorta. The Offset-Left configuration of Aorta A also has a predominantly clockwise rotation, again producing left handed helical structures, apart from in the aortic valve region where the fluid has an anti-clockwise motion.

There is a core of slow moving fluid located at the centre of the ascending aorta in all configurations of Aorta B but is only clearly distinguishable in the Offset-Right

configuration of Aorta A (Figure 6-6). This is believed to be due to the smaller geometric size of Aorta A, the radius of the ascending aorta (in the valve region) is approximately 22 mm compared to approximately 29 mm in Aorta B. In all cases the extent of the low velocity region is most pronounced in the ascending aorta, reducing in size as the fluid moves through the aortic arch and by the time the fluid enters the descending aorta the low velocity region is significantly reduced in all models and is no longer apparent in Aorta A or the Centred location of Aorta B (Figure 6-6 – Plane F).

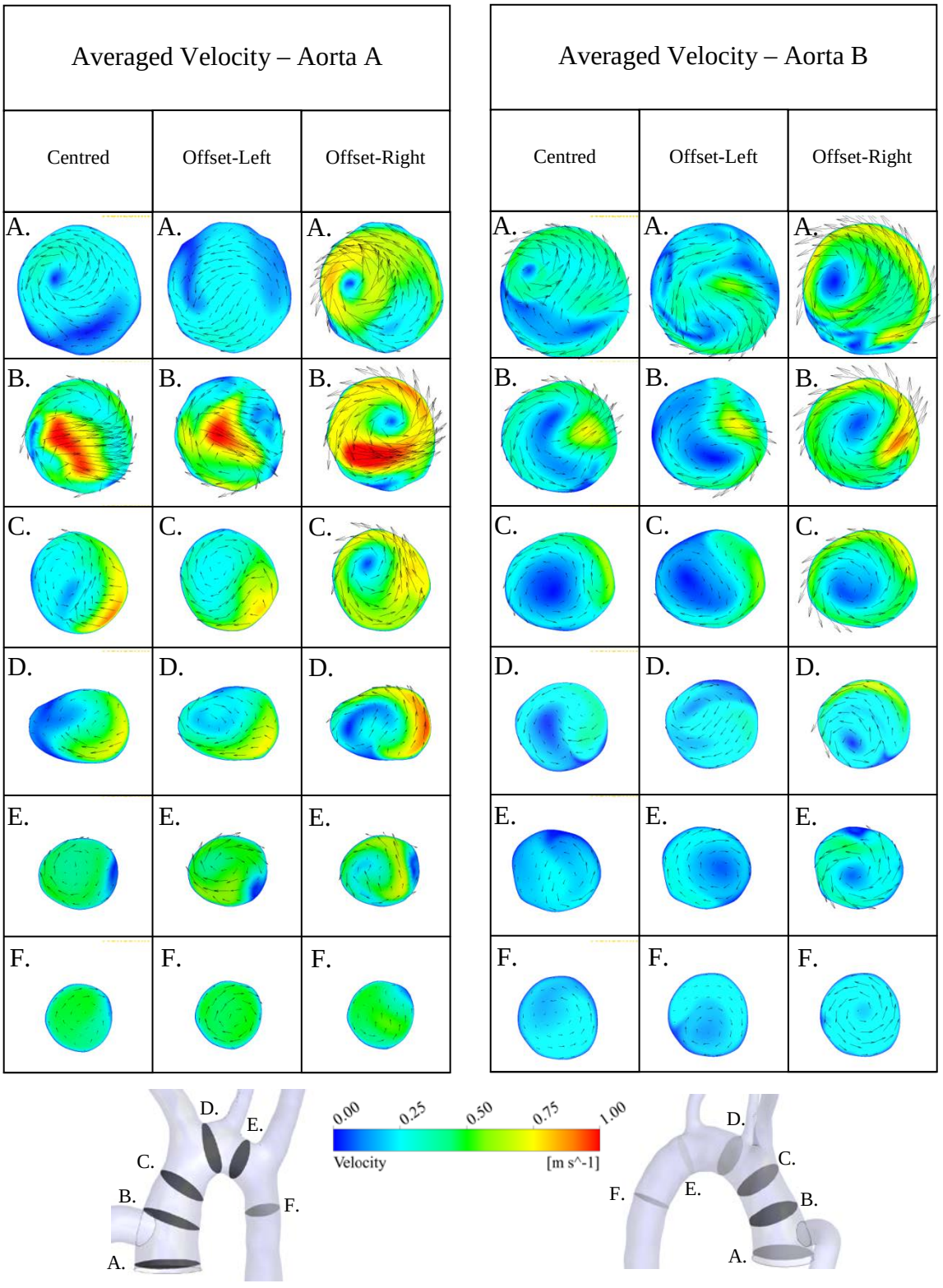

FIGURE 6-6 - COMPARISON OF PLANAR CYCLE AVERAGED VELOCITY CONTOURS; AORTA A – LEFT, AORTA B - RIGHT, IN THE THREE ALTERNATIVE ANASTOMOSIS CONFIGURATIONS.

The HFI is summarised in Figure 6-7 and is evaluated at three points throughout the cardiac-LVAD cycle. As one would expect in a system with such a small degree of pulsatility, the HFI is relatively stable across the cycle, with the largest variation occurring in the Centred configuration in both Aorta A (4.6% cycle variation) and Aorta B (7% cycle variation). In Aorta A the Offset-Left configuration consistently results in the largest values of HFI while the Offset-Right configuration results in the minimum. This is in direct contrast to Aorta B where the Offset-Left configuration produces the smallest values of HFI, while the Offset-Right produces the largest. With the exception of the Offset-Left configuration in Aorta A, the HFI in both aortas fall within the range reported by Morbiducci et al [66], which illustrates that the assisted flow fields contain a similar degree of helical flow, even if the form of the structures may differ, to the native haemodynamics of the aorta. As discussed previously the HFI is a valuable quantitative measure of the domain averaged helical flow but its greatest limitation is the lack of detailed information on the form of these helical structures.

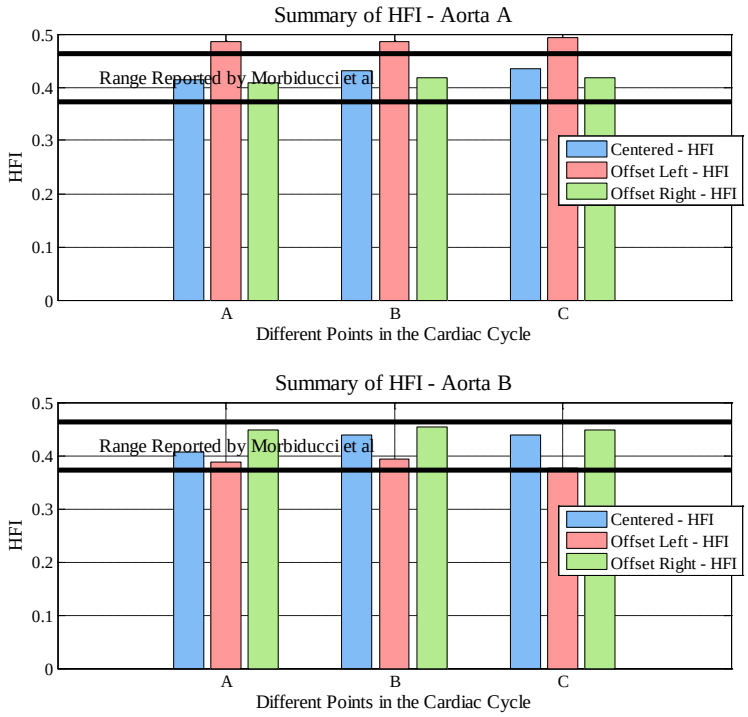

FIGURE 6-7 - COMPARISON OF HFI IN THE ALTERNATIVE CANNULA CONFIGURATIONS OF AORTA A (TOP) AND AORTA B (BOTTOM) AT A NUMBER OF POINTS IN THE CARDIAC CYCLE (A = START OF CYCLE, B = PEAK FLOW AND C = MINIMUM FLOW).

Comparison of the cycle-averaged wall shear stress (avWSS) distributions further illustrates the influence of cannula position on the haemodynamics of the assisted aorta (Figure 6-8 and Figure 6-9). In the Offset-Right configuration of both Aorta A and Aorta B, the rapid attachment of the fluid to the wall of the ascending aorta results in increased magnitudes of avWSS when compared to the alternative configurations. In contrast the lower velocities around the aortic valve in the Centred and Offset-Left configurations result in regions of low avWSS which could be at risk of stasis and the development of atherosclerosis (Figure 6-8 and Figure 6-9).

It has been noted by Nishimura *et al.* that long term continuous VAD support results in morphological changes to the aortic wall [25], which may suggest high regions of avWSS are also to be avoided. However, there are no clinical case studies which report problems with the integrity of the aortic wall. This is supported by communications with Berlin Heart, who suggest it is the regions of low avWSS that are of greatest concern.

Based on this understanding it is suggested that the Offset-Left position is the least favourable with the largest regions of low avWSS in the aortic valve region and throughout the ascending aorta. The Offset-Right configuration is the most advantageous with consistently smaller regions of low avWSS throughout the aorta (Figure 6-8 and Figure 6-9).

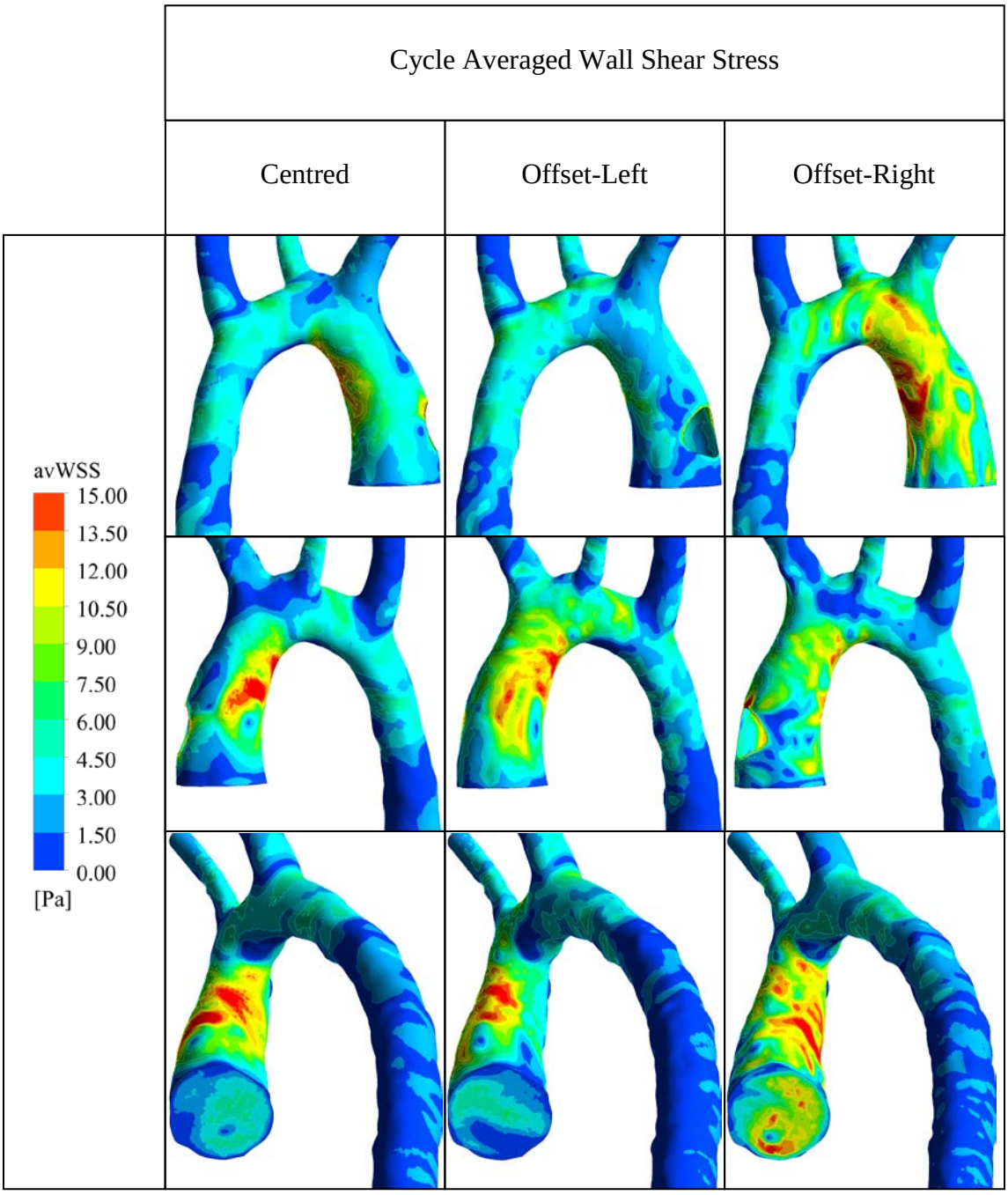

FIGURE 6-8 - COMPARISON OF CYCLE AVERAGED WALL SHEAR STRESS IN THE THREE ANASTOMOSIS CONFIGURATIONS, AORTA A.

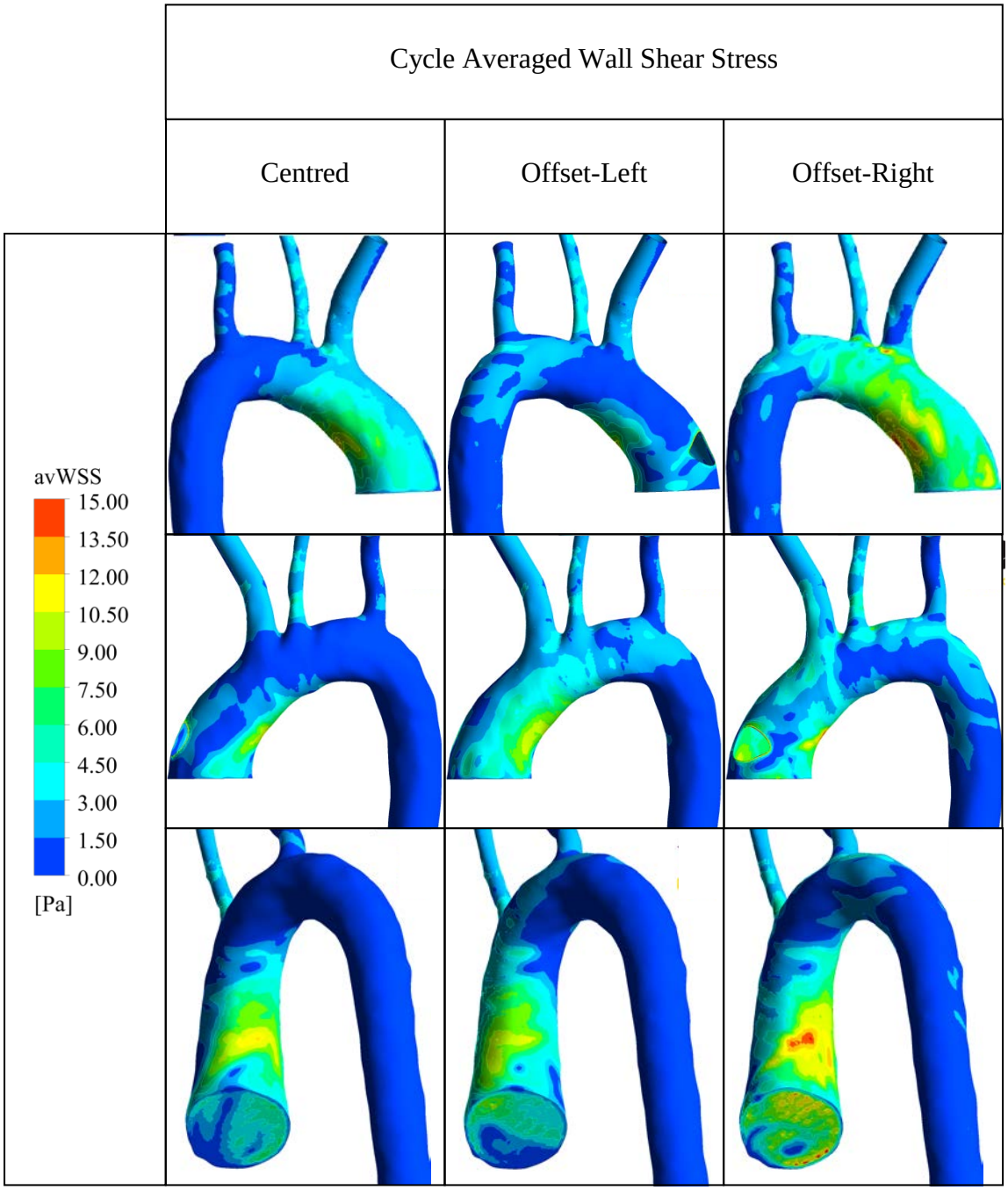

FIGURE 6-9 - COMPARISON OF CYCLE AVERAGED WALL SHEAR STRESS IN THE THREE ANASTOMOSIS CONFIGURATIONS, AORTA B.

QUANTIFICATION OF MIXING AND RESIDENCE TIME 6.3.1

As discussed in section 6.2.2, a quantitative measure of particle mixing may be useful for characterisation and comparison of assisted aortic flow fields. In the following section the results of the relative information entropy and the residence time analysis are presented for the three cannula locations in both aortic geometries. To put into perspective the degree of mixing that occurs in the assisted aorta an additional simulation, with patient-specific clinical flow measurements applied at the inlet of the aorta (i.e. native flow), was conducted in both aortae and the degree of mixing computed.

The distribution of the coloured particles is shown at a number of cross-sections (located at the same positions as the velocity contours in Figure 6-6) along the two aortae (Figure 6-10 and Figure 6-11). Flow in the assisted aorta is highly complex, with numerous helical structures and recirculating regions. Thus, when computing the degree of information entropy only the first intersection of the path-line and plane of interest is considered. The resulting relative entropy values (Equation 6-2) are shown graphically in Figure 6-12.

In the native flow configurations no mixing occurs in the ascending aorta, in fact the relative entropy of the cross-sections decrease when moving through the aorta due to the reduced number of boxes contributing to the entropic measure (Figure 6-12). The particle distributions remain ordered throughout the aorta, with the only variation occurring due to particles moving into the brachiocephalic and other supra-aortic vessels (Figure 6-10 and Figure 6-11). It is acknowledged that the application of a flat velocity profile in the native flow simulations is a simplification and in truth the profile will induce a degree of particle mixing. However for the purposes of this comparison a flat profile is believed to be an appropriate assumption. In contrast the assisted configurations produced highly disordered (i.e. mixed) particle distributions by the second plane of interest (Figure 6-10 and Figure 6-11 – Plane B). Somewhat surprisingly, the use of this analysis method in the assisted aorta results in regions of some cross-sections to be devoid of any intersecting particle. This effect is most clearly apparent in the ascending aorta, especially in the Offset-Right models (Figure 6-10 and Figure 6-11). Animation of the particles demonstrates that these empty

regions are real and result from the high velocity, tight helical structures that form in the ascending aorta. These structures draw the particles into the swirling vortex and the near steady flow field ensures there is only a small area through which the particles can intersect the plane. As the fluid moves through the arch and enters the descending aorta the particles become more evenly distributed throughout the cross-section but areas devoid of particles remain. The unusual distributions and local concentrations of the intercepting particles beg the question; *'Is there stagnant fluid in the regions devoid of particle intersections or is the fluid coming directly from the cannula?'*. This question of stagnation is best answered by investigating the results of residence time and is explored subsequently.

The flow fields with the cannula offset to the right are dominated by a single secondary vortex which is also visible in the vectors overlaying the velocity contours in Figure 6-6. In Aorta A the flow field of the Offset-Left configuration is composed of two secondary vortices, one of which gains dominance as the fluid moves through the arch. There is no indication of such vortices in the flow field of the Centred location but the particles appear well mixed, which is confirmed by the relative entropy measure (Figure 6-12). In Aorta B two secondary vortices are apparent in the Centred and Offset-Left configurations, although the minor vortex in the Offset-Left position is no longer present as the fluid moves into the descending aorta.

In both aortae the Centred configuration results in the highest values of relative entropy, although in Aorta B the Offset-Left position produce qualitatively similar degrees of mixing (Figure 6-12) but with a maximum percentage difference of 23.4%, occurring at plane D. In general, the Offset-Right location results in the smallest value of relative entropy. This is believed to be due to the particles intercepting the planes of interest through a comparatively small area. This effect is clear in the Offset-Right location of Aorta B, where the relative mixing increases at planes E and F which corresponds to a more even distribution of intercepting particles (Figure 6-11).

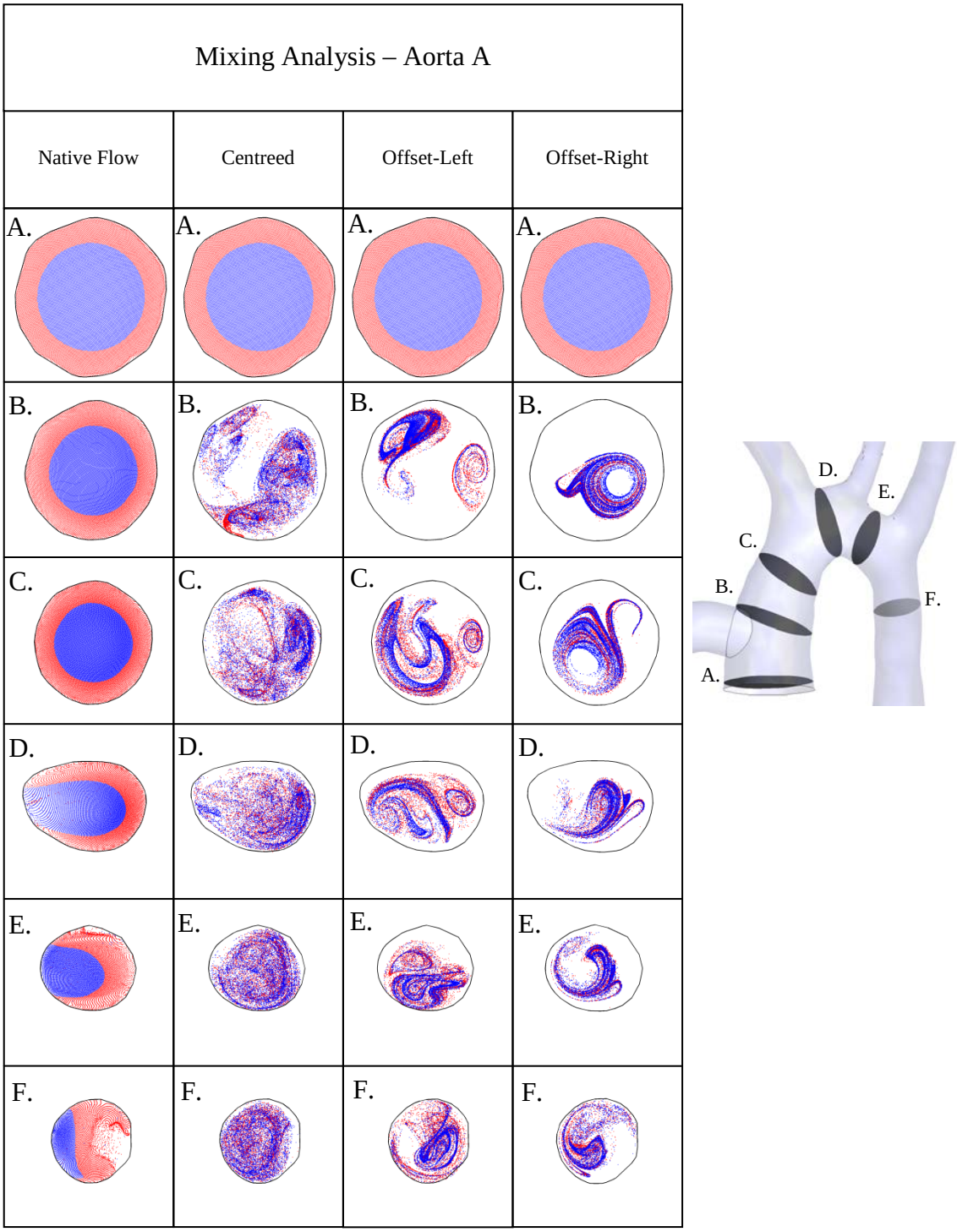

FIGURE 6-10 – ILLUSTRATION OF THE PARTICLE MIXING IN EACH OF THE ALTERNATIVE CANNULA CONFIGURATIONS, AORTA A

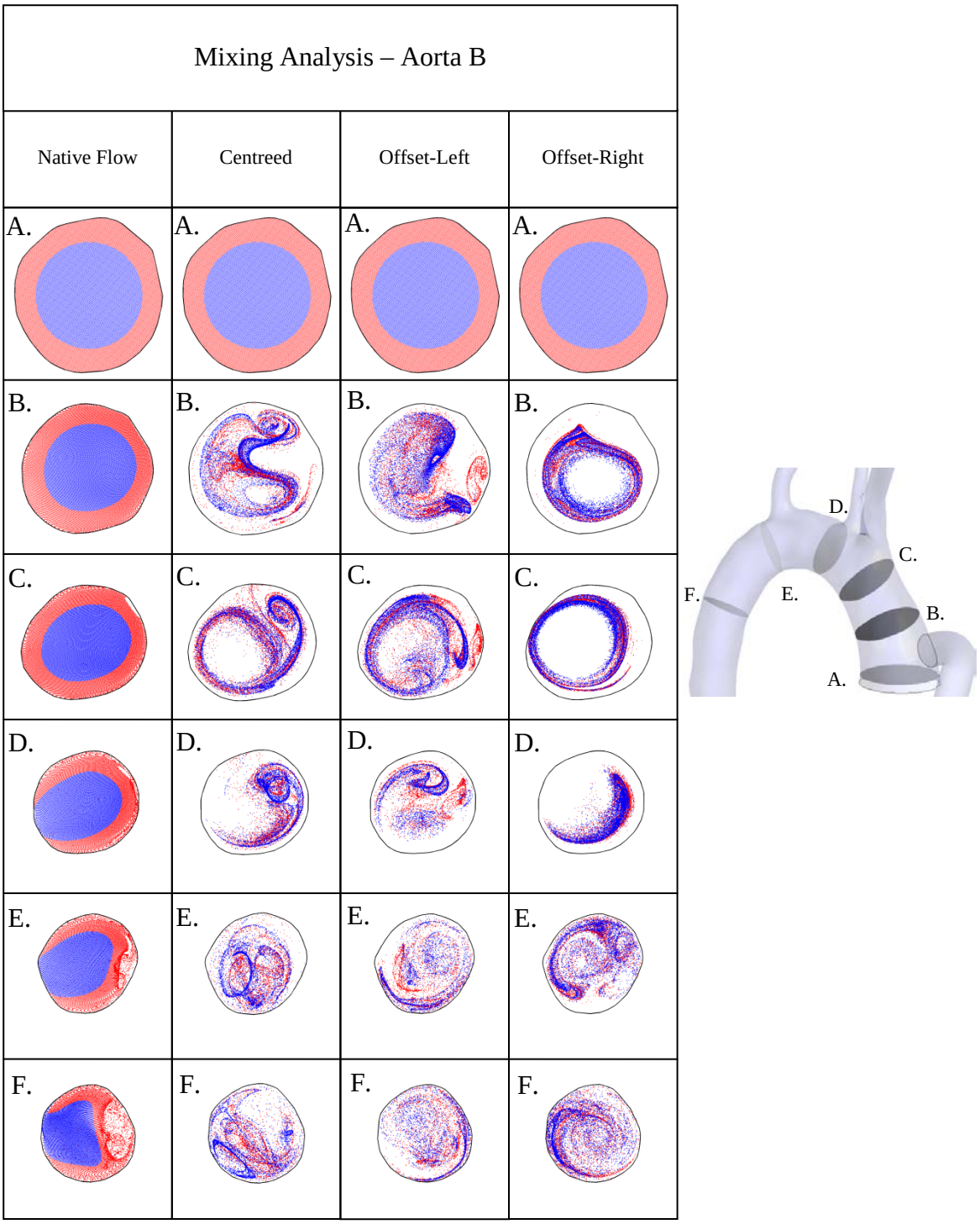

FIGURE 6-11 - ILLUSTRATION OF THE PARTICLE MIXING IN EACH OF THE ALTERNATIVE CANNULA CONFIGURATIONS, AORTA B

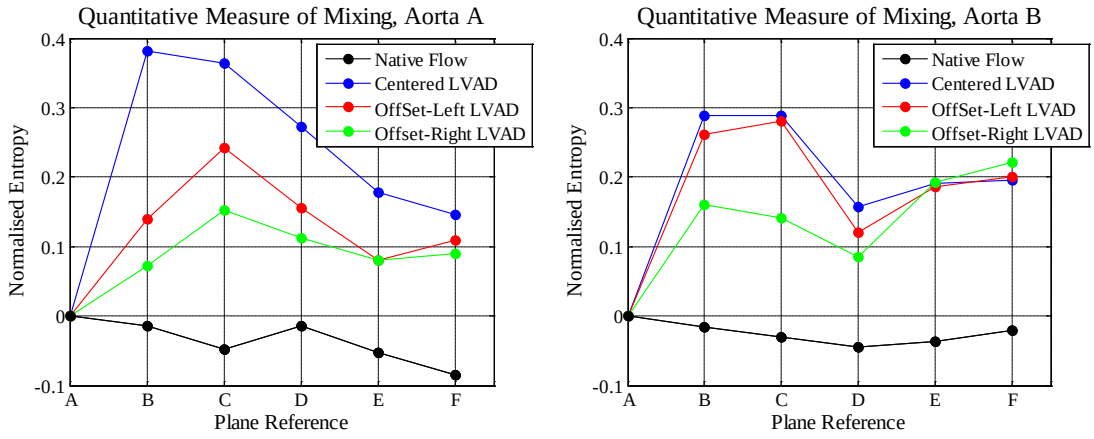

FIGURE 6-12 – NORMALISED INFORMATION ENTROPY (K) IN AORTA A AND B FOR ALL CONFIGURATIONS

To investigate further the question previously posed: *'Is there stagnant fluid in the regions devoid of particle intersections?'*, isovolumes of residence time have been depicted to show the age of the fluid in the aorta, which in turn demonstrate the influence of cannula location on vascular washout (Figure 6-13 and Figure 6-14). The domain averaged residence time of the fluid within each configuration is reported in Table 6.1.

In Aorta A the Offset-Right position produces the most rapid washing out of the ascending aorta (Figure 6-13) and as such has the lowest domain averaged residence time (Table 6.1). As discussed previously in this configuration the fluid attaches to the wall and it is clear from the isovolume showing fluid with a residence time greater than or equal to 0.4s that this results in a rapid washing out of the fluid around the aortic wall of the ascending aorta. A central core of older fluid remains in the ascending aorta, the majority of which is cleared by 0.5 s and is fully removed by 0.75 s. The Centred position in Aorta A performs worst in terms of vascular washout, with the largest domain averaged residence time and the greatest regions of high residence time isovolumes (Table 6.1 and Figure 6-13). However, the difference between the best and worst domain averaged residence time is just 1.77% suggesting that, although the Offset-Right configuration is the most advantageous, all the cannula locations presented result in an acceptable degree of vascular washout.

In Aorta B the period over which the ascending aorta is completely washed out is greater (1.5 s) and, in turn, the domain averaged residence times are also greater (Table 6.1). This is to be expected, as since the geometry is larger, the velocities in

the domain will be reduced for the same flow rate. This can be seen in the velocity contours (Figure 6-6) where the velocities in Aorta B are generally lower. The phenomenon, seen in the Offset-Right configuration, due to the fluid attaching to the aortic wall, leaving a core of older fluid, is also apparent in Aorta B in the isovolume with a residence time of greater than or equal to 0.5s. Interestingly, the trends in the domain averaged residence time are not the same as in Aorta A but are in fact completely reversed. The fluid in the Offset-Right configuration has the largest average residence time, 2.96% greater than the Centred configuration which has the lowest (Table 6.1). However, as discussed in relation to Aorta A all configurations produce an acceptable degree of vascular washout. Perhaps more important is the finding that, in regard to the analysis of particle mixing, the regions of a cross-section which are devoid of particle interceptions do NOT, in the case of the assist aorta, correlate to regions of stagnant fluid.

This work has demonstrated the importance of using multiple analysis techniques to fully investigate a flow field of interest. It is vital that conclusions are not drawn based on a limited knowledge.

	Isovolumes of Residence Time			
	t ≤ 0.4 s	t ≤ 0.5 s	t ≤ 0.75 s	t ≤ 1.5 s
Centred				
Offset-L				
Offset-R				

FIGURE 6-13 – ISOVOLUMES OF FLUID RESIDENCE TIME, AORTA A

	Isovolumes of Residence Time			
	t ≤ 0.4 s	t ≤ 0.5 s	t ≤ 0.75 s	t ≤ 1.5 s
Centred			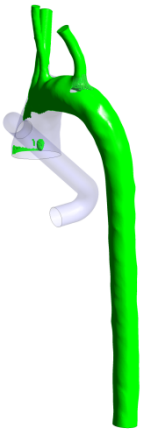	
Offset-L			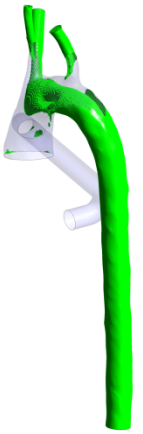	
Offset-R				

FIGURE 6-14 – ISOVOLUMES OF FLUID RESIDENCE TIME, AORTA B

	Average Residence Time (s)		
	Centred	Offset-Left	Offset-Right
Aorta A	0.453	0.446	0.445
Aorta B	0.787	0.804	0.811

TABLE 6.1 – DOMAIN AVERAGED RESIDENCE TIME

CONCLUSIONS 6.4

In this chapter a number of anastomotic configurations have been investigated in two patient-specific aortae. The results have been analysed using standard measures employed in the analysis of haemodynamics (i.e. velocity contours, avWSS and residence time) as well as presenting the first use of a quantitative entropic measure of mixing applied to a realistic cardiovascular geometry.

The results demonstrate that the planar location of the LVAD cannula connection to the ascending aorta significantly alters the haemodynamics.

For the specific cases presented the Offset-Right configuration is the only position which facilitates fluid attachment to the wall almost immediately at the site of the anastomosis. The attachment is believed to be a result of the orientation of the velocity profile as the fluid moves through the anastomosis. This itself is a product of the LVAD profile and the geometry of the cannula. Fluid that becomes attached to the wall has the advantage of reducing regions of low avWSS which are thought to be prone to the development of atherosclerosis.

All cannula positions resulted in good levels of mixing, especially when compared to that of the native configuration, with the Centred configuration producing the largest degree of mixing in both geometries. Analysis of residence time showed that all configurations perform similarly in terms of vascular washout and there are no regions of the ascending aorta which suffer from prolonged fluid stagnation.

Based on the finding presented in this chapter it is suggested that when connecting the Berlin Heart INCOR VAD to the ascending aorta, with the specific design of outflow cannula described, it is beneficial to offset the cannula to the right, thereby promoting wall attachment and minimizing the risk of low wall shear stress regions.

CHAPTER 7

FULLY COUPLED MODEL

MOTIVATION 7.1

A natural progression from employing 0D models at the outlet boundary, of a CFD simulation, is to also describe the inlet boundary condition in terms of a lumped parameter model. In the following chapter this concept is taken a step further by embedding the 3D model in a closed loop description of the entire vasculature. The fully coupled model has the advantage of being able to predict the system wide response as well as interrogating the detailed flow characteristics in the chosen region of interest, offering the possibility of a powerful predictive tool.

The coveted outcome of VAD support is complete ventricular recovery, to the extent that the pump can be successfully explanted. However, a common and well-documented complication of LVAD (2^{nd} and 3^{rd} generation) support is aortic valve commissural fusion [19-22, 120]. Valve fusion is caused by the lack of flow through the aortic valve during ventricular support, resulting in fibrous tissue being laid down across the leaflets, fixing them together. In the event of myocardial recovery the explantation procedure can be complicated by valve fusion necessitating

replacement of the damaged valve with an artificial valve, exposing an already fragile patient to the trauma of further heart surgery.

In the following work the fully coupled model is used to explore the hypothesis that by reducing the operating speed of the pump the aortic valve will open, changing the flow field, inhibiting fusion of the valve commissaries and additionally improving left ventricular washout.

METHODOLOGY 7.2

A comprehensive 0D model of the assisted cardiovascular system [53, 121] was modified to incorporate the supra-aortic arteries and coupled to a 3D model of an assisted aorta (Figure 7.1).

0D SYSTEM MODEL 7.2.1

The 0D description of the cardiovascular system, designed and coded by Dr Yubing Shi, is composed of five main compartments; the aortic sinus, the systemic circulation, the heart, the pulmonary sinus and the pulmonary circulation. The systemic and pulmonary circulation compartments can be further decomposed into elements that represent the arteries, arterioles, capillaries and veins. Each 0D element is designed to capture the gross behaviour of the system it represents. For example the capillaries have a mainly resistive effect and thus are modelled as a single resistor, while the venous system has a significant compliance and are represented using a two element Windkessel (Figure 7-1). A comprehensive review by Shi *et al.* provides further details [34]. An additional compartment is incorporated to describe the Berlin Heart INCOR LVAD. The pump inlet is connected to the apex of the left ventricle and the outlet to the 3D representation of the outflow cannula. The characteristics of the pump are expressed as a polynomial function (Equation 7-1), derived from experimental data that describes the pressure-flow relationship of the INCOR pump under different operating speeds. The explicit details of this function are not included for commercial reasons.

$$\Delta P = P(Q, \omega)$$

EQUATION 7-1

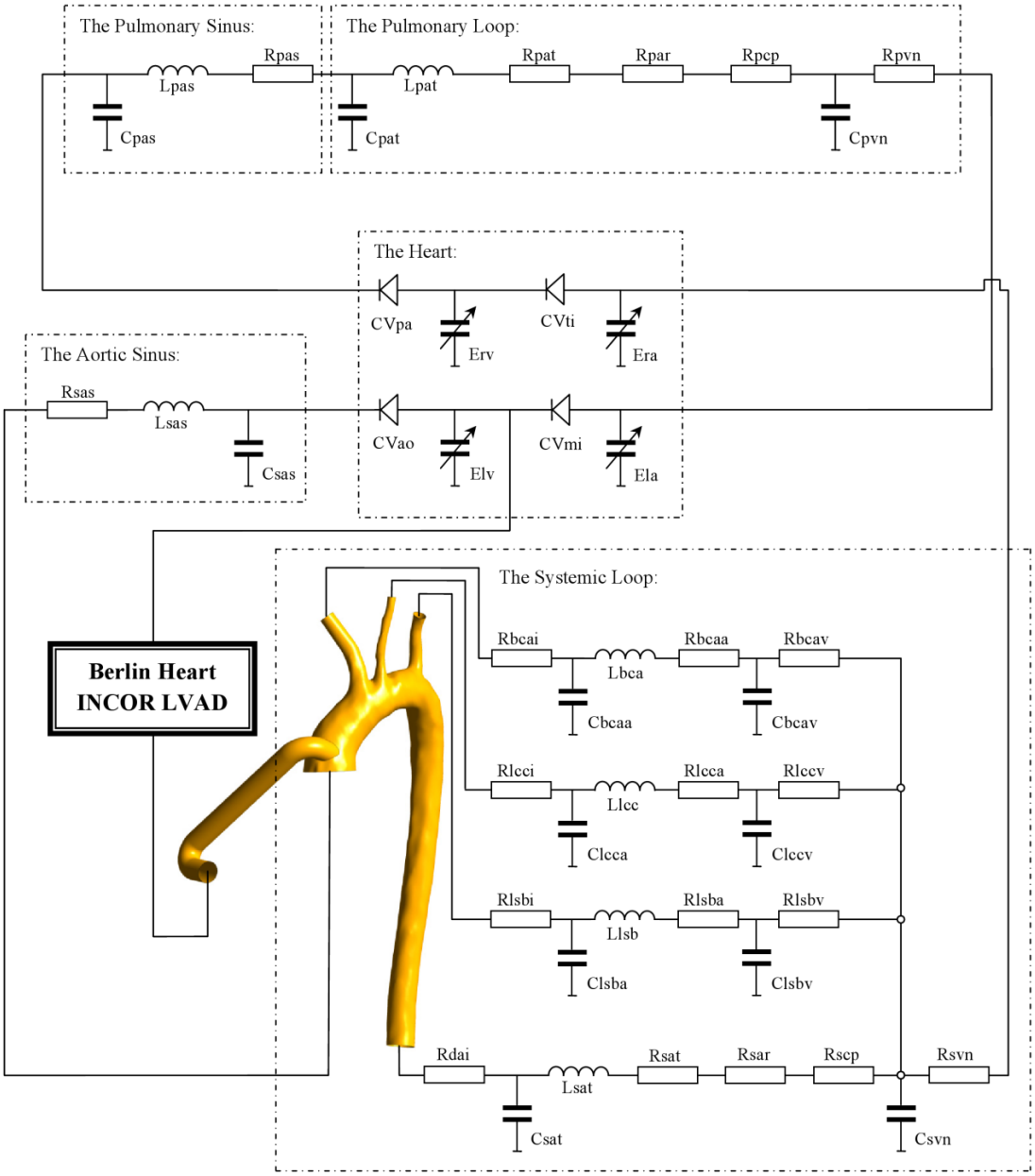

FIGURE 7-1- ILLUSTRATION OF THE FULLY COUPLED 0D-3D MODEL

The mechanics of the individual chambers of the heart are each described by the commonly used elastance model, proposed by Suga *et al.* [69] with one way diodes controlling the direction of flow. The variable elastance model (as described in Chapter 1) assumes the pressure within a chamber can be described by a linear relationship between the chamber volume and elastance, with the instantaneous

change in volume computed from the difference between the flow rate into and out of the chamber (Equation 7-2).

$$\frac{dV_i}{dt} = Q_{i,in} - Q_{i,out}$$

EQUATION 7-2

Where V_i is the volume of the i^{th}chamber, while $Q_{i,in}$ and $Q_{i,out}$ are the volume flow into and out of the i^{th}chamber respectively.

The chamber elastance is a time-varying function, with a period equal to that of the heart cycle, which describes the action of the heart (Equation 7-3).

$$e_i(t) = E_{i,d} + \frac{E_{i,s} - E_{i,d}}{2} \cdot \overline{e_i}(t)$$

EQUATION 7-3

Where $E_{i,d}$ and $E_{i,s}$ are the characteristic elastance of the i^{th}chamber at diastole and systole respectively and $\overline{e_i}(t)$ is an activation function, which for the ventricles takes the form shown in Equation 7-4 and for the atria Equation 7-5.

$$\overline{e_{i,ventricle}}(t) = \begin{cases} 1 - \cos\left(\frac{t}{T_s}\pi\right) & : \quad 0 \le t \ge T_s \\ 1 + \cos\left(\frac{t - T_s}{{}^3\!/_2\, T_s - T_s}\pi\right) & : \quad T_s \le t \ge {}^3\!/_2\, T_s \\ 0 & : \quad {}^3\!/_2\, T_s \le t \ge T \end{cases}$$

EQUATION 7-4

$$\overline{e_{i,artia}}(t) = \begin{cases} 0 & : \quad 0 \le t \ge T_{pwb} \\ 1 - \cos\left(\frac{t - T_{pwb}}{T_{pww}}\pi\right) & : \quad T_{pwb} \le t \ge (T_{pww} + T_{pwb}) \\ 0 & : \quad (T_{pww} + T_{pwb}) \le t \ge T \end{cases}$$

EQUATION 7-5

Where T is the period of the cardiac cycle and T_s, T_{pwb} and T_{pww} are time constants that correspond to the contraction period of the heart chambers.

The chamber pressure is then calculated as the sum of the pressure at the previous time-step and the product of the instantaneous elastance and the change in chamber volume (Equation 7-6).

$$P_i(t) = P_i(t-1) + e_i(t)(V_i(t) - V_i(t-1))$$

EQUATION 7-6

Where $P_i$is the pressure within the i^{th}chamber.

The heart valves are modelled in either a fully open or fully closed position, with the fully open configuration modelled as a resistive component (Equation 7-7).

$$Q_j = \begin{cases} CV_j \cdot \sqrt{P_{down} - P_{up}} & : \quad P_{down} > P_{up} \\ 0 & : \quad P_{down} \leq P_{up} \end{cases}$$

EQUATION 7-7

Where CV_j is the flow coefficient of the j^{th} heart valve.

PARAMETER VALUES 7.2.2

The parameter values for the 0D system (Table 7.1) have been chosen to elicit a physiologically realistic response for a patient suffering from left heart failure [9, 52-54, 121]. The primary mechanisms of left heart failure are the reduced peak systolic contractility of the left ventricle, which in this case is represented by the systolic left ventricular elastance ($E_{lv,s}$), an increase in ventricular end diastolic wall stiffness, which in this case is represented by the diastolic left ventricular elastance ($E_{lv,d}$) and systemic vasoconstriction, with the purpose of maintaining systemic blood pressure.

Researchers have employed alternative approaches to simulate the characteristics of left heart failure. Shi *et al.* defined the systolic left ventricular elastance as 25% of that in the healthy condition ($E_{lv,s} = 6.67 \times 10^7$ kgm^{-4}s^{-2} in heart failure), while leaving all other parameters unchanged [52, 53, 121, 122]. Tsuruta *et al.* described a number of categories of left heart failure from A-D with the systolic and diastolic ventricular elastance values ranging from 31.6-52.5% and 140.5-220.2% of the healthy case respectively [54]. They also quantify the decrease in systolic left

ventricular elastance (27.9% of healthy) such that the model simulates a patient with Class IV heart failure as described by Forrester's classification [123]. Hanson *et al.* reduced the contractility of both the left and right ventricles by 50% to simulate ischaemic heart disease while also increasing the peripheral resistance to simulate vasoconstriction [124]. Wu *et al.* modified the contractile strength of both the left and right ventricles as well as increasing the heart rate and the peripheral resistance [125]. Morley *et al.* investigated the effects of partial ventricular support and characterised three categories of heart failure; mild, moderate and severe [126]. In all categories the heart rate and systemic resistance were increased and the elastance values of all heart chambers were reduced, with the systolic left ventricular elastance defined as 28%, 17% and 13% of the healthy condition. These corresponded to mild, moderate and severe left heart failure respectively.

In the following work left ventricular failure is characterised by a reduction in the left ventricular peak systolic contractility and an increase in the end diastolic wall stiffness. The peripheral resistance is not altered. This is justified by the inclusion of an LVAD, which will maintain the blood pressure within a physiological range thereby removing the stimulus that initiates vasoconstriction. The systolic left ventricular elastance is reduced to approximately 30% of the healthy condition, relating to class IV heart failure as described by Forrester *et al.* and mild heart failure according to Morley *et al.* [54, 126]. The value is proposed to represent a patient who has received LVAD support for a period of time such that the left ventricle has partially recovered.

3D MODEL 7.2.3

The 3D model, embedded in the closed loop description of the cardiovascular system, is the patient-specific normal aorta introduced in Chapter 6. The representation of the Berlin Heart INCOR LVAD cannula is attached in the Offset-Right configuration, following the results of the investigation into the anastomosis design (Chapter 6).

The model configuration is as described in Section 6.2.1, with the SAS-SST turbulence model used to solve the Reynolds Averaged Navier-Stokes equations and a compressible fluid employed to capture the gross characteristics of the propagating

waves. To ensure stability of the fully coupled system a 3D time-step of $1x10^{-3}$s is required.

COUPLING STRATEGY 7.2.4

The 0D model was coded in FORTRAN by a colleague, Dr Yubing Shi. The model is coupled to the 3D domain via an explicit coupling scheme which passes information between the 3D and 0D models at the end of every time-step of the 3D model (as described in Chapter 3, Section 3.3). The governing equations of the 0D model are no longer solved using an implicit method and instead are solved using an explicit first order scheme (forward Euler), with a time-step of $1x10^{-4}$ s. Therefore at the end of every 3D time-step calculation the 0D model solves 10 time-steps before passing the appropriate parameters to the 3D domain.

The 3D model receives flow at all inlets and pressure at all outlets from the 0D model, while the 0D model receives pressure at all inlets and flow at all outlets from the 3D model.

Heart Compartment Parameters				
Parameter	**Value**	**Parameter**	**Value**	**Units**
CVao	$9.00x10^{-7}$	CVmi	$1.50x10^{-6}$	$m^{3.5}\,kg^{0.5}$
CVpa	$9.00x10^{-7}$	CVti	$1.50x10^{-6}$	$m^{3.5}\,kg^{0.5}$
$E_{lv,s}$	$9.99x10^{7}$	$E_{lv,d}$	$9.33x10^{6}$	$kg\,m^{-4}s^{-2}$
$E_{la,s}$	$3.73x10^{7}$	$E_{la,d}$	$2.40x10^{7}$	$kg\,m^{-4}s^{-2}$
$E_{rv,s}$	$1.53x10^{8}$	$E_{rv,d}$	$9.33x10^{6}$	$kg\,m^{-4}s^{-2}$
$E_{ra,s}$	$3.33x10^{7}$	$E_{ra,d}$	$2.00x10^{7}$	$kg\,m^{-4}s^{-2}$
T	1	Ts	0.3	s
Tpwb	0.92	Tpww	0.09	s
Aortic Sinus Compartment Parameters				
Rsas	$6.67x10^{5}$			$kg\,m^{-4}s^{-1}$
Csas	$1.50x10^{-9}$			$m^{4}s^{2}\,kg^{-1}$
Lsas	$5.60x10^{3}$			$kg\,m^{-4}$
Systemic Loop Compartment Parameters				
Rbcai	$2.67x10^{7}$	Rbcaa	$4.93x10^{8}$	$kg\,m^{-4}s^{-1}$
Rbcav	$2.93x10^{8}$	Rlcci	$2.67x10^{7}$	$kg\,m^{-4}s^{-1}$
Rlcca	$9.7.x10^{8}$	Rlccv	$6.67x10^{8}$	$kg\,m^{-4}s^{-1}$
Rlsbi	$2.67x10^{7}$	Rlsba	$1.06x10^{9}$	$kg\,m^{-4}s^{-1}$
Rlsbv	$5.87x10^{8}$	Rdai	$4.93x10^{7y}$	$kg\,m^{-4}s^{-1}$
Rsat	$1.33x10^{7}$	Rsar	$6.03x10^{7}$	$kg\,m^{-4}s^{-1}$
Rscp	$6.03x10^{8}$	Rsvn	$6.67x10^{6}$	$kg\,m^{-4}s^{-1}$
Cbcaa	$4.45x10^{-9}$	Cbcav	$3.75x10^{-9}$	$m^{4}s^{2}\,kg^{-1}$
Clcca	$1.50x10^{-9}$	Clccv	$3.00x10^{-9}$	$m^{4}s^{2}\,kg^{-1}$
Clsba	$3.00x10^{-9}$	Clsbv	$3.38x10^{-9}$	$m^{4}s^{2}\,kg^{-1}$
Csat	$7.50x10^{-9}$	Csvn	$1.54x10^{-7}$	$m^{4}s^{2}\,kg^{-1}$
Lbca	$8.93x10^{4}$	Llcc	$2.75x10^{5}$	$kg\,m^{-4}$
Llsb	$7.33x10^{4}$	Lsat	$2.67x10^{4}$	$kg\,m^{-4}$
Pulmonary Loop Compartment Parameters				
Rpas	$2.67x10^{5}$	Rpat	$1.33x10^{7}$	$kg\,m^{-4}s^{-1}$
Rpar	$6.67x10^{6}$	Rpcp	$9.33x10^{6}$	$kg\,m^{-4}s^{-1}$
Rpvn	$8.00x10^{5}$			$kg\,m^{-4}s^{-1}$
Cpas	$1.35x10^{-9}$	Cpat	$2.85x10^{-8}$	$m^{4}s^{2}\,kg^{-1}$
Cpvn	$1.54x10^{-7}$			$m^{4}s^{2}\,kg^{-1}$
Lpas	$6.93x10^{3}$	Lpat	$2.27x10^{5}$	$kg\,m^{-4}$
VAD Compartment Parameters				
Ω	3000-8000			rpm

TABLE 7.1 – SUMMARY OF 0D MODEL PARAMETERS

RESULTS AND DISCUSSION 7.3

A three dimensional assisted aorta has been embedded in a 0D description of the cardiovascular system to investigate flow through the aortic valve under different LVAD operating conditions. Table 7.2 summarises the predicted response of the system, identifying whether the aortic valve opens (AV flow) and showing the time averaged left ventricular (LV) load and total cardiac output, which is defined as a combination of the flow through the LVAD and the aortic valve. As a reference, the healthy cardiac output for this particular patient, obtained from 2D MR flow data (as described in Chapter 3), is 4.54 $Lmin^{-1}$. The coupled model predicts the native valve will open when the pump is operating between 3000-5000 rpm. However, an appropriate cardiac output is only achieved when the pump is operating at 8000 rpm (Table 7.2). The average mechanical loading of the LV reduces as the pump operating rate is increased and importantly the volume remains positive, suggesting there is no ventricular suction in these configurations.

LVAD operation (rpm)	**AV flow?**	**Average LV load Volume (L)/Pressure (mmHg)**	**Cardiac Output ($Lmin^{-1}$)**
3000	Yes	0.1494/31.11	2.56
4000	Yes	0.1434/30.01	2.70
5000	Yes	0.1317/27.97	2.94
6000	No	0.1167/24.96	3.21
7000	No	0.0840/17.40	3.80
8000	No	0.0442/9.24	4.42

TABLE 7.2 – SUMMARY OF FULLY COUPLED LVAD SIMULATIONS

A detailed comparison of the systemic cardiovascular response, at four LVAD operating rates (4000, 5000, 6000 and 8000 rpm), are presented in Figure 7-2.

At pump rotation rates of ≤ 5000 rpm the ventricular pressure rises above the aortic pressure and the aortic valve opens (Figure 7-2). During this period flow through the

LVAD reduces and at rotation rates of ≤ 4000 rpm regurgitant flow is observed through the pump (Figure 7-2). The polynomial description of the LVAD is valid for negative flows but it is a phenomenon to be avoided as it is potentially detrimental to the patient. During ventricular support small thrombi/biological material builds up in regions of the impeller where the shear rates are insufficient to prevent adhesion. These deposits are generally asymptomatic and remain within the LVAD. However, in the event of regurgitant flow the distribution of the fluid shear stresses are altered and the deposits may become dislodged, passing into the systemic circulation and in the worst case resulting in a stroke or tissue ischemia due to the occlusion of an upstream vessel. Left ventricular pressure decreases as the pump rotation rate is increased, while the systemic pressure is seen to increase (Table 7.2 and Figure 7-2). The mechanical unloading (pressure and volume) of the LV has been identified as a positive factor in the reverse remodelling process of the myocardium [127, 128], and it thus important in achieving the end goal of pump explantation.

The work done by the LV can be computed from the area encompassed by the ventricular pressure-volume loop (Figure 7-3 - left), while the meridional LV wall stress (Figure 7-3 - right) can be approximated based on Laplace's law for thin walled structures (Equation 7-8) [52, 129, 130].

$$\sigma_\theta = \frac{P_{lv}{D_{lv}}^2}{4{h_{lv}}^2 - 4D_{lv}h_{lv}}$$

EQUATION 7-8

Where P_{lv}, D_{lv} and h_{lv} are the left ventricular pressure, diameter and thickness respectively. It is assumed that h_{lv} is 10mm and uniform throughout the chamber.

As the rotational rate of the pump is increased there is a reduction in the amount of work done by the LV (Figure 7-3 - left). There is a significant reduction in area and a change in the shape of the pressure-volume loops observed at pump speeds greater than 5000 rpm. The loops become narrower and more cone-like and correlate to configurations where the aortic valve no longer opens. This result suggests that although it is beneficial to open the aortic valve, to prevent aortic valve fusion and improve washout of the LV, in doing so the unloading of the LV and the cardiac

output is compromised. This presents a set of conflicting requirements which the engineers at Berlin Heart have attempted to resolve by developing an automatic speed reduction algorithm. The speed reduction strategy ensures good mechanical unloading of the LV and an appropriate total cardiac output is maintained for the majority of the time. However, the algorithm periodically reduces the pump rotation rate to encourage opening of the aortic valve. It is suggested that the current fully coupled modelling approach could be used to identify the reduction in speed necessary to ensure flow through the aortic valve, while preventing regurgitant flow in the LVAD.

The stresses experienced by the impaired myocardium follow a similar trend to the ventricular work and the ventricular pressure (Figure 7-2), reducing as the LVAD rotation rate is increased.

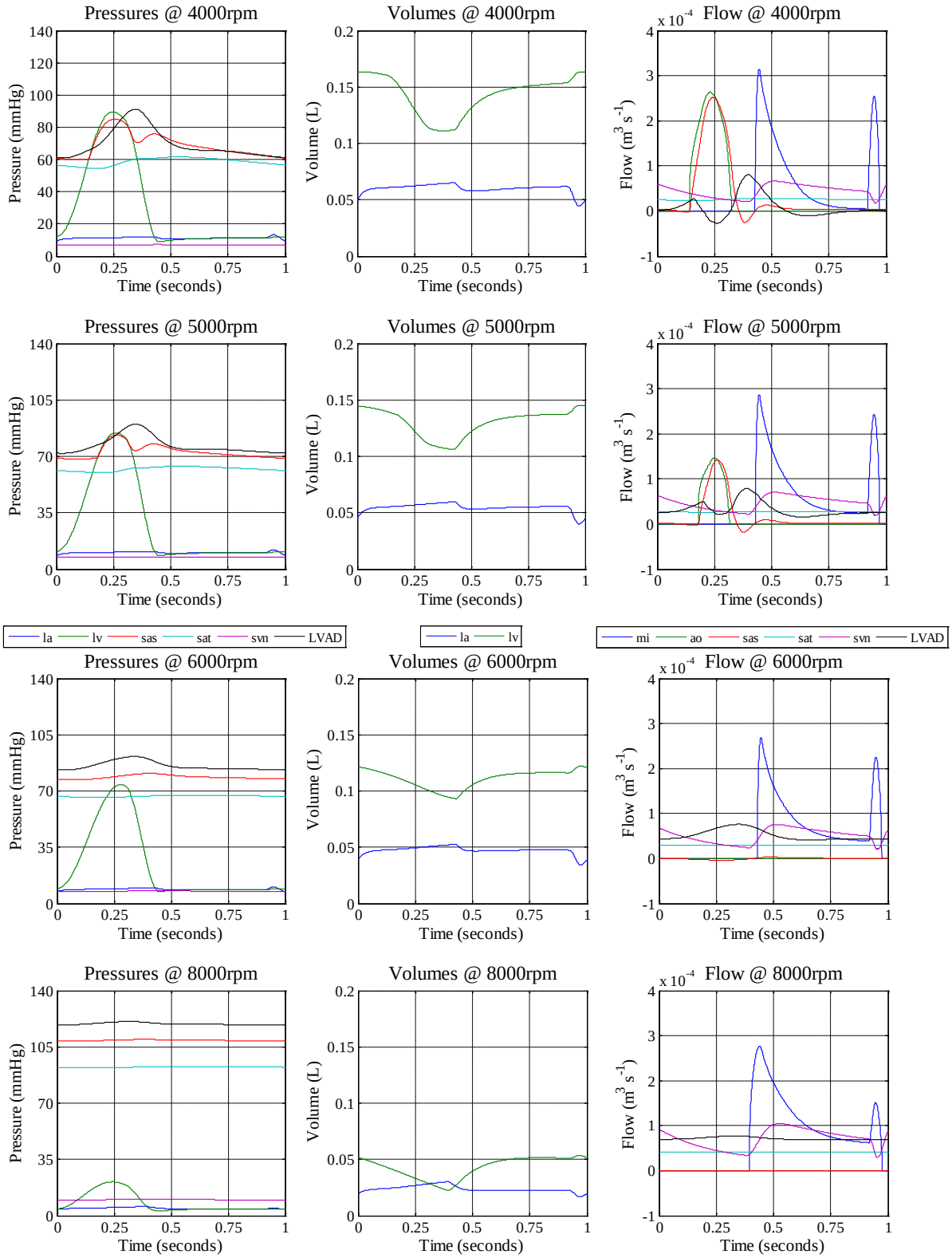

FIGURE 7-2 – COMPARISON OF SYSTEMIC RESPONSE AT DIFFERENT PUMP SPEEDS

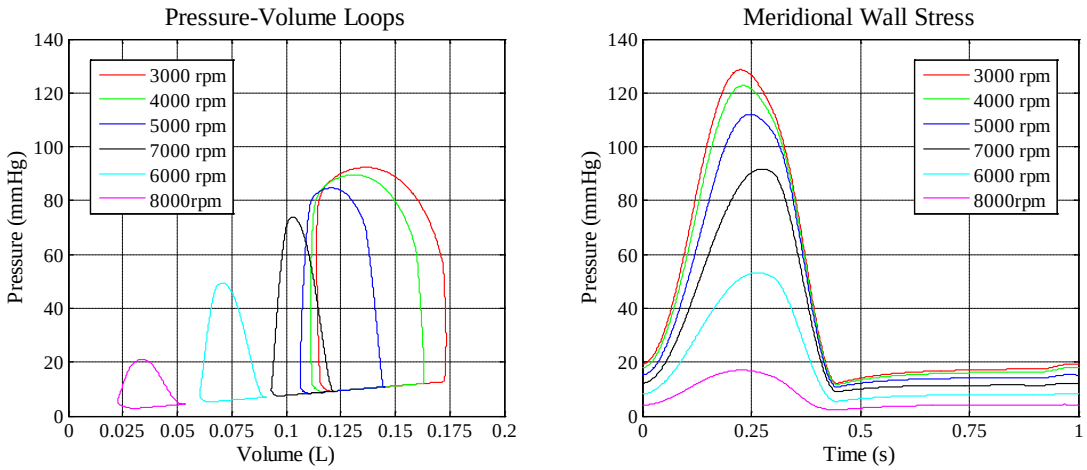

FIGURE 7-3 – LEFT VENTRICULAR PRESSURE-VOLUME LOOPS FOR THE DIFFERENT PUMP SPEEDS (LEFT) AND THE CIRCUMFERENTIAL WALL STRESS IN THE LEFT VENTRICLE (RIGHT)

An evaluation of the local haemodynamics in the assisted aorta is presented for at least two rates of rotation, namely 5000 rpm and 8000 rpm (Figure 7-5). Pump speeds of 5000 rpm and 8000 rpm were chosen as they represent conditions where the aortic valve opens but without regurgitant flow through the pump (5000 rpm) and where the patients required cardiac output is achieved (8000 rpm).

Figure 7-4 illustrates the influence of LVAD rotation rate on the fractional distribution of the blood and the form of the mass flow waveforms at the 3D model outlet boundaries. In all configurations where the aortic valve opens (3000-5000 rpm) the waveforms contain a significant degree of pulsatility. There is a delay of approximately 0.04 s between the opening of the aortic valve and the foot of the waveform reaching the descending aorta (Figure 7-2 and Figure 7-4). The length of the aorta is approximately 0.28 m, corresponding to a wave speed of 7 ms^{-1}. Although this is to be expected, since the properties of the compressible fluid were chosen to produce a wave speed of 7 ms^{-1}, the result gives further confidence in the results of the coupled simulation. It is worth noting that the apparent delay in the flow waveform, when the LVAD is operating at 5000 rpm compared to 3000/4000 rpm, is not due to a reduced wave speed in the aorta but rather the aortic valve opens later due to the increased aortic pressure. The fractional distribution of blood is maintained to within 1% in all model configurations. This result is similar to that reported in Chapter 6, where the use of a simple Windkessel termination ensured that

the local cannula position had little effect on the distribution of blood and further illustrates the merit of employing reduced order boundary conditions.

Cycle averaged velocity contour plots, at a number of cross-sections along the aorta and with vectors overlaid, are shown in Figure 7-5. In the 8000 rpm model the magnitudes are significantly higher than in the model with a slower operating speed (5000 rpm). This is to be expected since the cardiac output is lower in the 5000 rpm model. However, the vectors illustrate that, even in the presence of flow through the valve, the time averaged structure of the flow field is comparable to the configuration where the aortic valve does not open. It is stressed that this may not hold true as the heart undergoes reverse remodelling and hence the amount of flow through the valve increases. It is also not clear from the velocity contours whether the mixing of the fluid in the aorta is comparable at different pump speeds.

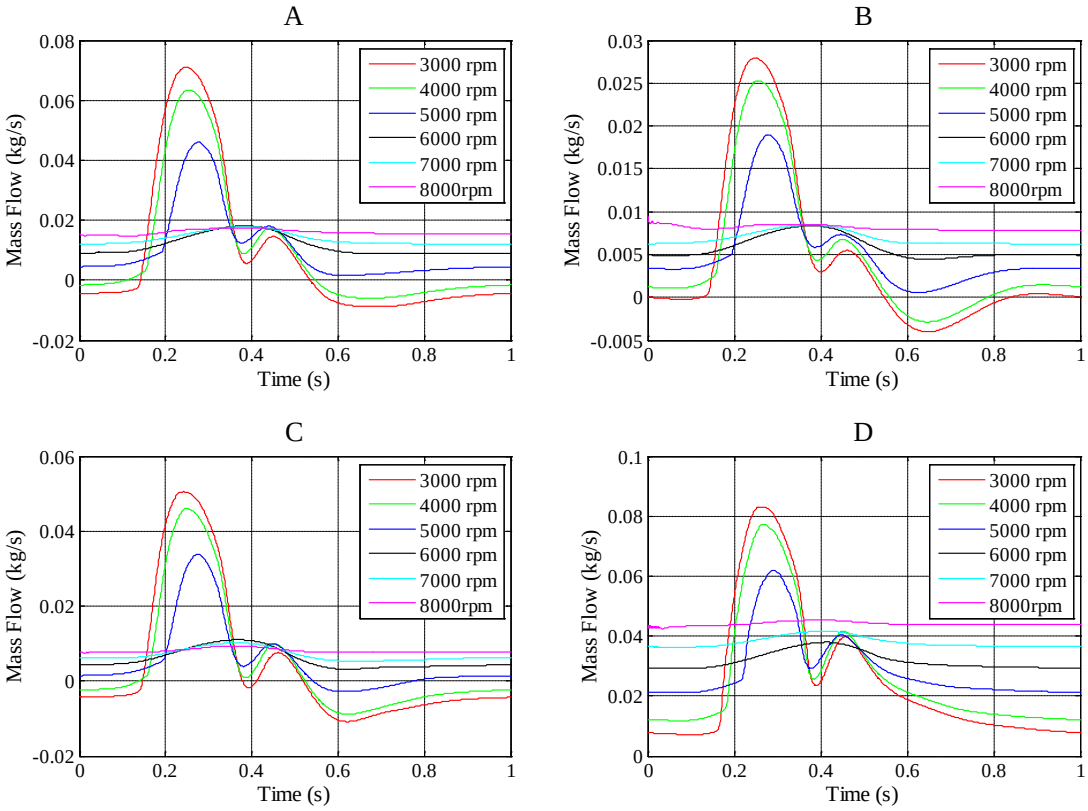

	A	B	C	D
3000 rpm	0.210	0.112	0.113	0.565
4000 rpm	0.210	0.110	0.112	0.568
5000 rpm	0.210	0.110	0.111	0.569
6000 rpm	0.211	0.110	0.111	0.568
7000 rpm	0.210	0.108	0.110	0.572
8000 rpm	0.210	0.108	0.110	0.572

FIGURE 7-4 – INFLUENCE OF LVAD OPERATING CONDITIONS ON THE MASS FLOW WAVEFORMS AND FRACTIONAL DISTRIBUTION, FULLY COUPLED MODEL.

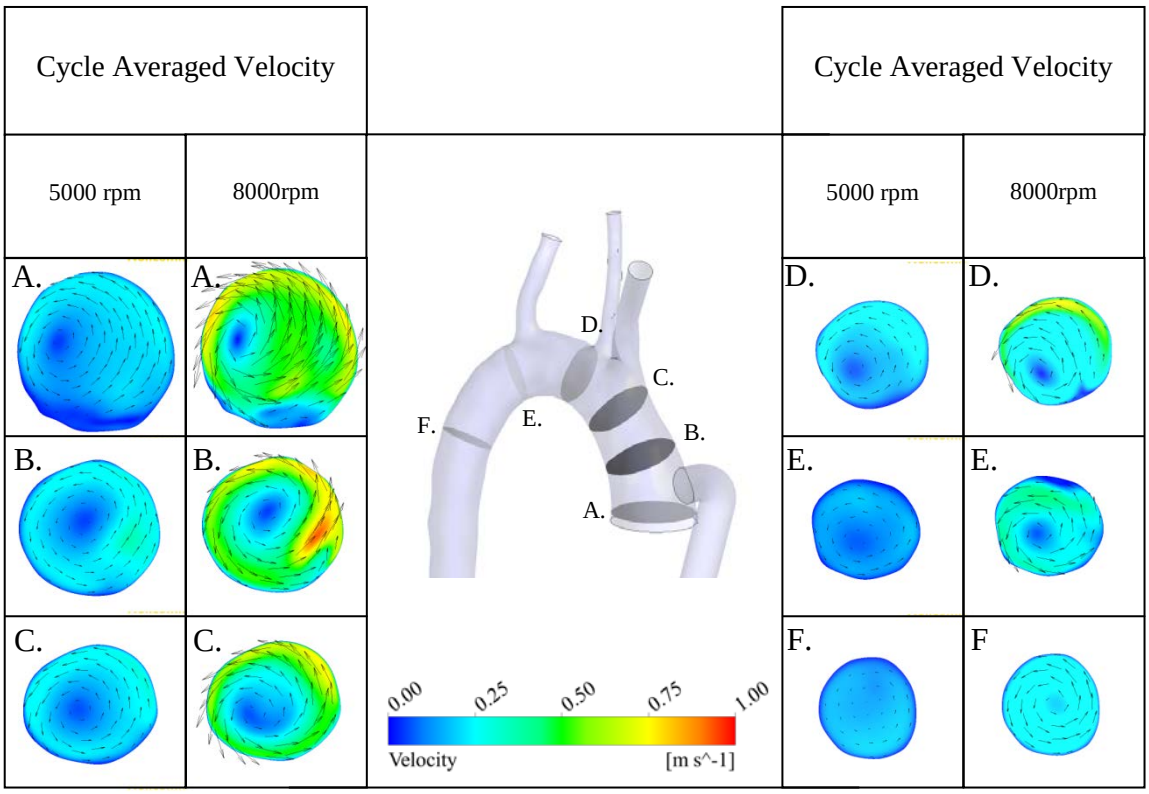

FIGURE 7-5 – COMPARISON OF CYCLE AVERAGED VELOCITY CONTOURS AS PREDICTED BY THE FULLY COUPLED MODEL, WITH THE LVAD OPERATING AT 5000 RPM AND 8000 RPM.

The quantitative measure of mixing, presented initially in Chapter 6, is employed to compare the degree of mixing in the assisted aorta under the varying levels of LVAD support. As before the particles are released from a plane located in the aortic valve region (Figure 7-5, plane A). Figure 7-6 illustrates the relative entropy at a number of planes of interest, for all LVAD operating conditions, and the particle distributions are shown in Figure 7-7. Visualisation of the particle distribution clearly illustrates the differences in the aortic flow field under the varying degrees of LVAD support. With the LVAD operating at 3000 rpm the particle distributions are similar to those of the native flow field (Figure 6.11) and the fluid moving up into the supra-aortic arteries appears to come from the central core of fluid (blue particles). In contrast, as the LVAD rotation rate is increased to 4000 rpm and 5000 rpm the distribution of particles appears visibly more mixed (this observation is supported by the relative entropy measure, Figure 7-6) and the fluid moving up into the supra-aortic arteries now appears to have come from both the central core and the annulus of fluid near the wall of the aorta (blue and red particles respectively). The

point at which the aortic valve no longer opens is clearly identifiable from the particle distributions. In configurations where the LVAD is operating at greater than 5000 rpm the particles in the ascending aorta are no longer distributed across the entire plane but instead cluster around the wall (Figure 7-7). This phenomenon was explored in Chapter 6 and is a result of the fluid attaching to the wall, forming a fast moving spiral structure that remains attached as it moves along the ascending aorta and through the arch.

In simulations where the aortic valve remains closed the relative entropy or mixing increases to a plateau in the ascending aorta, which reduces to a minimum in the aortic arch (Figure 7-6 - plane D) before rising again as it enters the descending aorta. In the models where the aortic valve opens (excluding 3000 rpm) there is a slower steady increase in the relative entropy as the fluid moves through the aorta before reaching a peak in the descending aorta. Once again with the exception of the slowest rotation rate, the quantitative degree of mixing appears to be converging for all LVAD rotation rates at the final plane (Figure 7-6 - plane F).

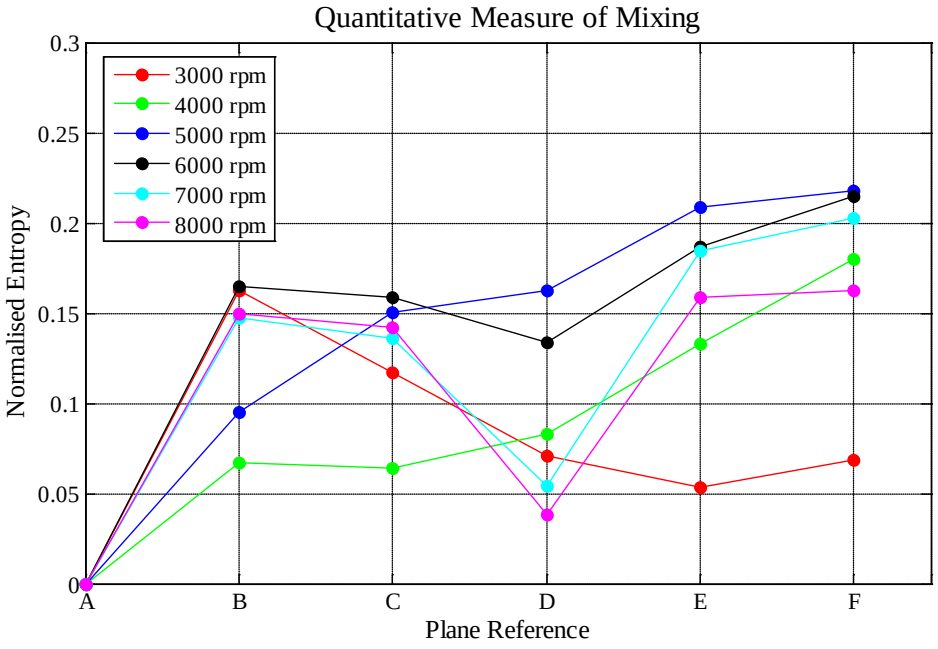

FIGURE 7-6 – NORMALISED INFORMATION ENTROPY (κ) IN THE ASSISTED AORTA AT THE DIFFERENT LVAD ROTATION RATES.

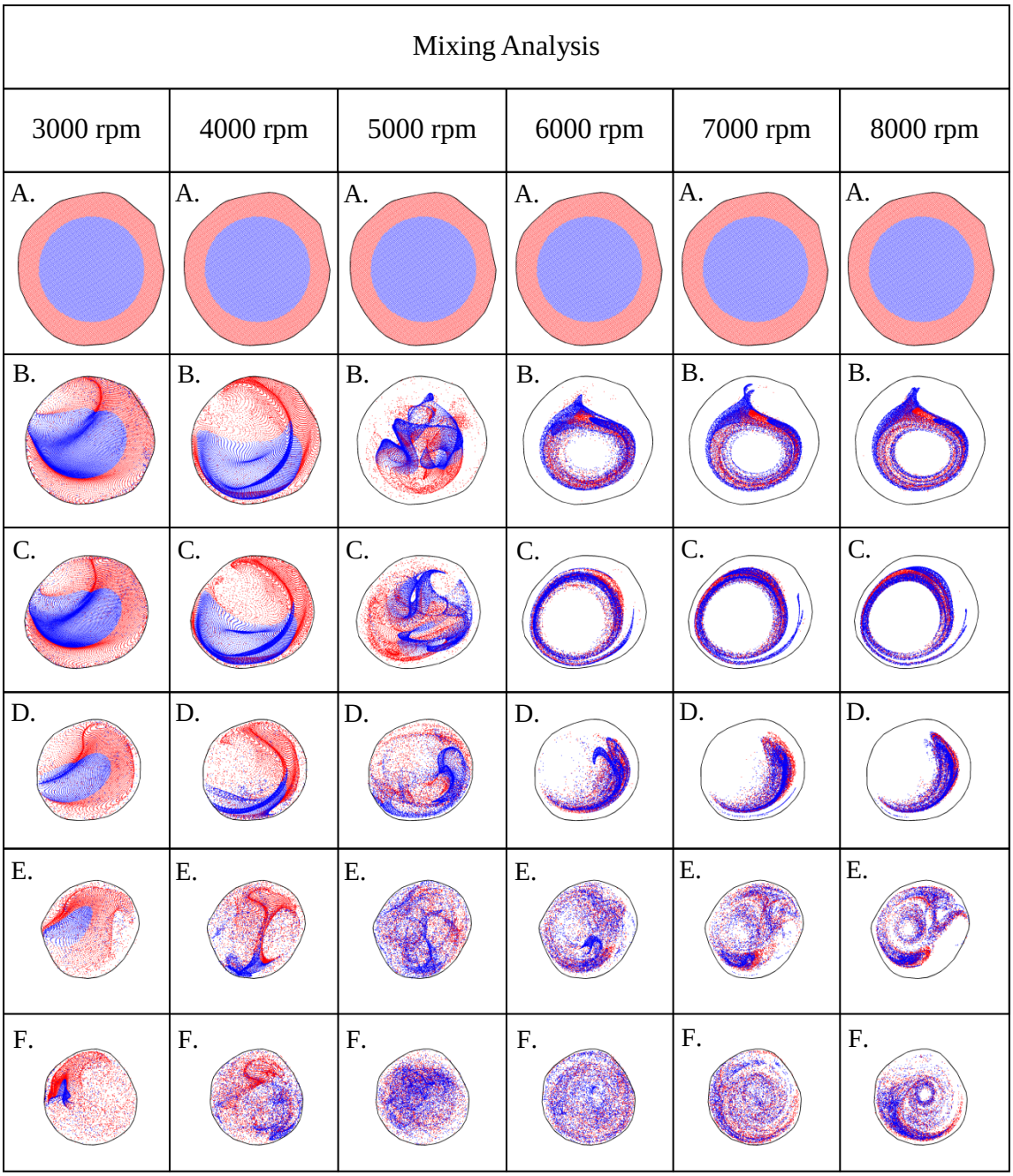

FIGURE 7-7 – ILLUSTRATION OF THE PARTICLE MIXING IN THE ASSISTED AORTA AT THE DIFFERENT LVAD ROTATION RATES (PLANE LOCATIONS CORRESPOND TO FIGURE 7.5).

CONCLUSIONS 7.4

A three dimensional model of a patient-specific thoracic aorta has been embedded in a comprehensive 0D description of the assisted vasculature. The fully coupled simulation has been used to identify under what LVAD operating conditions the aortic valve will open. This is particularly important to inhibit aortic valve fusion and has the additional advantage of improving the washout of the left ventricle.

The entropic measure of mixing, initially introduced in Chapter 6, was used to evaluate the degree of mixing in the aortic flow field under the different LVAD operating conditions. The higher pump speeds resulted in greater immediate levels of fluid mixing in the ascending aorta, which decayed rapidly through the aortic arch. In contrast the lower operational speeds produced shallower gradients of the mixing quantity in the ascending aorta but grew steadily along the length of the aorta.

The fully coupled simulations demonstrated that in the particular case investigated, i.e. a patient suffering from mild left ventricular failure, LVAD (Berlin Heart INCOR) rotation rates of 5000 rpm or less resulted in flow through the aortic valve. In order, to prevent regurgitant flow through the pump the rotation rate must be greater than 4000 rpm. At a pump speed of 5000 rpm the total cardiac output is 2.94 $Lmin^{-1}$. This is 1.6 $Lmin^{-1}$ lower than the required cardiac output and is clearly insufficient to ensure adequate perfusion of the peripheral vasculature. To achieve the required output the LVAD must operate at approximately 8000 rpm, in which case the aortic valve remains closed. These two goals present conflicting requirements. To overcome this, the Berlin Heart INCOR LVAD implements an automatic speed reduction algorithm that periodically reduces the pump speed to allow the aortic valve to open. It is proposed that the described model presents an exciting opportunity to tune the speed reduction algorithm to ensure the aortic valve will open but without the occurrence of regurgitant flow through the pump.

CHAPTER 8

CONCLUSIONS

The aim of this thesis was to characterise the local aortic and systemic haemodynamics in the presence of a left ventricular assist device.

The first step in achieving this goal was to assess the accuracy of the local flow field predictions using CFD (ANSYS-CFX). An idealised benchmark, designed by the FDA to replicate flow fields relevant to the cardiovascular system and specifically to cardiovascular devices, was simulated at a number of flow rates and the results compared to data acquired experimentally. The CFD predictions were in close agreement to the experimental data whilst the flow remained laminar but were found to vary downstream of the sudden expansion as the flow field became turbulent. The CFD predictions for the transitional and turbulent flow fields, when compared to the experimental data, were found to be overly dissipative as the fluid moved through the sudden expansion. It was proposed that this variation would be reduced in an aortic geometry. Numerical prediction of the onset location of turbulence in an unimpeded jet of fluid is notoriously difficult, especially in symmetrical systems with such sensitive flow rates. In the case of the aorta any jet of blood that rises from the flow field will interact with a wall after a relatively short distance.

A challenging aspect of CFD simulation is the application of appropriate and realistic boundary conditions. In this thesis a minimisation approach was developed and implemented in Matlab to tune the parameters of a simple 0D representation of the downstream vasculature to elicit a desired response. The approach was tested in a single outlet system with an exact solution and performed well. The added complexity posed by a real situation in terms of multiple branches and the lack of an exact solution, for the 0D parameters, was shown to require multiple iterations of both the 3D solution and the optimisation algorithm before a reasonable match to the clinical data could be achieved.

To faithfully represent the local haemodynamics of the cardiovascular system one should employ numerical simulations which consider the interaction of the blood with the elastic vessel wall. However, these simulations suffer from high computational requirements and the need for detailed information regarding wall thickness, material properties and external support that may not be available. An alternative approach, employing a compressible fluid to capture the gross wave propagation effects, was compared to a full FSI simulation and a rigid walled incompressible fluid model in three geometries:

1. Uniform cylindrical vessel with properties similar to the aorta
2. Patient-specific aorta
3. Patient-specific aorta in the presence of an LVAD

The compressible fluid model accurately captured the time lag associated with the propagating waves and required approximately $1/20^{th}$ of the computational time needed to perform an FSI simulation. As one might expect, rigid walled models were unable to accurately predict the FSI WSS magnitudes but the compressible fluid model produced comparable distributions of WSS. As such it is suggested that the compressible fluid model offers a computationally efficient alternative to full FSI models especially in situations where multiple configurations require testing (e.g. LVAD cannula placement).

The peak Reynolds number in the human aorta is reported to range from 400-8900 [75], encompassing both laminar and turbulent regimes. However, aortic flow is pulsatile and since turbulence requires time to develop there is a divided opinion in

the scientific community as to whether a turbulence model is required, or if current models are appropriate for the transitional state, to accurately simulate aortic haemodynamics. In this thesis the influence of a turbulence model was assessed in both steady state and transient simulations of a native and assisted patient specific aorta. Mesh sensitivity studies were conducted for both the assisted and unassisted case, employing steady state analyses. It was concluded that to ensure mesh independence in both native and assisted aortas a maximum edge length of ≤ 0.75 mm is required, correlating to a number of elements of the order 10^6.

Steady state laminar simulations of the native aorta at peak flow failed to converge, while the laminar and turbulent simulations demonstrated close agreement under steady state conditions at a Reynolds number of approximately 1000. Under transient conditions the laminar and turbulent simulations are also in agreement with the same structures predicted by both numerical models. In this specific case the laminar model is appropriate. However, since the turbulent model can capture the characteristics of the flow field under both low and high Reynolds number conditions it is suggested that it should be the analysis method of choice.

In the assisted aorta the steady laminar simulations also failed to converge but unlike the native aorta the transient laminar simulations predicted different structures in the flow field when compared to the turbulent simulation. Based on the findings in Chapter 2 and the results for the native aorta the turbulence model is considered imperative when simulating assisted aortic flow fields.

The finding described in Chapters 4 and 5 were combined in Chapter 6 to investigate the influence of the local LVAD outflow cannula position on the aortic flow field. A turbulent simulation, with a compressible fluid, was used to simulate the different flow fields and an entropic measure was employed to evaluate the degree of mixing in each cannula configuration. It was discovered that by offsetting the cannula to the right, on a transverse plane normal to the axis of the ascending aorta, the fluid swiftly attached to the vessel wall, resulting in a more rapid washout of the ascending aorta and reduced regions of low wall shear stress, which are associated with the development of atherosclerosis.

To fully achieve the aim of this thesis, i.e. *"to characterise the local and systemic haemodynamics in the presence of a LVAD"*, a 3D model of patient-specific assisted aorta was embedded in a comprehensive 0D description of the assisted cardiovascular system. The fully coupled model allows detailed interrogation of the local flow features in the assisted aorta while modelling the gross behaviour of the systemic and pulmonary loops as well as the function of the heart. This model was employed to identify conditions under which the aortic valve opened, thereby reducing the risk of aortic valve fusion and improving washout of the left ventricle. In the specific case investigated, a patient with mild left heart failure simulating partial recovery of the myocardium, blood flowed through the aortic valve when the LVAD was operating at 5000 rpm or less. However, to achieve a reasonable cardiac output the LVAD was required to operate at 8000 rpm. The Berlin Heart INCOR LVAD incorporates an automatic speed reduction algorithm which periodically reduces the pump speed to encourage the aortic valve to open while maintaining a reasonable cardiac output for the rest of the time. It is proposed that the fully coupled model could compliment this control strategy by quantifying the degree of speed reduction necessary for a specific patient's aortic valve to open.

FUTURE WORK 8.1

Although attempts have been made to ensure the numerical models faithfully represent the physics of the system (FDA benchmark, analysis strategies and laminar vs. turbulent work), further experimental validation within a realistic aortic or assisted aortic geometry would give further confidence in the local flow field predictions and the subsequent conclusions that are drawn.

In the author's view an even more important continuation of this work is the evaluation of the fully coupled model as a tool to improve LVAD control strategies for individual patients. In this thesis the 0D model of the cardiovascular system was tuned to elicit a generic response in a patient suffering from left ventricular failure. As such the results, although demonstrating the potential of the tool, are at present purely academic. Detailed patient data would allow the parameters of the 0D model

to be personalised, enabling the simulations to offer a truly useful and informative tool.

Another area that would benefit from further study is the effect of backward travelling waves on the apparent wave speed (i.e. the rate at which a pressure or flow wave propagates) in an elastic vessel. Currently the apparent aortic wave speed is often used to infer the mechanical properties of the aortic wall. However, the analytical investigation of a uniform cylinder, presented in Chapter 4, demonstrates that the relative magnitude of the forward and backward travelling waves also influences the apparent wave speed.

REFERENCES

[1] P. Scarborough, P. Bhatnagar, K. Wickramasinghe, K. Smolina, C. Mitchel, and M. Rayner, "Coronary Heart Disease Statistics 2010 Edition," British Heart Foundation Health Promotion Research Group, Department of Public Health, University of Oxford2010.

[2] NHS, "Transplant Activity in the UK," ed, 2008.

[3] I. Avrahami, M. Rosenfeld, and S. Einav, "The hemodynamics of the berlin pulsatile VAD and the role of its MHV configuration," *Annals of Biomedical Engineering,* vol. 34, pp. 1373-1388, 2006.

[4] H. G. Wood, A. L. Throckmorton, A. Untaroiu, and X. W. Song, "The medical physics of ventricular assist devices," *Reports on Progress in Physics,* vol. 68, pp. 545-576, 2005.

[5] A. K. Mahmood, J. M. Courtney, S. Westaby, M. Akdis, and H. Reul, "Critical review of current left ventricular assist devices," *Perfusion-Uk,* vol. 15, pp. 399-420, 2000.

[6] D. Legendre, P. Antunes, E. Bock, A. Andrade, J. F. Biscegli, and J. P. Ortiz, "Computational fluid dynamics investigation of a centrifugal blood pump," *Artificial Organs,* vol. 32, pp. 342-348, 2008.

[7] A. L. Throckmorton, A. Untaroiu, P. E. Allaire, H. G. Wood, G. P. Matherne, D. S. Lim, B. B. Peeler, and D. B. Olsen, "Computational analysis of an axial flow pediatric ventricular assist device," *Artif Organs,* vol. 28, pp. 881-91, Oct 2004.

[8] S. Vandenberghe, T. Nishida, P. Segers, B. Meyns, and P. Verdonck, "The impact of pump speed and inlet cannulation site on left ventricular unloading with a rotary blood pump," *Artificial Organs,* vol. 28, pp. 660-667, 2004.

[9] T. Korakianitis and Y. Shi, "Numerical comparison of hemodynamics with atrium to aorta and ventricular apex to aorta VAD support," *ASAIO Journal,* vol. 53, pp. 537-48, Sep-Oct 2007.

[10] M. McCormick, D. Nordsletten, D. Kay, and N. Smith, "Modelling left ventricular function under assist device support," *International Journal for Numerical Methods in Biomedical Engineering,* vol. 27, pp. 1073-1095, Jul 2011.

[11] K. N. Litwak, S. C. Koenig, R. C. Cheng, G. A. Giridharan, K. J. Gillars, and G. M. Pantalos, "Ascending aorta outflow graft location and pulsatile ventricular assist provide optimal hemodynamic support in an adult mock circulation," *Artificial Organs,* vol. 29, pp. 629-635, 2005.

[12] P. L. DiGiorgi, D. L. Smith, A. D. Can, and M. C. Oz, "Flow differences between ascending and descending LVAD outflow," *The Journal of Heart and Lung Transplantation*, vol. 21, pp. 151-152, 2002.

[13] B. Kar, R. M. Delgado, O. H. Frazier, I. D. Gregoric, M. T. Harting, Y. Wadia, T. J. Myers, R. D. Moser, and J. Freund, "The effect of LVAD investigation aortic outflow-graft placement on hemodynamics and flow - Implantation technique and computer flow modeling," *Texas Heart Institute Journal*, vol. 32, pp. 294-298, 2005.

[14] K. D. May-Newman, B. K. Hillen, C. S. Sironda, and W. Dembitsky, "Effect of LVAD outflow conduit insertion angle on flow through the native aorta," *J Med Eng Technol*, vol. 28, pp. 105-9, May-Jun 2004.

[15] M. Laumen, T. Kaufmann, D. Timms, P. Schlanstein, S. Jansen, S. Gregory, K. C. Wong, T. Schmitz-Rode, and U. Steinseifer, "Flow Analysis of Ventricular Assist Device Inflow and Outflow Cannula Positioning Using a Naturally Shaped Ventricle and Aortic Branch," *Artificial Organs*, vol. 34, pp. 798-806, Oct 2010.

[16] A. G. Brown, Y. Shi, A. Arndt, J. Mueller, P. Lawford, and D. R. Hose, "Importance of realistic LVAD profiles for assisted aortic simulations: evaluation of optimal outflow anastomosis locations," *Computer Methods in Biomechanics and Biomedical Engineering*, 2011.

[17] M. Minakawa, I. Fukuda, J. Yamazaki, K. Fukui, H. Yanaoka, and T. Inamura, "Effect of cannula shape on aortic wall and flow turbulence: Hydrodynamic study during extracorporeal circulation in mock thoracic aorta," *Artificial Organs*, vol. 31, pp. 880-886, 2007.

[18] S. Stuehle, D. Wendt, H. Jakob, and W. Kowalczyk, "Numerical simulation of hemodynamics in the ascending aorta induced by different aortic cannulas," *Minimally Invasive Therapy & Allied Technologies*, vol. 20, pp. 125-131, Apr 2011.

[19] J. H. Connelly, J. Abrams, T. Klima, W. K. Vaughn, and O. H. Frazier, "Acquired commissural fusion of aortic valves in patients with left ventricular assist devices," *J Heart Lung Transplant*, vol. 22, pp. 1291-5, Dec 2003.

[20] A. G. Rose, S. J. Park, A. J. Bank, and L. W. Miller, "Partial aortic valve fusion induced by left ventricular assist device," *Annals of Thoracic Surgery*, vol. 70, pp. 1270-1274, 2000.

[21] J. O. Mudd, J. D. Cuda, M. Halushka, K. A. Soderlund, J. V. Conte, and S. D. Russell, "Fusion of aortic valve commissures in patients supported by a continuous axial flow left ventricular assist device," *J Heart Lung Transplant*, vol. 27, pp. 1269-74, Dec 2008.

[22] J. E. Banchs, B. Dawn, A. Abdel-Latif, A. Qureshi, N. Agrawal, M. Bouvette, and M. F. Stoddard, "Acquired aortic cusp fusion after chronic left ventricular assist device support," *J Am Soc Echocardiogr,* vol. 19, pp. 1401 e1-3, Nov 2006.

[23] J. Muller, "Private Communication - Berlin Heart GmbH," ed, 2009.

[24] J. A. Crestanello, D. A. Orsinelli, M. S. Firstenberg, and C. Sai-Sudhakar, "Aortic valve thrombosis after implantation of temporary left ventricular assist device," *Interact Cardiovasc Thorac Surg,* vol. 8, pp. 661-2, Jun 2009.

[25] T. Nishimura, E. Tatsumi, S. Takaichi, Y. Taenaka, Y. Wakisaka, T. Nakatani, T. Masuzawa, Y. Takewa, M. Nakamura, S. Endo, M. Nakata, and H. Takano, "Prolonged nonpulsatile left heart bypass with reduced systemic pulse pressure causes morphological changes in the aortic wall," *Artif Organs,* vol. 22, pp. 405-10, May 1998.

[26] Y. C. Fung, *Biomechanics: Circulation*, 2nd Edition ed.: Springer, 1997.

[27] J. R. Womersley, "Oscillatory flow in arteries: the constrained elastic tube as a model of arterial flow and pulse transmission," *Physics in Medicine & Biology,* vol. 2, pp. 178-87, Oct 1957.

[28] G. K. Batchelor, *An Introduction to Fluid Mechanics*: Cambridge University Press, 1967.

[29] T. Korakianitis and Y. Shi, "Numerical simulation of cardiovascular dynamics with healthy and diseased heart valves," *J Biomech,* vol. 39, pp. 1964-82, 2006.

[30] F. Liang and H. Liu, "A Closed-Loop Lumped Parameter Computational Model for Human Cardiovascular System," *JSME International Journal,* vol. 48, p. 10, 2005.

[31] J. R. Womersley, "Method for the calculation of velocity, rate of flow and viscous drag in arteries when the pressure gradient is known," *Journal of Physiology,* vol. 127, pp. 553-63, Mar 28 1955.

[32] J. R. Womersley, "Oscillatory flow in arteries: effect of radial variation in viscosity on rate of flow," *Journal of Physiology,* vol. 127, pp. 38-9P, Feb 28 1955.

[33] F. N. van de Vosse and N. Stergiopulos, "Pulse Wave Propagation in the Arterial Tree," *Annual Review of Fluid Mechanics, Vol 43,* vol. 43, pp. 467-499, 2011.

[34] Y. Shi, P. Lawford, and R. Hose, "Review of zero-D and 1-D models of blood flow in the cardiovascular system.," *Biomed Eng Online,* vol. 10, p. 33, 2011.

[35] N. Westerhof, N. Stergiopulos, and M. I. M. Noble, *Snapshots of Hemodynamics: An Aid for Clinical Research and Graduate Education*: Springer, 2005.

[36] C. Caro, T. Pedley, R. Schroter, and W. Seed, *The Mechanics of the Circulation*: Oxford University Press, 1978.

[37] O. Frank, "Die Grundfurm des arteriellen Pulses. Erste Abhandlung. Mathematische Analyse," *Z. Biol,* vol. 37, pp. 483-526, 1899.

[38] C. M. Quick, D. S. Berger, D. A. Hettrick, and A. Noordergraaf, "True arterial system compliance estimated from apparent arterial compliance," *Annals of Biomedical Engineering,* vol. 28, pp. 291-301, 2000.

[39] M. S. Olufsen and A. Nadim, "On deriving lumped models for blood flow and pressure in the systemic arteries," *Mathematical Biosciences and Engineering,* vol. 1, pp. 61-80, Jun 2004.

[40] S. M. Toy, J. Melbin, and A. Noordergraaf, "Reduced models of arterial systems," *IEEE Transactions on Biomedical Engineering,* vol. 32, pp. 174-6, Feb 1985.

[41] W. W. Nichols, C. R. Conti, W. E. Walker, and W. R. Milnor, "Input impedance of the systemic circulation in man," *Circulation Research,* vol. 40, pp. 451-8, May 1977.

[42] J. P. Murgo, N. Westerhof, J. P. Giolma, and S. A. Altobelli, "Aortic input impedance in normal man: relationship to pressure wave forms," *Circulation,* vol. 62, pp. 105-16, Jul 1980.

[43] G. Landes, "Einige untersuchungen an elektrischen analogieschaltungen zum kreitslaufsystem," *Z.Biol,* vol. 101, pp. 418-429, 1943.

[44] N. Westerhof, G. Elzinga, and P. Sipkema, "An artificial arterial system for pumping hearts," *Journal of Applied Physiology,* vol. 31, pp. 776-81, Nov 1971.

[45] J. K. Li, "Time domain resolution of forward and reflected waves in the aorta," *IEEE Transactions on Biomedical Engineering,* vol. 33, pp. 783-5, Aug 1986.

[46] G. F. Mitchell, J. C. Tardif, J. M. Arnold, G. Marchiori, T. X. O'Brien, M. E. Dunlap, and M. A. Pfeffer, "Pulsatile hemodynamics in congestive heart failure," *Hypertension,* vol. 38, pp. 1433-9, Dec 1 2001.

[47] R. Burattini and G. Gnudi, "Computer identification of models for the arterial tree input impedance: comparison between two new simple models and first experimental results," *Medical & Biological Engineering & Computing,* vol. 20, pp. 134-44, Mar 1982.

[48] P. Segers, E. R. Rietzschel, M. L. De Buyzere, N. Stergiopulos, N. Westerhof, L. M. Van Bortel, T. Gillebert, and P. R. Verdonck, "Three- and four-element Windkessel models: assessment of their fitting performance in a large cohort of healthy middle-aged individuals," *Proceedings of the Institution of Mechanical Engineers,* vol. Part H - Journal of Engineering in Medicine. 222, pp. 417-28, May 2008.

[49] B. Deswysen, A. A. Charlier, and M. Gevers, "Quantitative evaluation of the systemic arterial bed by parameter estimation of a simple model.," *Med Biol Eng Comput,* vol. 18, pp. 153-66, Mar 1980.

[50] M. K. Sharp, G. M. Pantalos, L. Minich, L. Y. Tani, E. C. McGough, and J. A. Hawkins, "Aortic input impedance in infants and children," *Journal of Applied Physiology,* vol. 88, pp. 2227-2239, Jun 2000.

[51] T. Korakianitis and Y. Shi, "A concentrated parameter model for the human cardiovascular system including heart valve dynamics and atrioventricular interaction," *Medical Engineering & Physics,* vol. 28, pp. 613-28, Sep 2006.

[52] Y. Shi and T. Korakianitis, "Numerical simulation of cardiovascular dynamics with left heart failure and in-series pulsatile ventricular assist device," *Artificial Organs,* vol. 30, pp. 929-48, Dec 2006.

[53] Y. Shi, A. G. Brown, and D. R. Hose, "Computational Modelling and Evaluation of Cardiovascular Response under Pulsatile Impeller Pump Support," *Interface Focus,* vol. [In Press], 2011.

[54] H. Tsuruta, T. Sato, M. Shirataka, and N. Ikeda, "Mathematical-Model of Cardiovascular Mechanics for Diagnostic-Analysis and Treatment of Heart-Failure .1. Model Description and Theoretical-Analysis," *Medical & Biological Engineering & Computing,* vol. 32, pp. 3-11, Jan 1994.

[55] M. Ursino, "A mathematical model of the carotid baroregulation in pulsating conditions," *IEEE Trans Biomed Eng,* vol. 46, pp. 382-92, Apr 1999.

[56] C. A. J. Fletcher, *Computational Techniques for Fluid Dynamics* vol. 1: Springer-Verlag, 1988.

[57] S. J. Weston, N. B. Wood, G. Tabor, A. D. Gosman, and D. N. Firmin, "Combined MRI and CFD analysis of fully developed steady and pulsatile laminar flow through a bend," *Jmri-Journal of Magnetic Resonance Imaging,* vol. 8, pp. 1158-1171, Sep-Oct 1998.

[58] S. C. Shadden, M. Astorino, and J.-F. Gerbeau, "Computational analysis of an aortic valve jet with Lagrangian coherent structures," *Chaos,* vol. 20, Mar 2010.

[59] I. E. Vignon-Clementel, C. A. Figueroa, K. E. Jansen, and C. A. Taylor, "Outflow boundary conditions for three-dimensional finite element modeling

of blood flow and pressure in arteries," *Computer Methods in Applied Mechanics and Engineering,* vol. 195, pp. 3776-3796, 2006.

[60] P. Moireau, N. Xiao, M. Astorino, C. A. Figueroa, D. Chapelle, C. A. Taylor, and J. F. Gerbeau, "External tissue support and fluid-structure simulation in blood flows," *Biomech Model Mechanobiol,* Feb 10 2011.

[61] H. J. Kim, I. E. Vignon-Clementel, C. A. Figueroa, J. F. LaDisa, K. E. Jansen, J. A. Feinstein, and C. A. Taylor, "On Coupling a Lumped Parameter Heart Model and a Three-Dimensional Finite Element Aorta Model," *Annals of Biomedical Engineering,* vol. 37, pp. 2153-2169, Nov 2009.

[62] J. A. Feinstein, J. S. Coogan, F. P. Chan, and C. A. Taylor, "Computational Fluid Dynamic Simulations of Aortic Coarctation Comparing the Effects of Surgical- and Stent-Based Treatments on Aortic Compliance and Ventricular Workload," *Catheterization and Cardiovascular Interventions,* vol. 77, pp. 680-691, Apr 1 2011.

[63] Y. Bazilevs, J. R. Gohean, T. J. R. Hughes, R. D. Moser, and Y. Zhang, "Patient-specific isogeometric fluid-structure interaction analysis of thoracic aortic blood flow due to implantation of the Jarvik 2000 left ventricular assist device," *Computer Methods in Applied Mechanics and Engineering,* vol. 198, pp. 3534-3550, 2009.

[64] P. J. Kilner, G. Z. Yang, R. H. Mohiaddin, D. N. Firmin, and D. B. Longmore, "Helical and retrograde secondary flow patterns in the aortic arch studied by three-directional magnetic resonance velocity mapping," *Circulation,* vol. 88, pp. 2235-47, Nov 1993.

[65] U. Morbiducci, R. Ponzini, G. Rizzo, M. Cadioli, A. Esposito, F. M. Montevecchi, and A. Redaelli, "Mechanistic insight into the physiological relevance of helical blood flow in the human aorta: an in vivo study," *Biomechanics and Modeling in Mechanobiology,* vol. 10, pp. 339-355, Jun 2011.

[66] U. Morbiducci, R. Ponzini, G. Rizzo, M. Cadioli, A. Esposito, F. De Cobelli, A. Del Maschio, F. M. Montevecchi, and A. Redaelli, "In Vivo Quantification of Helical Blood Flow in Human Aorta by Time-Resolved Three-Dimensional Cine Phase Contrast Magnetic Resonance Imaging," *Annals of Biomedical Engineering,* vol. 37, pp. 516-531, Mar 2009.

[67] T. A. Hope, M. Markl, L. Wigstrom, M. T. Alley, D. C. Miller, and R. J. Herfkens, "Comparison of flow patterns in ascending aortic aneurysms and volunteers using four-dimensional magnetic resonance velocity mapping," *Journal of Magnetic Resonance Imaging,* vol. 26, pp. 1471-1479, Dec 2007.

[68] H. K. Moffatt and A. Tsinober, "HELICITY IN LAMINAR AND TURBULENT-FLOW," *Annual Review of Fluid Mechanics,* vol. 24, pp. 281-312, 1992 1992.

[69] H. Suga, K. Sagawa, and A. A. Shoukas, "LOAD INDEPENDENCE OF INSTANTANEOUS PRESSURE-VOLUME RATIO OF CANINE LEFT VENTRICLE AND EFFECTS OF EPINEPHRINE AND HEART-RATE ON RATIO," *Circulation Research,* vol. 32, pp. 314-322, 1973 1973.

[70] C. A. Figueroa, I. E. Vignon-Clementel, K. E. Jansen, T. J. R. Hughes, and C. A. Taylor, "A coupled momentum method for modeling blood flow in three-dimensional deformable arteries," *Computer Methods in Applied Mechanics and Engineering,* vol. 195, pp. 5685-5706, 2006.

[71] S. Stewart, "Computational Fluid Dynamics: An FDA Crtitical Path Initiative," 2008.

[72] F. Durst, S. Ray, B. Unsal, and O. A. Bayoumi, "The development lengths of laminar pipe and channel flows," *Journal of Fluids Engineering-Transactions of the Asme,* vol. 127, pp. 1154-1160, Nov 2005.

[73] K. Ahmad, M. Abdullah, and J. Watterson, "CFD Simulations of Oscillating Sub-Boundary Layer Vortex Generators for Diffuser Flow Seperation Control," *International Journal of Engineering and Technology,* vol. 5, pp. 25-35, 2008.

[74] T. P. Chiang and T. W. H. Sheu, "A numerical revisit of backward-facing step flow problem," *Physics of Fluids,* vol. 11, pp. 862-874, Apr 1999.

[75] W. W. Nichols and M. F. O'Rourke, *McDonald's Blood Flow in Arteries*, 3rd Edition ed.: Edward Arnold, 1990.

[76] H. Tennekes and J. L. Lumley, *A First Course in Turbulence*: The MIT Press, 1972.

[77] J. O. Hinze, *Turbulence*: McGraw-Hill, 1959.

[78] ANSYS, "ANSYS CFX, Release 12.0, ANSYS CFX-Solver Theory Guide," 2009.

[79] F. R. Menter, "Two-Equation Eddy-Viscosity Turbulence Models for Engineering Applications," *AIAA Journal,* vol. 32, 1994.

[80] F. Menter, "Turbulence Modeling for Engineering Flows," *A Technical Paper from ANSYS Inc.,* p. 25, 2011.

[81] F. Nicoud and F. Ducros, "Subgrid-scale stress modelling based on the square of the velocity gradient tensor," *Flow Turbulence and Combustion,* vol. 62, pp. 183-200, 1999.

[82] Y. Egorov and F. Menter, "Development and application of SST-SAS turbulence model in the DESIDER project," *Advances in Hybrid Rans-Les Modelling,* pp. 261-270, 2008.

[83] P. J. Roache, "Perspective - a Method for Uniform Reporting of Grid Refinement Studies," *Journal of Fluids Engineering-Transactions of the Asme,* vol. 116, pp. 405-413, Sep 1994.

[84] P. J. Roache, "Quantification of uncertainty in computational fluid dynamics," *Annual Review of Fluid Mechanics,* vol. 29, pp. 123-160, 1997.

[85] S. Stewart, S. Day, G. W. Burgreen, E. G. Paterson, K. B. Manning, P. Hariharan, S. Deutsch, M. Giarra, C. Cheek, V. Reddy, M. R. Berman, M. R. Myers, and R. A. Malinauskas, "Preliminary Results of FDA's "Critical Path" Project to Validate Computational Fluid Dynamic Methods Used in Medical Device Evaluation (abstract)," *ASAIO J,* vol. 55, 2009.

[86] D. R. Hose, A. J. Narracott, J. M. T. Penrose, D. Baguley, I. P. Jones, and P. V. Lawford, "Fundamental mechanics of aortic heart valve closure," *Journal of Biomechanics,* vol. 39, pp. 958-967, 2006.

[87] A. G. Brown, Y. Shi, A. Marzo, C. Staicu, I. Valverde, P. Beerbaum, P. Lawford, and D. R. Hose, "Accuracy vs. computational time: Translating aortic simulations to the clinic," *Journal of Biomechanics,* vol. [eprint], 2011.

[88] N. Westerhof, J.-W. Lankhaar, and B. E. Westerhof, "The arterial Windkessel," *Medical & Biological Engineering & Computing,* vol. 47, pp. 131-141, Feb 2009.

[89] F. C. Thomas and Y. Y. Li, "On the Convergence of Interior-Reflective Newton Methods for Nonlinear Minimization Subject to Bounds," *Mathematical Programming,* vol. 67, pp. 189-224, Nov 17 1994.

[90] G. Watson and J. Moré, "The Levenberg-Marquardt algorithm: Implementation and theory," in *Numerical Analysis*. vol. 630, ed: Springer Berlin / Heidelberg, 1978, pp. 105-116.

[91] D. R. Hose, P. V. Lawford, A. J. Narracott, J. M. T. Penrose, and I. P. Jones, "Fluid-solid interaction: benchmarking of an external coupling of ANSYS with CFX for cardiovascular applications," *Journal of Medical Engineering & Technology,* vol. 27, pp. 23-31, Jan-Feb 2003.

[92] D. M. McQueen and C. S. Peskin, "A three-dimensional computer model of the human heart for studying cardiac fluid dynamics," *Computer Graphics-Us,* vol. 34, pp. 56-60, Feb 2000.

[93] S. Z. Zhao, X. Y. Xu, and M. W. Collins, "The numerical analysis of fluid-solid interactions for blood flow in arterial structures. Part 1: A review of models for arterial wall behaviour," *Proceedings of the Institution of Mechanical Engineers. Part H - Journal of Engineering in Medicine,* vol. 212, pp. 229-40, 1998.

[94] P. Causin, J. F. Gerbeau, and F. Nobile, "Added-mass effect in the design of partitioned algorithms for fluid-structure problems," *Computer Methods in Applied Mechanics and Engineering,* vol. 194, pp. 4506-4527, 2005.

[95] C. Y. Wen, A. S. Yang, L. Y. Tseng, and J. W. Chai, "Investigation of Pulsatile Flowfield in Healthy Thoracic Aorta Models," *Annals of Biomedical Engineering,* vol. 38, pp. 391-402, Feb 2010.

[96] A. Marzo, P. Singh, P. Reymond, N. Stergiopulos, U. Patel, and R. Hose, "Influence of inlet boundary conditions on the local haemodynamics of intracranial aneurysms," *Computer Methods in Biomechanics and Biomedical Engineering,* vol. 12, pp. 431-444, 2009.

[97] M. Grigioni, C. Daniele, U. Morbiducci, C. Del Gaudio, G. D'Avenio, A. Balducci, and V. Barbaro, "A mathematical description of blood spiral flow in vessels: application to a numerical study of flow in arterial bending," *J Biomech,* vol. 38, pp. 1375-86, Jul 2005.

[98] C. Lentner, *Geigy Scientific Tables: 5. Heart and Circulation,* 8th Edition ed.: CIBA-GEIGY, 1990.

[99] S. A. Berger, L. Talbot, and L. S. Yao, "FLOW IN CURVED PIPES," *Annual Review of Fluid Mechanics,* vol. 15, pp. 461-512, 1983 1983.

[100] K. Yamamoto, T. Akita, H. Ikeuchi, and Y. Kita, "EXPERIMENTAL-STUDY OF THE FLOW IN A HELICAL CIRCULAR TUBE," *Fluid Dynamics Research,* vol. 16, pp. 237-249, Sep 1995.

[101] K. Yamamoto, A. Aribowo, Y. Hayamizu, T. Hirose, and K. Kawahara, "Visualization of the flow in a helical pipe," *Fluid Dynamics Research,* vol. 30, pp. 251-267, Apr 2002.

[102] F. P. P. Tan, A. Borghi, R. H. Mohiaddin, N. B. Wood, S. Thom, and X. Y. Xu, "Analysis of flow patterns in a patient-specific thoracic aortic aneurysm model," *Computers & Structures,* vol. 87, pp. 680-690, 2009.

[103] T. A. S. Kaufmann, M. Hormes, M. Laumen, D. L. Timms, T. Schmitz-Rode, A. Moritz, O. Dzemali, and U. Steinseifer, "Flow Distribution During Cardiopulmonary Bypass in Dependency on the Outflow Cannula Positioning," *Artificial Organs,* vol. 33, pp. 988-992, Nov 2009.

[104] T. A. S. Kaufmann, T. Schmitz-Rode, O. Dzemali, A. Moritz, and U. Steinseifer, "The Impact of Outflow Cannula Positioning on Cerebral Perfusion during Cardiac Support: A Cfd Study," *International Journal of Artificial Organs,* vol. 32, pp. 399-400, Jul 2009.

[105] A. C. Benim, A. Nahavandi, A. Assmann, D. Schubert, P. Feindt, and S. H. Suh, "Simulation of blood flow in human aorta with emphasis on outlet boundary conditions," *Applied Mathematical Modelling,* vol. 35, pp. 3175-3188, Jul 2011.

[106] L. Kadem and Z. Keshavarz-Motamed, "3D pulsatile flow in a curved tube with coexisting model of aortic stenosis and coarctation of the aorta," *Medical Engineering & Physics,* vol. 33, pp. 315-324, Apr 2011.

[107] K. M. Tse, P. X. Chiu, H. P. Lee, and P. Ho, "Investigation of hemodynamics in the development of dissecting aneurysm within patient-specific dissecting aneurismal aortas using computational fluid dynamics (CFD) simulations," *Journal of Biomechanics,* vol. 44, pp. 827-836, Mar 15 2011.

[108] X. Liu, Y. Fan, X. Deng, and F. Zhan, "Effect of non-Newtonian and pulsatile blood flow on mass transport in the human aorta," *Journal of Biomechanics,* vol. 44, pp. 1123-1131, Apr 7 2011.

[109] C. Karmonik, J. Bismuth, M. G. Davies, D. J. Shah, H. K. Younes, and A. B. Lumsden, "A Computational Fluid Dynamics Study Pre- and Post-Stent Graft Placement in an Acute Type B Aortic Dissection," *Vascular and Endovascular Surgery,* vol. 45, pp. 157-164, Feb 2011.

[110] X. Y. Xu, Z. Cheng, F. P. P. Tan, C. V. Riga, C. D. Bicknell, M. S. Hamady, R. G. J. Gibbs, and N. B. Wood, "Analysis of Flow Patterns in a Patient-Specific Aortic Dissection Model," *Journal of Biomechanical Engineering-Transactions of the Asme,* vol. 132, May 2010.

[111] A. F. Osorio, A. J. Kassab, E. A. Divo, I. R. Argueta-Morales, and W. M. DeCampli, "Computational Fluid Dynamics Analysis of Surgical Adjustment of Ventricular Assist Device Implantation to Minimize Stroke Risk," *Imece2009: Proceedings of the Asme International Mechanical Engineering Congress and Exposition, Vol 2,* pp. 213-221, 2010.

[112] M. Markl, C. Canstein, P. Cachot, A. Faust, A. F. Stalder, J. Bock, A. Frydrychowicz, J. Kuffer, and J. Hennig, "3D MR flow analysis in realistic rapid-prototyping model systems of the thoracic aorta: Comparison with in vivo data and computational fluid dynamics in identical vessel geometries," *Magnetic Resonance in Medicine,* vol. 59, pp. 535-546, Mar 2008.

[113] Y. Tokuda, M. H. Song, Y. Ueda, A. Usui, T. Akita, S. Yoneyama, and S. Maruyama, "Three-dimensional numerical simulation of blood flow in the aortic arch during cardiopulmonary bypass," *European Journal of Cardio-Thoracic Surgery,* vol. 33, pp. 164-167, Feb 2008.

[114] F. P. P. Tan, G. Soloperto, S. Bashford, N. B. Wood, S. Thom, A. Hughes, and X. Y. Xu, "Analysis of flow disturbance in a stenosed carotid artery bifurcation using two-equation transitional and turbulence models," *Journal of biomechanical engineering,* vol. 130, p. 061008, 2008-Dec 2008.

[115] D. N. Ku, D. P. Giddens, C. K. Zarins, and S. Glagov, "Pulsatile Flow and Atherosclerosis in the Human Carotid Bifurcation - Positive Correlation between Plaque Location and Low and Oscillating Shear-Stress," *Arteriosclerosis,* vol. 5, pp. 293-302, 1985.

[116] T. G. Kang and T. H. Kwon, "Colored particle tracking method for mixing anlysis of chaotic micromixers," *Journal of Micromechanics and Microengineering,* vol. 14, pp. 891-899, Jul 2004.

[117] A. N. Cookson, D. J. Doorly, and S. J. Sherwin, "Mixing through stirring of steady flow in small amplitude helical tubes," *Ann Biomed Eng,* vol. 37, pp. 710-21, Apr 2009.

[118] A. Cookson, "Computational Investigation of Helical Pipe Geometries From a Mixing Perspective," PhD, Department of Aeronautics, Imperial College London, 2009.

[119] C. E. Shannon, "A MATHEMATICAL THEORY OF COMMUNICATION," *Bell System Technical Journal,* vol. 27, pp. 379-423, 1948 1948.

[120] J. Mudd, J. D. Cuda, J. V. Conte, M. K. Halushka, and S. D. Russell, "Fusion of the aortic valve commissures during continuous axial flow left ventricular assist device support," *Circulation,* vol. 116, pp. 373-373, Oct 16 2007.

[121] Y. Shi, T. Korakianitis, and C. Bowles, "Numerical simulation of cardiovascular dynamics with different types of VAD assistance," *Journal of Biomechanics,* vol. 40, pp. 2919-33, 2007.

[122] D. Burkhoff, I. Mirsky, and H. Suga, "Assessment of systolic and diastolic ventricular properties via pressure-volume analysis: a guide for clinical, translational, and basic researchers," *American Journal of Physiology-Heart and Circulatory Physiology,* vol. 289, pp. H501-H512, 2005.

[123] J. E. Madias, "Killip and Forrester classifications - Should they be abandoned, kept, reevaluated, or modified?," *Chest,* vol. 117, pp. 1223-1226, May 2000.

[124] B. M. Hanson, M. C. Levesley, K. Watterson, and P. G. Walker, "Hardware-in-the-loop-simulation of the cardiovascular system, with assist device testing application," *Medical Engineering & Physics,* vol. 29, pp. 367-374, Apr 2007.

[125] Y. Wu, P. E. Allaire, G. Tao, and D. Olsen, "Modeling, estimation, and control of human circulatory system with a left ventricular assist device," *Ieee Transactions on Control Systems Technology,* vol. 15, pp. 754-767, 2007.

[126] D. Morley, K. Litwak, P. Ferber, P. Spence, R. Dowling, B. Meyns, B. Griffith, and D. Burkhoff, "Hemodynamic effects of partial ventricular support in chronic heart failure: Results of simulation validated with in vivo data," *Journal of Thoracic and Cardiovascular Surgery,* vol. 133, pp. 21-U62, Jan 2007.

[127] A. Barbone, J. W. Holmes, P. M. Heerdt, A. H. S. The, Y. Naka, N. Joshi, M. Daines, A. R. Marks, M. C. Oz, and D. Burkhoff, "Comparison of right and left ventricular responses to left ventricular assist device support in patients with severe heart failure - A primary role of mechanical unloading underlying reverse remodeling," *Circulation,* vol. 104, pp. 670-675, 2001.

[128] J. D. Madigan, A. Barbone, A. F. Choudhri, D. L. S. Morales, B. Cai, M. C. Oz, and D. Burkhoff, "Time course of reverse remodelling of the left ventricle during support with a left ventricular assist device," *Journal of Thoracic and Cardiovascular Surgery,* vol. 121, pp. 902-908, May 2001.

[129] S. Vandenberghe, P. Segers, B. Meyns, and P. Verdonck, "Unloading effect of a rotary blood pump assessed by mathematical modeling," *Artificial Organs,* vol. 27, pp. 1094-1101, 2003.

[130] H. L. Falsetti, R. E. Mates, C. Grant, D. G. Greene, and I. L. Bunnell, "Left ventricular wall stress calculated from one-plane cineangiography.," *Circ Res,* vol. 26, pp. 71-83, Jan 1970.

APPENDIX 1

PUBLICATIONS

JOURNAL ARTICLES A1.1

1. Brown, A.G., Shi, Y., Mueller, J., Graichen, K., Lawford, P. and Hose, D.R. (2012) *Outflow cannula placement in left ventricular assist device patients.* [Submitted]

2. Brown, A.G., Shi, Y., Marzo, A., Staicu, C., Valverde, I., Beerbaum, P., Lawford, P. and Hose, D.R. (2011) *Accuracy vs. computational time: Translating aortic simulations to the clinic.* Journal of Biomechanics, **45**:516-523, [eprint].

3. Brown, A.G., Shi, Y., Arndt, A., Mueller, J., Lawford, P. and Hose, D.R. (2011) *Importance of realistic LVAD profiles for assisted aortic simulations: evaluation of optimal outflow anastomosis locations.* Computer Methods in Biomechanics and Biomedical Engineering, [eprint].

4. Shi, Y., Brown, A.G. and Hose, D.R. (2011) *Computational modelling and evaluation of cardiovascular response under pulsatile impeller pump support.* (2011) Interface Focus, [eprint].

CONFERENCE PUBLICATIONS A1.2

ORAL PRESENTATIONS A1.2.1

Brown, A.G., Shi, Y., Hose, D.R. and Lawford, P. (2010) *The influence of swirling flow in a patient-specific aorta under LVAD support.* European Society of Biomechanics.

Brown, A.G., Shi, Y., Hose, D.R. and Lawford, P. (2010) *The importance of LVAD imparted swirl when evaluating assisted aortic flow fields.* Virtual Physiological Human.

POSTER PRESENTATIONS A1.2.2

Brown, A.G. (2010) *VAD induced swirl significantly effects the aortic flow field.* SET for BRITAIN.

Hose, D.R., Shi, Y., Brown, A.G. and Lawford, P. (2011) *Coupled 0D/3D haemodynamic modelling under aortic coarctation condition.* Physiological Fluid Mechanics Conference.

Valverde, I., Staicu, C., Grotenhuis, H., Marzo, A., Rhode, K., Shi, Y., Brown, A.G., Tzifa, A., Hussain, T., Greil, G., Lawford, P., Razavi, R., Hose, D.R. and Beerbaum, P., (2011) *Predicting haemodynamics in native and residual coarctation: preliminary results of Rigid-Wall CFD model validated against clinically invasive pressure measurements at rest and during pharmacological stress.* Journal of Cardiovascular Magnetic Resonance.

Computer Methods in Biomechanics and Biomedical Engineering
iFirst article, 2011, 1–12

Taylor & Francis
Taylor & Francis Group

Importance of realistic LVAD profiles for assisted aortic simulations: evaluation of optimal outflow anastomosis locations

Alistair Graham Brown[a]*, Yubing Shi[a1], Andreas Arndt[b2], Jörg Müller[b3], Patricia Lawford[a4] and David Rodney Hose[a5]

[a]*Group of Medical Physics, School of Medicine and Biomedical Sciences, The Royal Hallamshire Hospital, University of Sheffield, Room I108, Beech Hill Road, Sheffield S10 2RX, UK;* [b]*Berlin Heart GmbH, Berlin, Germany*

(*Received 4 August 2010; final version received 18 January 2011*)

Left ventricular assist devices (LVADs) are carefully designed, but the significance of the implantation configuration and interaction with the vasculature is complex and not fully determined. The present study employs computational fluid dynamics to investigate the importance of applying a realistic LVAD profile when evaluating assisted aortic flow fields and subsequently compares a number of potential anastomosis locations in a patient-specific aortic geometry. The outflow profile of the Berlin Heart INCOR® device was provided by Berlin Heart GmbH (Berlin, Germany) and the cannula was attached at a number of locations on the aorta. Simulations were conducted to compare a flat profile against the real LVAD profile. The results illustrate the importance of applying an LVAD profile. It not only affects the magnitude and distribution of oscillatory shear index, but also the distribution of flow to the great arteries. The ascending aorta was identified as the optimal location for the anastomosis.

Keywords: left ventricular assist device; aortic flow; CFD; outflow cannula

Introduction

Heart failure (HF) is a major cause of morbidity and mortality in the western world, with around 400,000 deaths attributed to this condition in World-Health-Organisation (2004). For patients with advanced-stage HF, there are only two options for intervention; one possibility is a heart transplant but, the last decade has seen the number of available donor hearts almost halve (NHS Blood and Transplant. Transplant Activity in the UK 2009) to a figure that is wholly inadequate to meet the demand. The alternative is the implantation of a ventricular assist device (VAD).

VADs are mechanical blood pumps that support the diseased heart and ensure adequate perfusion of the body and vital organs. Depending on the requirements of the patient, these can be used to support the left ventricle or both left and right ventricles, but for the majority of patients implantation of a left VAD (LVAD) is sufficient.

When LVADs were first introduced in the 1960s, they were considered only as a bridge to transplant (Kormos et al. 1991). However, advances in pump design and efficiency have led to their use as a destination therapy in patients for whom transplantation is not an option (Rose et al. 2001). An exciting development in this context is that clinical experience has shown that the mechanical unloading of the diseased ventricle associated with the implantation of the LVAD can aid myocardial recovery enabling, for some patients, successful explantation of the device (Dandel et al. 2005; Simon et al. 2005). The potential use of the LVAD as a bridge to recovery brings with it the need for patient-specific optimisation of the LVAD configuration and operating parameters to promote myocardial recovery and to reduce any detrimental effects of LVAD support on the native vasculature.

Since their first introduction, VAD designs have undergone significant improvements. The present, third generation, devices are small, efficient, highly engineered and optimised ones (Birks 2010). However, identification of the ideal configuration for the assisted vasculature presents a significant challenge as it is likely to be highly dependent on the patient's anatomy and the specific clinical aim. For example, in the case of destination therapy, there is a need to maintain physiologically realistic stresses on the aortic wall to minimise the potential for aneurysm growth and the development of atherosclerosis. If the clinical aim is as a bridge to recovery, an important consideration will be to maintain the efficacy of the aortic valve to prevent further interventional procedures (implantation of a prosthetic heart valve) in the event of device explantation.

It was demonstrated, both *in vivo* (Kono et al. 2003) and numerically (Korakianitis and Shi 2007), that in order to achieve maximal volume and pressure unloading of the left ventricle (factors known to be important in myocardial recovery) (Barbone et al. 2001), the inflow anastomosis should be located at the ventricular apex. The optimal location of the outflow cannula is less well characterised; current attachment sites are the ascending or descending aorta. A small number of studies, both *in vitro* (Litwak

*Corresponding author. Email: a.g.brown@sheffield.ac.uk

ISSN 1025-5842 print/ISSN 1476-8259 online

DOI: 10.1080/10255842.2011.556628
http://www.informaworld.com

et al. 2005) and numerical (May-Newman et al. 2004; Bazilevs et al. 2009), have investigated the effects of an LVAD on the aortic flow field, but only Bazilevs et al. (2009) employed a patient-specific geometry. All of these studies agree that having the outflow cannula attached to the descending aorta results in regions of flow stasis within the aortic arch resulting in a site prone to the formation of blood clots (Wootton and Ku 1999). May-Newman et al. (2004) investigated the effect of insertion angle in a simplified aorta–cannula configuration. Although the aorta and cannula were represented as cylindrical tubes, the results clearly demonstrated the significant influence of the insertion angle on the flow field. To the best of our knowledge, no studies have investigated alternative cannulation sites in the aortic arch or the upper region of the descending aorta, both of which could prevent flow stasis in the arch and may prove to be advantageous over the ascending aorta as the site of outflow anastomosis.

Helical flow is an important feature of the flow field in the aorta and is thought to be produced by a combination of the torsional contraction and trabecular structure in the left ventricle, the complex curvature of the arch and the non-orthogonality of the plane of the aortic valve (Thomas 1990; Kilner et al. 1993; Black et al. 1995; Caro et al. 1996; Morbiducci et al. 2009). Swirling flows result in physiologically advantageous phenomena such as improved vascular washout and relatively uniform distributions of wall shear stress (WSS) (Caro et al. 2005). Regions of excessively high WSS were associated with endothelial cell damage, leading to an inflammatory response and possible plaque formation, whereas regions of low and oscillating WWS were linked with atherosclerotic plaque growth (Malek et al. 1999; Buchanan et al. 2003). In bypassing the heart, LVADs reduce the rotational component applied to the blood during ventricular ejection. However, continuous flow LVADs (axial pumps) impart a degree of rotational velocity to the blood via the rotating impeller. This rotational component, which up to this point has been neglected in previous studies (May-Newman et al. 2004; Kar et al. 2005; Bazilevs et al. 2009), may itself induce helical flow structures, thereby improving WSS distributions and vascular washout.

The aim of this study is to investigate the advantages and disadvantages of different outflow cannula positions in a numerical model in order to determine the importance of applying a realistic LVAD velocity profile when evaluating the assisted flow field in a patient-specific aorta.

Methods

Model construction

The surface geometry of a patient-specific thoracic aorta (Figure 1(a)) was extracted from MRI data of a healthy normal, using an in-house registration toolkit (Barber et al. 2007). The geometry of the outflow cannula, of the Berlin Heart INCOR LVAD, was constructed and attached, *in silico*, to the thoracic aorta at three sites of interest: the ascending aorta (Figure 1(b)), the aortic arch (Figure 1(c)) and the upper descending aorta (Figure 1(d)), referred to from here on as AscAo, AoArch and UpDeAo models, respectively. A computational mesh containing approxi-

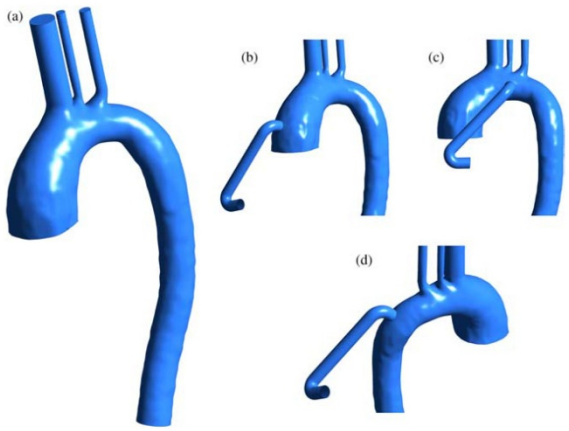

Figure 1. (a) Surface geometry of the patient-specific aorta constructed from MRI data (b–d). Surface geometry of the patient-specific aorta with the Berlin Heart INCOR outflow cannula at three sites of interest; (b) AscAo, (c) AoArch and (d) UpDeAo.

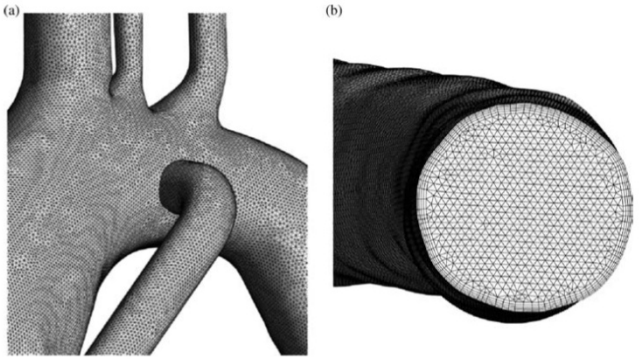

Figure 2. Overview of the computational mesh (left) and close-up of outlet mesh with improved wall resolution via five layers of prism elements (right).

mately 1.6 million elements (Figure 2(a)) was created for each model using ICEM computational fluid dynamics (CFD) (ANSYS Inc., Canonsburg, PA, USA). The internal structure of the fluid domain was meshed with tetrahedral elements and five layers of prism elements were incorporated at the wall to improve the near-wall resolution (Figure 2(b)).

It was assumed that the aortic valve remained closed throughout the simulation and hence all the flow passed through the LVAD, simulating the condition of severe left ventricular failure. The compliance of the vessel wall was neglected and a non-slip condition was enforced at this boundary. Time-varying boundary conditions were taken from a previously validated 0D model of the assisted vasculature (Shi et al. 2007) and applied directly as pressures and a flow rate at the outlets and inlet, respectively (Figure 3).

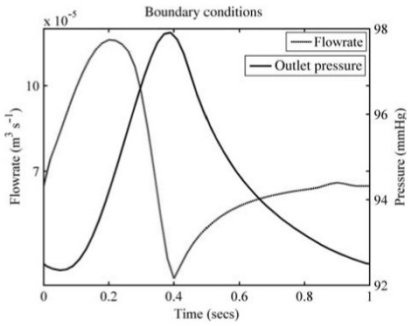

Figure 3. Time-varying pressure and flow rate employed as the boundary conditions to the 3D model.

To investigate the importance of using a realistic LVAD velocity profile, each of the three models was run with a flat inlet velocity profile and a real LVAD velocity profile (Figure 4). The LVAD velocity profile was supplied by Berlin Heart and was taken from a validated CFD simulation of the Berlin Heart INCOR LVAD, operating at a constant impellor speed of 8000 rpm (Muller 2009). The real LVAD profile differs from the flat profile in its radial distribution of the normal velocity components and the inclusion of a rotational component. The non-uniform radial distribution is an artefact of the impeller geometry, whereas the rotational component is a result of the rotating impeller. The slight asymmetry of the INCOR LVAD velocity profile is a consequence of the geometrical configuration of the stationary vanes located downstream of the rotating impeller. The velocity profile was scaled to follow the time-varying inlet flow rate of the 0D model to allow comparisons to be made against simulations with a flat inlet profile.

Blood was modelled as a Newtonian fluid, as is appropriate for the larger blood vessels (Wilmer and O'Rourke 1990), with a constant density and viscosity of $1056\,\mathrm{kg\,m^{-3}}$ and $0.0035\,\mathrm{Pa\,s}$, respectively. The time-varying Navier–Stokes and continuity Equations (1)–(4) were solved for an incompressible fluid using the ANSYS CFX, Version 12.0.

$$\rho\left(\frac{\partial u}{\partial t}+u\frac{\partial u}{\partial x}+v\frac{\partial u}{\partial y}\right)=-\frac{\partial P}{\partial x}+\mu\left(\frac{\partial^2 u}{\partial x^2}+\frac{\partial^2 u}{\partial y^2}+\frac{\partial^2 u}{\partial z^2}\right), \quad (1)$$

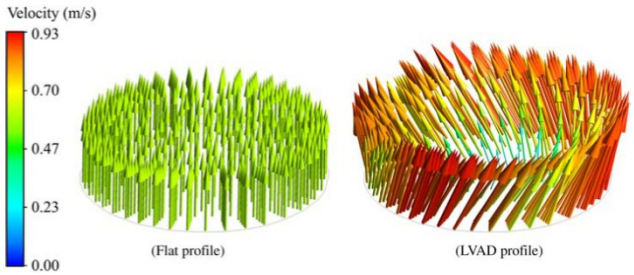

Figure 4. Velocity vector plots of the flat (left) and real LVAD (right) velocity profile.

$$\rho\left(\frac{\partial v}{\partial t}+u\frac{\partial v}{\partial x}+v\frac{\partial v}{\partial y}\right)=-\frac{\partial P}{\partial y}+\mu\left(\frac{\partial^2 v}{\partial x^2}+\frac{\partial^2 v}{\partial y^2}+\frac{\partial^2 v}{\partial z^2}\right), \quad (2)$$

$$\rho\left(\frac{\partial w}{\partial t}+u\frac{\partial w}{\partial x}+v\frac{\partial w}{\partial y}\right)=-\frac{\partial P}{\partial z}+\mu\left(\frac{\partial^2 w}{\partial x^2}+\frac{\partial^2 w}{\partial y^2}+\frac{\partial^2 w}{\partial z^2}\right), \quad (3)$$

$$\frac{\partial u}{\partial x}+\frac{\partial v}{\partial y}+\frac{\partial w}{\partial z}=0, \quad (4)$$

where u, v and w are the velocity components in x-, y- and z-coordinates, respectively. P is the pressure, ρ is the fluid density and μ represents the fluid viscosity.

The use of a laminar model is justified by evaluation of the peak Reynolds number in the aorta. The inlet flow waveform has a peak flow rate of 1.16×10^{-4} m^3 s^{-1}. Assuming an average velocity, this equates to a peak Reynolds number of 970 and 1582 in ascending and descending aorta, respectively. In fact, the Reynolds number in the descending aorta will be less, as a proportion of the flow will leave the domain via the great arteries.

Each time step was taken to be numerically converged once the root mean-squared residuals of pressure and momentum, in all three directions, reached a value below 1×10^{-6}. The simulations employed a time step of 2 ms and were run for a number of cardiac cycles to remove any initialisation effects.

Post-processing techniques

A challenging problem in cardiovascular CFD is the meaningful evaluation of transient flow fields and more specifically the extraction of informative parameters. The two most common evaluation parameters are cycle-averaged wall shear stress (avWSS) and oscillatory shear index (OSI) (Ku et al. 1985; Bazilevs et al. 2009; Marzo et al. 2009; Wen et al. 2010). OSI is described by Equations (5)–(7):

$$\mathrm{OSI}=\frac{1}{2}\left(1-\frac{\tau_{\mathrm{mean}}}{\tau_{\mathrm{abs}}}\right), \quad (5)$$

$$\tau_{\mathrm{mean}}=\left|\frac{1}{T}\int_0^T\tau\,\mathrm{d}t\right|, \quad (6)$$

$$\tau_{\mathrm{abs}}=\frac{1}{T}\int_0^T|\tau|\,\mathrm{d}t, \quad (7)$$

where τ is the shear stress tensor and T is the period of a cardiac cycle.

This measure can be conceptualised as the proportion of the cardiac cycle during which the orientation of the instantaneous WSS is different to the average direction of the WSS. That is to say, in regions where the flow direction changes rapidly, the OSI will be high. OSI has a maximum theoretical value of 0.5. It was suggested that OSI values of greater than 0.2 represent detrimental flow conditions that can be prone to the development of atherosclerosis (Goubergrits et al. 2008).

Grigioni et al. (2005) proposed a mathematical term, the helical flow index (HFI), to describe the degree of helical flow within a fluid domain. The HFI is evaluated along N_s streamlines and follows Equation (8). This measure provides an opportunity to compare the degree of helical flow found in the native aorta with that of an assisted aorta and offers an informative parameter to evaluate the importance of the inlet profile. The HFI of the flow field in a healthy aorta was investigated *in vivo* by Morbiducci et al. (2009). The study reported values for the HFI ranging from 0.372 to 0.464 and a cycle-averaged HFI of 0.414. As one would expect, the peak values occurred after peak systole, in the deceleration phase

$$\mathrm{HFI}=\frac{1}{N_s}\sum_{k=1}^{N_s}\frac{1}{N_k}\sum_{j=1}^{N_k}\left|\frac{\nabla(\nabla\times\nabla)}{|\nabla|\nabla\times\nabla|}\right|, \quad 0\le\mathrm{HFI}\ge1, \quad (8)$$

where $\vec{V}$ and $(\nabla \times \vec{\nabla})$ are the vectors of velocity and vorticity and N_k is the number of points $j(j = 1, \ldots, N_k)$ along the kth streamline $(k = 1, \ldots, N_s)$.

The HFI is evaluated along N_s streamlines, which means there is a potential dependence on the number of streamlines. A simple study was conducted to identify the number of streamlines necessary to ensure independence of the calculated value using the AscAo model, with a flat inlet profile. It was shown that using 2500 streamlines to compute the HFI ensured, within a 0.5% error, that the value was independent of the number of streamlines.

Results and discussion

An assisted, patient-specific, aortic flow field was simulated with the inclusion of the Berlin Heart INCOR LVAD outflow cannula. The importance of applying a realistic LVAD profile is first investigated, followed by comparison and evaluation of three clinically viable sites of outflow anastomosis (Figure 1(b–d)). The results presented refer to the fourth simulated cardiac cycle, thereby removing initialisation effects.

Importance of applying a realistic LVAD profile

Contour plots of avWSS are shown for all the cannula positions of interest (Figure 5). The colour range of the plots is capped at a value of 7 Pa, a figure identified by Malek et al. (1999) as the upper range of WSS in the native vasculature. In the AscAo case, neglecting the real velocity profile results in a larger area of high avWSS in the aortic valve region and a reduced area of high avWSS where the jet of blood impacts on the aortic wall (Figure 5-arrows). Both the flat and real AoArch models predict an extensive region of high avWSS, where the jet of blood impinges on the aortic wall. In this configuration, the LVAD profile causes a greater area of potentially detrimental high avWSS (Figure 5-circled), a likely result of the high velocities around the outer ring of the profile. This is also true of the AscAo and UpDeAo model in which a larger region of high avWSS can be seen when the real LVAD profile is applied (Figure 5-boxed).

Figures 6–8 illustrate the distribution of OSI for each of the outflow configurations, with and without the inclusion of a real LVAD profile. In the AscAo model, OSI is higher around the roots of the major arteries and the minor curvature of the aortic arch when the flat profile is applied (Figure 6-circled). However, when the real profile was used, increased levels of OSI are associated with the ascending aorta (Figure 6-arrow). Such regions of high OSI can often be an indicator of regions prone to atherosclerosis.

In the AoArch simulations, the real LVAD profile reduces the OSI at the aortic valve and sinus region, as described above, identifying a region prone to the formation of atherosclerosis (Figure 7-circled). The

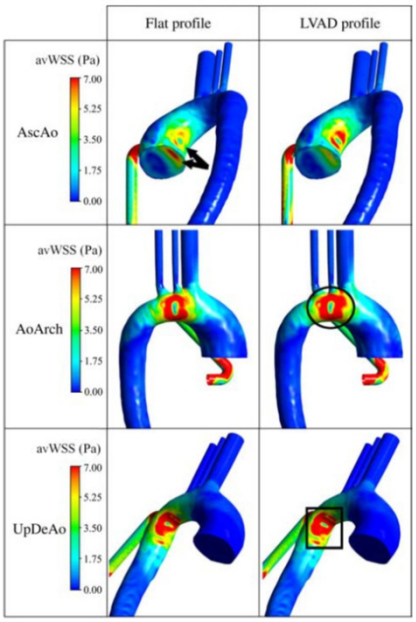

Figure 5. Comparison of avWSS contour plots employing a real LVAD profile (right) and a flat inlet profile (left) in a patient-specific assisted aorta. Upper, AscAo model; middle, AoArch model and lower, UpDeAo model.

LVAD profile led to an increase in OSI within the brachiocephalic artery (BCA) and down the posterior wall of the descending aorta (Figure 7-arrows).

Large regions of high OSI can be seen around the aortic valve in both UpDeAo simulations (Figure 8-circled), with the LVAD profile resulting in an increase in the size and magnitude of this region. Such widespread areas of high OSI can be attributed to low flow velocities. On further investigation of the velocity vector field (Figure 11), a region of stagnant flow was apparent, suggesting an area that is susceptible to thrombus formation. Elevated values of OSI on the wall of the left subclavian (LSUB) artery suggest that, in comparison with alternative configurations, a reduced amount of flow passes through this branch (Figure 8-arrows). Graphical plots of flow distribution shown in Figure 9 support this conclusion.

The application of a realistic LVAD profile alters the calculated values of HFI in all cases (Table 1). However, it is worth noting that the AscAo model has the greatest amount of variation between the flat profile and LVAD profile simulations. In this case, the simulation with a real

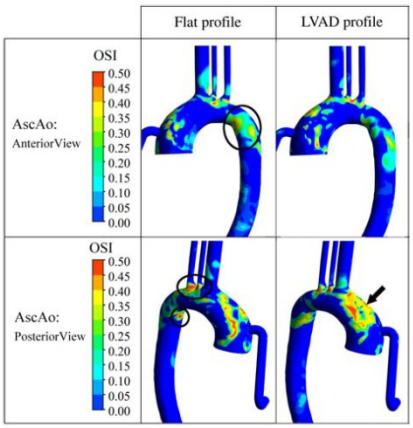

Figure 6. Comparison of OSI contour plots in AscAo model, with a real LVAD profile (right) and a flat inlet profile (left), in a patient-specific assisted aorta. Upper, anterior view of the assisted aorta and lower, posterior view of the assisted aorta.

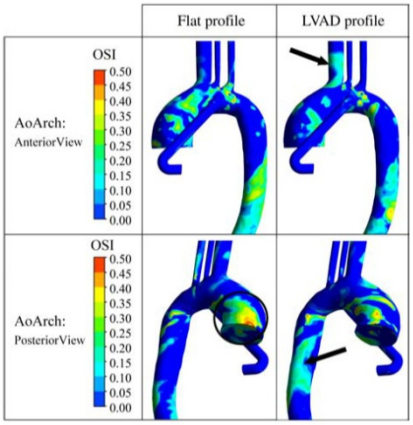

Figure 7. Comparison of OSI contour plots in the AoArch model, with a real LVAD profile (right) and a flat inlet profile (left), in a patient-specific assisted aorta. Upper, anterior view of the assisted aorta and lower, posterior view of the assisted aorta.

LVAD profile is closer in HFI range to the previously reported values of Morbiducci et al. (2009) (0.372–0.464). This suggests that the real profile promotes a flow field with a physiologically realistic helical content and hence is an important and advantageous phenomenon.

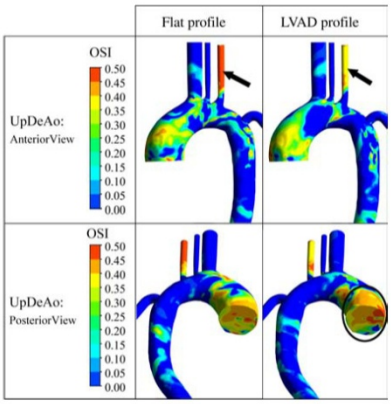

Figure 8. Comparison of OSI contour plots in the UpDeAo model, with a real LVAD profile (right) and a flat inlet profile (left), in a patient-specific assisted aorta. Upper, anterior view of the assisted aorta and lower, posterior view of the assisted aorta.

Time-varying flow rates at the outlets of the BCA, left common carotid (LCC) and LSUB arteries and the descending aorta are shown graphically in Figure 9. Note that the boundary condition (pressure) applied to the outlets is identical for both inlet conditions. The flow distributions in the models with and without a realistic LVAD profile have a qualitatively similar form. However, the real LVAD profile can be seen to affect the amount of flow moving through each outlet. It is recognised that this choice of boundary condition will tend to emphasise the differences between the flow fields produced using the real and flat inlet velocity profiles. Alternative boundary conditions at these branches, such as the Windkessel models, would reduce the differences, because the increased flow would be limited by an associated increase in pressure, but we would anticipate that the trends would be the same. The effects differ depending on the cannula location. In the AscAo model, the LVAD profile causes an increased proportion of flow through the BCA and a subsequent reduction in the flow through the descending aorta. While for the UpDeAo model, the use of the real LVAD profile reduces the amount of flow through the BCA and increases the flow in the descending aorta. In the AoArch model, the real inlet profile has less effect on the amount of flow through each of the branches. It is acknowledged that the flow variations associated with the different profiles are small (Figure 9). As flow in the aorta is dominated by the axial component, with minimal influence from the secondary flow structures, this is not unexpected. In view of this, it is interesting to note that the secondary flow components, resulting from the application

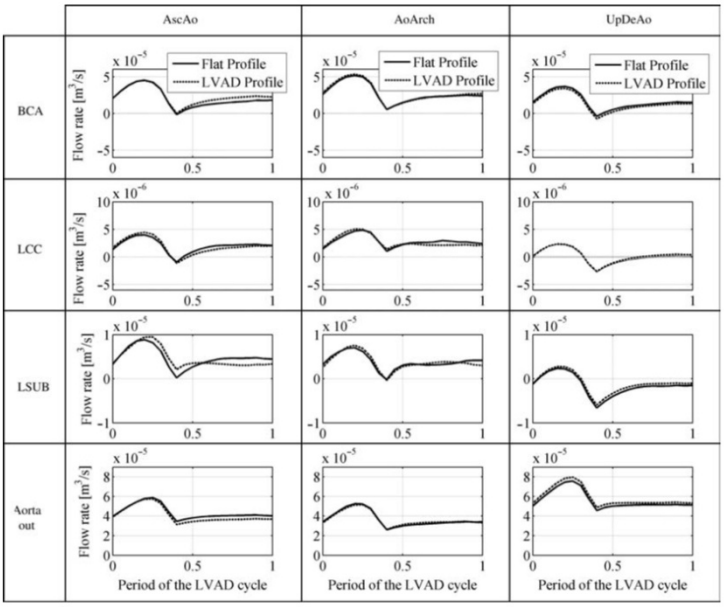

Figure 9. Graphical comparison of how the inlet profile affects the outlet flow rates at the BCA, a; LCC, b; LSUB, c and Aorta outlet, d; in all three models (AscAo, left; AoArch, middle and UpDeAo, right).

of an LVAD profile, are in fact strong enough to influence the distribution of the flow.

Accurate computation of the flow distribution in an assisted aorta could be of crucial importance when employing such models to optimise the LVAD-vasculature configuration for an individual patient.

When comparing the contour plots of avWSS, in simulations with and without a real LVAD profile (Figure 5), there is a variation in the magnitude of the avWSS, but in terms of distribution, they are qualitatively similar. This is not true for OSI (Figures 6–8) and suggests that the complex flow structures within the assisted aorta are significantly altered by the inclusion of a more realistic inlet flow profile. This conclusion is further enforced by the variation in the calculated HFI (Table 1) and by the differing flow rate distributions (Figure 9). These results highlight the importance of applying a realistic inlet flow profile when evaluating the flow field of an assisted aorta.

Table 1. HFI values calculated for each cannula configuration with and without a realistic LVAD profile at a number of points throughout the cardiac cycle.

Model of interest	HFI (peak flow)	HFI (min flow)	HFI (end of cycle)
AscAo – flat profile	0.384	0.569	0.438
AscAo – LVAD profile	0.405	0.486	0.497
AoArch – flat profile	0.426	0.512	0.417
AoArch – LVAD profile	0.424	0.512	0.442
UpDeAo – flat profile	0.403	0.482	0.431
UpDeAo – LVAD profile	0.393	0.513	0.435

Interestingly, the degree of flow-field variation between the two inlet profiles appears to depend on the gross location of the anastomosis. At this point, it is prudent to note that the incidence angle (in this study maintained at 90°) is likely to have a significant effect on the flow field and is an ongoing consideration that aims to be dealt with in future correspondence. In the present work, the influence of the anastomosis location appears to depend on the distance the jet of blood, leaving the cannula, travels before impinging on the aortic wall. If this distance is relatively long, the effects of the LVAD inlet profile are more widespread than if it encounters the aortic wall after a shorter distance. That is to say, the swirling jet has a greater distance over which to influence the flow field. Figure 10 is an isosurface of velocity in the AscAo model (Figure 10-upper) and the AoArch model (Figure 10-lower), taken

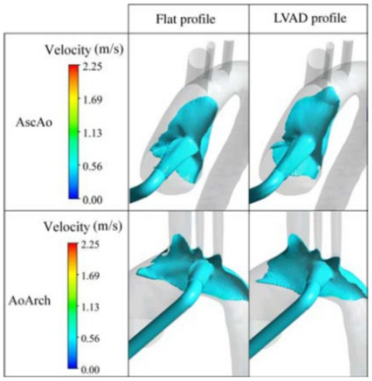

Figure 10. Isosurface of velocity, comparison of the different inlet conditions (left, flat profile and right, LVAD profile) and their effects on the dispersion of the fluid jet entering the aorta. Upper, AscAo model and lower, AoArch model.

at peak flow. In the AscAo model, the flat velocity profile results in a more disperse jet than when the real LVAD profile is employed. This result is somewhat counter-intuitive, because one would expect the rotational component associated with the real LVAD profile to be more dissipative than the flat profile. It is suggested that the non-uniform radial distribution of the normal velocity components is responsible for this result. The higher velocities at the edge of the profile will result in a stable jet being maintained for longer and in this case outweigh the dissipation due to the rotational component. This effect accounts for the increased area of high avWSS in the LVAD profile AscAo case (Figure 5). The jet of blood impacts on the aortic wall after a shorter distance in the AoArch model, resulting in a smaller degree of dissipation in the flat profile case and in turn a smaller variation between the results of the two profiles under investigation.

Optimal location of the LVAD outflow cannula

The importance of applying a realistic inlet profile to numerically predict the flow field within a patient-specific

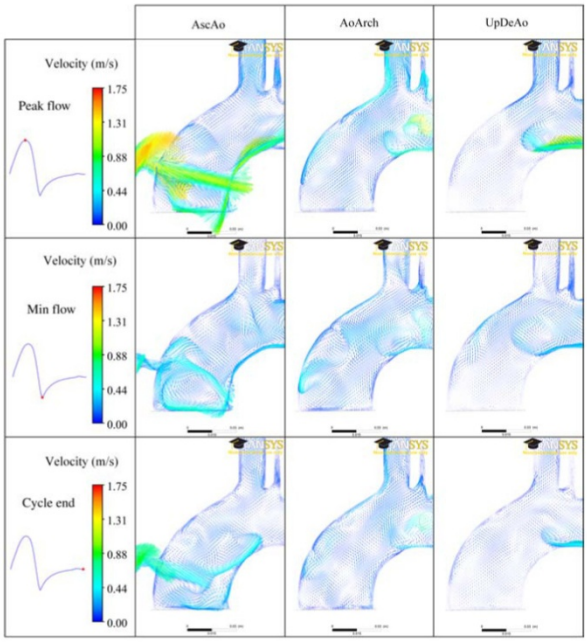

Figure 11. Evaluation of the velocity vectors for the three models (left, AscAo; middle, AoArch and right, UpDeAo) within the ascending aorta at three points within the cardiac cycle (upper, peak flow; middle, min flow and lower, end of cardiac cycle).

assisted aorta is clear and so, the evaluation of the three cannulation sites focuses on those results which employed the real LVAD inlet profile. Figure 11 shows the velocity vectors on a planar surface within the ascending aorta. This region was identified in previous studies as an area susceptible to flow stagnation (Kar et al. 2005; Bazilevs et al. 2009) and thus is of particular interest. Vectors were plotted at peak flow, minimum flow and at the end of the pseudo cardiac cycle. The AscAo model shows no indication of flow stagnation at any point during the cycle, and complex flow structures in the ascending aorta show that the area is thoroughly washed out during each cycle. The AoArch model has a region of stagnant flow around the aortic valve at peak flow and at the end of the cardiac cycle, but this region is washed out during the low flow period reducing the potential of thrombosis. The UpDeAo simulation shows very little flow in the ascending aorta region, identifying a high-risk area prone to the formation of thrombus. There is also a large amount of reverse flow and a recirculation zone that is not present in either of the alternative configurations at the inlet to the LCC artery at minimum flow and the end of the cycle, respectively. As a result, the proportion of the flow through the LCC artery is far less than that seen for the AscAo and AoArch models (Figure 12).

Figure 12 demonstrates that the AoArch configuration results in a relatively large proportion of flow through the BCA and LCC arteries and a small proportion passing through the outlet of the aorta. In the UpDeAo configuration, the majority of the flow is directed down the descending aorta, resulting in a very small proportion of flow through the branching arteries and large amounts of reverse flow, especially in the LCC and LSUB arteries. This distribution is a consequence of the angle of jet impingement on the aortic wall and the resulting direction of the velocity vectors (Figure 13). It is suggested that this configuration may be improved by a more proximal attachment of the cannula in the descending aorta, at a point where the angle of jet impingement directs the flow into the ascending aorta rather than the descending aorta.

Figure 13 shows a number of cross-sectional velocity vector profiles along the assisted aorta at peak flow, minimum flow and at the end of the cardiac cycle. The AscAo configuration results in complex flow structures in the ascending aorta. Two recirculation zones dominate the flow throughout the cardiac cycle ensuring that flow stagnation is avoided. The flow is slow moving on the upper wall of the aortic arch, becoming more developed as it moves into the descending aorta. AoArch cannulation produces two vortices in the aortic arch, and the flow

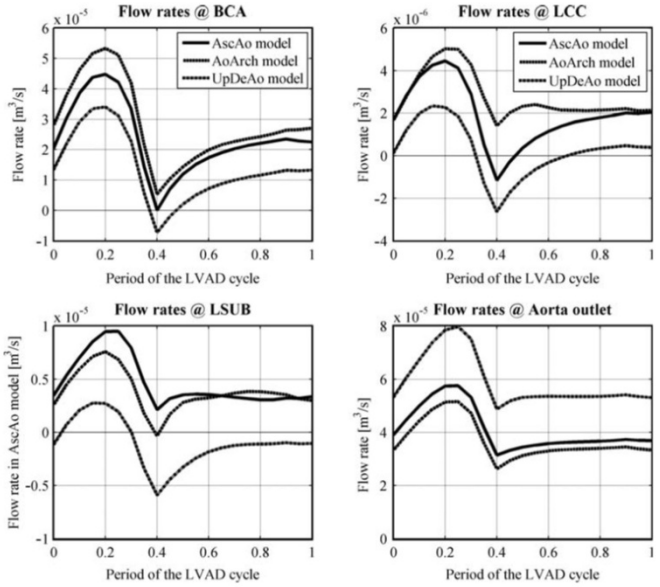

Figure 12. Graphical comparison of the effects of the different cannula configurations on the outlet flow distributions.

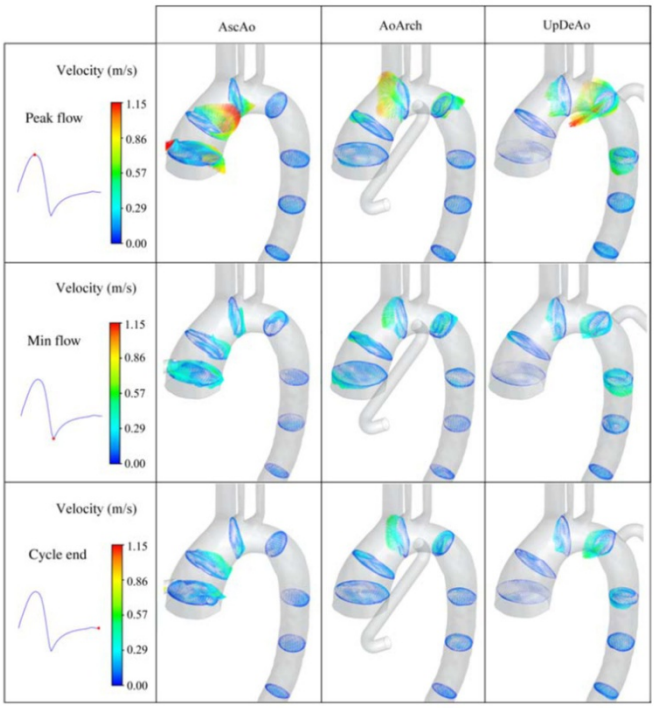

Figure 13. Evaluation of the velocity vectors at a number of cross sections for the three models (left, AscAo; middle, AoArch and right, UpDeAo) at three points within the cardiac cycle (upper, peak flow; middle, min flow and lower, end of cardiac cycle).

retains a degree of rotational velocity as it moves along the descending aorta. Velocities are far greater along the posterior wall of the aortic arch and ascending aorta, before growing more developed as the flow moves along the descending aorta. The jet of blood leaving the cannula in the UpDeAo model impinges on the aortic wall at an angle such that the majority of the flow is directed down the descending aorta. Flow that is directed into the aortic arch has higher velocities along the lower wall, but, with very little flow seen in the ascending aorta. There is a vortical structure present throughout the flow field in the upper region of the descending aorta but, as in all the other configurations, the flow develops as it moves away from the anastomosis and down the descending aorta.

Limitations of this study

The simulations employ a rigid-walled aorta, ignoring the compliance of the natural vessel. The justification for this being that constant flow axial LVADs reduce the degree of pulsation in the system. Thus, any wall motion is expected to be small, having a minimal influence on the aortic geometry and in turn the flow field.

This study has used the velocity profile from the Berlin Heart INCOR LVAD. The assumption that all constant flow axial LVADs will have a similar effect on the flow field must be true, because in all such devices drive the blood via a rotating impeller, thereby imparting a rotational component to the velocity field. The question that is yet to be addressed is whether the specifics of the device design have an additional effect.

The use of a healthy aortic geometry represents the system immediately post implantation. It cannot be discounted that in the longer term, aortic wall remodelling may occur in response to the non-physiological flow field. As yet, there are no data published describing aortic remodelling in patients with LVADs.

Conclusions

A numerical study was conducted to investigate the importance of applying a real LVAD velocity profile on the flow field of a patient-specific assisted aorta, and a number of previously unexplored anastomosis locations were evaluated.

The computational results have demonstrated the importance of a realistic inlet flow profile. The inclusion of such a profile was shown to alter the degree of HFI, the distribution and magnitude of OSI and even the distribution of blood flow to the branches coming off the aortic arch. It is noted that the degree of variation in the flow distribution and HFI appear to be dependent on the distance between the anastomosis and the site of jet impingement on the aortic wall. If this distance is reduced, the variation in flow distribution and HFI are also reduced. The distribution of OSI is significantly altered in all the reported cases, independent of this distance.

Three anastomotic locations were simulated, the AscAo, the AoArch and the UpDeAo. The UpDeAo configuration suffered from a region of high OSI around the aortic valve and ascending aorta, illustrating an area of stagnant blood present throughout the cardiac cycle. This configuration also resulted in low distributions of blood flow and large periods of reverse flow in the great arteries. While the AoArch simulation also suffered from flow stagnation around the aortic valve region, this region was washed out periodically during the pseudo cardiac cycle. The optimal anastomosis location was the AscAo, as there was no region of stagnant blood in the ascending aorta and it resulted in the minimum area of high avWSS.

Acknowledgements

This research was funded by the European Community's Seventh Framework Programme (FP7/2007-2013) under grant agreement no. 224495 (euHeart project).

Notes

1. Email: y.shi@sheffield.ac.uk
2. Email: arndt@berlinheart.de
3. Email: mueller@berlinheart.de
4. Email: p.lawford@sheffield.ac.uk
5. Email: d.r.hose@sheffield.ac.uk

References

Barber DC, Oubel E, Frangi AF, Hose DR. 2007. Efficient computational fluid dynamics mesh generation by image registration. Med Image Anal. 11(6):648–662.

Barbone A, Holmes JW, Heerdt PM, The AHS, Naka Y, Joshi N, Daines M, Marks AR, Oz MC, Burkhoff D. 2001. Comparison of right and left ventricular responses to left ventricular assist device support in patients with severe heart failure: a primary role of mechanical unloading underlying reverse remodeling. Circulation. 104(6):670–675.

Bazilevs Y, Gohean JR, Hughes TJR, Moser RD, Zhang Y. 2009. Patient-specific isogeometric fluid–structure interaction analysis of thoracic aortic blood flow due to implantation of the Jarvik 2000 left ventricular assist device. Comput Methods Appl Mech Engin. 198(45–46):3534–3550.

Birks EJ. 2010. Left ventricular assist devices. Heart. 96(1): 63–71.

Black MM, Hose DR, Lawford PV. 1995. The origin and significance of secondary flows in the aortic arch. J Med Eng Technol. 19(6):192–197.

Buchanan JR, Kleinstreuer C, Hyun S, Truskey GA. 2003. Hemodynamics simulation and identification of susceptible sites of atherosclerotic lesion formation in a model abdominal aorta. J Biomech. 36(8):1185–1196.

Caro CG, Cheshire NJ, Watkins N. 2005. Preliminary comparative study of small amplitude helical and conventional ePTFE arteriovenous shunts in pigs. J R Soc Interface. 2(3):261–266.

Caro CG, Doorly DJ, Tarnawski M, Scott KT, Long Q, Dumoulin CL. 1996. Non-planar curvature and branching of arteries and non-planar-type flow. Proc R Soc Lond Series A-Math Phys Eng Sci. 452(1944):185–197.

Dandel M, Weng Y, Siniawski H, Potapov E, Hetzer R. 2005. Long-term outcome in patients with idiopathic dilated cardiomyopathy after weaning from left ventricular assist devices. J Heart Lung Transplant. 24(2):S107.

Goubergrits L, Kertzscher U, Schoneberg B, Wellnhofer E, Petz C, Hege HC. 2008. CFD analysis in an anatomically realistic coronary artery model based on non-invasive 3D imaging: comparison of magnetic resonance imaging with computed tomography. Int J Cardiovasc Imaging. 24(4):411–421.

Grigioni M, Daniele C, Morbiducci U, Del Gaudio C, D'Avenio G, Balducci A, Barbaro V. 2005. A mathematical description of blood spiral flow in vessels: application to a numerical study of flow in arterial bending. J Biomech. 38(7): 1375–1386.

Kar B, Delgado RM, Frazier OH, Gregoric ID, Harting MT, Wadia Y, Myers TJ, Moser RD, Freund J. 2005. The effect of LVAD investigation aortic outflow-graft placement on hemodynamics and flow: implantation technique and computer flow modeling. Tex Heart Inst J. 32(3):294–298.

Kilner PJ, Yang GZ, Mohiaddin RH, Firmin DN, Longmore DB. 1993. Helical and retrograde secondary flow patterns in the aortic arch studied by three-directional magnetic resonance velocity mapping. Circulation. 88(5 Pt 1):2235–2247.

Kono S, Nishimura K, Nishina T, Yuasa S, Ueyama K, Hamada C, Akamatsu T, Komeda M. 2003. Autosynchronized systolic unloading during left ventricular assist with a centrifugal pump. J Thorac Cardiovasc Surg. 125(2):353–360.

Korakianitis T, Shi Y. 2007. Numerical comparison of hemodynamics with atrium to aorta and ventricular apex to aorta VAD support. ASAIO J. 53(5):537–548.

Kormos RL, Borovetz HS, Armitage JM, Hardesty RL, Marrone GC, Griffith BP. 1991. Evolving experience with mechanical circulatory support. Ann Surg. 214(4):471–477.

Ku DN, Giddens DP, Zarins CK, Glagov S. 1985. Pulsatile flow and atherosclerosis in the human carotid bifurcation: positive correlation between plaque location and low and oscillating shear–stress. Arteriosclerosis. 5(3):293–302.

Litwak KN, Koenig SC, Cheng RC, Giridharan GA, Gillars KJ, Pantalos GM. 2005. Ascending aorta outflow graft location and pulsatile ventricular assist provide optimal hemodynamic support in an adult mock circulation. Artif Organs. 29(8):629–635.

Malek AM, Alper SL, Izumo S. 1999. Hemodynamic shear stress and its role in atherosclerosis. JAMA. 282(21):2035–2042.
Marzo A, Singh P, Reymond P, Stergiopulos N, Patel U, Hose R. 2009. Influence of inlet boundary conditions on the local haemodynamics of intracranial aneurysms. Comput Methods Biomech Biomed Engin. 12(4):431–444.
May-Newman KD, Hillen BK, Sironda CS, Dembitsky W. 2004. Effect of LVAD outflow conduit insertion angle on flow through the native aorta. J Med Eng Technol. 28(3): 105–109.
Morbiducci U, Ponzini R, Rizzo G, Cadioli M, Esposito A, De Cobelli F, Del Maschio A, Montevecchi FM, Redaelli A. 2009. *In vivo* quantification of helical blood flow in human aorta by time-resolved three-dimensional cine phase contrast magnetic resonance imaging. Ann Biomed Eng. 37(3):516–531.
Muller J. 2009. Private communication. Berlin: Berlin Heart GmbH.
NHS Blood and Transplant. Transplant Activity in the UK [Internet]. 2009. Bristol: NHS; [cited 2010 08 02].
Rose EA, Gelijns AC, Moskowitz AJ, Heitjan DF, Stevenson LW, Dembitsky W, Long JW, Ascheim DD, Tierney AR, Levitan RG. et al. 2001. Long-term use of a left ventricular assist device for end-stage heart failure. N Engl J Med. 345(20):1435–1443.
Shi Y, Korakianitis T, Bowles, C. 2007. Numerical simulation of cardiovascular dynamics with different types of VAD assistance. J Biomech. 40(13):2919–2933.
Simon MA, Kormos RL, Murali S, Nair P, Heffernan M, Gorcsan J, Winowich S, McNamara DM. 2005. Myocardial recovery using ventricular assist devices: prevalence, clinical characteristics, and outcomes. Circulation. 112(9):I32–I36.
Thomas JD. 1990. Flow in the descending aorta: a turn of the screw or a sideways glance. Circulation. 82(6):2263–2265.
Wen CY, Yang AS, Tseng LY, Chai JW. 2010. Investigation of pulsatile flowfield in healthy thoracic aorta models. Ann Biomed Eng. 38(2):391–402.
Wilmer NW, O'Rourke MF. 1990. McDonald's blood flow in arteries. London: Edward Arnold. p. 456.
Wootton DM, Ku DN. 1999. Fluid mechanics of vascular systems, diseases, and thrombosis. Annu Rev Biomed Eng. 1:299–329.
World-Health-Organisation. The Global Burden of Disease [Internet]. 2004. Geneva: [cited 2010 Aug 2]. Available from: http://www.who.int/healthinfo/global_burden_disease/GBD_report_2004update_full.pdf.

Journal of Biomechanics 45 (2012) 516–523

Contents lists available at SciVerse ScienceDirect

Journal of Biomechanics

journal homepage: www.elsevier.com/locate/jbiomech
www.JBiomech.com

Accuracy vs. computational time: Translating aortic simulations to the clinic

Alistair G. Brown [a,*], Yubing Shi [a], Alberto Marzo [b], Cristina Staicu [a], Isra Valverde [c], Philipp Beerbaum [c], Patricia V. Lawford [a], D. Rodney Hose [a]

[a] Medical Physics Group, Department of Cardiovascular Science, University of Sheffield, Sheffield, UK
[b] Principal Research Scientist, Sheffield Teaching Hospitals NHS Foundation Trust, Sheffield, UK
[c] Imaging Sciences, Kings College London

ARTICLE INFO

Article history:
Accepted 18 November 2011

Keywords:
Haemodynamics
Aorta
Computational fluid dynamics (CFD)
Fluid structure interaction (FSI)

ABSTRACT

State of the art simulations of aortic haemodynamics feature full fluid-structure interaction (FSI) and coupled 0D boundary conditions. Such analyses require not only significant computational resource but also weeks to months of run time, which compromises the effectiveness of their translation to a clinical workflow. This article employs three computational fluid methodologies, of varying levels of complexity with coupled 0D boundary conditions, to simulate the haemodynamics within a patient-specific aorta. The most comprehensive model is a full FSI simulation. The simplest is a rigid walled incompressible fluid simulation while an alternative middle-ground approach employs a compressible fluid, tuned to elicit a response analogous to the compliance of the aortic wall. The results demonstrate that, in the context of certain clinical questions, the simpler analysis methods may capture the important characteristics of the flow field.

1. Introduction

A major challenge for the engineering simulation community is to translate its technologies into clinical application. The use of computational fluid dynamics (CFD) to characterise haemodynamics in vascular systems has the potential to assist diagnosis and to improve prognosis. The European project @neurIST developed a workflow that employed CFD to evaluate haemodynamic indices within intracranial aneurysms and sought a correlation between these indices and the risk of aneurysm rupture (Villa-Uriol et al., 2011). The workflow was tested by a number of clinically trained personnel, of whom a large proportion (88%), believed that CFD had an exciting future as a clinical tool (Singh et al., 2009). Any CFD model or workflow that is intended for clinical application should capture the important physical characteristics, but should be no more complex than it needs to be. State of the art CFD simulations of cardiovascular mechanics consider not only the motion of the fluid but also the motion of the vessel wall. Such fluid-structure interaction (FSI) models require information about the thickness and properties of the vessel wall and about how the structure is mechanically constrained, often none of which is available, and they are computationally expensive.

A consideration when constructing any CFD model is the application of realistic boundary conditions. Conventionally, the gold standard is to apply time varying clinical measurements of pressure and flow to boundaries of the fluid domain (Wolters et al., 2005; Lam et al., 2008; Brown et al., 2011). However, this requires invasive measurements, which may not be possible as part of the current clinical protocol. These boundary conditions present a further complication regarding the alignment of the waveforms. Even with electrocardiogram (ECG) gated measurements there is likely to be a mismatch between the real and simulated wave speeds, which results in artificial reflections within the computational domain. A further constraint is that the boundary conditions are obviously measured in a particular physiological state, which might not be representative of the important physiological conditions for diagnosis and prognosis. The use of coupled 0D system models to prescribe boundary conditions for detailed 3D simulations can overcome these issues and have been applied to clinically relevant research questions (Formaggia et al., 2001; Lagana et al., 2005; Migliavacca et al., 2006; Vignon-Clementel et al., 2006; Bazilevs et al., 2009; Kim et al., 2009; Spilker and Taylor, 2010; Moireau et al., 2011).

In this paper we focus on characterising the flow field in two test cases. The first is a simple cylindrical vessel and the second is a patient-specific thoracic aorta. We examine the physics of the flow in the two geometries in an effort to establish, which phenomena are important and how they can be most effectively and efficiently modelled as part of a clinical workflow.

Kim et al. (Kim et al., 2009) present a comprehensive patient-specific analysis of the haemodynamics of an aortic coarctation, featuring full FSI and a coupled tuned systemic 0D model to describe the fluid boundary conditions. The structure was mechanically constrained with fixed supports at the inlet and all outlets.

* Corresponding author. Tel.: +44 114 271 2234; fax: +44 114 271 1863.
E-mail address: a.g.brown@sheffield.ac.uk (A.G. Brown).

0021-9290/$ - see front matter © 2011 Elsevier Ltd. All rights reserved.
doi:10.1016/j.jbiomech.2011.11.041

Bazilevs et al. (2009) report an FSI simulation of the flow field changes in an aorta induced by the inclusion of an LVAD. Again the outlet boundary conditions were represented by 0D models, but the inlet flow was prescribed. The model was also supported with fixed constraints. Moireau et al. (2011) present a more realistic method for tethering the native aorta, modelling the external tissue structure using combinations of springs and dampers.

The effects of wave transmission in the aorta are believed to be important. Given an average wave speed of the order of 6 m/s (Lentner, 1990), we might expect a delay in the timing of the peak pressure and flow pulses of the order of 60 ms between the ascending and descending aorta. The pulse wave speed is less than an order of magnitude higher than the peak velocities in the system. Rigid-walled incompressible fluid models, in which the wave speed is effectively infinite, cannot capture these effects. This understanding drives us towards the sort of comprehensive FSI analysis reported by Bazilevs et al. (2009); Kim et al. (2009); Moireau et al. (2011). Unfortunately, it is rare that we have an accurate assessment of patient specific wall thickness or material properties, and nor do we have great confidence in the commonly employed structural constraints, although those presented by Moireau et al. offer an exciting improvement. An interesting compromise might be to employ a rigid walled, compressible fluid model, as described by Hose et al. (2006) in the context of aortic valve analysis. The compressibility of the fluid can be tuned to approximate the compliance of the vessel wall and thus to capture, at least grossly, the 1D wave transmission characteristics at greatly reduced computational cost. It is stressed that changes in fluid density represent the capacity for changes of fluid mass within a cross-section, analogous to vessel wall compliance. Discussion on the validity of the approach is presented in the results section.

The current study uses a three element Windkessel model at the distal boundaries with prescribed inlet flows. The results of a full FSI simulation are quantitatively compared with results from the proposed analogous compressible fluid methodology and from an incompressible rigid walled model.

2. Methodology

2.1. 3D–0D coupling strategy

ANSYS-CFX (ANSYS Inc, Canonsburg, USA) was used to solve the governing equations of the fluid. The 3D domain is coupled to a Windkessel model (Fig. 1) via a FORTRAN user subroutine that is called at the end of every time-step. In a simple explicit coupling, the 3D domain passes a value of flow (Q), to the subroutine, which solves the governing equation of the Windkessel (1) using a first order backward Euler approach. The computed value of pressure (P) is then passed back to the 3D domain where it is applied as the boundary condition for the next time-step calculation.

$$Q = C\frac{d(P-QR_i)}{dt} + \frac{P-QR_i}{R} \tag{1}$$

The pressure at the outlet of the 0D model is set to zero. This is a common assumption (Shi et al., 2011) in all models that do not explicitly represent the venous system.

2.2. Model construction

The patient-specific aorta was extracted from MR data using an in-house image registration tool, ShIRT (Barber et al., 2007). The extracted surface was meshed using ICEM-CFD (ANSYS Inc, Cannonsburg, USA) with approximately 500,000 tetrahedral elements employed to discretise the fluid domain. This is comparable to other aortic analyses reported in the literature (Lagana et al., 2005; Migliavacca et al., 2006; Benim et al., 2011; Moireau et al., 2011). The structural domain was discretised with approximately 35,000 tri-noded shell elements.

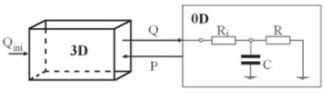

Fig. 1. Illustration of the *3D–0D* Windkessel coupling.

To evaluate mesh sensitivity, the incompressible fluid model was run on two additional mesh densities, with 150,000 elements (coarse) and 1.3 million elements (fine). A point by point comparison of the predicted pressures at the model boundaries was conducted. A maximum error of less than 2% was found when comparing the final mesh to the coarse mesh and less than 1% when compared to the fine mesh.

Windkessel models were employed at the outlets and a flat velocity profile, based on the clinically measured ascending aortic flow, was applied as the inlet condition (Fig. 2). The Windkessel parameters were tuned to match clinically measured pressure and flow data from the individual (Table 1).

The transient Navier–Stokes and continuity equations were solved with a time-step of 5 ms. ANSYS-CFX implements an implicit time-marching FSI methodology and so to ensure numerical stability the relaxation factor described in Causin et al. (2005) was employed.

2.3. FSI material properties and constraints

All analyses used an incompressible, Newtonian fluid with density of 1056 kg/m^3 and viscosity 0.0035 Pa s. For the FSI analysis, the aortic wall was modelled as linear elastic, with a Young's Modulus of 1×10^6 Pa and a constant thickness of 0.8 mm. The aorta was longitudinally tethered at each of the fluid boundaries and a novel constraint method was developed to represent the external structural constraints along the aorta. Essentially the aim is to constrain the motion of the centreline whilst leaving the vessel free to dilate according to the wall stiffness and thus, importantly, to capture the effects of wave transmission along the vessel. This is achieved by constraining rings of nodes on cross-sections normal to the centreline in such a way that the average displacements of the nodes in the plane, for each ring at any load step, are the displacements of the centreline. Given that the global motion of the aorta is determined by structures that are not included in the model, it is suggested that this is a natural and reasonable constraint. In the current analysis the centreline displacement is taken to be zero, but in future the motion could be constrained based on measurements from a 4D medical image. The effect is that the centroid of each cross-section is fixed but the vessel wall is free to dilate. Three such rings were defined in the descending aorta and at the inlet and outlets of the model. With the exception of the fluid boundaries, no out of plane constraints are applied, and no attempt has been made to simulate the motion of the inlet plane associated with cardiac motion.

2.4. Compressible fluid properties

The compressible fluid model uses the ideal gas law (2) to describe the fluid density (ρ). The fluid wave speed (c) is a function of pressure (P), fluid density and the specific heat capacity ratio (γ) (3).

$$P = \frac{R_c T\rho}{M} \tag{2}$$

where R_c is the universal gas constant, M is the molar mass and T is the temperature.

$$c^2 = \gamma\frac{P}{\rho} \tag{3}$$

Combining (2) and (3) with the assumption of an isothermal process ($\gamma=1$), produces a relationship between pressure and density (4), in which the values of temperature and molar mass can be altered to ensure the wave speed and average density within the fluid are analogous to the system of interest.

$$P = \frac{(R_c T)}{M}\rho = c^2\rho \tag{4}$$

Knowledge of the required wave speed (7 m/s) and fluid density (1056 kg/m^3) were combined, with an arbitrary choice of constant temperature (310 K), to compute a value for the molar mass (52.6 kg/mol) that would effectively simulate the vessel wall compliance. The fluid viscosity remains constant with a value of 0.0035 Pa s.

In the compressible fluid model the inlet boundary condition is prescribed as the mass flow rate rather than the volume flow rate. This is done to ensure that the mass considered in the alternative methodologies is consistent. The analogy breaks down if the density changes are too great as a proportion of the actual fluid density.

3. Results and discussion

To prove that the compressible flow analogy can indeed capture wave transmission we have compared results from an analytical solution of a 1D straight tube, with the same properties

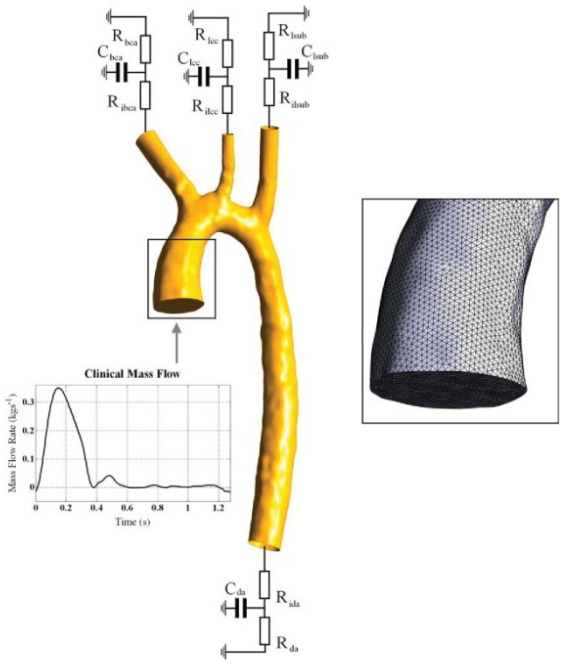

Fig. 2. The Patient specific aorta with boundary conditions and mesh density (Descending aorta (da), Brachiocephalic artery (BCA), Left common carotid artery (LCC) and Left subclavian artery (LSUB)).

Table 1
Windkessel parameter values for the descending aorta (DescAo), brachiocephalic artery (BCA), left common carotid artery (LCC) and left subclavian artery (LSUB) where R_i is the input resistance, C is the compliance and R is the second resistance.

	BCA	LCC	LSUB	DescAo
R_i (kg m^{-4} s^{-1})	1.42×10^{7}	1.59×10^{8}	5.98×10^{7}	1.31×10^{7}
C (m^4 s^2 kg^{-1})	3.45×10^{-9}	1.60×10^{-9}	2.11×10^{-9}	1.61×10^{-8}
R (kg m^{-4} s^{-1})	5.97×10^{8}	1.41×10^{9}	1.57×10^{9}	2.22×10^{8}

as the aorta, with a cardiac inlet flow wave and a coupled 3 element Windkessel outlet (Fig. 3), with the results of a numerical simulation.

It is assumed that the pressure and flow waveforms can be expressed as a sum of their harmonic components and the fast Fourier transform (FFT) was used to decompose the inlet cardiac waveform. In the following analysis the first 30 harmonics are considered (n=30). The analytical solution is based on the description of the pressure and flow waves, in terms of the flow components (Q_1, Q_2, Q_3 and Q_4), as shown in (5) and (6), respectively.

$$P(z,t)=\sum_{j=1}^{n}\sqrt{\frac{L'}{C'}}\{((Q_{1,j}-Q_{3,j})\cos(k_jz)+(Q_{2,j}-Q_{4,j})\sin(k_jz))\cos(\omega_jt)+((-Q_{2,j}-Q_{4,j})\cos(k_jz)+(Q_{1,j}+Q_{3,j})\sin(k_jz))\sin(\omega_jt)\} \quad (5)$$

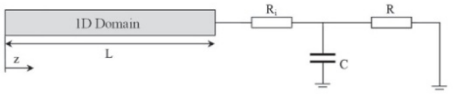

Fig. 3. Illustration of the analytical tube with a Windkessel termination.

where ω_j is the angular frequency of the jth harmonic, t is time, $k_j=\omega_j/c_o$, c_0 is the wave speed described by the Moens–Kortweg relation and z is the axial position along the vessel (see Fig. 3).

$$Q(z,t)=\sum_{j=1}^{n}\{Q_{1,j}\cos(k_jz-\omega_jt)+Q_{2,j}\sin(k_jz-\omega_jt)\}+\{Q_{3,j}\cos(k_jz+\omega_jt)+Q_{4,j}\sin(k_jz+\omega_jt)\} \quad (6)$$

The flow components can be related to the electrical elements of the Windkessel model and the characteristics of the 1D domain (i.e. Inertance, L', and compliance, C', per unit length and the vessel length, L) by (7) and (8).

$$\left(\left\{\sqrt{\frac{L'}{C'}}-R_i\right\}\cos(k_jL)+\frac{R}{1+R^2C^2\omega_j^2}(-\cos(k_jL)+RC\omega_j\sin(k_jL))\right)Q_{1,j}+\left(\left\{\sqrt{\frac{L'}{C'}}-R_i\right\}\sin(k_jL)+\frac{R}{1+R^2C^2\omega_j^2}(-\sin(k_jL)-RC\omega_j\cos(k_jL))\right)Q_{2,j}$$

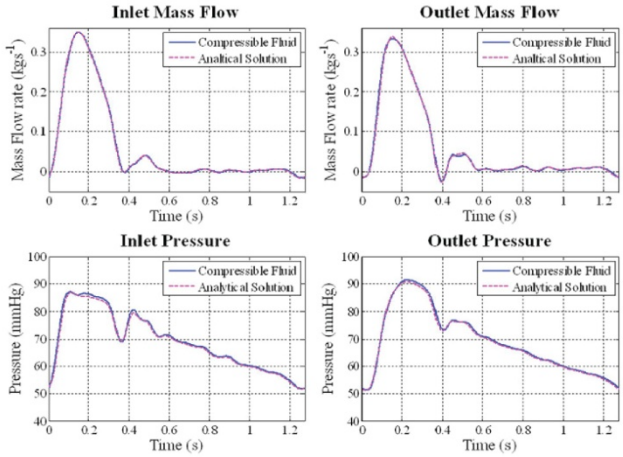

Fig. 4. Analytical vs. compressible fluid methodology in a uniform Tube: comparison of inlet and outlet pressure and mass flow.

$$+\left(\left\{-\sqrt{\frac{L'}{C'}}-R_i\right\}\cos(k_jL)+\frac{R}{1+R^2C^2\omega_j{}^2}(-\cos(k_jL)-RC\omega_j\sin(k_jL))\right)Q_{3,j}$$
$$+\left(\left\{-\sqrt{\frac{L'}{C'}}-R_i\right\}\sin(k_jL)+\frac{R}{1+R^2C^2\omega_j{}^2}(-\sin(k_jL)+RC\omega_j\cos(k_jL))\right)Q_{4,j}=0 \quad (7)$$

$$\left(\left\{\sqrt{\frac{L'}{C'}}-R_i\right\}\sin(k_jL)+\frac{R}{1+R^2C^2\omega_j{}^2}(-RC\omega_j\cos(k_jL)-\sin(k_jL))\right)Q_{1,j}$$
$$+\left(\left\{-\sqrt{\frac{L'}{C'}}-R_i\right\}\cos(k_jL)+\frac{R}{1+R^2C^2\omega_j{}^2}(-RC\omega_j\sin(k_jL)+\cos(k_jL))\right)Q_{2,j}$$
$$+\left(\left\{\sqrt{\frac{L'}{C'}}-R_i\right\}\sin(k_jL)+\frac{R}{1+R^2C^2\omega_j{}^2}(-RC\omega_j\cos(k_jL)+\sin(k_jL))\right)Q_{3,j}$$
$$+\left(\left\{-\sqrt{\frac{L'}{C'}}-R_i\right\}\cos(k_jL)+\frac{R}{1+R^2C^2\omega_j{}^2}(-RC\omega_j\sin(k_jL)-\cos(k_jL))\right)Q_{4,j}=0 \quad (8)$$

Combining (7) and (8) with the knowledge that $(Q_{1,j}+Q_{3,j})=Q_{\cos,j}$ and $(-Q_{2,j}+Q_{4,j})=Q_{\sin,j}$, where $Q_{\cos,j}$ and $Q_{\sin,j}$ are the magnitudes of the cosine and sine waves of the jth harmonic, computed from the FFT, allows the computation of the flow components. The flow components can then be substituted into (5) and (6) to describe fully the forward and backward travelling pressure and flow waveforms in the 1D system of interest.

Fig. 4 shows the inlet and outlet pressure and mass flow predictions of the compressible fluid model compared to the analytical solution. The results are in close agreement (Fig. 4) and demonstrate the validity of the compressible fluid model as an analogy for the vessel wall compliance. The variation between the analytical solution and the CFD prediction is due to the assumption of an inviscid fluid associated with the analytical derivation. As one would expect in this situation the results are in near perfect agreement when the fluid acceleration is high and the system is dominated by inertia (early systole), while during regions of low or zero acceleration the viscous effects become greater and hence the CFD model predicts greater values of pressure than the inviscid analytical solution. However, in the system of interest the Womersley number is approximately 13.4 suggesting the viscous effects are small, which is verified by a maximum percentage difference of 2.4% and 3.7% corresponding to the inlet and outlet pressure waveforms, respectively.

Table 2
Summary of computational expense.

	Fluid structure interaction	Compressible fluid	Incompressible fluid
Number of cycles to reach periodicity	7	3	3
Computational time to reach periodicity	145 h 30 mins	7 h 48 mins	6 h 48 mins

The flow field in a patient–specific aorta, with a mild coarctation, has been predicted using each of the CFD methodologies discussed previously. As the focus of this paper is on accuracy vs. computational expense, Table 2 summarises the number of cardiac cycles required to reach a periodic state for each methodology and the corresponding run times on a particular platform.[1] The most complex and comprehensive simulation (FSI) required 7 cycles to reach a period state and took 145.5 h, while the incompressible and compressible fluid models required 3 cycles, taking 6.8 h and 7.8 h, respectively (Table 2). It is immediately apparent that, on the computing platform described, the long run-time of the FSI model limits its practicality as a diagnostic clinical tool, although it might be useful for planning of elective surgery. In contrast the rigid walled models, which run approximately 20 times faster than the FSI solutions, may be more feasible for routine diagnostic clinical use.

The computed pressures and mass flow rates for each of the methodologies have been compared at the model boundaries: all give comparable results (Fig. 5). This does not appear to support

[1] All simulations were solved on a Dell PowerEdge T710 using 4, 2.93 GHz Intel Xeon X5570 processors in local parallel.

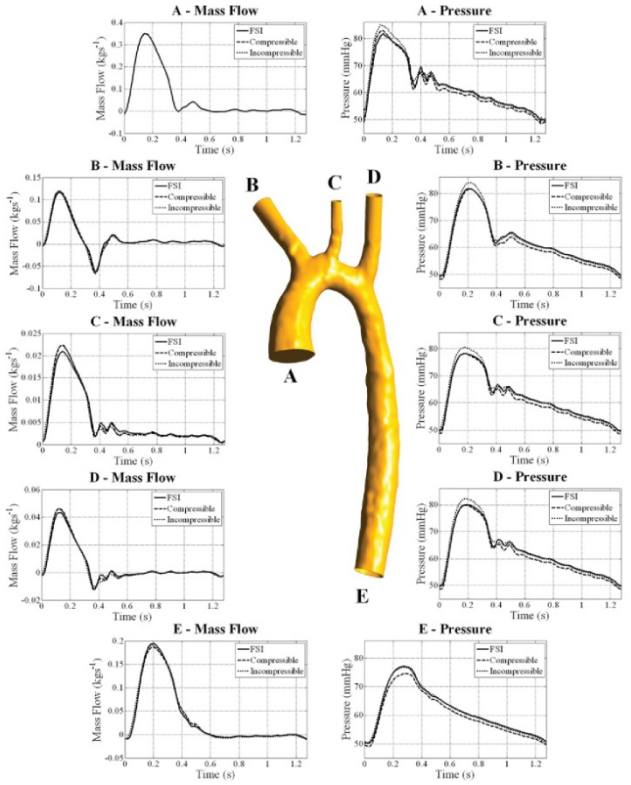

Fig. 5. Comparison of pressure and mass flow rate as predicted by the different CFD methodologies (Solid line—FSI, Dashed line—Compressible Fluid and Dotted line—Incompressible Fluid).

Table 3
Summary of the peak velocity for each CFD methodology at a number of points in the cardiac cycle.

	Max velocity (m/s)		
	FSI	Compressible fluid	Incompressible fluid
Early systole (t=0.05 s)	0.670	0.776	0.930
Peak systole (t=0.15 s)	2.218	2.758	2.847
Late systole (t=0.25 s)	1.895	2.275	2.347
Mid diastole (t=0.95 s)	0.155	0.158	0.151
End diastole (t=1.275 s)	0.114	0.137	0.141

Table 4
Summary of the helical flow index (HFI) for each CFD methodology at a number of points in the cardiac cycle.

	HFI		
	FSI	Compressible fluid	Incompressible fluid
Early systole (t=0.05 s)	0.334	0.309	0.303
Peak systole (t=0.15 s)	0.384	0.386	0.389
Late systole (t=0.25 s)	0.448	0.461	0.461
Mid diastole (t=0.95 s)	0.490	0.441	0.429
End diastole (t=1.275 s)	0.322	0.287	0.271

the commonly held belief that the propagation effects due to the compliance of the aortic wall play a significant effect in the form and magnitude of the travelling waves—even in the presence of the mild coarctation. The peak pressure (in the ascending aorta) in the rigid-walled incompressible fluid simulation is 85.13 mmHg, 3.8% higher than that in the 'gold-standard' FSI simulation. The compressible fluid analogy, by capturing some of the wave transmission characteristics, reduces the error to 1.2% in the ascending aorta. There is a noticeable time lag in the pressure and flow waveforms at the outlets, compared with those at the inlets, in both the FSI and compressible fluid methodologies, which is of course not present in the incompressible fluid methodology. The compressible fluid model is able to accurately capture the time lag when one considers the rising edge of the

Table 5
Summary of the maximum wall shear stress for each cfd methodology at a number of points in the cardiac cycle.

	Max WSS (Pa)		
	FSI	Compressible fluid	Incompressible fluid
Early systole (t=0.05 s)	6.01	7.30	8.62
Peak systole (t=0.15 s)	18.19	23.01	23.49
Late systole (t=0.25 s)	17.72	21.94	22.14
Mid diastole (t=0.95 s)	0.94	0.96	0.93
End diastole (t=1.275 s)	0.73	0.87	0.83

travelling waves. Interestingly the peaks of the pressure and flow waves in the branches (Fig. 5B–D) of the FSI model occur marginally earlier than in the compressible fluid model. This is a limitation of the current compressible fluid methodology. The wave speed is related to the compressibility of the fluid, which is constant throughout the domain, while in the FSI case (and in reality) the wave speed increases in the branches due to the reduced vessel radius.

One of the limitations of the current compressible flow method is that the wave speed is, in principle, constant along the domain. It would be valuable to develop the method further to remove this limitation, for example for the analysis of

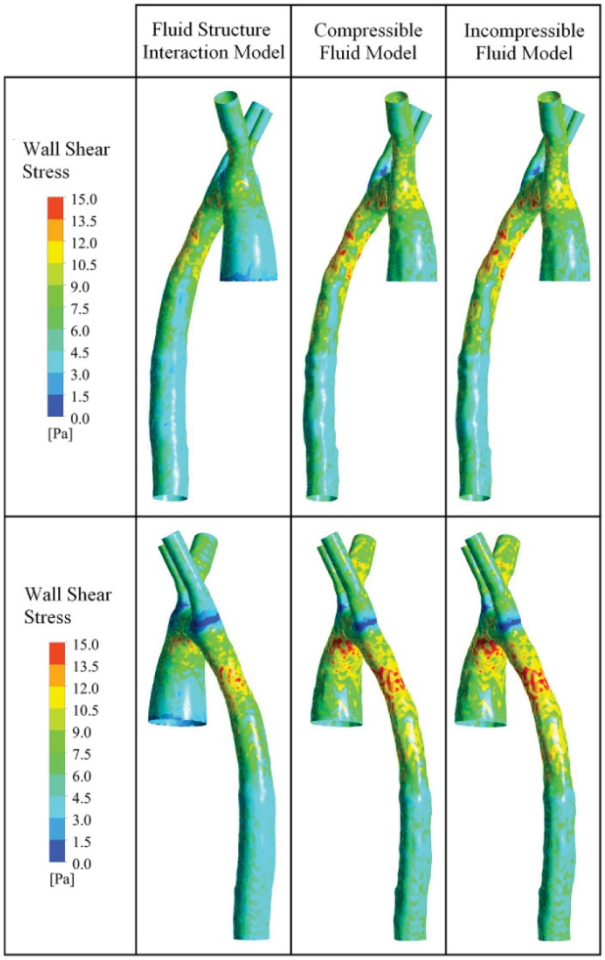

Fig. 6. Comparison of wall shear stress at peak systole (FSI—left, compressible fluid—middle and incompressible fluid—right).

stenosed and tapered vessels. This would require an alternative definition to describe the relationship between pressure and fluid density, which is certainly possible within ANSYS-CFX. It is also possible that a nonlinear pressure–volume relationship could be defined to simulate the non-linear characteristics of the vessel wall, but these developments are beyond the scope of the current paper.

It is important that not only the periodic forms of the flow and pressure waves are accurately captured by the alternative methodologies but also the complex features within the flow field must be comparable and accurately resolved by the simplified models for them to be of use in the clinical setting. In an attempt to compare the flow features the maximum fluid velocity, helical flow index (HFI) and wall shear stress (WSS) were evaluated. The HFI is a measure of the degree of helical flow within a fluid domain (Grigioni et al., 2005; Brown et al., 2011) and can be defined, in an Eulerian manner, as shown:

$$HFI = \int_V \left| \frac{V(\nabla \times V)}{V|\nabla \times V|} \right| dV \quad 0 \le HFI \le 1 \tag{9}$$

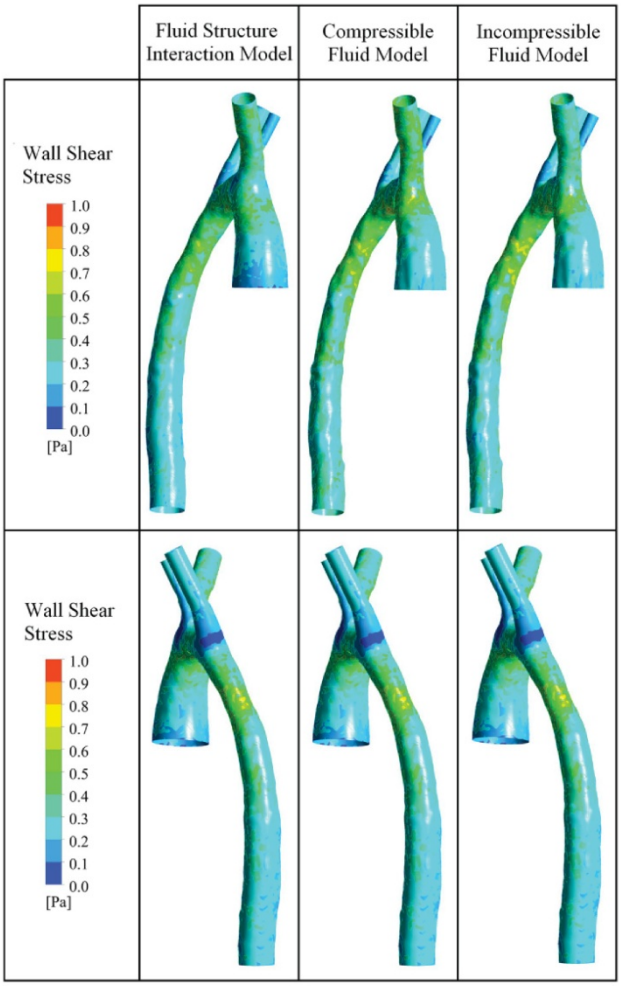

Fig. 7. Comparison of wall shear stress at end diastole (FSI—left, compressible fluid—middle and incompressible fluid—right).

where V and $(\nabla \times V)$ are the vectors of velocity and vorticity and V is the fluid volume.

Tables 3 and 4 summarise the maximum velocity and HFI at a number of points in the cycle.

The rigid-walled models over-predict the maximum velocities in the fluid domain during systole (Table 3) but show good agreement during diastole. These differences in systole are due to the increased fluid volume in the FSI simulation associated with vessel dilation. In contrast the HFI shows better agreement during systole, which could be explained by the elastic recoil of the aorta producing increased helical flow during diastole (Table 4).

In cardiovascular fluid dynamics it is common to use wall shear stress (WSS) as an evaluation parameter for alternative intervention options or device design. Table 5 evaluates the maximum WSS in each model at a number of points across the cardiac cycle, while Fig. 5 and Fig. 6 depict the distribution of WSS at peak systole and end diastole, respectively. The magnitude of WSS in the FSI simulation differs from that computed in the rigid-walled approaches by up to 29% at peak systole. The distribution of the WSS at peak systole is comparable in all three models, with regions of high WSS under the aortic arch and through the restriction in the upper section of the descending aorta, whilst regions of low WSS are predicted at the entrance to the left subclavian and the left common carotid arteries (Fig. 6). This region of low wall shear stress is also apparent at end diastole (Fig. 7) suggesting the flow is detached from the wall in this area at peak systole and end diastole.

Although the errors in the absolute magnitudes of WSS in the rigid-walled models are up to 29% in this patient case, this might nevertheless be within the bounds of our ability to interpret the results in the clinical context. It is likely also that trends and changes, associated for example with prospective interventions, will be well-predicted by the simpler analyses, and this might be very important if many simulations of alternatives need to be performed.

4. Conclusions

In conclusion we have presented the flow field results of a patient-specific aorta as computed from three CFD methodologies of varying levels of complexity. The results have been compared and contrasted in the context of potential clinical practicality. The results suggest that the magnitude and form of the pressure and flow waves are not massively dependent on the compliance of the aortic wall, suggesting that, for some purposes such as computation of pressure gradients, it may be appropriate to employ a simple CFD model rather than a more complex FSI simulation.

It has been shown that the use of a compressible fluid model, tuned to produce the desired wave speed, is able to capture the gross effects of the propagating waves. The resulting waveforms are significantly closer to those obtained from a full FSI analysis than those produced by the more normal incompressible fluid analysis, but at relatively low additional computational cost. Although the compressible flow analysis over-estimates the wall shear stress during systole, it does capture the relative distribution of WSS and may offer a computationally viable alternative to a full FSI model for diagnosis and, in particular, for interventional planning where the analysis of multiple options is required.

Acknowledgements

This research was funded by the European Community's Seventh Framework Programme (FP7/2007–2013) under grant agreement no. 224495 (euHeart project).

References

Barber, D.C., Oubel, E., Frangi, A.F., Hose, D.R., 2007. Efficient computational fluid dynamics mesh generation by image registration. Medical Image Analysis 11, 648–662.

Bazilevs, Y., Gohean, J.R., Hughes, T.J.R., Moser, R.D., Zhang, Y., 2009. Patient-specific isogeometric fluid-structure interaction analysis of thoracic aortic blood flow due to implantation of the Jarvik 2000 left ventricular assist device. Computer Methods in Applied Mechanics and Engineering 198, 3534–3550.

Benim, A.C., Nahavandi, A., Assmann, A., Schubert, D., Feindt, P., Suh, S.H., 2011. Simulation of blood flow in human aorta with emphasis on outlet boundary conditions. Applied Mathematical Modelling 35, 3175–3188.

Brown, A.G., Shi, Y., Arndt, A., Mueller, J., Lawford, P., Hose, D.R., 2011. Importance of realistic LVAD profiles for assisted aortic simulations: evaluation of optimal outflow anastomosis locations. Computer Methods in Biomechanics and Biomedical Engineering.

Causin, P., Gerbeau, J.F., Nobile, F., 2005. Added-mass effect in the design of partitioned algorithms for fluid-structure problems. Computer Methods in Applied Mechanics and Engineering 194, 4506–4527.

Formaggia, L., Gerbeau, J.F., Nobile, F., Quarteroni, A., 2001. On the coupling of 3D and 1D Navier–Stokes equations for flow problems in compliant vessels. Computer Methods in Applied Mechanics and Engineering 191, 561–582.

Grigioni, M., Daniele, C., Morbiducci, U., Del Gaudio, C., D'Avenio, G., Balducci, A., Barbaro, V., 2005. A mathematical description of blood spiral flow in vessels: application to a numerical study of flow in arterial bending. Journal of Biomechanics 38, 1375–1386.

Hose, D.R., Narracott, A.J., Penrose, J.M.T., Baguley, D., Jones, I.P., Lawford, P.V., 2006. Fundamental mechanics of aortic heart valve closure. Journal of Biomechanics 39, 958–967.

Kim, H.J., Vignon-Clementel, I.E., Figueroa, C.A., LaDisa, J.F., Jansen, K.E., Feinstein, J.A., Taylor, C.A., 2009. On coupling a lumped parameter heart model and a three-dimensional finite element aorta model. Annals of Biomedical Engineering 37, 2153–2169.

Lagana, K., Balossino, R., Migliavacca, F., Pennati, G., Bove, E.L., de Leval, M.R., Dubini, G., 2005. Multiscale modeling of the cardiovascular system: application to the study of pulmonary and coronary perfusions in the univentricular circulation. Journal of Biomechanics 38, 1129–1141.

Lam, S., Fung, G., Cheng, S., Chow, K., 2008. A computational study on the biomechanical factors related to stent-graft models in the thoracic aorta. Medical & Biological Engineering & Computing 46, 1129–1138.

Lentner, C., 1990. Geigy Scientific Tables: 5. Heart and Circulation. CIBA-GEIGY.

Migliavacca, F., Balossino, R., Pennati, G., Dubini, G., Hsia, T.Y., de Leval, M.R., Bove, E.L., 2006. Multiscale modelling in biofluidynamics: application to reconstructive paediatric cardiac surgery. Journal of Biomechanics 39, 1010–1020.

Moireau, P., Xiao, N., Astorino, M., Figueroa, C.A., Chapelle, D., Taylor, C.A., Gerbeau, J.F., 2011. External tissue support and fluid-structure simulation in blood flows. Biomechanics and Modeling in Mechanobiology.

Shi, Y., Lawford, P., Hose, R., 2011. Review of 0-D and 1-D models of blood flow in the cardiovascular system. Biomedical Engineering Online 10, 33.

Singh, P.K., Marzo, A., Coley, S.C., Berti, G., Bijlenga, P., Lawford, P.V., Villa-Uriol, M.C., Rufenacht, D.A., McCormack, K.M., Frangi, A., Patel, U.J., Hose, D.R., 2009. The role of computational fluid dynamics in the management of unruptured intracranial aneurysms: a clinicians' view. Computational Intelligence and Neuroscience, 760364.

Spilker, R.L., Taylor, C.A., 2010. Tuning multidomain hemodynamic simulations to match physiological measurements. Annals of Biomedical Engineering 38, 2635–2648.

Vignon-Clementel, I.E., Figueroa, C.A., Jansen, K.E., Taylor, C.A., 2006. Outflow boundary conditions for three-dimensional finite element modeling of blood flow and pressure in arteries. Computer Methods in Applied Mechanics and Engineering 195, 3776–3796.

Villa-Uriol, M.C., Berti, G., Hose, D.R., Marzo, A., Chiarini, A., Penrose, J., Pozo, J., Schmidt, J.G., Singh, P., Lycett, R., Larrabide, I., Frangi, A.F., 2011. @neurIST complex information processing toolchain for the integrated management of cerebral aneurysms. Interface Focus 1, 308–319.

Wolters, B.J.B.M., Rutten, M.C.M., Schurink, G.W.H., Kose, U., de Hart, J., van de Vosse, F.N., 2005. A patient-specific computational model of fluid-structure interaction in abdominal aortic aneurysms. Medical Engineering & Physics 27, 871–883.